Local polarization dynamics in ferroelectric materials

2010 Rep. Prog. Phys. 73 056502

(http://iopscience.iop.org/0034-4885/73/5/056502)

Rep. Prog. Phys. **73** (2010) 056502 (67pp) doi:10.1088/0034-4885/73/5/056502

Local polarization dynamics in ferroelectric materials

Sergei V Kalinin[1,5], **Anna N Morozovska**[2], **Long Qing Chen**[3] and **Brian J Rodriguez**[4,5]

[1] The Center for Nanophase Materials Sciences and Materials Sciences and Technology Division, Oak Ridge National Laboratory, Oak Ridge, TN 37831, USA
[2] V. Lashkaryov Institute of Semiconductor Physics, National Academy of Sciences of Ukraine, 41, pr. Nauki, 03028 Kiev, Ukraine
[3] Department of Materials Science and Engineering, The Pennsylvania State University, University Park, PA, 16802, USA
[4] Conway Institute of Biomolecular and Biomedical Research, University College Dublin, Belfield, Dublin 4, Ireland

E-mail: sergei2@ornl.gov and brian.rodriguez@ucd.ie

Received 13 July 2009, in final form 7 January 2010
Published 7 April 2010
Online at stacks.iop.org/RoPP/73/056502

Abstract
Ferroelectrics and multiferroics have recently emerged as perspective materials for information technology and data storage applications. The combination of extremely narrow domain wall width and the capability to manipulate polarization by electric field opens the pathway toward ultrahigh (>10 TBit inch^{-2}) storage densities and small (sub-10 nm) feature sizes. The coupling between polarization and chemical and transport properties enables applications in ferroelectric lithography and electroresistive devices. The progress in these applications, as well as fundamental studies of polarization dynamics and the role of defects and disorder on domain nucleation and wall motion, requires the capability to probe these effects on the nanometer scale. In this review, we summarize the recent progress in applications of piezoresponse force microscopy (PFM) for imaging, manipulation and spectroscopy of ferroelectric switching processes. We briefly introduce the principles and relevant instrumental aspects of PFM, with special emphasis on resolution and information limits. The local imaging studies of domain dynamics, including local switching and relaxation accessed through imaging experiments and spectroscopic studies of polarization switching, are discussed in detail. Finally, we review the recent progress on understanding and exploiting photochemical processes on ferroelectric surfaces, the role of surface adsorbates, and imaging and switching in liquids. Beyond classical applications, probing local bias-induced transition dynamics by PFM opens the pathway to studies of the influence of a single defect on electrochemical and solid state processes, thus providing model systems for batteries, fuel cells and supercapacitor applications.

(Some figures in this article are in colour only in the electronic version)

[5] Authors to whom any correspondence should be addressed.

Contents

1. Physics and applications of ferroelectric materials

1.1. Ferroelectric materials and applications

Ferroelectric materials have become the prototypical example of functional oxides since the discovery of ferroelectricity in $BaTiO_3$ (BTO) in the mid-1940s [1, 2]. For several decades, ferroelectric ceramics and single crystals were explored as materials for ultrasonic transducers in SONAR systems and, later, medical ultrasound imaging [3–7]. Correspondingly, much of the early research in the field was driven by the applications of ferroelectrics as electromechanically active materials [8]. The advances in thin film synthesis and microfabrication technologies in the last two decades have resulted in rapid development of electromechanical applications of ferroelectrics on the micrometer scale in microelectromechanical systems and actuators [9–12].

The synergy between the advances in single crystal growth and basic studies of ferroelectrics in the 1950s and 1960s has enabled a broad spectrum of applications in electro-optical systems and photothermal imaging [13–16]. As with electromechanical applications, the current trend in miniaturization of device component size resulted in multiple applications of ferroelectric materials for tunable nanoscale optics, nanophotonics and plasmonics [17, 18].

From the early days of ferroelectrics, much attention has been paid to the applications of ferroelectrics in information technologies. The presence of two or more stable polarization states (figure 1(*a*)), the ease of polarization switching by electric field and the small domain wall width suggested extraordinarily high storage densities, while coupling between polarization and optical and transport properties held the promise of efficient read-out mechanisms. Since the early 1950s, a number of patents on ferroelectric memory diodes, ferroelectric field-effect transistors and domain wall based storage have been filed [19–21]. However, the large switching biases ($\gg$10 V) required for polarization manipulation in single crystals rendered these applications impractical at that time. The advances in sol–gel film synthesis of thin films with coercive biases well below $\sim$10 V in the early 1990s rendered the information technology applications of ferroelectrics feasible [22, 23]. The first examples were the ferroelectric random access memories (FeRAM), in which the dielectric in a standard dynamic random access memory (DRAM) capacitor is substituted with a ferroelectric, adding the advantage of non-volatility. Similarly, the combination of a semiconductor channel and a ferroelectric gate enabled ferroelectric gate transistors. The seminal work by Ahn *et al* has demonstrated the potential of ferroelectric field effect manipulation in superconducting, semiconductor and organic materials [24–26]. Future progress in this area requires ferroelectric–semiconductor integration technologies that preserve interface quality [27–29].

Advances in understanding order parameter coupling in strongly correlated oxides and atomic-level control of film growth in molecular beam epitaxy and pulsed laser deposition (PLD) [30–32] have stimulated interest in magnetoelectric and multiferroic applications [33–37]. Extensive analysis of the potential applications and relevant fundamental scientific issues are now available [38–41]. The recently studied relationship between ferroelectricity and electronic transport suggests tremendous potential for resistive memory applications [42–44]. Extending beyond the realm of electronic devices, the photovoltaic effect on ferroelectric surfaces and polarization-controlled reactivity has also been demonstrated [45–48], and ferroelectric lithography has been used to fabricate nanostructures [49–51].

The fundamental property of ferroelectric materials that enables their application in functional materials and heterostructures is the presence of switchable polarization and associated domain structures. Polarization switching directly underpins the functionality of data storage [13, 52], FeRAMs [30, 53] and electroresistive [42, 54] memories. The motion of domain walls and interface boundaries enables high electromechanical coupling coefficients in polycrystalline ferroelectrics and relaxors. The continuous tendency for miniaturization of electronic and optical components necessitates the understanding of ferroelectric phase stability

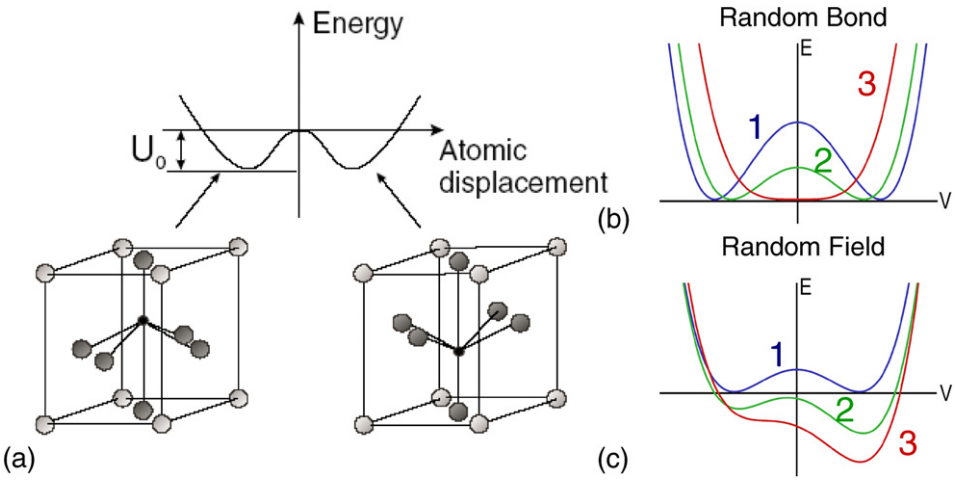

Figure 1. (*a*) Double well potential and ferroelectric unit cell. (*b*) Random bond (symmetric) and (*c*) random field (asymmetric) disorder in a ferroelectric material. Curves (1) correspond to a defect-free material, (2) to the presence of a weak random bond (*b*) and random field (*c*) defect and (3) to the limiting of a non-polar phase and polar non-ferroelectric phases, respectively. Panel (*a*) reproduced with permission from [64], copyright 2002 by The American Physical Society. Panels (*b*), (*c*) reproduced from [65], copyright 2008, Nature Publishing Group.

and particularly of polarization switching in dimensionally confined systems, such as thin films, nanowires and nanoparticles [55–63]. Complementary to these is the need to understand the role of defects and long-range strain and electrostatic fields on polarization switching. Below, we summarize some of the relevant aspects of ferroelectric physics.

1.2. Ferroelectrics at the nanoscale

1.2.1. Physics of low-dimensional ferroelectrics. The role of nanoscale confinement on ferroelectric phase stability, a necessary precondition to polarization switching, has been explored intensively since the early 1950s. A number of authoritative reviews [66–68] have been published recently, addressing this issue in detail. Generally, it is believed that the reduction in size lowers the stability of the ferroelectric phase by decreasing the effective Curie temperature and precipitating the transition to a cubic non-polar phase. In thin films, the difference in boundary conditions can result in large built-in electric fields, stimulating the transition to a polar non-ferroelectric phase. These mechanisms can be linked to random bond and random field disorder potential components, as shown in figures 1(*b*) and (*c*).

The primary factors controlling ferroelectric phase stability are depolarization field effects arising from the termination of polarization at ferroelectric surfaces. These effects govern domain formation and are influenced by chemical screening, surface chemistry and size and strain effects. At critical values of the depolarization field, toroidal ferroelectric polarization states are expected to exist as predicted by Ginzburg *et al* [69], Gorbatsevich *et al* [70], and later studied on atomistic level by Naumov *et al* [71], Bellaiche and Prosandeev and by several other groups [72–76]. Recently, experimental evidence consistent with the formation of vortex domain states has been reported in circular capacitor structures [77] and nanoferroelectric $PbZr_xTi_{1-x}O_3$ (PZT) arrays [78].

1.2.2. Physics of polarization reversal processes. To parallel the understanding of fundamental aspects of ferroelectric behavior at the nanoscale, a large number of studies have been focused on the applied physics of ferroelectric materials, particularly on mechanisms of polarization switching, including domain nucleation, phase stability and domain wall motion.

The mechanism of polarization reversal was first addressed in the seminal paper by Landauer [79], who analyzed the free energy of a ferroelectric nucleus and demonstrated that experimentally observed nucleation fields correspond to unphysically large critical nuclei and activation energies. This study strongly suggests that polarization switching, similar to other first order phase transitions, is controlled by defects. In parallel, a number of authors have explored alternative mechanisms to address the Landauer paradox, including the lowering of the nucleation bias due to suppression of depolarization fields by tunneling [80], the presence of built-in electrostatic fields (which is equivalent to defects) [81] and correlated switching [82]. The work by Kay and Dunn (KD) has extended the Landauer model to study the thickness dependence of the coercive bias, giving rise to the famous 2/3 power law [83]. Remarkably, despite the number of the overly restrictive approximations underpinning the KD model, the law has been experimentally demonstrated to be valid down to the nanometer level [84].

The second key aspect of polarization switching processes is domain wall motion. The seminal studies by Merz have explored the field–velocity relationship for walls in crystals [85]. The fundamental mechanism of wall motion was studied by Miller and Weinreich, who predicted that the small width of the domain wall necessitates motion through the formation of 2D domains [86]. This model was extended by Burtsev and Chervonobrod [87] to include the effects of finite lattice potential and wall width. Finally, the recent studies by the Rappe group [88] have elucidated the atomistic mechanisms for domain wall motion.

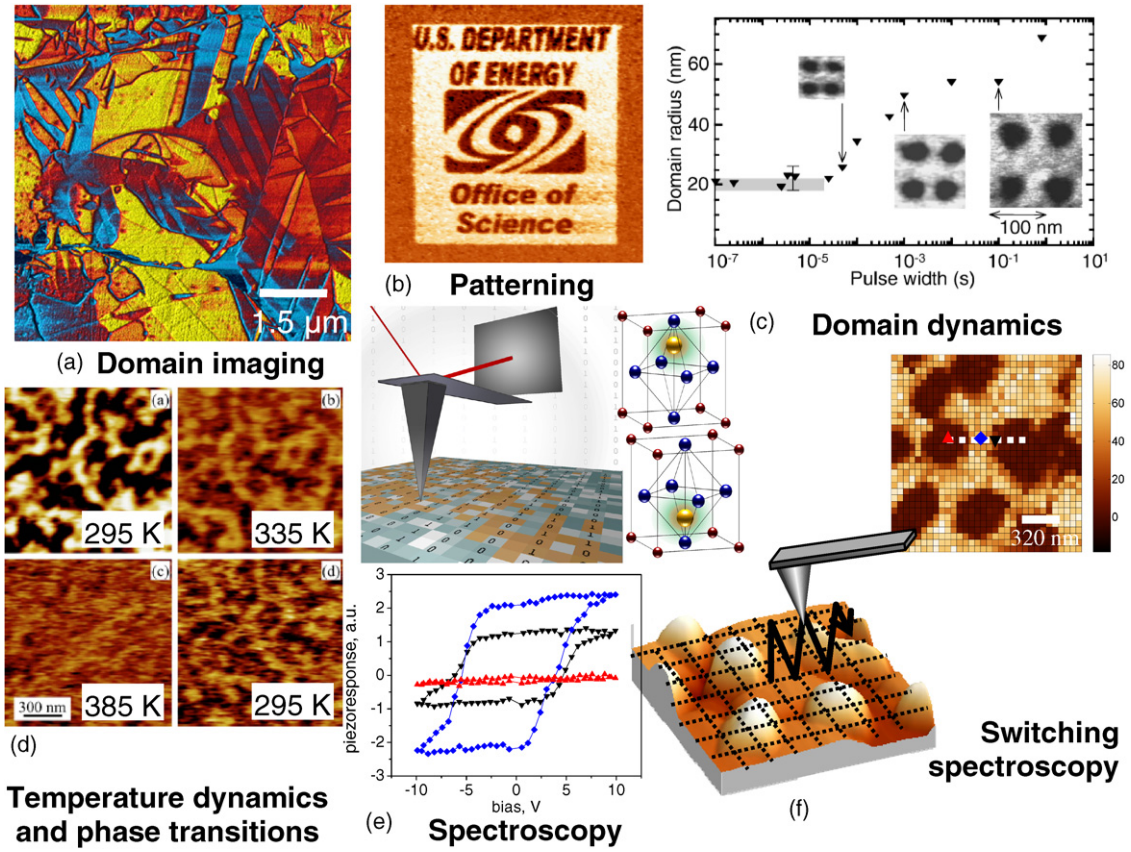

Figure 2. Applications of PFM. (*a*) Domain imaging (*b*) domain patterning, (*c*) studies of domain dynamics, (*d*) phase transformations, (*e*) spectroscopy and (*f*) switching spectroscopy mapping. Panel (*a*) reproduced with permission from [102]. Panel (*c*) reproduced with permission from [64] and copyright 2002, American Physical Society. Panel (*d*) reproduced with permission from [103]. Copyright 2007, American Institute of Physics. Panels (*e*) and (*f*) are reproduced from [104]. Copyright 2007, IOP Publishing.

Domain wall motion and geometry are strongly affected by the presence of defects that can act as pinning centers. The interplay between the driving force and disorder gives rise to a broad spectrum of domain wall motion dynamics, including reversible vibrations, creep and sliding. The interface dynamics in disordered media was studied by Natterman [89] and Giamarchi [90] and experimental studies have recently been summarized by Kleeman [91]. Remarkably, most statistical theories are universal and can be developed for a given class of order parameter for cases of the pinning controlled by single defects (strong pinning) or by fluctuations in defect densities (weak pinning). The elementary mechanisms of pinning and defect–domain wall interactions were studied on a mesoscopic level by Sidorkin [92].

In most materials, the nucleation and wall motion proceed simultaneously, resulting in complex kinetics. The realization of the role of defects on polarization switching led to a number of statistical theories for the description of switching phenomena by extending the Kolmogorov–Avrami [93, 94] theory to polarization switching [95–97]. In these approaches, the spatial and energy distribution of defects become the fundamental parameter describing the switching process. Finally, a number of authors report on unusual physical phenomena during domain nucleation, including wall-mediated switching (see, e.g., [98]) and skyrmion emission [99].

1.3. Local probing of ferroelectric materials

Understanding polarization reversal mechanisms and domain wall dynamics on the nanometer scale has received a huge impetus from the development of imaging probes capable of addressing domain behavior locally. Since the 1950s, optical microscopy observations [4] in polarized light, using domain decoration or chemical etching, have been used to explore domain structures and geometries and kinetics of wall motion [3, 4, 100, 101]. The limiting factor has been the destructive nature of etching and low (∼micrometers) spatial resolution of optical methods that limited the studies to single crystals and large ($>1\ \mu$m) grain ceramics.

The revolution in nanoscale domain studies occurred with the invention of piezoresponse force microscopy (PFM), the primary topic of this review. The multitude of PFM applications is illustrated in figure 2. Here, we focus on the basic mechanism underpinning PFM operation, imaging and resolution theory, and the theory of tip-induced polarization switching on ideal surfaces and in the presence of defects. Furthermore, we discuss recent applications of spectroscopic imaging modes in PFM, including space- and time-resolved spectroscopies, and illustrate their applications for probing local switching behavior in nanoscale ferroelectrics. This review complements several recent reviews addressing phenomenological aspects of PFM imaging and applications [105–111].

2. Principles and instrumental aspects of PFM

2.1. Basic principles of PFM

The PFM approach for probing piezo- and ferroelectric properties at the nanoscale is based on the strong coupling between polarization and electromechanical behavior. Correspondingly, these behaviors can be addressed by applying a highly localized electric field to the material and probing the resultant minute surface displacements with ∼picometer precision. Atomic force microscopy (AFM) [112] provides an ideal platform for these studies due to intrinsically high vertical resolutions, and high localization of electric fields at the junction between the metalized tip and the surface. Hence, PFM is a contact-mode AFM technique in which an electrically biased conductive AFM tip is used as a probe of local electromechanical coupling via the converse piezoelectric effect. Remarkably, the basic image formation mechanism in PFM is complementary to force-based AFM methods (force is applied and the tip deflection is measured) and scanning tunneling microscopy (STM) [113] (bias is applied, and a current is measured). This unique mechanism defines all aspects of PFM operation, including resolution, quantitativeness and the potential for the use of resonance enhancement, as discussed below.

Following the invention of STM (1982) and AFM (1986) [112–114], the first instances of measuring bias-induced sample deformation in piezoelectric materials by a scanning probe came in 1991 when piezoelectric response, or piezoresponse (PR), was measured using scanning acoustic microscopy [115] and STM [116]. Shortly thereafter, the first papers on piezoelectric measurements [117] and ferroelectric domain visualization [118, 119] by AFM were reported. Papers by Takata *et al* [120, 121] (using strain imaging via tunneling acoustic microscopy), Franke *et al* [122], Kolosov *et al* [123], Gruverman *et al* [124–128] and Hidaka *et al* [129] followed. The work of Gruverman *et al* is particularly notable for demonstrating imaging and switching in inorganic ferroelectrics and coining the terms 'Piezoresponse' and 'PFM' which have now become standard. In the past decade and a half, PFM has become the premier tool for studying static and dynamic properties of ferroelectric materials, as evidenced by a number of recent books and reviews [106–111]. PFM has been extended beyond ferroelectric thin films, ceramics and crystals to ferroelectric polymers [130–137], piezoelectric semiconductors (GaN [138, 139] AlN [140, 141] and ZnO [142–144]) and piezoelectric biopolymers, including collagen [145–152] and chitin [153, 154].

2.1.1. Elementary theory of PFM. In PFM, a voltage is applied to a conductive tip

$$V_{\text{tip}} = V_{\text{dc}} + V_{\text{ac}}\cos(\omega t) \tag{2.1}$$

in contact with a piezoelectric material. Here V_{dc} is the dc bias (switching bias), V_{ac} is the ac bias (probing bias) and ω is the ac bias frequency (driving frequency).

As the sample expands and contracts due to the converse piezoelectric effect, the tip deflection is monitored using a lock-in amplifier so that the tip oscillation

$$A = A_0 + A_{1\omega}\cos(\omega t + \varphi)\,, \tag{2.2}$$

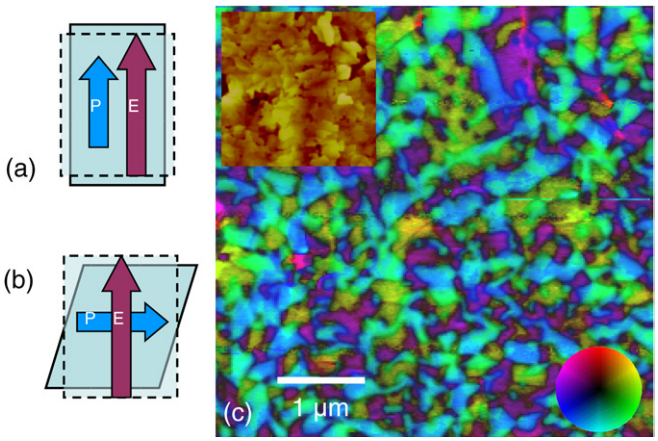

Figure 3. The sample deformation can be detected via a tip deflection caused by the (*a*) expansion or contraction of the piezoelectric material or via a tip torsion caused by the (*b*) shear deformation of the material. The deflection and torsion signals represent vector components of the polarization and can be combined to determine the real space polarization orientation via (*c*) vector PFM ($BiFeO_3$ (BFO) film, topography inset). Reprinted from [111]. Copyright 2008, Cambridge University Press.

and hence the sample deformation at the driving frequency of the ac voltage, $A_{1\omega}$, is recorded simultaneously with topography. Here A_0 is the static surface displacement and φ is the phase shift between the driving voltage V_{ac} and the voltage-induced deformation, $A_{1\omega}$. The PFM amplitude provides information on the magnitude of the local electromechanical coupling, while the PFM phase image provides information on the ferroelectric domain orientation. Typically the imaging resolution of PFM is less than ∼10–30 nm as determined from half of the width of a domain wall in the mixed PFM signal,

$$PR = A_{1\omega} \cdot \cos(\varphi)\,. \tag{2.3}$$

The resolution is ultimately limited by the tip–sample contact area (nominally determined by the radius of the tip apex), though additional mechanisms for broadening such as electrostatic interactions and the formation of a liquid neck in the tip–surface junction are possible. Note that PFM can also be used to visualize the domain structure through a metal electrode. In this case, the field is applied uniformly across the ferroelectric capacitor, and the resolution is limited by the thicknesses of the top electrode and ferroelectric layer [155].

In addition to the time-dependent flexural vibration signals, the torsional oscillation of the cantilever can be monitored in order to measure piezoelectric shear deformations via the frictional force resulting from any in-plane component of polarization. This in-plane PFM, commonly called lateral PFM (LPFM) in contrast to out-of-plane PFM or vertical PFM (VPFM), was first demonstrated by Eng *et al* [156, 157] and has been applied to a number of materials systems including films, crystals, nanostructures and capacitors [158–163]. The in- and out-of-plane polarization information can be combined to reconstruct the real space polarization via vector PFM [164] (figure 3).

2.1.2. PFM versus other SPMs. The fundamental factors underpinning the contrast formation mechanism in any

scanning probe microscopy (SPM) method are (a) the tensorial nature of the signal, (b) the signal dependence on contact radius (contact) or tip–surface separation (non-contact) and (c) the signal dependence on the cantilever spring constant. These factors determine the strategies for instrumentation and technique development and the potential for quantitative measurements. The image formation mechanism in PFM as compared with conventional current based (e.g. STM and conductive AFM) and force-based (AFM) techniques has been analyzed recently [110] and was shown to be complementary to that in other SPMs. In particular, a weak dependence of the PFM signal on the contact area implies that electromechanical measurements are (a) intrinsically quantitative, and do not require extensive probe calibration and (b) the signal is relatively insensitive to topographic cross-talk at low frequencies. On the other hand, resonance enhancement cannot be directly employed in PFM, since the resonance frequency is determined by mechanical, rather than electromechanical, properties of the material, necessitating the development of resonance-tracking methods based on the amplitude-signal feedback [165], fast lock-in sweeps [166], fast imaging [167] and broad-band excitation schemes [168]. Finally, quadratic bias dependence of electrostatic forces, as compared with linear piezoelectric interactions, suggests that the electromechanical signal cannot be unambiguously distinguished from the electrostatic signal [169, 170]. These considerations suggest strategies for improving PFM resolution and sensitivity, as discussed in section 2.3.

2.2. Contact mechanics of PFM

Analysis of SPM contrast requires an understanding of fundamental tip–surface interactions. In the case of PFM, this is equivalent to contact electromechanics, or the relationship between indentation force, probe displacement and tip bias. These $F_c(h, V_{tip})$ surfaces provide the 2D analog of force–distance curves in standard force based SPMs [171].

2.2.1. Exact solution for contact electromechanics. The rigorous solution of the piezoelectric indentation problem, i.e. the $F_c(h, V_{tip})$ dependence, is currently available only for the case of transversally isotropic materials in the continuum mechanics limit [172–174]. In this case, the electric field generated outside the contact area is neglected due to the large difference in dielectric constants between the piezoelectric and ambience. Karapetian *et al* [175, 176] have derived stiffness relations linking the applied force, P, and the concentrated charge, Q, with indentor displacement, w_0, indentor potential, ψ_0, indentor geometry and materials properties. The solutions for flat, spherical and conical indentor geometries have the following phenomenological structure:

$$P = \frac{2}{\pi}\theta\left(h^{n+1}C_1^* + (n+1)\,h^n\psi_0 C_3^*\right), \tag{2.4}$$

$$Q = \frac{2}{\pi}\theta\left(-h^{n+1}C_3^* + (n+1)\,h^n\psi_0 C_4^*\right), \tag{2.5}$$

where h is the total indentor displacement, θ is a geometric factor ($\theta = a$ for flat indentors with contact radius a, $\theta = (2/3)R^{1/2}$ for spherical indentors with curvature R and $\theta = (1/\pi)\tan\alpha$ for conical indentors with conic angle α) and the power $n = 0$ for flat, $n = 1/2$ for the spherical and $n = 1$ for the conical indentors, respectively.

These stiffness relations provide an extension of the corresponding results of Hertzian mechanics [177] and continuum electrostatics [178, 179] to the transversely isotropic piezoelectric medium. From this analysis, the maximum information that can be obtained from SPM or nanoindentation experiments on transversally isotropic materials is limited to the indentation elastic stiffness, C_1^*, the indentation piezocoefficient, C_3^*, and the indentation dielectric constant, C_4^*. Indentation stiffnesses are complex functions of electroelastic constants of a material, $C_i^* = C_i^*(c_{ij}, e_{ij}, \varepsilon_{ij})$, where c_{ij} are elastic stiffnesses, e_{ij} are piezoelectric constants and ε_{ij} are dielectric constants. The tip–surface resonance frequency (i.e. the signal in atomic force acoustic microscopy) is related to C_1^*, while electromechanical response (PFM signal amplitude) is given by C_3^*/C_1^*. It has been shown that for most materials $C_3^*/C_1^* \sim d_{33}$ (within a factor of ~2) and $C_4^* \approx \sqrt{\varepsilon_{11}\varepsilon_{33}}$ (within ~10–20%). The electroelastic fields produced by the indentor rapidly adopt the form of a point charge/point force at distances comparable to the contact radius, justifying the use of this approximation for analysis of switching dynamics at late stages. The early stages of switching and nucleation necessitate the analysis of complete field structure, as analyzed below.

2.2.2. Decoupling approximation in contact electromechanics. The necessity for calculating the PFM signal for materials of general symmetry as well as calculation of response at micro- and nanostructural elements such as domain walls, cylindrical domains and topographically inhomogeneous ferroelectrics such as nanoparticles have stimulated theoretical attempts to derive approximate solutions for position-dependent PFM signal in inhomogeneous materials.

A general approach for the calculation of the electromechanical response is based on the decoupling approximation. In this case, (a) the electric field in the material is calculated using a rigid electrostatic model (no piezoelectric coupling, $d_{ijk} = e_{ijk} = 0$), (b) the strain or stress field is calculated using constitutive relations for a piezoelectric material, $X_{ij} = E_k e_{kij}$ and (c) the displacement field is evaluated using the elasticity theory for an isotropic or anisotropic solid. A simplified 1D version of the decoupling model was originally suggested by Ganpule [180] to account for the effect of 90° domain walls on PFM imaging. A similar 1D approach was adapted by Agronin *et al* [181] to yield closed-form solutions for the PFM signal. The 3D version of this approach was developed by Felten *et al* [182] using the analytical form for the corresponding Green's function. Independently, Scrymgeour and Gopalan [183] have used the finite element method to model PFM signals across domain walls. Recently, Kalinin *et al* [184], Eliseev *et al* [185] and Morozovska *et al* [186] have applied the decoupling theory to derive analytical expressions

for the PFM response of materials with low symmetry, derive analytical expressions for the PFM resolution function and domain wall profiles, and interpret PFM spectroscopy data, as described below.

In the decoupling approximation, the PFM signal, i.e. the surface displacement $u_i(\boldsymbol{x}, \boldsymbol{y})$ at location $\boldsymbol{x}$ induced by the tip at position $\boldsymbol{y} = (y_1, y_2)$ is given by

$$u_i(\boldsymbol{x},\boldsymbol{y}) = \int_{-\infty}^{\infty} d\xi_1 \int_{-\infty}^{\infty} d\xi_2 \int_{0}^{\infty} d\xi_3 \frac{\partial G_{ij}(x_1-\xi_1, x_2-\xi_2, \xi_3)}{\partial \xi_k} \times E_l(\boldsymbol{\xi}) c_{kjmn} d_{\ln m}(y_1+\xi_1, y_2+\xi_2, \xi_3). \quad (2.6)$$

Here, coordinate $\boldsymbol{x} = (x_1, x_2, z)$ is linked to the indentor apex, coordinates $\boldsymbol{y} = (y_1, y_2)$ denote indentor position in the sample coordinate system, $\boldsymbol{y}$. Coefficients $d_{lnm}(\boldsymbol{y})$ and c_{kjmn} are position dependent components of the piezoelectric strain and elastic stiffness tensors, respectively. $E_l(\boldsymbol{x})$ is the electric field strength distribution produced by the probe. Green's function for a semi-infinite medium $G_{3j}(\boldsymbol{x} - \boldsymbol{\xi})$ links the eigenstrains $d_{lnm} c_{kjmn} E_l(\boldsymbol{x})$ to the displacement field, and thus allows calculating the *nonlocal* displacement field from *local* field-induced strains. For most inorganic ferroelectrics, the elastic properties are weakly dependent on orientation and hence can be approximated as elastically isotropic, and integrals in equation (2.6) can be evaluated in the closed form. The corresponding Green's tensor, $G_{ij}(\boldsymbol{x} - \boldsymbol{\xi})$, for an elastically isotropic half-plane is given by Lur'e [187] and Landau and Lifshitz [188].

This approach is rigorous for materials with small piezoelectric coefficients. A simple validity estimation is based on the value of the square of the dimensionless electromechanical coupling coefficients $k_{ij}^2 = (d_{ij})^2/(s_{jj}\varepsilon_{ii})$. For instance, for barium titanate (BTO) single crystal: $k_{15}^2 \approx 0.32$, $k_{31}^2 \approx 0.10$ and $k_{33}^2 \approx 0.31$, for the ceramics lead zirconate titanate (PZT) [PZT6B grade]: $k_{15}^2 \approx 0.14$, $k_{31}^2 \approx 0.02$ and $k_{33}^2 \approx 0.13$ and for a quartz single crystal: $k_{11}^2 \approx 0.01$, suggesting that the error in the decoupling approximation does not exceed ~30% for strongly piezoelectric materials and is on the order of ~1% for weak piezoelectrics.

2.2.2.1. Approximate solution for homogeneous media. The use of the decoupling approximation reduces an extremely complex coupled contact mechanics problem with mixed boundary conditions to the solutions of much simpler electrostatic and mechanical Green's function problems, and numerical or analytical integration of the result. We note that the dielectric and particularly elastic properties described by positively defined second- and fourth-rank tensors (invariant with respect to 180° rotations) are necessarily more isotropic than the piezoelectric properties described by third-rank tensors (anti-symmetric with respect to 180° rotations). Hence, elastic and dielectric properties of a material can often be approximated as isotropic. In this case, integrals in equation (2.6) can be evaluated, and surface displacement can be written in the form $u_i(\boldsymbol{x}) = V_Q W_{ijlk}(\boldsymbol{x}) d_{kjl}$, where the tensor $W_{ijlk}(\boldsymbol{x})$ is symmetrical on the transposition of the indices j and l. In Voigt notation, the displacements are [184]

$$u_1(0) = V_Q(W_{111}d_{11} + W_{121}d_{12} + W_{131}d_{13} + W_{153}d_{35} + W_{162}d_{26}), \quad (2.7a)$$

$$u_2(0) = V_Q(W_{121}d_{21} + W_{111}d_{22} + W_{131}d_{23} + W_{153}d_{34} + W_{162}d_{16}), \quad (2.7b)$$

$$u_3(0) = V_Q(W_{313}(d_{31}+d_{32}) + W_{333}d_{33} + W_{351}(d_{24}+d_{15})). \quad (2.7c)$$

The non-zero elements of the tensor $W_{i\alpha k}$ are

$$W_{111} = -(13+4\nu)/32, \quad W_{121} = (1-12\nu)/32, \quad W_{131} = -1/8, \quad W_{153} = -3/8, \quad (2.8a)$$

$$W_{162} = -(7-4\nu)/32, \quad W_{313} = -(1+4\nu)/8, \quad W_{333} = -3/4, \quad W_{351} = -1/8. \quad (2.8b)$$

Here V_Q is the electrostatic potential at the point $\boldsymbol{x} = (0, 0, 0)$ produced by a probe represented by the set of image charges located on a vertical line. Thus, the response is shown to be proportional to the potential induced by the tip on the surface. The latter fundamental result was generalized as response theorems [185].

Response theorem 1. For a transversally isotropic piezoelectric solid in an isotropic elastic approximation and an arbitrary point charge distribution in the tip (not necessarily constrained to a single line), the vertical surface displacement is proportional to the surface potential induced by tip charges in the point of contact.

Response theorem 2. For an anisotropic piezoelectric solid in the limit of dielectric and elastic isotropy, the vertical and lateral PFM signals are proportional to the potential on the surface induced by the tip if the tip charges and the point of contact are located on the same line along the surface normal.

Equations (2.8*a*) and (2.8*b*) thus constitute approximate PFM contrasts for anisotropic materials in the limit of elastic and dielectric isotropy. For lower material symmetries, the analytical expressions of the displacement fields induced by the point charge allow response calculations for asymmetric tips or probes with special geometry [185].

2.2.2.2. Orientational imaging. In piezoelectric materials, the strong orientation dependence of electromechanical response [189–194] opens the pathway to orientation imaging [148]. Briefly, the orientation of a 3D object in the laboratory coordinate system is given by three Euler angles (θ, φ, ψ). The relationship between the d_{ijk} tensor in the laboratory coordinate system and the d_{ijk}^0 tensor in the crystal coordinate system is $d_{ijk} = A_{il}A_{jm}A_{kn}d_{lmn}^0$, where $A_{ij}(\theta, \varphi, \psi)$ is the rotation matrix [195]. Experimentally, PFM measures three components of the response vector. Hence, local crystallographic orientation can be determined from the solutions of equations (2.7*a*)–(2.7*c*), which can graphically be represented as response surfaces. As an example, we compare vertical displacement, u_3, surfaces with piezoelectric tensors, d_{33}, and surfaces for tetragonal $PbTiO_3$ (PTO) and

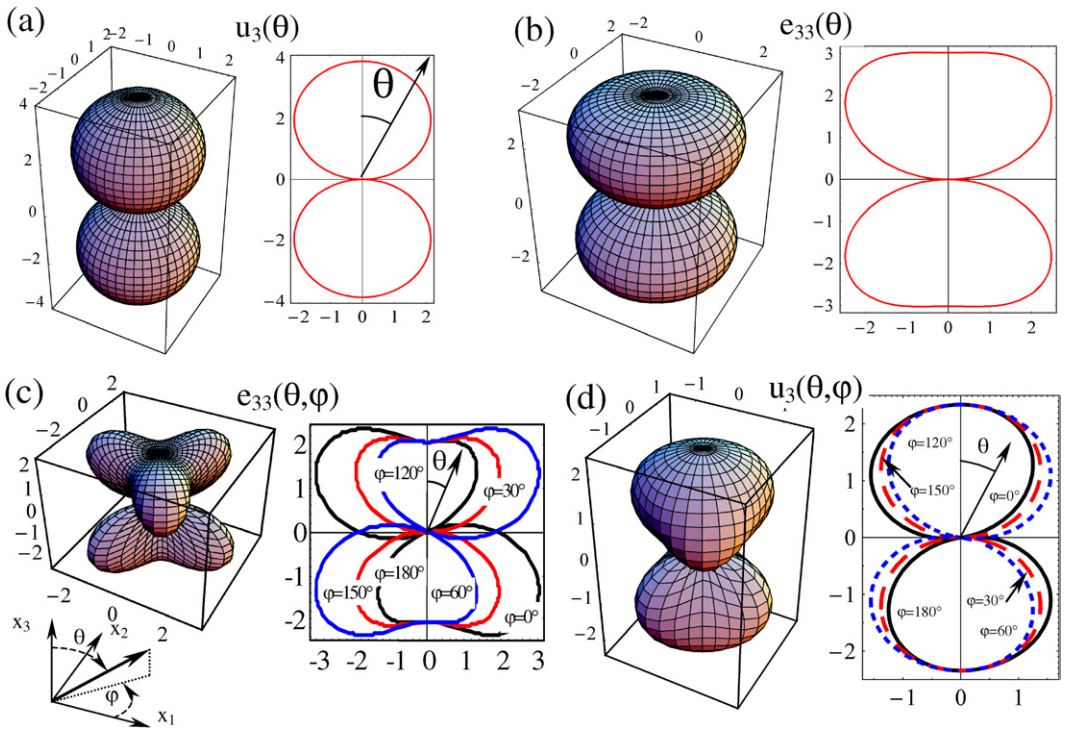

Figure 4. The dependence of (*a*) displacement u_3, (*b*) piezoelectric tensor component e_{33}, for $PbTiO_3$ (PTO, $\nu = 0.3$ (Poisson's ratio)) on Euler's angle θ in the laboratory coordinate system. The dependence of (*c*) piezoelectric tensor component e_{33} and (*d*) displacement u_3 for $LiTaO_3$ (LTO, $\nu = 0.25$) on Euler's angles φ, θ in the laboratory coordinate system. Reproduced from [185]. Copyright 2007, American Institute of Physics.

trigonal $LiTaO_3$ (LTO) model systems in figure 4. Note that while in this analysis, the dielectric properties of the material are assumed to be close to isotropic and hence the electric field distribution is insensitive to sample orientation, similar analysis can be performed for full dielectric and elastic anisotropy.

The dependence of the piezoelectric tensor component e_{35} versus the orientation of the crystallographic axes with respect to the laboratory coordinate system for a LTO crystal is shown in the upper row of figure 5. The horizontal displacement below the tip versus the orientation of the crystallographic axes with respect to the laboratory coordinate system for a LTO crystal is shown in the bottom row of figure 5.

A common feature of the displacement surfaces shown in figures 4 and 5 is that the u_1 angular distribution is smoother, much more symmetric and convex than the one for e_{35}. Similarly to the longitudinal components of the piezoelectric tensors e_{33} and d_{33}, the d_{35} surfaces are very similar to e_{35} surfaces.

2.3. Resolution theory in PFM

One of the basic parameters characterizing performance of a microscope is the spatial resolution. Despite the ubiquity of usage and 'intuitive' meaning, the resolution in SPM is typically defined *ad hoc*. A quantitative imaging theory in PFM (and other SPMs) is required in order to:

- define the resolution and information limits in PFM and establish their dependence on tip geometry and materials properties, hence suggesting strategies for high-resolution imaging;
- develop the pathways for calibration of tip geometry in the PFM experiment for quantitative data interpretation;
- interpret the imaging and spectroscopy data in terms of intrinsic domain wall widths and the size of the nascent domain below the tip;
- reconstruct the ideal image from experimental data (deconvolute tip contribution), and establish applicability limits and errors associated with such deconvolution processes.

In this section, we describe the basic principles of linear imaging theory, provide definitions of resolution and information limit and describe instrumental and theoretical aspects of resolution function theory in PFM.

2.3.1. Linear imaging theory: transfer function, resolution and information limit. The definition of spatial resolution and resolution theory have originally evolved in the context of optical and electron microscopy (EM). In optics, the Rayleigh criterion [196] defines the resolution as the minimum distance by which two point scatterers must be separated in order to be discernible for a given imaging system. A commonly used alternative reading of the criterion postulates that for two Gaussian-shaped image features of similar intensity to be resolved, the dip between the two maxima should be at least 21% of the maximum. This criterion is illustrated in figure 6(*a*) and shows the transition of the two features from completely resolved to unresolved as a function of the separating distance. Note that the criterion is not absolute. It is possible that for a system with a sufficiently high signal-to-noise ratio, peaks separated by less than Rayleigh's resolution can be discernible

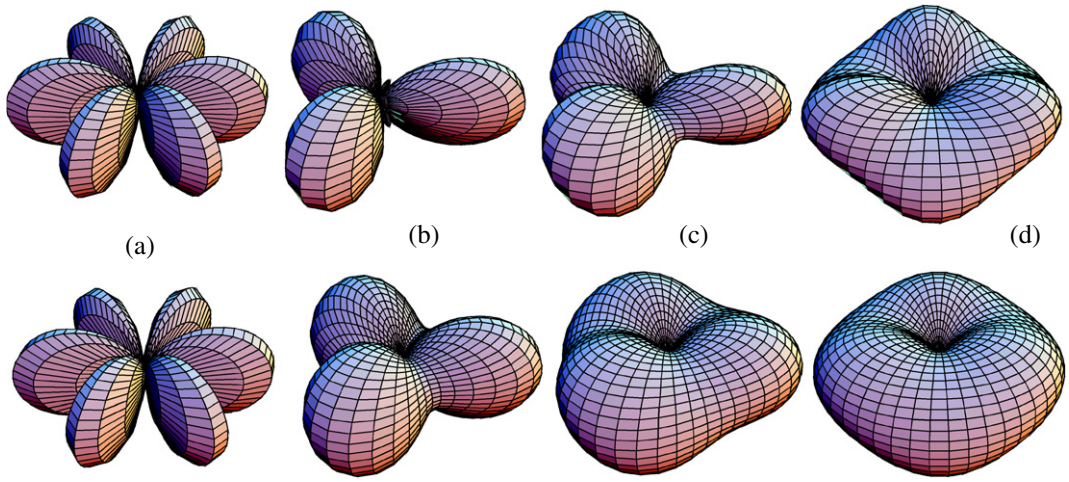

Figure 5. The dependence of LTO piezoelectric tensor component e_{35} (upper row) and displacement u_1 (bottom row) Euler's angles φ, θ and $\psi = 0^\circ, 30^\circ, 60^\circ, 90^\circ$ in the laboratory coordinate system (*a*), (*b*), (*c*), (*d*).

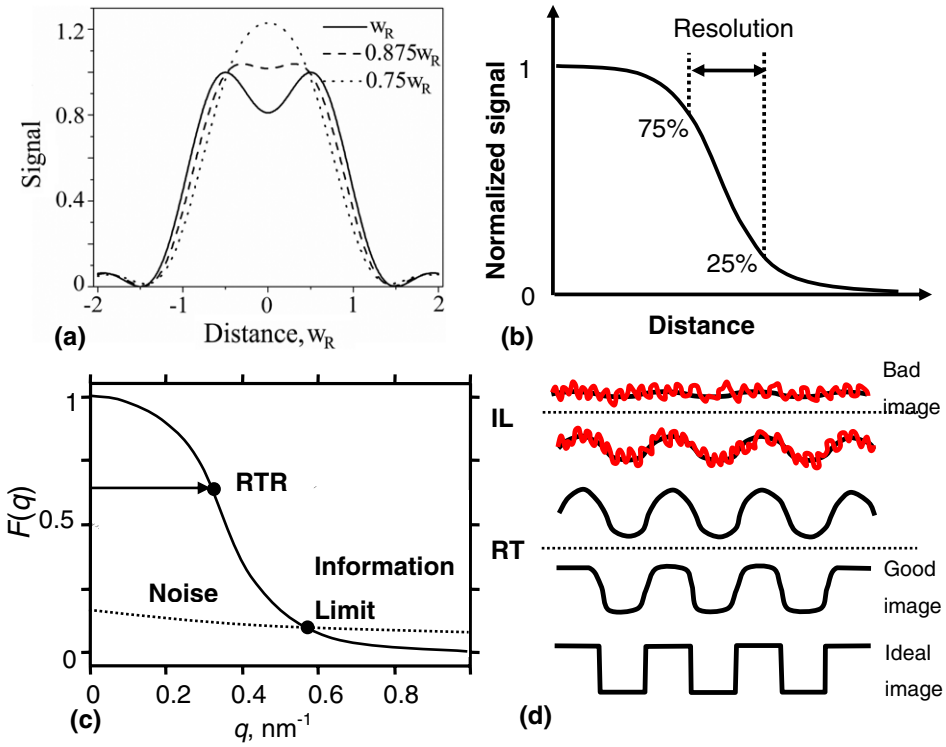

Figure 6. Definition of resolution. (*a*) Rayleigh criterion. The dotted lines correspond to Rayleigh two-point resolution limit and the information limit (IL). (*b*) '25–75' rule for resolution. (*c*) Definition of RTR and information limit in PFM in terms of the object transfer function. (*d*) Schematic demonstrating the minimum feature size that can be determined in the presence of noise. (*a*) Reproduced from [197]. Copyright 2006, IOP Publishing. (*c*), (*d*) Reproduced from [186]. Copyright 2007, American Institute of Physics.

(for example, the dashed line in figure 6(*a*)), or that a system with a low signal-to-noise ratio will require larger separations. Furthermore, while the concept of a point scatterer is applicable in electron (nuclei) and optical microscopy, it typically does not have direct analogs in PFM or SPM in general. An alternative definition used in low-resolution EM is the '25–75' resolution guideline, defined as the distance between signal changing by 25% and 75% between constant signal regions.

The unambiguous definition of spatial resolution and information limit is possible for the case of linear imaging. In these, the measured image $I(\boldsymbol{x})$, where $\boldsymbol{x}$ is a set of spatial coordinates, is given by the convolution of an *ideal image* (representing material properties) $I_0(\boldsymbol{x} - \boldsymbol{y})$ with the resolution function, $F(\boldsymbol{y})$:

$$I(\boldsymbol{x}) = \int I_0(\boldsymbol{x} - \boldsymbol{y})\, F(\boldsymbol{y})\, \mathrm{d}\boldsymbol{y} + N(\boldsymbol{x}), \qquad (2.9a)$$

where $N(\boldsymbol{x})$ is the noise function. The Fourier transform of equation (2.9*a*) is

$$I(\boldsymbol{q}) = I_0(\boldsymbol{q})\, F(\boldsymbol{q}) + N(\boldsymbol{q}), \qquad (2.9b)$$

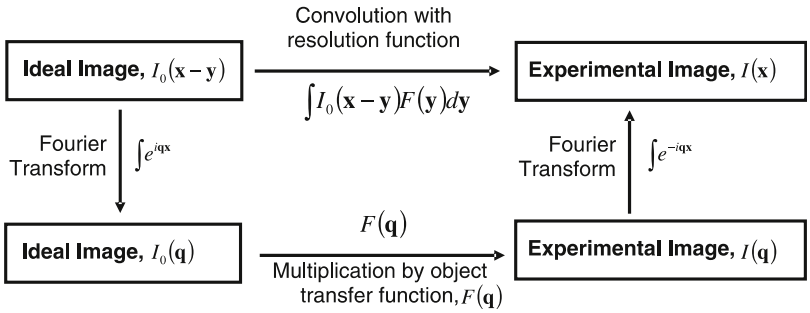

Figure 7. Relation between ideal image and experimental image in real and Fourier spaces. Object transfer function is a Fourier transform of resolution function. Reproduced from [197]. Copyright 2006, IOP Publishing.

where $I(q) = \int I(x)e^{iqx}dx$, $I_0(q)$ and $N(q)$ are the Fourier transforms of the measured image, ideal image and noise, respectively. The object transfer function (OTF), $F(q)$, is defined as a Fourier transform of the resolution function, $F(y)$. The object transfer function, $F(q)$, and the resolution function, $F(y)$, can then be determined directly provided that the ideal image, $I_0(q)$, is known. Alternatively, the resolution function can be approximated assuming that some information on its functional behavior (e.g. function is monotonic) is available (blind reconstruction, Bayesian methods). The veracity of this determination is limited by the noise level, $N(q)$. Then, once the resolution function is determined for a known calibration standard, it can be used to extract the ideal image, $I_0(x)$, from a measured image, $I(x)$, for an arbitrary sample. The relationship between the ideal image, experimental image and resolution and object transfer functions is illustrated in figure 7.

For the PFM OTF shown in figure 6(*c*), two parameters describing resolution can be introduced. The first definition can be derived from the Rayleigh or 25–75 criteria [198]. This Rayleigh two-point resolution (RTR) establishes a conservative definition of resolution as a characteristic object size for which response can still be measured *quantitatively*. In comparison, the information limit defines the minimum feature size that can still be detected *qualitatively* in the presence of noise, as illustrated in figure 6(*d*).

Beyond definition of resolution, equations (2.9*a*) and (2.9*b*) suggest an approach to deconvolute the ideal image assuming that the resolution function is known or can be estimated. Note that direct deconvolution results in a spurious increase in the noise amplitude, necessitating the use of regularization methods that impose the constraints on the maximum roughness of the ideal image. Detailed analysis of the inverse imaging problem is available in the literature [199] and a number of commercial packages are available (MatLab, DigitalMicrograph). Furthermore, a number of references analyzing deconvolution theory in Kelvin probe force microscopy (KPFM), a technique closely related to PFM, have been reported [200].

2.3.2. *Phenomenological resolution theory in PFM*

2.3.2.1. Determining resolution. The OTF and information limit in PFM can be determined (a) using the analysis of the Fourier transforms (diffractograms) of periodic structures and (b) domain wall profiles. Periodic domain structures can be either created by writing or occur naturally, as in lamellar (*a*)–(*c*) domains of tetragonal ferroelectrics. Figure 8(*a*) shows the template pattern used to write domains on the PZT surface along with the corresponding diffractogram. For comparison, shown in figures 8(*c*) and (*d*) are the resultant domain patterns imaged by PFM and their Fourier transforms. Note that only a few low order reflections can be observed in the diffractogram as a consequence of finite instrumental resolution.

To illustrate the effect of imaging conditions on the PFM resolution, it is instructive to explore the effect of lock-in time constant, as studied in detail in [197] and is illustrated in figures 8(*b*)–(*e*). Imaging with a low time constant (0.5 ms) results in a sharp, but relatively noisy, image (as seen in both the real space and FT images). On increasing the time constant to 1 ms, the noise level decreases. However, increasing the time constant further, to 4, 10 and 20 ms, results in characteristic streaking in real-space images along the fast scan direction. Note the evolution of the noise background in the corresponding diffractograms from a rotationally isotropic noise pattern for small time constants (figures 8(*b*) and (*c*)) to a pronounced noise band for large time constants in figures 8(*d*)–(*e*), indicating a large anisotropy of noise in the slow and fast scan directions. Also note that despite the high smearing in figure 8(*e*) from the large time constant (the pattern is not visually discernible in the real-space image), the corresponding diffractogram still contains reflections corresponding to the written pattern.

The wave-vector dependence of the peak intensity of several (*hk*) reflections for different lock-in time constants is shown in figure 8(*f*). The peak intensities follow an exponential decay law, $I(hk) = I_0 \exp(-q/G)$, where the decay constant is independent of the lock-in settings, $G \approx 5\,\mu\text{m}^{-1}$, $q = \sqrt{h^2+k^2}/a$ and a is the periodicity of the lattice. Thus, the intensity of the (1 0) peak can be used as a measure of the overall peak-to-noise ratio of the diffractogram, and hence of the image quality. A plot of the intensity of the (1 0) peak as a function of lock-in settings is given in figure 8(*g*). The peak intensity is virtually constant for small time constants and rapidly becomes zero when the time constant becomes larger than the time corresponding to the pixel acquisition rate (5 ms), reflecting the evolution of image contrast in figure 8.

The experimental resolution function can be determined from the diffractogram as shown in figure 9. Note that the resolution and contrast transfer function above are defined

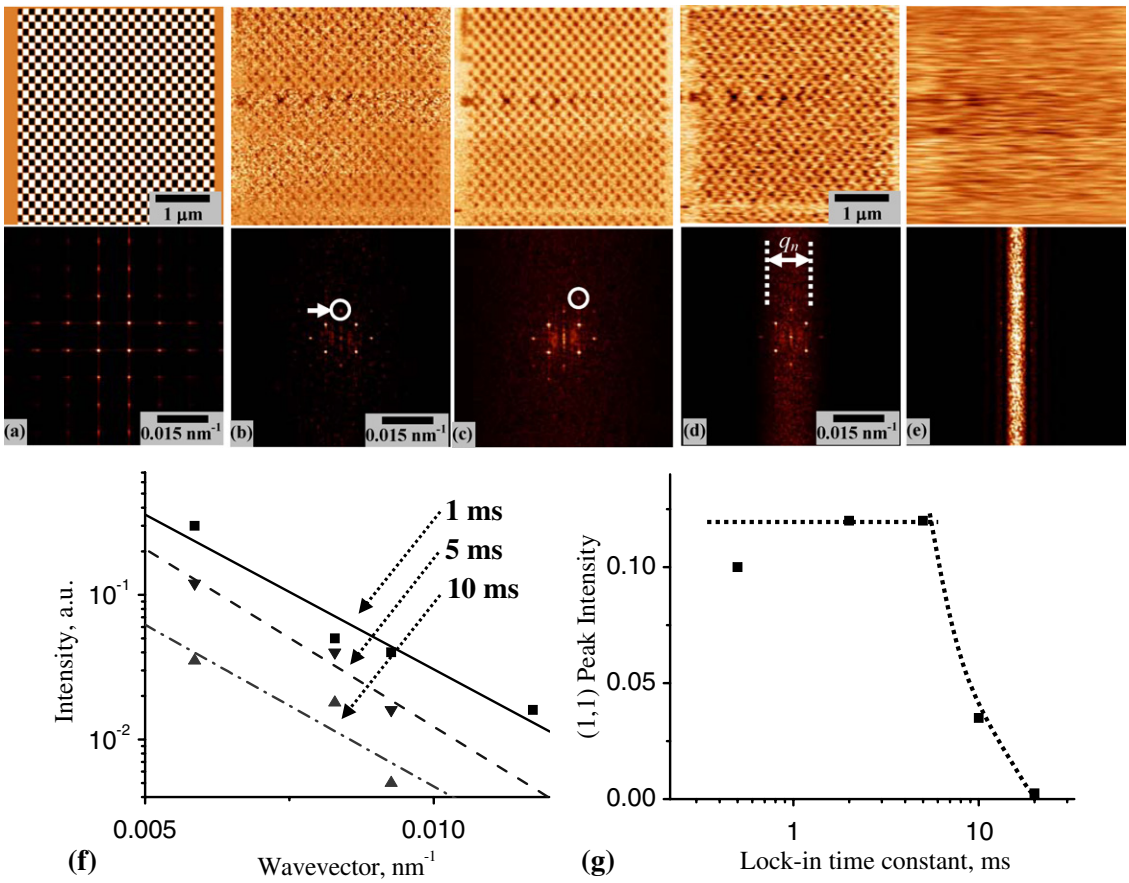

Figure 8. (*a*) Ideal image (writing signal) (top) and corresponding FFT image (bottom) illustrating that all frequency components are present. PFM images (top) and diffractograms (bottom) acquired with (*b*) 0.5 ms, (*c*) 1 ms, (*d*) 5 ms and (*e*) 20 ms lock-in time constants. (*f*) Wave-vector dependence of peak intensity for time constant (■) 1 ms, (▼) 10 ms and (▲) 5 ms. (*g*) Intensity of the (1 ,1) peak as a function of lock-in time constant. Reproduced from [197].

assuming the writing pattern is the ideal image. Hence, these definitions provide a quantitative measure of the information transfer from the desired template pattern to the actual image of the resulting domain structure, and thus describe the fidelity of ferroelectric data storage rather than reading resolution *per se*.

Complementary to diffractogram criterion, the PFM imaging resolution in real space can be determined from the measured width of the domain wall between antiparallel domains. Given that the intrinsic width of a ferroelectric domain wall is on the order of 1–2 unit cells (∼1 nm) [201], the typical effective domain wall width observed in PFM is presently on the order of 5–50 nm and therefore reflects primarily the spatial resolution of the microscope. Due to the symmetry properties of the dielectric, elastic and piezoelectric constant tensors, the piezoelectric constants change sign across a 180° domain wall, while the elastic and dielectric properties do not. Hence, the relationship between the 180° domain wall width and the resolution function can be established from equation (2.6), where, after normalization, the domain wall profile is given by

$$PR(x) = \int_{-\infty}^{x} \mathrm{d}x' \int_{-\infty}^{\infty} F\left(x', y\right) \mathrm{d}y - \int_{x}^{\infty} \mathrm{d}x' \int_{-\infty}^{\infty} F\left(x', y\right) \mathrm{d}y + N\left(\boldsymbol{x}\right). \tag{2.10}$$

Experimentally, the width of the domain wall image can be determined from the 25–75 criterion, or, alternatively from the derivative at the center, x_0, as $w_r = (PR^+ + PR^-)/2PR'(x_0)$. These definitions can also be used if the domain wall profile is fitted using a suitable function. For example, with a Boltzmann fit, $PR(x) = PR^- + (PR^+ - PR^-)/(1 + \exp[(x - x_0)/x_\mathrm{d}])$, the domain wall image width is $w_\mathrm{r} = 2x_\mathrm{d}$. Note that the signal gradient at the domain wall provides an upper limit of the 'sharpness' of any intrinsic feature in the image.

2.3.2.2. Resolution in phase images. One of the difficulties in defining the resolution in PFM stems from differences between the phase and mixed signal images. While the normalized PFM signal, pr, changes continuously between −1 and 1 on the lengthscale of w_d, the phase signal for zero noise changes abruptly from 0° for $pr < 0$ to 180° for $pr > 0$. Thus, the width of phase signal is effectively zero. In the presence of noise, the evolution of a phase signal can be understood from the schematics in figure 10(*a*). The phase achieves limiting values when the mixed signal is either significantly larger or smaller than the characteristic noise amplitude and changes rapidly in the region where the noise amplitude is sufficiently large to place the signal above or below the threshold value. Hence, the width of the domain wall in the phase image is estimated as $w_\varphi = \langle N \rangle / 2PR'(x_0)$, where $\langle N \rangle$ is the average

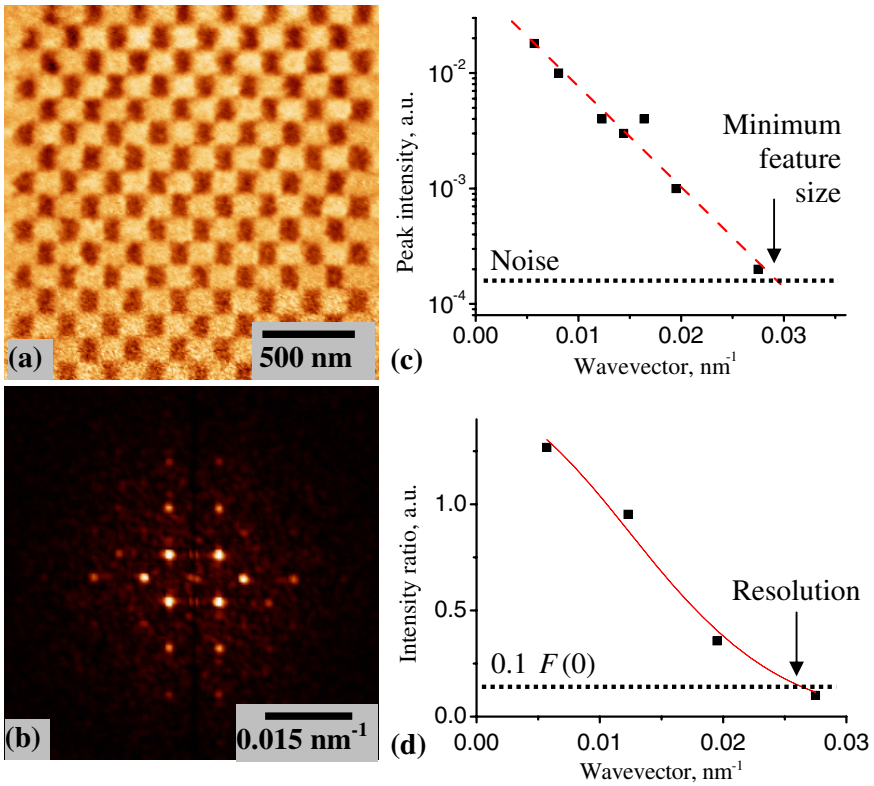

Figure 9. (*a*) PFM image of a grid pattern and (*b*) corresponding FFT image. (*c*) Wave-vector dependence of the FFT peak intensity illustrating the minimal feature size. (*d*) Calculated transfer function illustrating resolution. Reproduced from [197]. Copyright 2006, IOP Publishing.

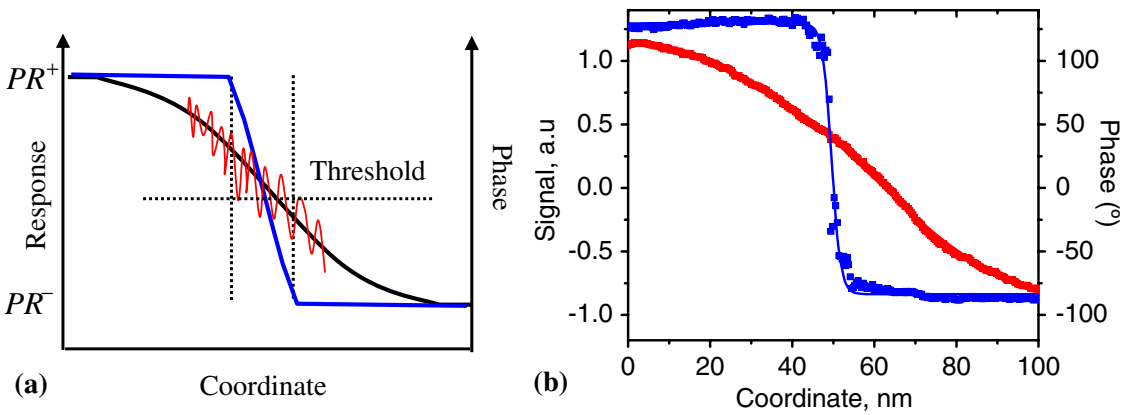

Figure 10. (*a*) Schematics of the domain wall profile and definition of domain wall width. (*b*) Relationship between domain wall width and resolution in mixed signal and phase images. Reproduced from [197]. Copyright 2006, IOP Publishing.

noise amplitude. Hence, the resolution as measured from the phase image is higher than that from the mixed signal, $w_\varphi = w_d(PR^+ + PR^-)/\langle N\rangle$, since the noise level is typically small compared with the signal. From the schematics in figure 10(*a*), it follows that the effective Rayleigh resolution for the phase signal corresponds to the information limit of the mixed PFM signal.

Experimentally, the domain wall width determined from the phase data is ∼0.5–1 orders of magnitude lower than that from the mixed signal, as illustrated by the PFM mixed-signal and phase data in figure 10(*b*). Given that the domain wall width in a mixed signal can be as small as 5–10 nm, the width in phase image can be sub-nanometer. However, since the phase signal contains only a fraction of the information contained in the mixed PFM image and the thresholding operation is non-linear, the object transfer function and the true Rayleigh resolution and material properties cannot be determined from the phase data until a proper model of tip–surface interactions is developed.

2.3.2.3. Image reconstruction in PFM. The experimentally determined resolution function can be used to reconstruct an 'ideal image', as demonstrated in figure 11. The template pattern and the corresponding domain pattern are shown in figures 11(*a*) and (*b*). For deconvolution, the recorded image diffractogram was divided by the transfer function and the Wiener filter was used as a regularization method. The resulting reconstructed image is shown in figure 11(*c*).

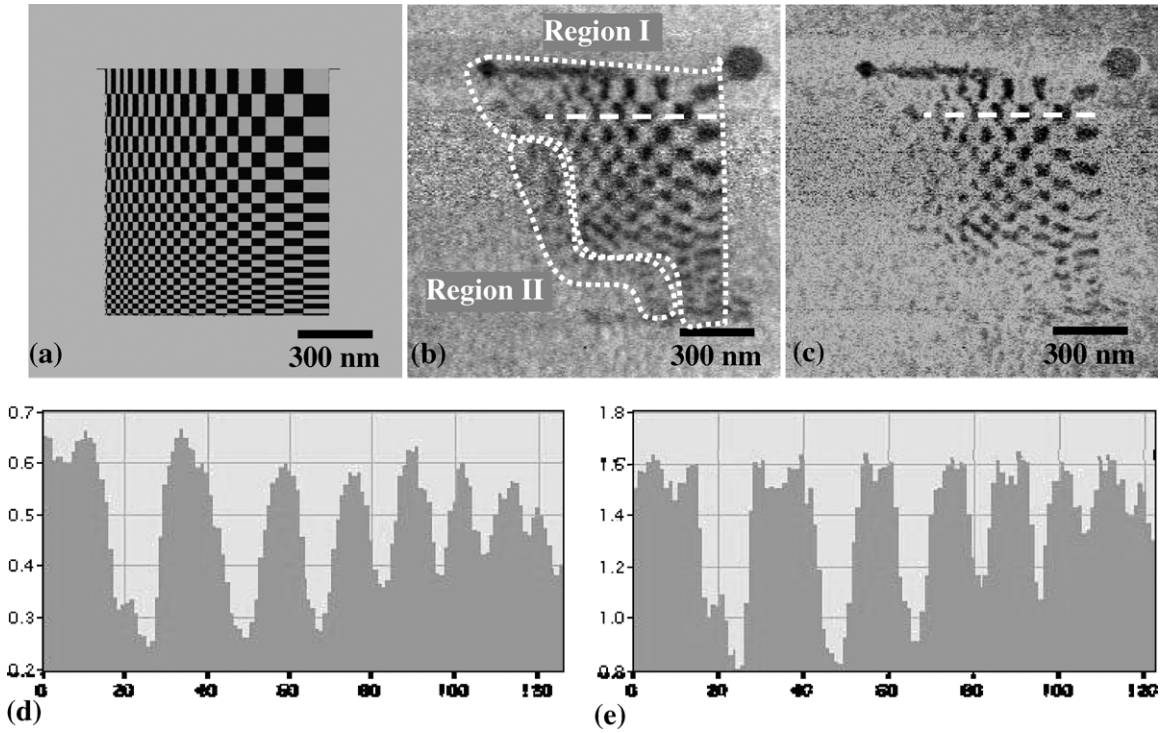

Figure 11. (*a*) Writing pattern, (*b*) original PFM image and (*c*) reconstructed PFM image using the transfer function. (*d*) Original and (*e*) reconstructed profiles along the dashed lines in (*b*), (*c*). Note the difference in domain wall width. Reproduced from [197]. Copyright 2006, IOP Publishing.

The reconstruction is successful only in region I, where the domain size is above the information limit. Note the difference in the image contrast and the effective wall width between the original and the reconstructed images and the corresponding line profiles. The minimum domain size detected by PFM in this case is limited by the resolution of the technique, suggesting that the reading resolution is a limiting factor precluding experimental observation of smaller domains that can be written by PFM.

The quality of the deconvoluted images can be significantly improved by the use of probability-based iterative methods such as maximum entropy reconstruction [202, 203] or Pixon reconstruction [204], previously used extensively for electron microscopic methods [205, 206]. Furthermore, progress can be achieved by the use of the analytical (i.e. independently known) resolution function, as discussed in detail in the next section.

2.3.3. Analytical resolution theory in PFM. To complement the experimental approach for the determination of the resolution function, the latter can be established theoretically and then used to deconvolute the experimental data. The deconvolution can be performed either with a completely known resolution function, or with a function defined down to several experimentally established parameters (e.g. tip radius of curvature determined from electron microscopy data or domain wall width measurements).

The decoupling approximation discussed in section 2.2.2 can be extended to yield the analytical expressions for the resolution function. The surface displacement $u_i(\boldsymbol{x}, \boldsymbol{y})$ at

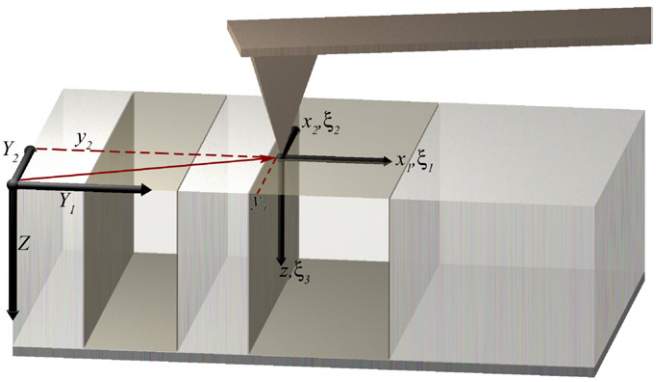

Figure 12. Coordinate systems in the PFM experiment. Reproduced from [186]. Copyright 2007, American Institute of Physics.

location $\boldsymbol{y}$ induced by the biased tip (probe) at position $\boldsymbol{x}$ is given by equation (2.6). Coordinate systems $\boldsymbol{x}$ and $\boldsymbol{\xi}$ are linked to the probe, coordinates $\boldsymbol{y} = (y_1, y_2)$ give the probe apex position in the sample coordinate system $\boldsymbol{y}$ (see figure 12).

If the sample is uniform in the z-direction on the scale of the penetration depth of the electric field, i.e. $c_{jlmn}d_{mnk}(\boldsymbol{x}, z) \approx c_{jlmn}d_{mnk}(\boldsymbol{x})$, vertical PFM response, equation (2.6), can be rewritten as

$$u_3(\boldsymbol{0}, \boldsymbol{y}) = \int_{-\infty}^{\infty} \mathrm{d}_{mnk}(\boldsymbol{y} - \boldsymbol{\xi}) \times \left(\int_{z=0}^{\infty} c_{jlmn} E_k(-\xi_1, -\xi_2, z) \frac{\partial}{\partial \xi_l} G_{3j}(\xi_1, \xi_2, z)\, \mathrm{d}z \right) \mathrm{d}\xi_1 \mathrm{d}\xi_2, \tag{2.11}$$

i.e. as a convolution of a function describing the spatial distribution of material properties, $d_{mnk}(\boldsymbol{x})$, and a function related to probe parameters (integral in parentheses). Note that equation (2.11) belongs to the linear model (equations (2.9*a*) and (2.9*b*)), with the term in parentheses being the resolution function and $d_{mnk}(\boldsymbol{y}-\boldsymbol{\xi})$ an ideal image.

Note that this analysis is rigorously valid in the point mechanical contact approximation, i.e. the displacement transferred to the tip is equal to the displacement at the tip–surface contact junction. In this case, the non-uniformity of strains within the contact area is neglected. This assumption is expected to be valid when the electric contact area significantly exceeds the mechanical contact area (e.g. due to the formation of a liquid droplet at the tip–surface junction) and to provide a good approximation when the response changes only weakly within the contact area. Experimentally, the two can be compared by comparing topographic resolution (e.g. width of step edges) with the PFM resolution (domain wall width). Approximately, this effect can be represented as a convolution of the calculated point-contact responses with an additional smoothing function with the half-width of the order of contact radius.

2.3.4.1. Electrostatic field structure. Determination of the resolution function in equation (2.11) necessitates the knowledge of the electrostatic field structure in the material. The detailed analysis of electric field structure for the uniform half-plane of arbitrary symmetry of dielectric properties is given in [185]. In particular, for symmetries of isotropic and transversally isotropic materials the electrostatic problems for spherical tip geometry can be solved using the image charge method, in which the tip is represented by a set of image charges chosen so that the corresponding isopotential contour represents the tip geometry [207–209]. For lower material symmetries and complex tip geometries, the image charge method, while not being rigorous, provides a good approximation (e.g. the line charge model for the conical part of the tip [210]).

For the case of transversally isotropic symmetry of dielectric properties, the potential V_Q in the point charge-based models of the tip has the form

$$V(\rho, z) = \frac{1}{2\pi\varepsilon_0(\varepsilon_e+\kappa)}\sum_{m=0}^{\infty}\frac{Q_m}{\sqrt{\rho^2+(z/\gamma+d_m)^2}}, \qquad (2.12)$$

where $\sqrt{x_1^2+x_2^2}=\rho$ and $\xi_3=z$ are the radial and vertical coordinates, respectively, ε_e is the dielectric constant of the ambient, $\kappa=\sqrt{\varepsilon_{33}\varepsilon_{11}}$ is the effective dielectric constant of the material, $\gamma=\sqrt{\varepsilon_{33}/\varepsilon_{11}}$ is the dielectric anisotropy factor, $-d_m$ is the z-coordinate of the point charge Q_m and summation is performed over the set of image charges representing the tip. The potential in the sphere–plane model can be obtained from equations (2.12)–(2.14), where the summation is performed over image charges. In the case of the rigorous sphere–plane model of a tip of curvature R_0 located at a distance ΔR from the sample surface, the image charges are given by recurrent relations

$$d_{m+1} = R_0+\Delta R-\frac{R_0^2}{R_0+\Delta R+d_m} \qquad (2.13)$$

and

$$Q_{m+1} = \frac{\kappa-\varepsilon_e}{\kappa+\varepsilon_e}\cdot\frac{R_0}{R_0+\Delta R+d_m}Q_m, \qquad (2.14)$$

where $Q_0=4\pi\varepsilon_0\varepsilon_e R_0 U$, $d_0=R_0+\Delta R$ and U is the tip bias.

An alternative approach to describe electric fields in the immediate vicinity of the tip–surface junction is the use of the effective point charge model, in which the charge magnitude and charge–surface separation are selected such that the corresponding isopotential surface reproduces the tip radius of curvature and tip potential. In this case, the tip is represented by a single charge $Q=2\pi\varepsilon_0\varepsilon_e R_0 U(\kappa+\varepsilon_e)/\kappa$ located at $d=\varepsilon_e R_0/\kappa$ [211]. Note that the intrinsic limitation of the point-charge model is that it can approximate only two out of three characteristic parameters—potential at the tip–surface junction, curvature of the isopotential surface and effective decay length of the field. However, its simplicity allows it to be used as a zero-order approximation.

Effective point charge parameters used to describe the spherical [211] or flattened [212] tip in the immediate vicinity or at the contact with the sample surface, corresponding to the typical geometry of PFM experiments, are summarized in table 1.

In the framework of the effective point charge model the isopotential surface curvature reproduces the tip curvature at the point of contact. This model is appropriate for electric field description in the immediate vicinity of the tip–surface junction, relevant for, e.g., modeling nucleation processes. For the film thickness $h\geqslant d$, the effective point charge model gives $d\approx\varepsilon_e R_0/\kappa$ for the spherical tip with curvature R_0.

The field structure in most part of the piezoresponse volume can be represented by the point charge model in which the effective charge value Q is equal to the product of tip capacitance on applied voltage. For the film thickness $h\geqslant d$, it gives the effective separation as $d\approx 2\varepsilon_e R_0\ln((\varepsilon_e+\kappa)/2\varepsilon_e)/(\kappa-\varepsilon_e)$ for the spherical tip with curvature R_0.

Finally, for the conductive disk of radius R_0 representing contact area, $d\approx 2R_0/\pi$. The proposed model should be clearly distinguished from the conventional capacitance approximation (with $d=R_0$) that describes electric field far from the tip only.

2.3.4.2. Resolution function and materials properties effect. In the case when $x_1=x_2=0$ (the displacement directly below the tip) and the strain piezoelectric coefficient $d_{klj}(\boldsymbol{\xi})$ is independent of ξ_3 (system is uniform in the z-direction), the Fourier transformation of the surface displacement (i.e. VPFM signal) is [186]

$$\tilde{u}_i(\boldsymbol{q}) = \tilde{d}_{klj}(\boldsymbol{q})\,\tilde{W}_{ijkl}(-\boldsymbol{q})+N(\boldsymbol{q}), \qquad (2.15)$$

where $\tilde{u}_i(\boldsymbol{q})=\int u_i(\boldsymbol{x})e^{i\boldsymbol{q}\boldsymbol{x}}\mathrm{d}\boldsymbol{x}$, $\tilde{d}_{klj}(\boldsymbol{q})$ and $N(\boldsymbol{q})$ are the Fourier transforms of the measured image, ideal image and

Table 1. Effective charge approach for different tip models in comparison with the capacitance approximation.

Tip model	Effective charge parameters for the ferroelectric film of thickness h
Sphere–plane model Reproduces the electric field of a conductive spherical tip with curvature R_0, located near the surface at a distance $\Delta R \ll R_0$.	Overall charge $Q(h) = C_t^{sph}(h)U$. At $\Delta R \ll R_0$ tip capacitance is $C_t^{sph}(h) = \begin{cases} 4\pi\varepsilon_0\varepsilon_e R_0 \frac{\kappa+\varepsilon_e}{\kappa-\varepsilon_e} \ln\left(\frac{\varepsilon_e+\kappa}{2\varepsilon_e}\right)\left(1+\frac{\gamma R_0}{h}\frac{2\varepsilon_e\kappa\ln(1-\chi)}{(\varepsilon_e-\kappa)^2}\ln\left(\frac{\varepsilon_e+\kappa}{2\varepsilon_e}\right)\right), & h \gg R_0 \\ 4\pi\varepsilon_0\varepsilon_e R_0 \frac{\kappa_b+\varepsilon_e}{\kappa_b-\varepsilon_e}\ln\left(\frac{\varepsilon_e+\kappa_b}{2\varepsilon_e}\right), & h \to 0 \end{cases}$ The effective distance $d(h) \approx \frac{C_t^{sph}(h)}{2\pi\varepsilon_0(\varepsilon_e+\kappa)}\left(1+\left(\frac{\kappa_b+\varepsilon_e}{\kappa-\kappa_b}+\frac{h}{\gamma R_0}\frac{\varepsilon_e-\kappa}{\kappa\ln(1-\chi)}\right)^{-1}\right)$. The field structure is adequately described in most of the piezoresponse volume, since $\varphi(0,0,-\Delta R) = U$ and $\varphi(r \gg R_0) \sim Q/r$. For $R_0 = 10$–100 nm, $\Delta R \leqslant 0.1$–1 nm, $\kappa = 50$–500 and $h \gg \gamma R_0$: $d = 0.02$–2 nm at $\varepsilon_e = 1$; $d = 15$–150 nm at $\varepsilon_e = 81$.
Effective point charge model Reproduces the electric field of a conductive spherical tip with curvature R_0 immediately below the tip apex.	Isopotential surface $\varphi(\boldsymbol{x}) = U$ has the tip curvature R_0 in the point $\{0,0,x_3 = -\Delta R\}$. At $\Delta R \ll R_0$ Pade approximations for effective distance and charge are valid: $d(h) \approx \frac{\varepsilon_e R_0}{\kappa}\frac{2(\varepsilon_e-\kappa)(\kappa_b-\kappa)\kappa^2h^2+\kappa\gamma^2R_0^2\varepsilon_e^3\mathrm{Li}_2(\chi)}{2(\varepsilon_e-\kappa)(\kappa_b-\kappa)\kappa^2h^2+\kappa_b\gamma^2R_0^2\varepsilon_e^3\mathrm{Li}_2(\chi)}$ ($\mathrm{Li}_n(\chi)$ is the polylogarithmic function), $Q(h,d) \approx \frac{2\pi\varepsilon_0(\varepsilon_e+\kappa)Ud}{1+\left(\frac{\kappa_b+\varepsilon_e}{\kappa-\kappa_b}+\frac{h}{\gamma d}\frac{\varepsilon_e-\kappa}{\kappa\ln(1-\chi)}\right)^{-1}}$. The field structure is adequately described in the immediate vicinity of the tip–surface junction. For parameters $R_0 = 10$–100 nm, $\Delta R \leqslant 0.1$–1 nm, $\kappa = 50$–500 and $h \gg \gamma R_0$: $d = 0.2$–10 nm at $\varepsilon_e = 1$; $d = 11$–110 nm at $\varepsilon_e = 81$.
Disk–plane model Reproduces the electric field of a conductive flattened apex represented by the disk of radius R_0 that touches the surface.	Overall charge $Q(h) = C_t^{disk}(h)U$. In contact ($\Delta R = 0$) disk capacitance is $C_t^{disk}(h) = \begin{cases} 4\varepsilon_0(\varepsilon_e+\kappa)R_0\left(1-\frac{2\gamma R_0}{\pi h}\frac{\kappa\ln(1-\chi)}{\varepsilon_e-\kappa}\right), & h \gg R_0 \\ 4\varepsilon_0(\varepsilon_e+\kappa_b)R_0, & h \to 0 \end{cases}$ Pade approximations for disk capacitance and effective distance are $C_t^{disk}(h) \approx \frac{4\varepsilon_0(\varepsilon_e+\kappa)R_0}{1+\left(\frac{\kappa_b+\varepsilon_e}{\kappa-\kappa_b}+\frac{\pi h}{2\gamma R_0}\frac{\varepsilon_e-\kappa}{\kappa\ln(1-\chi)}\right)^{-1}}$, $d(h) \approx \frac{2}{\pi}R_0$. The field structure is adequately described in the most part of piezoresponse volume, since $\varphi(\rho \leqslant R_0, 0) \approx U$ and $\varphi(r \gg R_0) \sim Q/r$. Estimation $d = 6$–60 nm for $R_0 = 10$–100 nm
Capacitance model Reproduces the electric field far from the tip apex (ΔR is the tip–surface separation)	For the case $\Delta R \ll R_0$ the tip charge $Q(h) = C_t(h)U$, where $C_t^{disk}(h)$ and $C_t^{sph}(h)$ are listed above. The potential $\varphi(0,0,x_3 = -\Delta R) \neq U$ is not fixed. Used for electric field description far from the tip apex at distances $r \gg R_0$: $\varphi(r) \sim Q/r$. Distance d is undetermined. For the case $\Delta R > R_0$ the tip charge $Q = C_t U$, where $C_t^{sph} \approx 4\pi\varepsilon_0\varepsilon_e R_0$, $C_t^{disk}(h) \approx 8\varepsilon_0\varepsilon_e R_0$. Distance $d \approx R_0 + \Delta R$ for a spherical tip, whereas $d \approx \Delta R$ for a disk.

noise, respectively. $\tilde{W}_{ijkl}(\boldsymbol{q})$ is the tensorial OTF, namely the Fourier image of the resolution function:

$$W_{ijkl}(\xi_1,\xi_2) = c_{kjmn}\int_0^\infty \mathrm{d}\xi_3 \frac{\partial G_{im}(-\xi_1,-\xi_2,\xi_3)}{\partial\xi_n} \times E_l(\xi_1,\xi_2,\xi_3). \tag{2.16}$$

The number of non-zero components of OTF depends on the material symmetry and for transversally isotropic materials (e.g. tetragonal perovskites) only the components $\tilde{W}_{333,\,313,\,351}$ are non-zero (in Voigt representation) and contribute to the vertical displacement, u_3. The vertical response in this case is $\tilde{u}_3(q) = \tilde{W}_{333}(q)d_{33} + \tilde{W}_{313}(q)d_{31} + \tilde{W}_{351}(q)d_{15}$. In most cases, the component W_{333} corresponding to a piezoelectric constant d_{33} provides the dominant (>50%) contribution to the overall signal [184].

The approximate analytical expressions for OTF components, $\tilde{W}_{ijkl}(\boldsymbol{q})$, are

$$\tilde{W}_{333}(q) \approx \begin{cases} -\frac{Q}{2\pi\varepsilon_0(\kappa+\varepsilon_e)d}\left(\frac{\gamma q d}{2}+\frac{(1+\gamma)^2}{1+2\gamma}\right)^{-1}, \\ \text{point charge model}, \\ -U\left(\frac{\varepsilon_e\gamma q R_0}{\varepsilon_e+\kappa}+\frac{(1+\gamma)^2}{1+2\gamma}\right)^{-1}, \\ \text{sphere–plane model}. \end{cases} \tag{2.17}$$

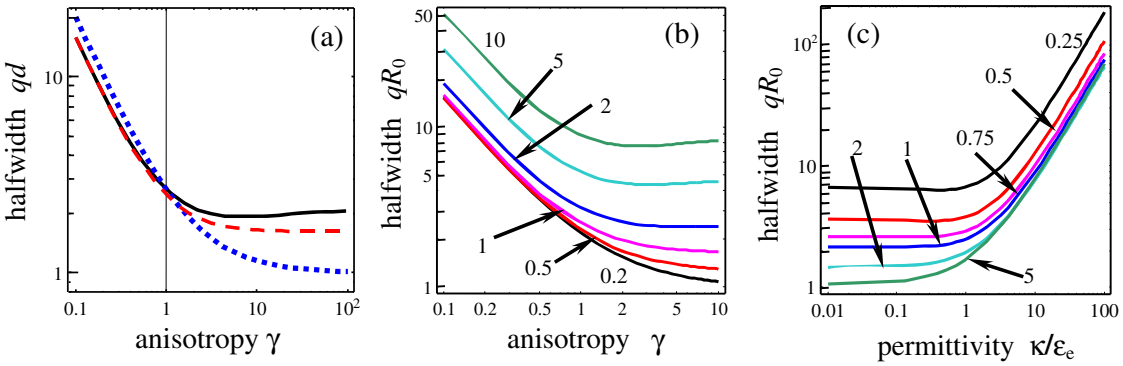

Figure 13. The half-width of OTF $\tilde{W}_{333}$ (*a*) for the point charge model of the tip versus the dielectric anisotropy, γ. Shown are results of exact calculations on the basis of equation (2.16) (solid curves) and Pade approximations (2.17) (dotted curves). (*b*), (*c*) The halfwidth calculated in the sphere–plane model of the tip versus the dielectric anisotropy, γ (*b*) and relative permittivity, κ/ε_e (*c*). Figures near the curves correspond to the values of the ratio κ/ε_e (*b*) and γ (*c*). Adapted from [186].

The dependence of dimensionless half-width q_{FWHM} of the $\tilde{W}_{333}$ (i.e. Rayleigh resolution) on dielectric anisotropy, γ, and relative permittivity, κ/ε_e, is illustrated in figure 13. For the point charge model, the half-width, $q\ d$, scales linearly with dielectric anisotropy, γ, for small γ, while it saturates for $\gamma \gg 1$. Hence, $\gamma \ll 1$ favors high-resolution imaging. For the sphere–plane model, the half-width, $q\ R_0$, decreases with the dielectric anisotropy factor, γ, and increases with the dielectric ratio κ/ε_e.

The Rayleigh resolution r_{min} in PFM experiments (i.e. in r-space) is determined as $r_{min} \cong 1/q_{FWHM}$. Using $d = \varepsilon_e R_0/\kappa$ in the point charge model, the relationship between resolution, tip geometry and materials' parameters can be derived as

$$r_{min} \cong \begin{cases} \dfrac{\gamma\varepsilon_e R_0}{2\kappa}\dfrac{1+2\gamma}{(1+\gamma)^2}, & \text{effective point charge model,} \\ \dfrac{\gamma\varepsilon_e R_0}{\varepsilon_e+\kappa}\dfrac{1+2\gamma}{(1+\gamma)^2}, & \text{sphere–plane model.} \end{cases} \tag{2.18}$$

Thus, the functional dependence, $r_{min} \sim \varepsilon_e R_0/\varepsilon_{11}$, is valid at $\varepsilon_e \ll \kappa$ for both the point charge and sphere–plane models of the tip. Hence, it is desirable to decrease external permittivity, ε_e (e.g. by imaging in dry air), and decrease tip radius, R_0 (sharp tips), in order to increase the lateral resolution of PFM, while maintaining good contact. Furthermore, the formation of liquid necks in the tip–surface junction will decrease the resolution due to an increase in ε_e (for dielectric liquid) or effective radius R_0 (conductive liquid). Note that higher lateral resolution is possible in materials with high ε_{11} values.

The resolution function and OTF approach allows approximate calculation of the piezoresponse from those domain structures for which the Fourier image, $\tilde{d}_{klj}(\boldsymbol{q})$, exists in a usual (e.g. single, multiple or periodic domain stripes, cylindrical domains, rings, etc) or generalized (infinite plane domain wall) sense.

2.3.4.3. The response near the flat domain wall. A natural experimental observable in PFM is a domain wall between antiparallel domains. Here, we apply the resolution function equation (2.16) to determine analytically the domain wall profile in vertical and lateral PFM, and establish the relationship between domain wall width, tip radius and materials properties.

The surface displacement vector below the tip located at distance a from the infinitely thin planar domain wall located at $y_1 = a_0$ (figure 14(*a*)) is given by equation (2.15) as

$$u_i(0,a) = \int_{-\infty}^{\infty} d\xi_1 \int_{-\infty}^{\infty} d\xi_2\, W_{ijkl}(-\xi_1,-\xi_2)\, d_{lkj} \times \mathrm{sign}(a - a_0 - \xi_1). \tag{2.19}$$

The resolution function W_{ijkl} is given by equation (2.16). For both the point charge and the sphere–plane models of the tip of curvature R_0 that touches the sample, the displacement components can be derived in the analytical form as

$$u_i(a-a_0) = \begin{cases} \dfrac{Q}{2\pi\varepsilon_0(\varepsilon_e+\kappa)d} g_{ijk}\left(\dfrac{a-a_0}{d},\gamma,\nu\right) d_{kj}, \\ \qquad \text{point charge model,} \\ U g_{ijk}\left(\dfrac{a-a_0}{fR_0},\gamma,\nu\right) d_{kj}, \\ \qquad \text{sphere–plane model,} \end{cases} \tag{2.20}$$

where $i = 1, 3$ (since $u_2 \equiv 0$) and $f = (2\varepsilon_e/(\kappa-\varepsilon_e))\ln((\varepsilon_e+\kappa)/2\varepsilon_e)$. Exact expressions of g_{ijk} and Pade-exponential approximations g^{Pade}_{ijk} are derived in [186]. In the case of weak dielectric anisotropy $\gamma \cong 1$ the signal components are the following:

$$g^{Pade}_{333}(s,\gamma,\nu) = -\frac{1+2\gamma}{(1+\gamma)^2}\frac{s}{|s|+1/4}, \tag{2.21a}$$

$$g^{Pade}_{133}(s,\gamma,\nu) = \left(\frac{8}{3} + \frac{(1+\gamma)^3}{\gamma}|s|\right)^{-1}, \tag{2.21b}$$

$$g^{Pade}_{351}(s,\gamma) = -\frac{\gamma^2}{(1+\gamma)^2}\cdot\frac{s}{|s|+3/4}, \tag{2.21c}$$

$$g^{Pade}_{151}(s,\gamma) = \left(\frac{1}{2/\pi - 3/8} + \frac{2(1+\gamma)^3}{(3+\gamma)\gamma^2}|s|\right)^{-1}, \tag{2.21d}$$

$$g^{Pade}_{313}(s,\gamma,\nu) = \left(\frac{1+2\gamma}{(1+\gamma)^2} - 2\frac{1+\nu}{1+\gamma}\right)\frac{s}{|s|+1/4}, \tag{2.21e}$$

$$g^{Pade}_{113}(s,\gamma,\nu) = -\left(\frac{8}{3} + \frac{(1+\gamma)^3}{\gamma}|s|\right)^{-1} + \frac{(1+\nu)}{1+(1+\gamma)^2|s|}. \tag{2.21f}$$

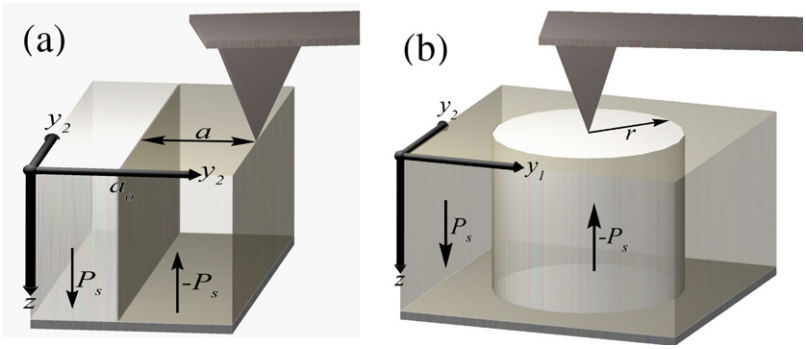

Figure 14. (*a*) Schematics of a PFM measurement across a 180° domain wall. (*b*) Piezoresponse calculation from cylindrical domain. Reproduced from [186]. Copyright 2007, American Institute of Physics.

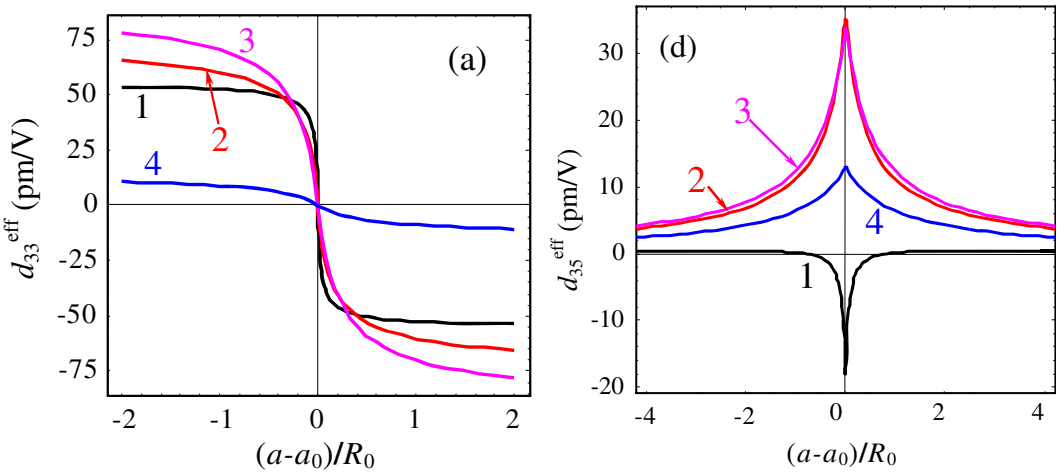

Figure 15. (*a*) Vertical and (*b*) lateral PFM signal. Domain wall piezoresponse for sphere–plane models of the tip calculated at $\nu = 0.35$ for different ferroelectric materials: BTO ($\gamma = 0.24$, curves 1), PZT6B ($\gamma = 0.99$, curves 2), PTO ($\gamma = 0.87$, curves 3), $LiNbO_3$ (LNO) ($\gamma = 0.60$, curves 4). Reproduced from [186]. Copyright 2007, American Institute of Physics.

Here, $s = (a - a_0)/d$ for the point charge model and $s = (a - a_0)/f\ R_0$ for the sphere–plane model.

When the tip is in contact, the piezoresponse signal components across the domain walls $d_{33,35}^{\text{eff}} = u_{3,1}/U$ are $d_{33}^{\text{eff}} = d_{33}g_{333} + d_{15}g_{351} + d_{31}g_{313}$ for the vertical signal and $d_{35}^{\text{eff}} = d_{33}g_{133} + d_{15}g_{151} + d_{31}g_{113}$ for the lateral signal. Domain wall profiles calculated for different ferroelectric materials are shown in figure 15.

Note, that the sphere–plane tip gives a slightly more 'rectangular' image of the ideal domain wall in comparison with the sloped one given by the point charge tip for the same values of dimensionless distance s (i.e. for $d = R_0$) [186]. Therefore, the sphere–plane tip has a higher lateral resolution in comparison with the point charge one for comparable characteristic dimensions. This behavior is anticipated due to the concentration of charges at the tip–surface junction in the sphere–plane model.

It also follows from figure 15 that for the materials studied, the highest lateral resolution can be achieved in BTO, whereas the lowest corresponds to the $LiNbO_3$ (LNO). The behavior of the lateral PFM signal, d_{35}^{eff}, is more complex. The resolution for BTO is the highest, but the signal changes sign, since the negative contribution of d_{15} dominates far from the domain wall.

As expected from the symmetry of the problem and in agreement with available experimental data, the surface vertical displacement u_3 (and thus vertical piezoresponse d_{35}^{eff}) is zero directly on the wall, whereas its lateral displacement u_1 (and thus lateral piezoresponse d_{35}^{eff}) is maximal. Earlier this behavior was established using numerical methods [183]. Note that contrary to several recent reports [213, 214], the lateral contrast at the 180° is an intrinsic feature of the 3D electromechanical model and does not necessarily indicate the presence of electrostatic interactions.

The analytical dependences in equations ((2.21*a*)–(2.21*f*)) establish the relationship between the response behavior, ferroelectric material properties, ambient and tip characteristics, e.g. $d_{33}^{\text{eff}} \sim (a - a_0)/d$ and $d_{33}^{\text{eff}} \sim 1/(C + |a - a_0|/d)$ near the domain wall ($y_1 = a_0$). Moreover, the obtained analytical expressions allow unknown parameters such as charge–surface separation d (or, equivalently, $f R_0$ for the spherical tip) and dielectric and piezoelectric material constants to be reconstructed by fitting the experimental data of the vertical and lateral piezoresponse components from a domain wall to a selected model. Specifically, for materials with known properties (calibration standard) the geometric parameters of a tip can be determined from experimentally measured domain wall profiles, as analyzed in section 2.4.

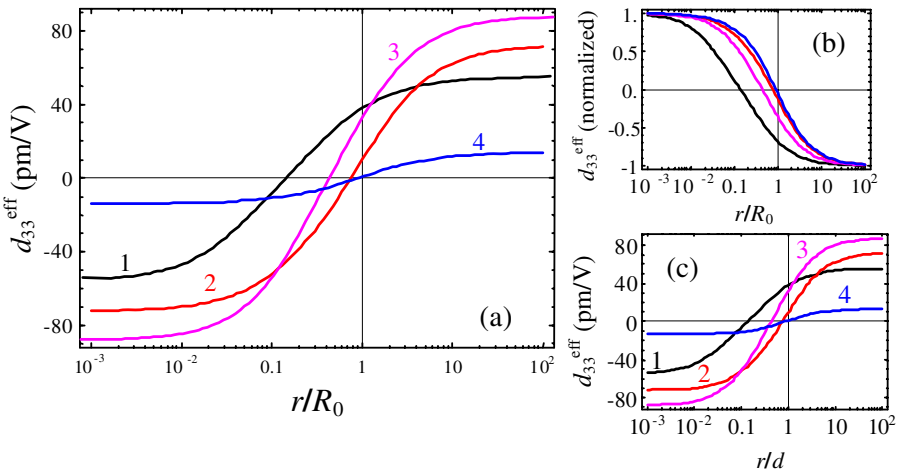

Figure 16. Absolute (*a*), (*c*) and normalized (*b*) piezoresponse $d_{33}^{\rm eff}(r)$ versus the domain radius for the point charge (*c*) and sphere–plane (*a*), (*b*) models of the tip at $\nu = 0.35$ for BTO (1), PZT6B (2), PTO (3), LNO (4). Reproduced from [186]. Copyright 2007, American Institute of Physics.

2.3.4.4. Response of axially symmetric cylindrical domain. The deconvolution of PFM spectroscopy data requires analysis of the PFM signal from a finite domain centered at the tip apex, as shown in figure 14(*b*). For most ferroelectric materials, domains form highly elongated needles extending deep into the material, whereas the electrostatic field is concentrated in the near-surface region. Hence, interpretation of PFM data can be performed using a model of a semi-infinite cylindrical domain. Hence, the response can be estimated assuming that the domain wall is purely cylindrical and the charged tip is located at the domain center (0,0,0). From equation (2.15), the displacement at the center of a domain is

$$u_3(\mathbf{0},r) = 2\pi\left(\int_0^\infty \rho \mathrm{d}\rho W_{3jkl}(\rho) - 2\int_0^r \rho \mathrm{d}\rho W_{3jkl}(\rho)\right) d_{lkj}. \tag{2.22}$$

Here the resolution function, $W_{3jkl}(\rho)$, is given by equation (2.16) for $\sqrt{\xi_1^2+\xi_2^2} = \rho$, while $u_1 = u_2 = 0$ as follows from the symmetry considerations. Both for the point charge and the sphere–plane models, the vertical displacement can be obtained in a simple analytical form as

$$u_3 = \begin{cases} \dfrac{Q}{2\pi\varepsilon_0(\varepsilon_e+\kappa)d} h_{jk}^{\rm Pade}\left(\dfrac{r}{d},\gamma,\nu\right) d_{kj}, \\ \qquad\qquad \text{point charge model}, \\ U h_{jk}^{\rm Pade}\left(\dfrac{r}{fR_0},\gamma,\nu\right) d_{kj}, \\ \qquad\qquad \text{sphere–plane model}. \end{cases} \tag{2.23}$$

Integral representations for functions $h_{jk}(s,\gamma,\nu)$ are derived in [186]. Their polynomial and exponential Pade approximations are derived in [186]. For $\gamma \cong 1$ and $s > 0.1$ the following simple approximations are obtained:

$$h_{33}^{\rm Pade}(s,\gamma) \approx -\frac{1+2\gamma}{(1+\gamma)^2} + 2\frac{1+2\gamma}{(1+\gamma)^2}\cdot\frac{s}{s+\pi/8}, \tag{2.24a}$$

$$h_{13}^{\rm Pade}(s,\gamma,\nu) \approx \frac{1+2\gamma}{(1+\gamma)^2} - \frac{2(1+\nu)}{1+\gamma} - 2\left(\frac{1+2\gamma}{(1+\gamma)^2} - \frac{2(1+\nu)}{1+\gamma}\right)\frac{s}{s+\pi/8}, \tag{2.24b}$$

$$h_{51}^{\rm Pade}(s,\gamma) \approx -\frac{\gamma^2}{(1+\gamma)^2} + 2\frac{\gamma^2}{(1+\gamma)^2}\cdot\frac{s^2}{2\frac{\gamma^2}{(1+\gamma)^2}+5\pi s/8+s^2}. \tag{2.24c}$$

For good tip–surface contact, the piezoresponse signal is $d_{33}^{\rm eff} = u_3(r)/U$ and can be written as $d_{33}^{\rm eff} = h_{13}d_{31} + h_{51}d_{15} + h_{33}d_{33}$. Piezoresponse $d_{33}^{\rm eff}(r)$ versus the cylindrical domain radius for the sphere–plane and point charge models of the tip for different ferroelectric materials is shown in figure 16. Similarly to domain wall imaging, the best sensitivity to small domains formed below the tip can be achieved in BTO, whereas the worst one corresponds to LNO independently of the tip representation.

From the data in figure 16, the coercive bias in the PFM hysteresis loop measurements (i.e. when the response is zero, corresponding to equality of the PFM signal from the nascent domain and the surrounding unswitched matrix) in the point contact approximation corresponds to a domain size of the order of $0.1R_0$ (for BTO) to $0.7R_0$ (for PZT6B and LNO). This suggests that the early steps of the switching process are local, i.e. the information is collected from the area below the characteristic tip size. Furthermore, the significant (~10%) deviations of the PFM signal from constant begin for domain sizes well below (factor of 10–30) the characteristic tip size. Therefore, the initial nucleation stages can be probed even when the domain is extremely small (on the order of several nanometers (for $R_0 = 50$ nm)). On the other hand, the response saturates fairly slowly with the domain size, and hence the 'tails' of the hysteresis loop contain information on domain sizes well above the tip size.

To summarize, the analytical expressions equations (2.23) and (2.24*a*)–(2.24*c*) relate the piezoresponse signal measured at the center of the domain $d_{33}^{\rm eff}(r)$ and the domain radius. This allows the domain radius–voltage dependence $r(U)$ to be reconstructed from the experimental data of the piezoresponse hysteresis $d_{33}^{\rm eff}(U)$ once the tip parameters are determined using an appropriate calibration procedure (e.g. from the domain wall profile).

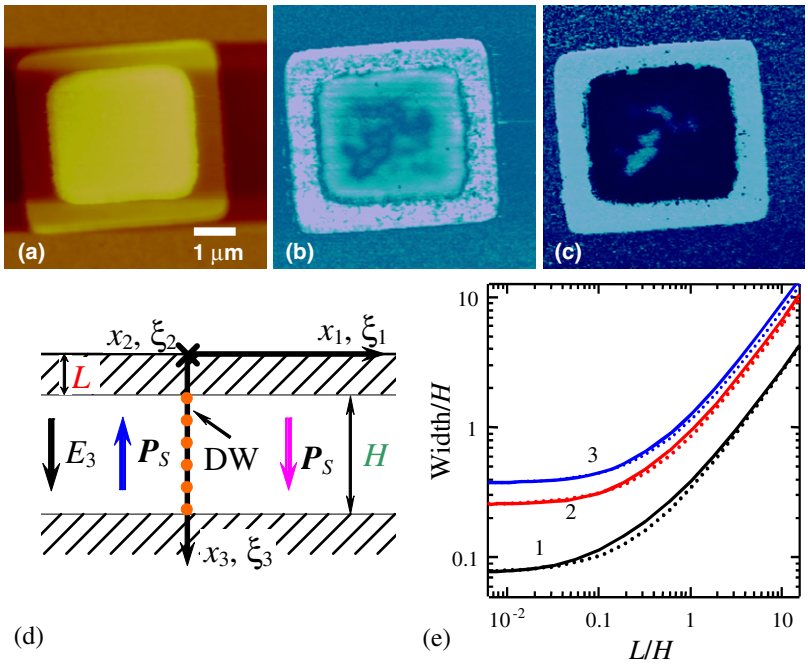

Figure 17. (*a*) Surface topography and (*b*) amplitude and (*c*) phase PFM images of an etched capacitor structure. (*d*) Coordinate systems in a global excitation PFM experiment. (*e*) Domain wall width at level $\eta = 0.76$ as a function of the top electrode thickness for $\nu = 0.3$ and $-d_{33}/d_{31} = 2, 3, 4$ (curves 1, 2, 3). Solid curves represent the exact and dashed the approximate (equations (2.28*a*)–(2.28*c*)) solutions. (*a*)–(*c*) Reproduced from [111]. Copyright 2008, Microscopy Society of America. (*d*), (*e*) Reproduced from [155] and copyright 2008 by the American Institute of Physics.

2.3.4.5. Imaging of ferroelectric capacitors. Applications of ferroelectric materials as non-volatile memory components have resulted in significant interest in theoretical and experimental studies of polarization dynamics in capacitor structures. In PFM of capacitor structures, a periodic uniform electric field is applied between the top and bottom electrodes, and the resulting surface displacement is measured locally by a SPM tip [215]. This global excitation method is different from standard (local excitation) PFM, in which both the electric field and the local strain are localized.

The domain wall width in PFM of capacitor structures with uniform (in the vertical direction) domain structure, i.e. the resolution limit in PFM with global excitation, can be analyzed similarly to tip–electrode experiments. The vertical PFM signal, i.e. the surface displacement $u_{3i}(\boldsymbol{x})$ at location $(x_1, x_2, 0)$ is given by equation (2.6) where the field is now uniform. Considering a domain structure with two opposite domains divided by a flat wall perpendicular to the film surface, we obtain that for the uniform excitation, equation (2.6) can be rewritten as follows:

$$u_3(x_1, x_2, 0) = -U(W_{33}(x_1, L, H)d_{33} + (1+2\nu)W_{31}(x_1, L, H, \nu)d_{31}). \quad (2.25)$$

Here, $U = HE_3$ is the potential difference between the top and the bottom electrodes. L is the thickness of the top electrode and H is the film thickness (see figure 17(*d*)). After cumbersome integrations, functions W_{33} and W_{31} are derived analytically as [155]

$$W_{33}(x_1, L, H) = f_1(x_1, L, H) + f_2(x_1, L, H), \quad (2.26)$$

$$W_{31}(x_1, L, H, \nu) = f_1(x_1, L, H) + \frac{\nu}{2(1+2\nu)} f_2(x_1, L, H), \quad (2.27)$$

where f_1 and f_2 are simple algebraic functions as analyzed in [155]. The piezoresponse signal in a uniformly poled capacitor is $u_3(x_1, x_2, 0)/U = -d_{33} - (1+2\nu)d_{31}$ (due to clamping). The non-zero contribution of d_{31} is directly related to the mechanical conditions at the boundary between the film and the bottom electrode, which are assumed to have identical mechanical properties. As an example, shown in figure 17(*a*)–(*c*) are topography, PFM amplitude and PFM phase images of a poled capacitor. Note that details within the capacitor are much coarser than on a free surface, indicative of lower spatial resolution.

The generalized domain wall width is defined as the distance between the points at which the response is saturated to the fraction, η, of the signal at infinity. Hence, the standard edge resolution is defined as $\eta = 0.5$. The width can be approximated as a bilinear function, $w(L, H) \cong aH + bL$, of the film and top electrode thicknesses:

$$w(L, H) \cong a\left(\eta, \nu, \frac{d_{31}}{d_{33}}\right) H + b\left(\eta, \nu, \frac{d_{31}}{d_{33}}\right) L, \quad (2.28a)$$

where coefficient, a, is the solution of the transcendental equation:

$$\arctan\left(\frac{a}{2}\right) + \frac{d_{33} + \nu d_{31}/2}{d_{33} + (1+2\nu)\, d_{31}} \ln\left(1 + \frac{4}{a^2}\right) \frac{a}{2} = \frac{\pi}{2}\eta, \quad (2.28b)$$

and coefficient b is

$$b = \eta \frac{\pi}{2} \frac{d_{33} + (1+2\nu)\, d_{31}}{d_{33} + \nu d_{31}/2}. \quad (2.28c)$$

Typical values for coefficient a vary from 0.08 to 0.4 at $\eta = 0.76$ and $-d_{33}/d_{31} = 2$–4. The dependence of the

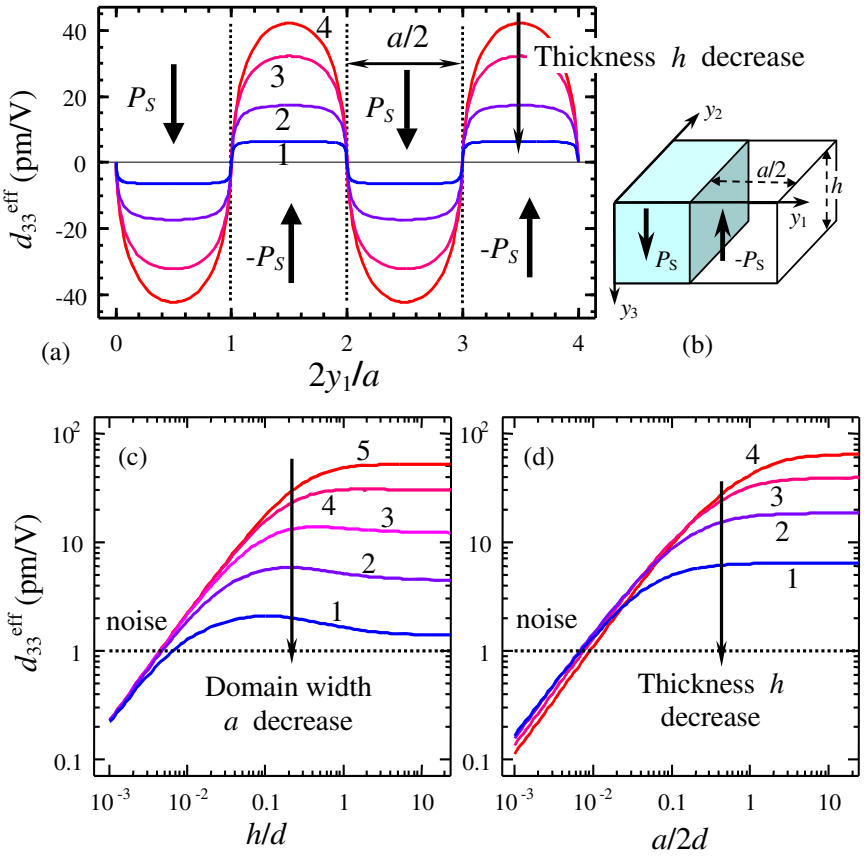

Figure 18. (*a*) PFM profile of a periodic stripe domain structure (*b*) in a PTO film ($\kappa = 121$, $\gamma = 0.87$) on a STO substrate ($\kappa_b = 260$, $\gamma = 1$) for different film thicknesses $h/d = 0.03,\ 0.1,\ 0.3,\ 1$ (curves 1, 2, 3, 4). (*c*) Maximal piezoresponse versus film thickness for different stripe periods $a/d = 0.03,\ 0.1,\ 0.3,\ 1,\ 3$ (curves 1, 2, 3, 4, 5). (*d*) Dependence of the response on the stripe period for different film thicknesses $h/d = 0.03,\ 0.1,\ 0.3,\ 1$ (curves 1, 2, 3, 4). Reproduced from [155]. Copyright 2007, American Institute of Physics.

domain wall width on the top electrode thickness obtained by the numerical calculation and approximately from equations (2.28*a*)–(2.28*c*) is shown in figure 17(*e*). The immediate consequence of equation (2.28*a*) is that for a mechanically uniform capacitor (no cracks, etc), the signal generation area in PFM, even for point mechanical contact, is determined by the total thickness of the capacitor structure. Note that the domain wall width scales linearly with sample thickness for thin top electrodes ($W/H = 0.08$–0.3 depending on piezoelectric anisotropy), and increases rapidly with top electrode thickness. This conclusion can readily be understood as a consequence of the presence of the primary length scale in the system, and similar behavior is anticipated for, e.g., synchrotron x-ray based measurements of domain structures.

For cases when the domain wall is also associated with the grain boundary and the grains are mechanically decoupled, the coefficient in equations (2.28*a*)–(2.28*c*) is $a = 0$. Here, the top electrode thickness is the only relevant length scale. For the case of intermediate coupling, the bulk contribution will be reduced, but the top-electrode contribution is expected to be constant. Finally, for a liquid top electrode (i.e. imaging in a conductive solution), $b = 0$. Finally, for the capacitor structure with non-uniform domain structures (e.g. in the presence of grains, etc), the characteristic grain size will be a limiting length scale for resolution.

2.3.4.6. Extrinsic size effect in PFM of ferroelectric thin films. The extrinsic (i.e. due to the tip size, rather than changes in materials' properties) size effect in PFM of ferroelectric and piezoelectric thin films on a nonpolar dielectric substrate with different elastic properties was analyzed in [216, 217] in the point mechanical contact approximation. PFM profiles of periodic stripe domain structures in a PTO film on a $SrTiO_3$ (STO) substrate for different film thicknesses, h/d, are shown in figures 18(*a*) and (*b*). It is clear that with a film thickness decrease, the profile $d_{33}^{eff}(y_1)$ acquires a rectangular shape, closer to the ideal image. The sharpness of the domain stripes image increases due to the object transfer function spectrum broadening. At the same time, the signal strength decreases for smaller film thicknesses, making the relative noise level higher (see figures 18(*c*) and (*d*)).

2.4. Calibration of PFM

2.4.1. Experimental determination of tip parameters. In the case when the electric field produced by the tip does not change across the sample, the resolution function is invariant along the sample surface and can be determined from the effective image charge distribution that represents the tip. The calibration of the tip geometry is thus equivalent to determining the set of N charges Q_i located along the surface normal at a distance d_i above the surface, as illustrated in figure 19(*a*). The image

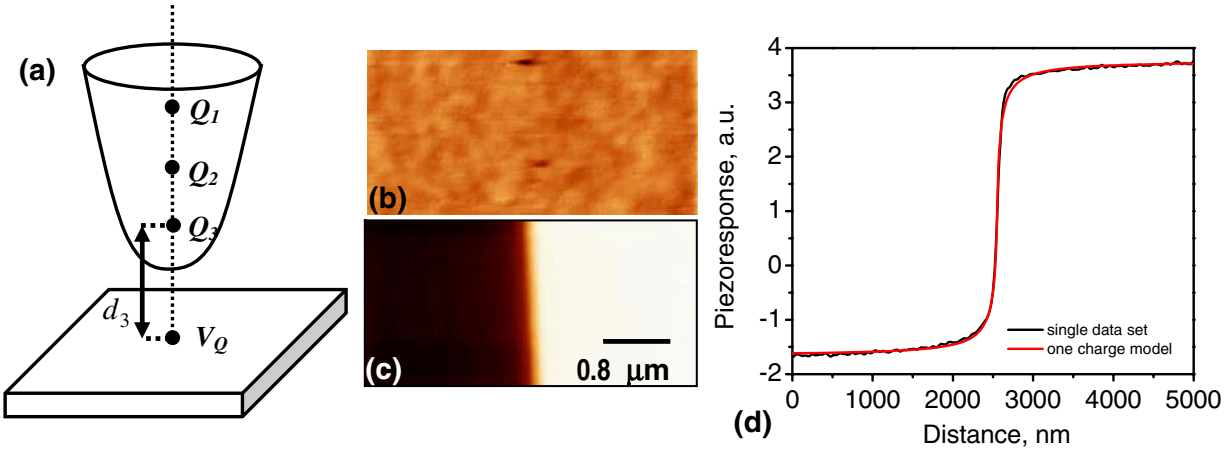

Figure 19. (*a*) Representation of a realistic tip by a set of image charges. (*b*) Surface topography and (*c*) PFM image of domain wall in LNO. (*d*) Fit of the extrapolated data set with equal weighting for all points. Reproduced from [218]. Copyright 2007, American Institute of Physics.

Table 2. Effective image charge parameters for different ferroelectrics.

Material	Wall width (nm)	Q	d (nm)	R_d(nm)	R_0 for $\varepsilon_e = 1(\mu m)$	R_0 for $\varepsilon_e = 80$ (nm)
$LiNbO_3$	96	1000	92	58.6	4.8	60
Epitaxial PZT	107	2550	125	79.6	5	62.5
PZT in air	58	723	86.5	55.1	44	541
PZT in liquid	6	104	11.8	7.5		75

charges can be deconvoluted from the experimental domain wall profile by minimizing the functional

$$F[u_3] = \int \left(PR(a) - \frac{1}{2\pi\varepsilon_0(\varepsilon_e + \kappa)} \sum_{m=0}^{N} \frac{Q_m}{d_m} \tilde{u}_3(s_m) \right)^2 da \tag{2.29}$$

with respect to the number, N, magnitude and charge–surface separation of a set of image charges $\{Q_i, d_i\}_N$ representing the tip. Here $PR(a)$ is the measured piezoresponse and integration is performed over all available a values. The dielectric constant of the medium can be fixed to the value of free air ($\varepsilon_e = 1$) or water in the tip–surface junction or imaging in liquid ($\varepsilon_e = 80$). The output of the fitting process is the set of reduced charges $q_i = Q_i/2\pi\varepsilon_0$ and the charge surface separation, d_i. Note that the charges and the dielectric constants cannot be determined independently, since only $Q_m/(\varepsilon_e + \kappa)$ ratios enter equation (2.29).

Shown in figures 19(*b*)–(*d*) is an example of a domain wall profile and the corresponding fit by equation (2.29) with $N = 1$ for LNO. The corresponding image charge parameters are summarized in table 2. To improve the fit quality, more complex fitting functions with $N = 2$ and $N = 3$ were attempted. However, independent of the choice of the initial values of the image charge, the fit converged to a single image charge, i.e. $d_i = d$ and $\sum Q_i = Q$. Similar behavior was observed for other domain walls.

This analysis suggests that the electrostatic field produced by the tip is consistent with a single point charge positioned at large separation from the surface, contrary to the behavior anticipated in contact mode imaging. The analysis was extended to the case of the sphere–plane (radius of curvature R_0) and disk–plane (radius R_d) models. The sphere parameters are calculated both from ambient and water environment to account for possible capillary condensation effects. From the data, it is clear that the use of the sphere/air model leads to implausibly large radii. Hence, experimental data are consistent either with the presence of a capillary water film in the sphere model, or conductive disk model [218].

2.4.2. Resolution for non-zero contact area. Extensive quantitative analysis of domain wall width, taking into account the finite contact tip–surface contact area, was reported by the Gopalan group [183]. The geometric structure of more than 100 SPM tips was ascertained using scanning electron microscopy to yield effective tip sizes [212], see figures 20(*a*) and (*b*). The domain wall width in periodically poled lithium niobate was measured as a function of tip radius. In parallel, the domain wall width was calculated using a numerical finite element analysis package, figure 20.

The comparison of the experimentally measured PFM signal and domain wall width as a function of tip radius with numerical and analytical theory predictions is shown in figure 21. The data clearly suggest that the PFM signal is independent of contact area, in agreement with the theory of Karapetian [175, 176]. At the same time, the domain wall width saturates at ∼100 nm, corresponding to a tip-independent domain wall width. This can be attributed both to the effect of an ambient environment on imaging, and to wall broadening, necessitating further studies in an ultra-high vacuum environment.

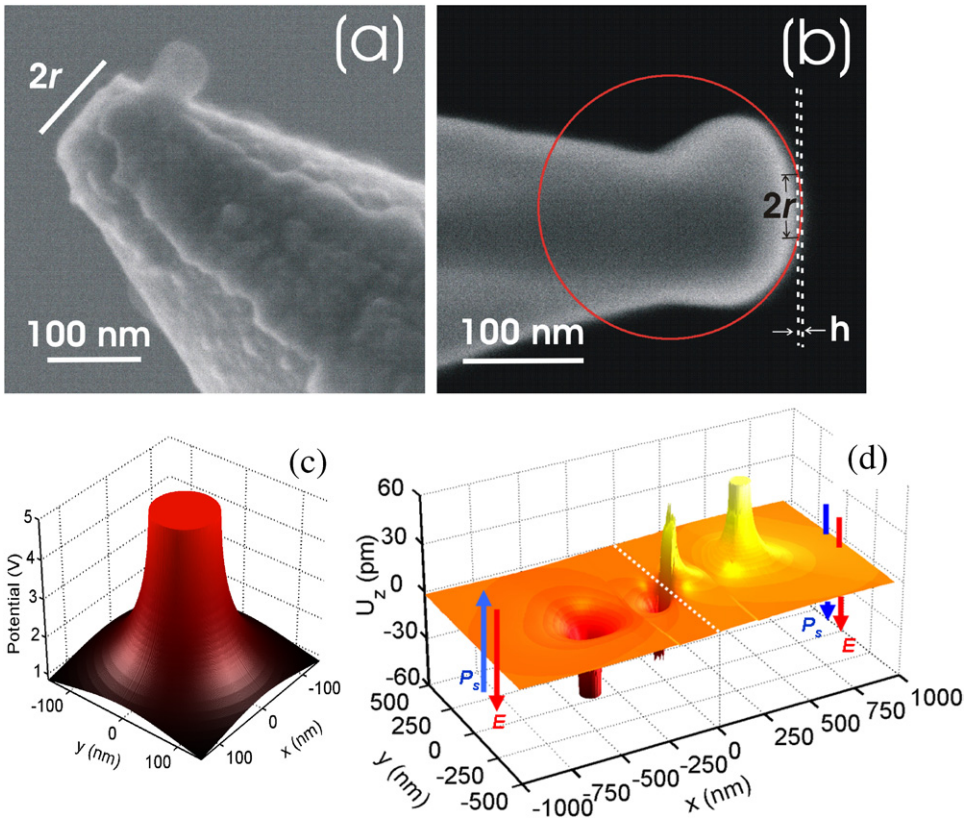

Figure 20. (*a*) Field emission (FE) SEM image of a used PFM tip with a circular disk-like end with a radius r. (*b*) FE-SEM image of a sphere-like PFM tip. The radius r of the contact circle for a weak indentation ($h \sim 1$–2 nm or 1 unit cell depth) is used to characterize the radius r of the tip as shown. (h is not to scale in the figure). (*c*) Finite element simulations of surface potential on LN surface under a 50 nm radius disk tip in contact with sample with 5 V applied. (*d*) FEM simulated piezoelectric displacements, U_z of a LNO z-surface. Displacements for three different tip locations are shown: tip located on the wall and away from the wall on either side. Reproduced from [212]. Copyright 2008, American Institute of Physics.

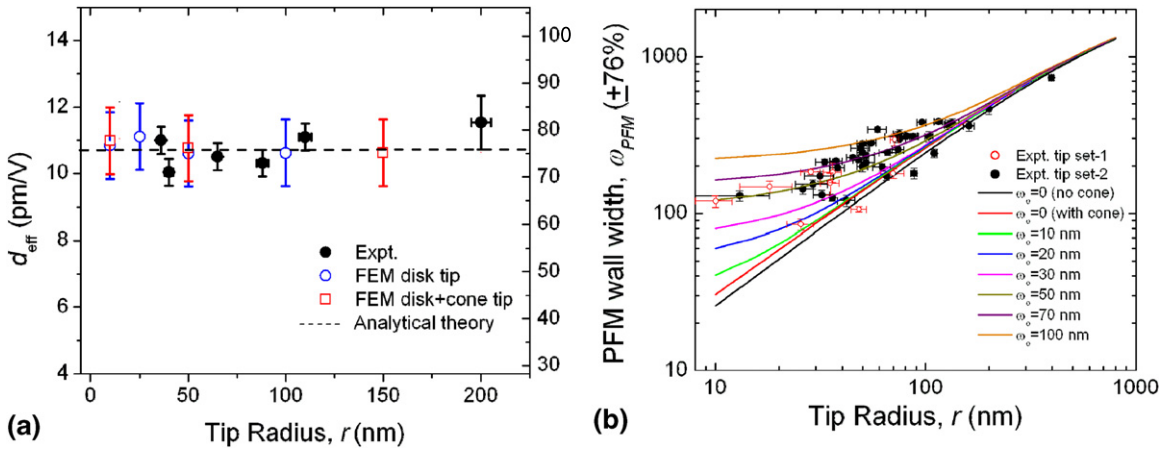

Figure 21. The maximum amplitude, $|U_z|$, away from the wall as a function of tip radius, r, is shown. Also shown overlapped are the analytical theory and finite element method (FEM) predictions. (*b*) PFM wall width as a function of tip radius for sphere-like and disk-like PFM tips. Also shown are analytical theory predictions for different intrinsic wall half-widths. Reproduced from [212]. Copyright 2008, American Institute of Physics.

2.5. Implications for PFM data analysis

Below, we summarize the implications of the contrast formation mechanism and resolution function analyses for the interpretation of PFM imaging and spectroscopy. The effect of finite resolution is that quantitative properties such as domain-specific effective electromechanical response can be measured only for domains much larger than the RTR value. At the same time, a domain will be visible above the information limit, but no quantitative measurements can be obtained. A good measure of the RTR is the domain wall width in the mixed PFM signal, while the IL can be determined from the domain wall width in the phase image.

The minimum writable domain size is not necessarily related to the information limit in PFM and can be either larger or smaller. This follows from the fact that while the signal generation volume in PFM is independent of the tip bias, the written domain size, and in particular, the critical size of the nucleated domain, has a strong bias dependence, i.e. minimum writable domain size can be smaller than the PFM resolution. This suggests that in some cases the resolution is a limiting factor precluding experimental observation of smaller domains created by PFM. Clearly, this conclusion is non-universal and strongly depends on the material, e.g. in polycrystalline films, the grain-by-grain switching will result in minimal writable bit sizes being larger than the resolution.

The resolution effect will clearly affect the analysis of the parameters such as domain size distributions in the disordered materials or geometry of the fractal and self-affine domain walls. For example, the structure factor will be $S(q) = S'(q)R(q)$, where $S'(q)$ is the intrinsic structure factor of the interface and $R(q)$ is the transfer function defining microscope resolution. Practically, $R(q) = 1$ for $q \ll q_c$ and $R(q) = q^{-n}$ for $q \gg q_c$, where power law n is determined by the image formation mechanism. For ultrathin interfaces such as ferroelectric walls, $q_c \sim 1/w_c$. Correspondingly, the fractal properties $h(x)$ for length scales below w_c are likely dominated by the scanner noise along the slow scan axis (which can be established from the topographic imaging of appropriate calibration standard, e.g. step edge of a cleaved graphite surface), and by the tails of the transfer function for the fast scan axis, rather than the intrinsic wall geometry [219].

3. Local polarization switching in ferroelectric materials by PFM

3.1. Polarization dynamics at the nanoscale

The key characteristic of ferroelectric materials is that the direction of spontaneous polarization can be reversed by the application of sufficient electric field. Not surprisingly, SPM of ferroelectrics has attracted considerable attention due to its potential to manipulate ferroelectric materials at the nanoscale by creating ferroelectric domains, studying their dynamics during growth and relaxation and mapping their interaction with structural and morphological defects [107, 108, 110]. In this section, we summarize the existing results on the kinetics of domain formation and relaxation, as well as theoretical models for the description of the domain growth process in the rigid ferroelectric approximation.

3.2. Experimental aspects of tip-induced polarization switching

3.2.1. Domain growth kinetics. PFM allows a straightforward approach to study the kinetics of domain formation and relaxation by combining the *writing* step of applying a bias pulse of preselected duration and magnitude, and the *reading* stage at which the size of the resulting domain is imaged. These studies have received a significant impetus in the context of ferroelectric data storage [25], and have been stimulated by the availability of high-quality epitaxial thin films that have low (below 10 V) switching voltages.

A broad range of studies of domain wall growth on sol–gel [220–223] ferroelectric films have been reported. The implementation of high-voltage PFM [224] has allowed studies of domain dynamics in single crystals as well, and particularly has enabled the kinetic studies as a function of pulse parameters [225–232]. As an example, shown in figure 22 is the morphology of ferroelectric domains in LNO single crystal. While for low bias pulses the domains are nearly round, large domains adopt well-defined crystallographic shapes, mirroring surface tension driven rounding of nanoparticles.

The radii of domains fabricated in lithium niobate single crystals were found to scale linearly with applied field and approximately logarithmically with time [226]. Similar scaling was found for other materials, suggesting the universality of this rate law.

The time dependence of domain-wall velocity was studied by several groups [128, 233, 234] in an attempt to relate domain growth kinetics to the dominant wall pinning mechanisms. The first link between wall velocity and disorder was established in the seminal papers by Tybell *et al* [64] and Paruch *et al* [234] and since then was actively studied by several groups [233, 235]. Domain growth in epitaxial films has also been compared with macroscopic measurements on capacitor structures [380].

Significant efforts have been directed at fabricating ultra-small domains and the determination of minimal stable domain size and associated lifetimes. Recently, 8 nm domain arrays have been fabricated and detected using scanning nonlinear dielectric microscopy [237, 238] (figure 23(*a*)). The Cho group has also demonstrated the formation of 7 nm arrays and 2.8 nm domains (see figure 23(*b*)) and has written images using the technique (figure 23(*c*)) [236]. This impressive result corresponds to a density of 160 Tb inch^{-2} (10 Tb inch^{-2} for 8 nm array), approaching molecular storage level [239].

One of the key uncertainties for the characterization of domain growth kinetics is the lack of quantitative information on the electrostatic field structure produced by the probe. In most studies to date, the field is approximated as a single point charge, a model well validated for tip apex at large separations from the contact area. On larger length scales, the conical part of the tip provides a slow-decaying field component, which is, however, attenuated by the dielectric gap effect. Furthermore, the point charge model is clearly inapplicable for small tip–surface separations of the order of the tip size (which in turn is related to the domain wall width, as discussed in section 2.3, on which the field is uniform). The second factor affecting domain growth kinetics is the effect of mobile surface charges, screening and liquid bridge formation, as discussed in section 3.3.

3.2.2. Domain relaxation and retention. The retention behavior of ferroelectric domains following local polarization reversal presents obvious interest for data storage and ferroelectric lithography applications. Retention behavior in epitaxial and polycrystalline PZT [240], the thermal stability [228] and the retention behavior [229] of fabricated domains

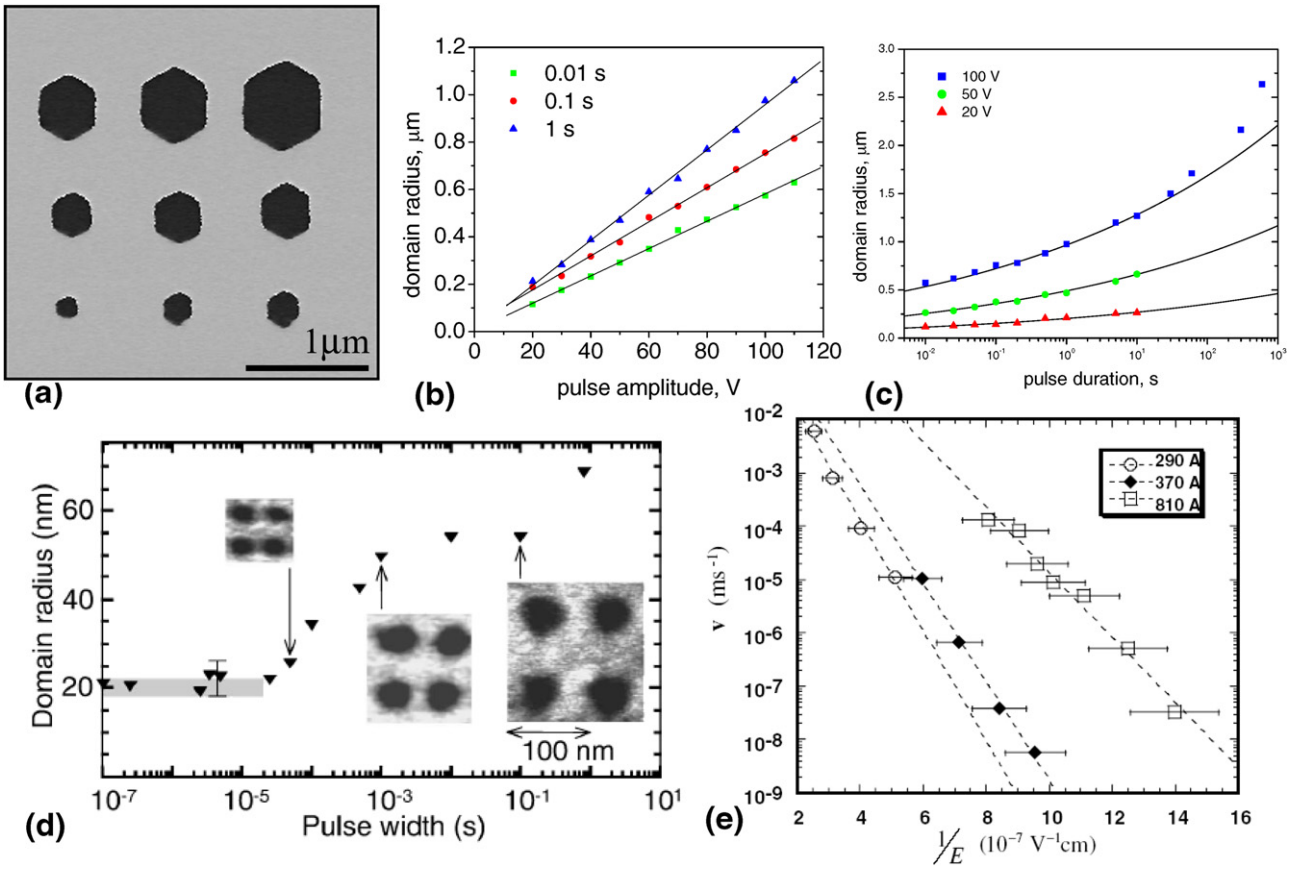

Figure 22. (*a*) PFM phase image of domains written in a lithium niobate crystal by varying the voltage pulse amplitude. Plots of domain radius versus (*b*) pulse amplitude and (*c*) pulse duration in a lithium niobate crystal. (*e*) Domain size as a function of pulse duration for a 370 Å thick PZT film. (*d*) Domain wall speed as a function of the inverse applied electric field for three PZT films of different thicknesses. Panels (*a*)–(*c*) reproduced with permission from [226], copyright 2005, American Institute of Physics, and panels (*d*),(*e*) reproduced with permission from [64], copyright 2002, American Physical Society.

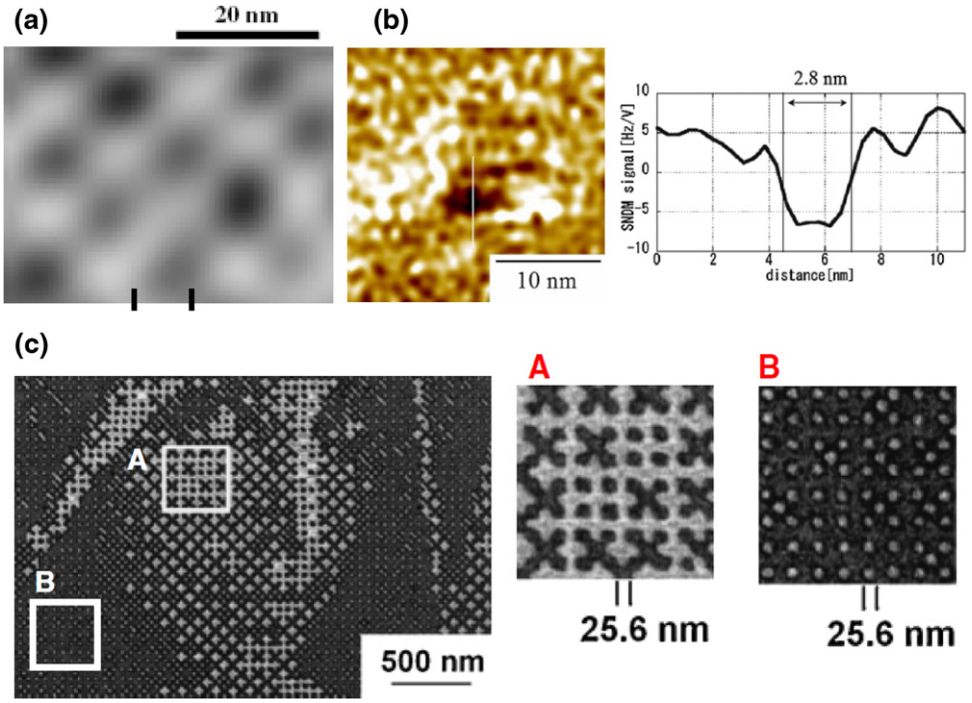

Figure 23. (*a*) 8 nm array of domains, (*b*) 2.8 nm domain and (*c*) nanoscale domains written to construct an image. (*a*) Reproduced from [52], copyright 2006 IOP Publishing and (*b*), (*c*) from [236], copyright 2007, Institute of Pure and Applied Physics.

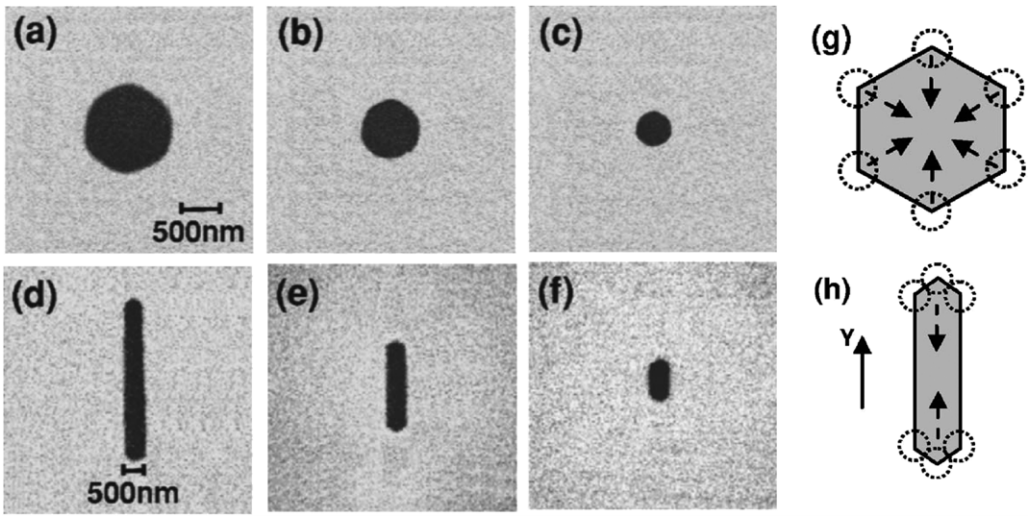

Figure 24. Piezoresponse images of (*a*), (*d*) written domains in stoichiometric lithium tantalate crystals. Domains after being heated to 100 °C and then cooled (*b*), (*e*) once and (*c*), (*f*) twice. (*g*), (*h*) Illustrations of domain shrinkage due to heat treatment where dotted circles mark domain corners and arrows show the domain shrinkage direction. Reprinted from [228], copyright 2006, American Institute of Physics.

in single crystals and even capacitors switched by external strain [241] have been studied in detail by PFM.

Extensive studies of the written domain stability in LNO and LTO single crystals have been performed by the Kitamura group. For large domain sizes, the relaxation driven by surface tension was observed at relatively low temperatures of ∼100 °C, indicative of the high mobility of domain walls in these materials [228] (figure 24). The role of surface adsorbates and ion implantation, i.e. the creation of new pinning centers, on domain stability has been investigated [242, 243]. The effect of intrinsic defects in congruent LNO and associated disorder on the domain relaxation was studied and shown to lead to highly serrated domain walls [244].

A very elegant and detailed study of domain relaxation in thinned lithium niobate (LNO) crystals as a function of domain size and crystal thickness has been reported by Kan *et al* [231] (figure 25). A two-step mechanism in which a slow relaxation stage involving lateral shrinking of cylindrical domains is followed by fast relaxation after the domain is pinched-off from the bottom surface has been reported. This study was later extended to abnormally switched 'bubble' domains, as discussed in section 3.2.5 [245].

Note that while domain growth in the field of an SPM probe is determined by the interplay of the probe-induced field distribution, the field-dependent wall velocity, and the surface charge diffusion and charge injection kinetics, the domain relaxation in the absence of external fields is driven only by wall tension and depolarization fields. Correspondingly it is easier to interpret and quantify, and allows one to study wall dynamics quantitatively. This behavior is reminiscent of, e.g., nanoindentation experiments based on the Oliver–Pharr method [246], where the formation of the contact during loading is not amenable for direct interpretation, whereas the unload curve with constant tip–surface contact offers quantitative information on mechanical properties. That said, while domain formation and growth can always be induced by applying a high enough field, relaxation is controlled by the wall pinning mechanism and driving force, and hence can be much slower (or faster) than the experimentally accessible time scales.

Polarization relaxation in ferroelectric polymers [247] and ferroelectric relaxors [248, 249] merits separate mention. While in classical ferroelectrics, relaxation occurs through the motion of domain walls, relaxors demonstrate a gradual fade out of contrast, consistent with slow relaxation of the effective order parameter [250]. In ferroelectric polymers, the dominant factor controlling slow dynamic response is chain rotation [251]. The time-resolved relaxation measurements in relaxors are discussed in detail in section 4.5.

3.2.3. Domain–defect interactions. The characteristic aspect of all realistic materials is the presence of defects that serve as nucleation sites and pinning centers for moving domain walls. In PFM-based point switching experiments, the concentration of the electric field in the vicinity of the probe apex typically results in nucleation at the probe apex and the as-formed domain grows rapidly. Hence, the observation of a defect effect on nucleation is possible only in the spectroscopic mapping PFM as discussed in section 4.4. At the same time, the domain wall pinning at the defects can be observed directly from the domain wall geometry and domain shape.

The first analysis of domain wall geometry in terms of the pinning mechanism was performed by Paruch *et al* [234] and extensively summarized in a recent review [222]. These studies were later extended to model domain energetics in ultrathin films [235]. The domain wall velocity in the presence of surface defects was also investigated [252]. A similar approach was adopted by Pertsev *et al* to address domain wall dynamics [233]. The extensive effort by the group of Kitamura [228, 242–244] has demonstrated control of pinning by artificial defects. The domain wall geometry represents the result of multiple defect interactions in which the effect of individual defects cannot generally be resolved. The study by Agronin *et al* [253] has addressed the pinning on macroscopic morphological defects.

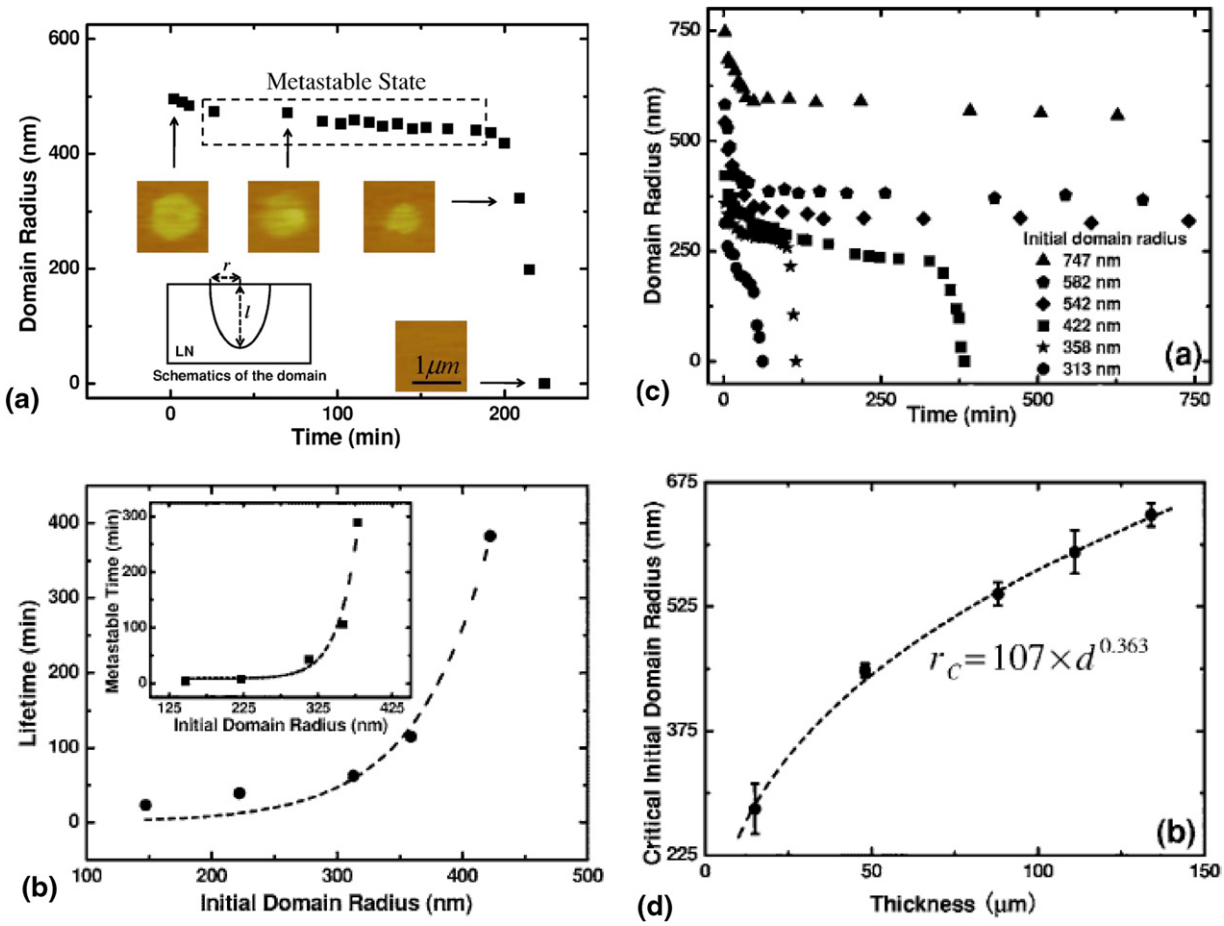

Figure 25. (*a*) Domain decay dynamics. (*b*) Domain lifetime dependence on the initial domain radius. (*c*) Decay process for different initial radii. (*d*) Critical initial domain radius for samples of different thicknesses. Reprinted from [231], copyright 2007, American Institute of Physics.

Fundamental studies of pinning mechanisms require the structure of defects to be known. Given that the width of a typical ferroelectric domain wall is on the order of 1–3 unit cells, the defect has to be defined on the atomic level, significantly narrowing the range of systems with known localized defects. Ferroelastic domain walls offer an advantage of known structure and geometry. The effect of ferroelastic domain walls and in-plane domain twins on ferroelectric switching and domain wall dynamics in (1 0 0) tetragonal ferroelectric films has been studied in detail by Ganpule *et al* [254, 255]. The switching in the vicinity of a 90° domain twin is shown to proceed through the correlated domain motion as illustrated in figure 26. This mechanism was recently confirmed by in-plane observations by Aravind *et al* [256]. The effect of ferroelastic domain walls on relaxation was studied on mesoscopic and single wall levels in [255], and the walls were found to serve as effective pinning centers. At the same time, within the cells formed by 90° twins, the formation of faceted domains was observed. These studies allowed the relaxation rate to be related to wall curvature (figure 27).

Finally, the effect of grain boundaries, the dominant defect type in polycrystalline films, was studied by Gruverman [128]. In many materials, the grain boundaries serve as natural barriers for wall motion, resulting in a single-grain switching. The analysis of the grain boundary–domain interaction is limited by the fact that the GB structure, including both the grain misorientation and the presence of secondary phases, charge, etc, is generally unknown. At the same time, EM methods such as aberration corrected EM and energy loss spectroscopy [257–259] that have been shown to be extremely powerful methods to analyze GB structure and charge are not yet compatible with PFM measurements [260]. Artificially engineered bicrystal defects offer an alternative, and the direct observation of domain wall pinning on a well-defined GB has recently been reported [261]. The use of well-defined defects allows the *deterministic* polarization switching mechanisms to be deciphered, as discussed in section 5.

3.2.4. Non-180° switching. In ferroelectric materials, the application of electric field in most cases induces only 180° polarization switching, since non-uniform ferroelastic (i.e. non-180°) switching increases the strain state of the system and is generally believed to be less likely. However, in multiaxial ferroelectrics and in disordered systems, non-180° switching was observed, and in some cases controlled, by PFM. In a polycrystalline film, elastic clamping between the domains can result in the mechanism when ferroelectric switching of one grain triggers in-plane switching of the neighboring grains. Similar effects were found in ferroelectric capacitors

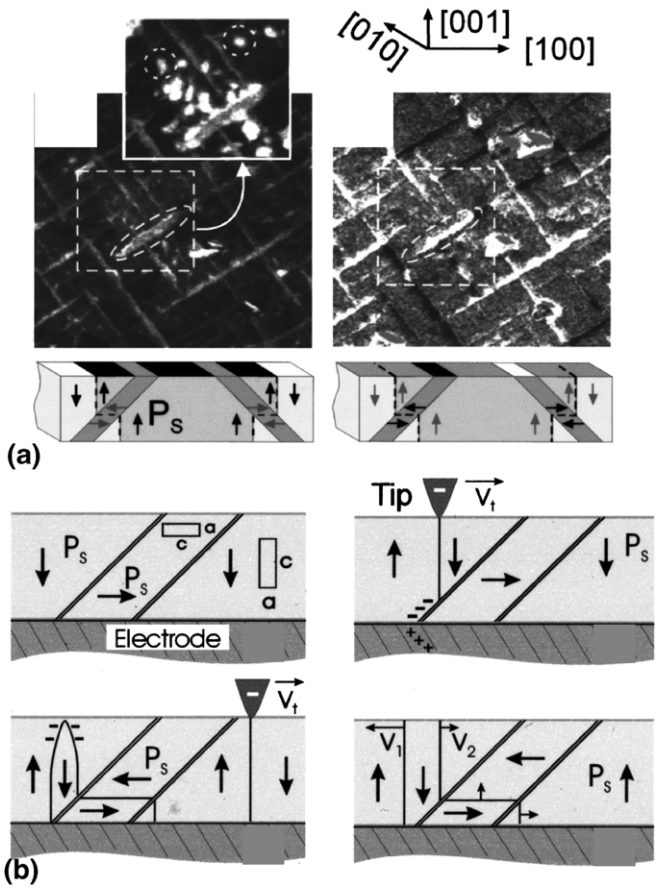

Figure 26. (*a*) Piezoresponse images of a twinned PZT film after poling. The 'out-of plane' PFM signal is shown on the left and the 'in-plane' signal is shown on the right. The polarization directions are shown schematically in the sketches below the PFM images. (*b*) The expected scenario of polarization switching and relaxation in polydomain PZT films: (upper left) the initial *c*/*a*/*c* domain state, (upper right) the domain configuration during tip-induced 180° switching, (lower left) forward growth of the *c* domain following the application of the field, (lower right) lateral motion of the 180° domain boundaries during backswitching. Reproduced from [161], copyright 2002, American Institute of Physics.

[162, 163], in which antiparallel switching was presumably triggered by elastic interactions [262]. Further examples of anomalous nucleation behavior were observed and analyzed theoretically [263].

In tetragonal (1 0 0) films, the formation of a 180° domain is associated with an elastic strain due to the piezoelectric coupling in the tip field. This strain can be compensated by the formation of 90° twin domains. This behavior was observed by Chen *et al* [264] as shown in figure 28. Remarkably, both the formation of stabilizing 90° twins and the formation of a surface depression after the bias is off (to compensate for strain) are observed. These observations illustrate the surprising ease with which non-180° domains can form (note that observations in figure 28 imply that not only ferroelastic domains are formed, but also remain stable in the zero-field state).

Recently, much interest has been directed toward applications of rhombohedral ferroelectrics and multiferroics, in which the presence and motion of ferroelastic 71° and 109° domain walls lead to improved electromechanical properties [265]. In ferroelectric–ferromagnetic heterostructures, non-180° switching opens up an effective pathway for strain-mediated multiferroic coupling [266] and strain-induced metal–insulator transitions in the second component [267]. In materials such as $BiFeO_3$ (BFO) enhanced conduction at 180° and 109° domain walls has been reported, raising the possibility for novel electronic and memory devices [268]. Finally, given that the magnetic ordering in BFO is ferromagnetic in (1 1 1) planes and antiferromagnetic between the planes, control of non-180° switching is crucial for the development of exchange-coupled devices [266]. In multiferroics, the control of magnetic and strain order parameters can be achieved by non-180° polarization switching. In addition, this will allow exotic polarization orderings such as vortex states and other topological defects to be created directly. However, simple symmetry considerations, namely the fact that the tip-induced field is rotationally invariant, forbid direct field manipulation of non-ferroelectric order parameters.

This fundamental limitation is belied by the number of phenomenological observations of non-180° switching in BFO. Cruz *et al* have explored domain switching in BFO using a biased SPM tip and have shown that for BFO grown on (1 1 0) STO, 180° walls are formed at lower voltages and 109° domain walls form at higher voltages [269]. The stability of otherwise unstable 109° domains was increased by the creation of a stack of 180° domain walls between a 71° domain wall and a 109° domain wall (domain wall architecture). Zavaliche *et al* have demonstrated that both ferroelectric and ferroelastic switching is possible during area poling of BFO grown on (0 0 1) STO; however, no further control of the switching process was reported [270]. The first control of the in-plane domain switching on (0 0 1) oriented BFO was done by Shafer *et al* by using an in-plane electrode structure [271]. 90° rotation of the stripe-like domains at the edges of the in-plane electrodes where the electric fields are inhomogeneous was observed. However, this approach is limited to switching between two domain patterns, whereas BFO provides eight possible sets of stripe domain patterns. Overall, the SPM single point, SPM area poling, capacitor-based and in-plane electrode-based switching experiments suggest that polarization switching can proceed along many competing pathways in a seemingly uncontrollable fashion. Recent studies by Balke *et al* [272] have demonstrated that in-plane domain engineering can be achieved using symmetry breaking by a moving SPM tip.

3.2.5. Anomalous local switching and ambient effects. One of the fundamental differences between the SPM-based and capacitor-based switching is the effect of the environment. Even in capacitors, the poor interface quality can result in rapid degradation, as well as significantly affect electrostatic field distribution due to the dead layer effect [273, 274]. In comparison, in SPM experiments, the tip is contacted with surfaces with water layers resulting from exposure to an ambient environment. Water layers are known to be responsible for phenomena such as anodic oxidation by AFM [275] and strongly affect SPM

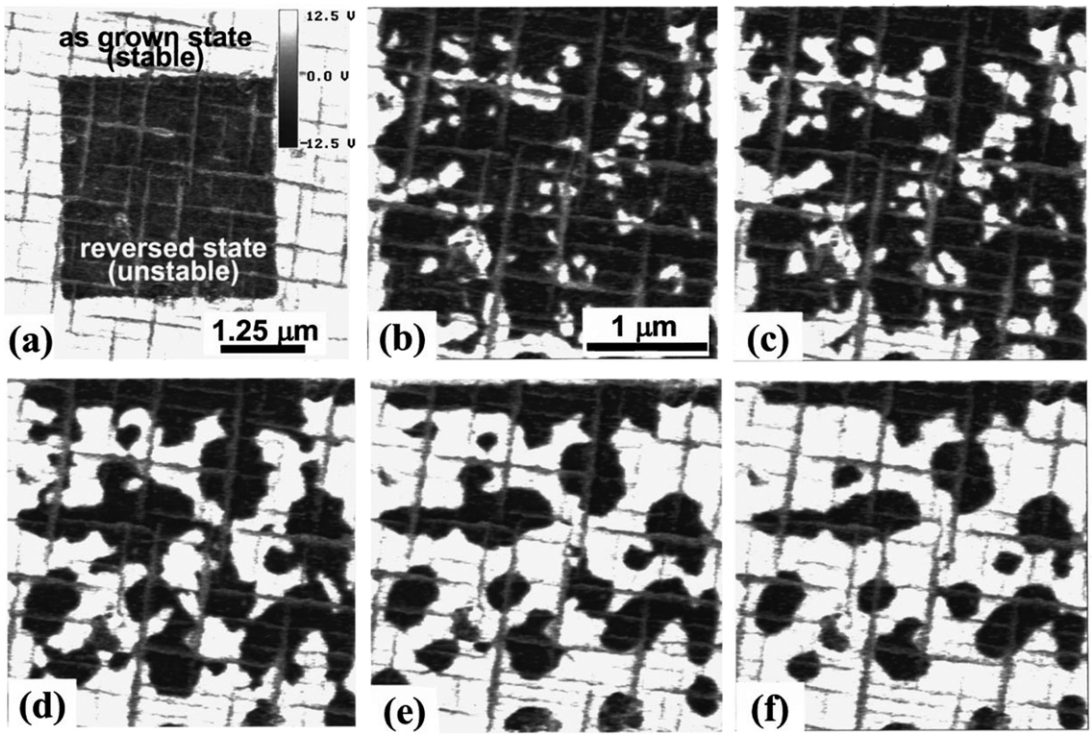

Figure 27. (*a*) Piezoresponse image of a PZT sample showing as-grown (light contrast) and reverse-poled (dark contrast) regions. (*b*)–(*f*) Piezoresponse images from the poled region in (*a*), which was switched into the opposite polarization (with respect to the as-grown state) state by scanning the surface with the tip biased at 210 V. Images taken after wait times of (*b*) 6.1×10^3, (*c*) 9.2×10^3, (*d*) 2.4×10^4, (*e*) 1.1×10^5 and (*f*) 2.8×10^5 s. Reproduced from [255], copyright 2001, American Physical Society.

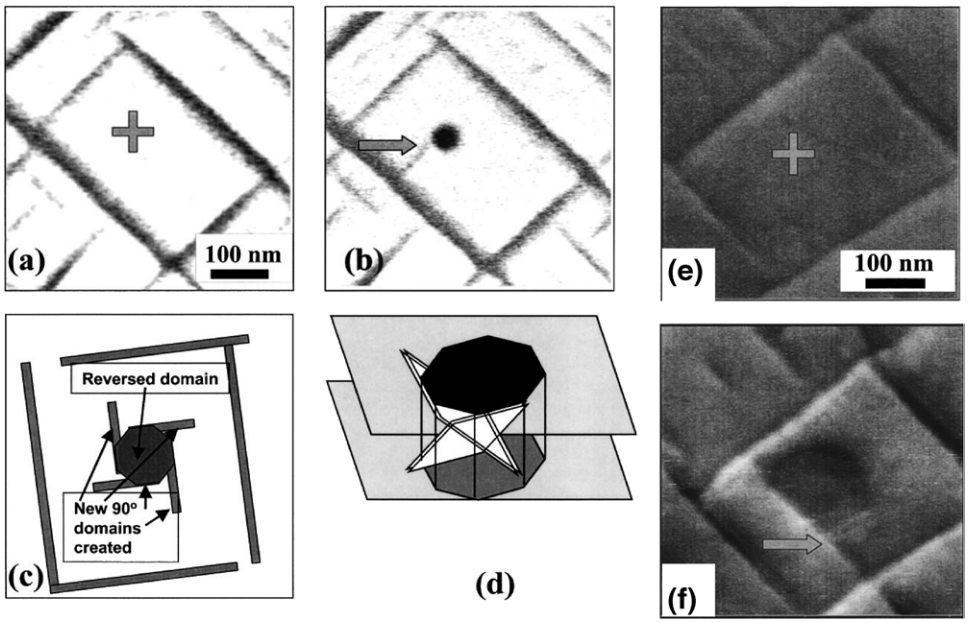

Figure 28. PFM domain structure (*a*) before and (*b*) after locally poling a PZT film. (*c*) Plan view and (*d*) 3D view of domain structure. (*e*) PFM domain structure image (*e*) before and (*f*) after switching a PZT film. Reproduced with permission from [264], copyright 2004, American Institute of Physics.

surface charge dynamics measurements [276], tip–surface adhesion forces [277], electrostatic tip–surface interactions [278, 279], tip-induced electrochemical reactions [280], etc. Variable temperature measurements of the surface potential above ferroelectric surfaces have established the fact that polarization is screened by mobile charges in air [281] and allow kinetic and thermodynamics parameters of the screening process to be established [282]. These observations have been corroborated by detailed surface studies [283]. For most perovskites, the surfaces are highly reactive [284, 285]. Furthermore, dissociative water adsorption is one of the favored mechanisms for the screening of ferroelectric

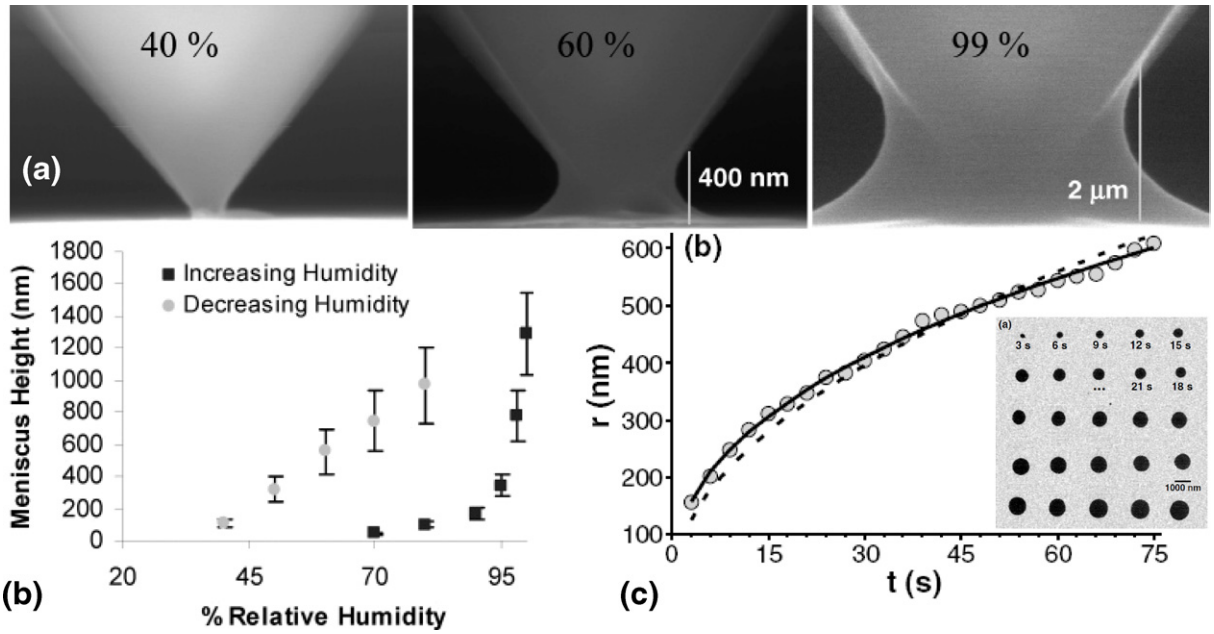

Figure 29. (*a*) Environmental EM observations of the water meniscus at the tip–surface contact junction as a function of humidity. (*b*) Hysteresis of meniscus size for increasing and decreasing humidity. (*c*) The kinetics of the alkanethiol drop spreading in the dip-pen lithography experiment. The kinetic law limited by surface diffusion is strongly reminiscent of ferroelectric domain switching kinetics observed in ambient environment. Inset shows the alkanethiol dot pattern. Panels (*a*), (*b*) reproduced from [299], copyright 2005, American Chemical Society. Panel (*c*) reproduced from [300], copyright 2002, American Physical Society.

surfaces [281, 282, 286–288]. These mechanisms result in the formation of a high-density hydroxylated layer and interstitial protons and oxygen vacancies. The effects of these charges have been observed by variable-temperature surface potential measurements by KPFM of ferroelectrics [288, 289], resulting in surface domain-related electrostatic potential contrast retention above the Curie temperature [281] and temperature-induced domain potential inversion [282]. Polarization-controlled physisorption has recently been studied by Altman and Bonnell groups [47, 290, 291] using electron spectroscopies and KPFM. The effect of surface charges on domain structures and stability has been studied in detail by the Argonne group [292, 293]. Finally, the effect of screening charges on PFM contrast [283, 294] and polarization switching [295] has recently been studied using ultra-high vacuum PFM.

Beyond chemisorption, for high partial pressure of water vapor (e.g. corresponding to atmospheric conditions) the hydrophilic surfaces develop thin (∼1–10 nm) wetting layers stabilized by disjoining pressure. These layers can support surface conductance through charged ion motion and have been directly observed in SPM experiments [276, 296]. The proximity of the tip results in the condensation of liquid at the tip–surface junction due to capillary and electrocapillary effects [297, 298]. Recent observations by environmental EM have provided spectacular depiction of the water droplet at the tip–surface junction and its slow formation and relaxation kinetics as a function of water partial pressure [299].

The full effect of surface contamination on domain dynamics is unclear, primarily because the charges are not observable directly in the PFM experiment and can be detected only by complementary measurements. The full set of observed data suggests that in poorly conductive materials, the surface charging and local charge injection may affect switching dynamics. Humidity-dependent liquid necks form at the tip–sample contact which changes the tip–sample contact area and can affect the lateral expansion of growing domains [301]. Interestingly, the observed nearly logarithmic kinetics of surface diffusion is highly reminiscent of the switching kinetics in the films, suggesting a relationship between the two. Furthermore, charge injection and the diffusion of charged species can lead to backswitching [302] and the formation of bubble domains [303, 304]. The mechanism is illustrated in figure 30. Here, the application of electric field to the probe results in both polarization switching and the formation of a charged surface layer on the surface, with effective overscreening of polarization charge. On continuous application of the bias, the charged area propagates on the surface. Note that thermodynamical analysis of polarization switching suggests that switching is possible only when the polarization charge is screened on the surface; hence the kinetics of screening charge spreading can be the controlling factor in domain growth kinetics observed in ambient. Finally, on switching the bias with the tip still in contact with the surface, the screening charges directly below and in close proximity to the tip are immediately compensated. However, the charges far from the surface remain, resulting in an electric field of opposite orientation to the original. This field can result in backswitching, as shown in figure 30 [301–304].

Finally, the aspect of ambient experiments that should be mentioned specifically is the electrochemical reactions at the tip–surface junction. Tip-induced electrochemistry is by now a well-developed paradigm, with multiple examples on metals, solid ionic electrolytes and semiconductors

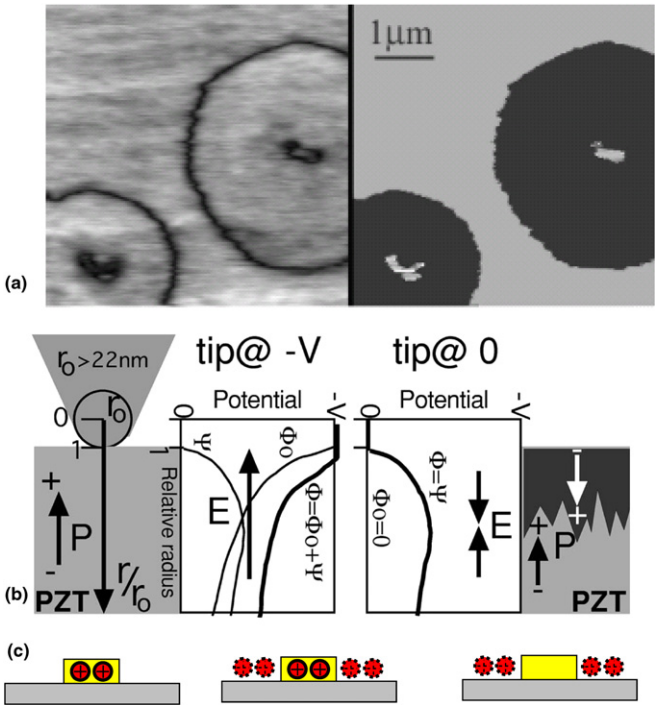

Figure 30. (*a*) Antipoling effect observed on epitaxial PZT. (*b*) Schematic representation of the effect: (left) poling at high voltage and (right) collection of surface charges and formation of opposite field, leading to polarization switching. The domain wall between the upper and lower regions reduces the electrostatic energy of the head-to-head configuration. In the center schematic the contributing potentials from the spherical model are presented. (*c*) Illustrates the surface charge distribution at the beginning and at the end of a biasing experiment, and after the bias is turned off. (*a*), (*b*) Reproduced with permission from [304], copyright 2005, American Physical Society.

known by now [305–307]. While the electrochemistry of classical ferroelectrics such as PZT and BTO in ultrathin films and in the presence of water vapor is not studied, experimental observations suggest that tip-induced electrochemical processes are extremely common. Typically, their onset is associated with the formation of 'switched' patterns with low contrast and highly disordered and broad domains walls. Often the process is associated with the formation of topographic features following the bias pattern. For high biases and humidities, the complete breakdown of the film and the formation of particulates are observed. Recent measurements suggest that the onset of the electrochemical processes is related to the leakage current flow. Note that these processes are closely related to the transport properties of ferroelectrics, actively studied in the context of resistive switching [42, 267, 268, 308], and hence must be considered in this context.

3.3. Theory of tip-induced polarization switching

The analysis of the tip-induced switching behavior by PFM necessitates the comparison between macroscopic and microscopic switching as a first step of theoretical analysis. The seminal work by Landauer has demonstrated that the experimentally observed switching fields correspond to impossibly large ($\sim 10^3$–10^5 kT) values for the nucleation activation energy [79]. This discrepancy is resolved by postulating the presence of discrete switching centers initiating low-field nucleation. The spatial and energy distribution of the nucleation center has become the central component of all statistical theories for polarization switching in macroscopic ferroelectrics [66, 95]. Notably, this behavior is universal to all first order phase transitions including solidification, martensitic transformations and phenomena such as plastic deformation and electrochemical reactions, in which the formation of a new phase is always initiated at a specific defect site or is controlled by defect dynamics. Given that typical spacings between extended defects are on the order of 10–100 nm, even high-quality epitaxial films will have multiple defects within a typical device structure such as a micrometer-sized capacitor.

In comparison, in an SPM experiment, the field is concentrated to a small (10–30 nm) volume within a material that may possess small number of defects or be (extended) defect free. This opens the pathway for probing defect-mediated switching in ferroelectrics on a single defect level. The original work by Landauer [79] utilized the rigid ferroelectric approximation (polarization is P or $-P$, domain walls are infinitely thin) to describe thermodynamics of domain formation in a uniform field. This approach was extended in a series of groundbreaking works by Molotskii *et al* [309–313] to the analysis of the domain formation induced by the inhomogeneous electric field of a biased SPM probe. This thermodynamic analysis was further developed by Morozovska *et al* to account for the finite electric field below the probe, surface and bulk screening and presence of defects [211, 314]. Below, we develop a general description of switching thermodynamics in the rigid approximation.

3.3.1. General formalism of the problem. The free energy of a nucleating ferroelectric domain is [314]

$$\Phi(\boldsymbol{r}, U) = \Phi_{\mathrm{d}}(\boldsymbol{r}) + \Phi_{\mathrm{Dom}}(\boldsymbol{r}, U), \qquad (3.1a)$$

where the domain geometry is described by the N-dimensional parameter vector, $\boldsymbol{r}$ (which can be, e.g., coordinates of all points on a domain wall, or the radius and length in the semi-ellipsoidal approximation) and U is the electric bias applied to the local probe in the proximity of the surface. The first term in equation (3.1*a*) is the contribution from the frozen disorder (i.e. random electric fields in the material), $\Phi_{\mathrm{d}}(\boldsymbol{r})$, within the volume of the domain. The second term in equation (3.1*a*) is the thermodynamic work of switching

$$\Phi_{\mathrm{Dom}}(\boldsymbol{r}, U) = \Phi_{\mathrm{S}}(\boldsymbol{r}) + \Phi_{\mathrm{p}}(\boldsymbol{r}, U) + \Phi_{\mathrm{D}}(\boldsymbol{r}). \qquad (3.1b)$$

It comprises the contributions of positive domain wall energy, $\Phi_{\mathrm{S}}(\boldsymbol{r}) = \psi_{\mathrm{S}} S$, where S is the domain surface and ψ_{S} is the domain wall energy density, $\Phi_{\mathrm{p}}(\boldsymbol{r}, U)$ is the energy density due to the probe field and $\Phi_{\mathrm{D}}(\boldsymbol{r})$ is the depolarization energy.

The analysis of the switching process can be simplified for a rigid piezoelectric, for which effective material constants are independent of the electric field. In this case, the interaction energy with the probe tip electric field, $E_3^{\mathrm{p}}(\boldsymbol{x})$,

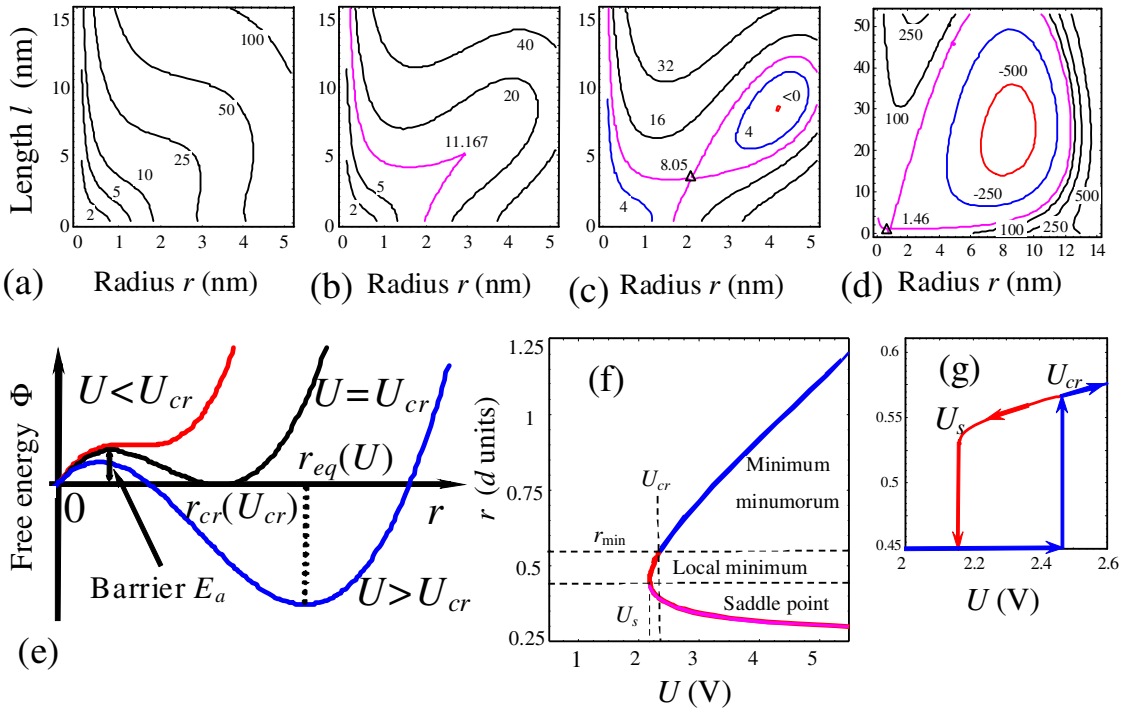

Figure 31. Contour plots of the free energy surface under increasing voltage: (*a*) domain is absent; (*b*) instability point—local minimum began to appear; (*c*) transition point—the stable domain appears ($U_{cr} = 2.467\,V$); (*d*) stable domain's growth ($U = 4\,V$). Figures near the contours are free energy values in eV. Triangles denote the saddle point (nuclei sizes). (*e*) Schematic dependence of the free energy on the domain radius at different biases U. Material parameters correspond to the lead zirconate titanate (PZT)6B solid solution and to the tip–surface characteristics: $\varepsilon_e = 81$, $R_0 = 50$ nm, tip touches the sample ($d = 8.1$ nm); uncompensated surface charges density $\sigma_S = -P_S$. (*f*) The dependence of domain radius r versus voltage U. (*g*) Zoomed ferroelectric hysteresis in thermodynamic limit. Reproduced from [317].

is $\Phi_p(\boldsymbol{r}, U) = -2P_S \int_V d^3x \cdot E_3^p(\boldsymbol{x}) = U\Phi_U(\boldsymbol{r})$, where P_S is the magnitude of material spontaneous polarization, $\boldsymbol{P} = (0, 0, P_S)$ and V is the domain volume. The depolarization field, $E_3^d(\boldsymbol{x})$, created by the uncompensated bulk and surface polarization charges, determines the positive depolarization energy, $\Phi_D(\boldsymbol{r}) = -P_S \int_V d^3x \cdot E_3^d(\boldsymbol{x})$. The corresponding field distribution must be found self-consistently for a given domain configuration and screening conditions. Note that the interaction energy should be negative for domain nucleation.

The stochastic dynamics of the system described by equations (3.1*a*) and (3.1*b*) is well-studied in the context of chemical reactions [315] and protein unfolding spectroscopy [316]. Typical energy barriers for polarization switching are much higher than thermal fluctuations in perfect ferroelectric materials (e.g. the barrier is much greater than $\sim 10^3 k_B T$ for the plain electrode geometry). Hence, the thermal disorder and variability of switching behavior on repetitive switching cycles are anticipated to be negligibly small, and the equilibrium domain growth will proceed along the lowest free energy path.

The domain nucleation can be represented as a transition process on an N-dimensional surface of $\Phi(\boldsymbol{r}, U)$. In the absence of defects, $\Phi(0, U) = 0$. Due to the local nature of the electro-elastic field produced by the tip, $\Phi(\infty, U) = \infty$. Alternatively, the domain nucleation will proceed spontaneously, corresponding to a different ground state of the system (surface state).

Stable domain configuration(s) correspond to local minima on the $\Phi(\boldsymbol{r}, U)$ surface, where minima corresponding to $\Phi(\boldsymbol{r}, U) > 0$ are metastable and the ones with $\Phi(\boldsymbol{r}, U) < 0$ are stable. In the case of first order phase transitions, the minima and coordinate origin are separated by saddle point(s). The voltage U at which the stable minima (i.e. a domain) appear is referred to as the critical voltage, U_{cr}. The voltage of the appearance of a saddle point, U_{sp}, corresponding to domain metastability, is usually close to U_{cr}. The evolution of the free energy surface with bias for typical tip and material parameters is illustrated in figures 31(*a*)–(*d*).

The analysis can be further extended assuming a prolate ellipsoid geometry for the domains, as analyzed in [317]. In this case, the domain shape is described by radius, r, and length, l, and the corresponding free energy terms in equations (3.1*a*) and (3.1*b*) can be evaluated analytically as functions of r and l. For small biases $U < U_S$, the free energy is a positively defined monotonic function of domain sizes, corresponding to the absence of a stable domain. For biases $U_S < U < U_{cr}$, the local minimum $\Phi_{min} > 0$ arises, corresponding to a metastable domain with r_{ms} and l_{ms}. Finally, for $U \geqslant U_{cr}$, the absolute minimum $\Phi_{min} < 0$ is achieved for r_{eq} and l_{eq}, corresponding to a thermodynamically stable domain. The value U_{cr} determines the point where the homogeneous polarization distribution becomes absolutely unstable. The minimum point (either metastable $\{r_{ms}, l_{ms}\}$ or stable $\{r_{eq}, l_{eq}\}$) and the coordinate origin are separated by the saddle point $\{r_S, l_S\}$. The corresponding energy $\Phi(r_S, l_S) = E_a$ is an activation barrier for domain nucleation, while domain parameters $\{r_S, l_S\}$ represent the critical nucleus size. Such

'threshold' domain nucleation is similar to the well-known first order phase transition (compare figure 31(*e*) with the well-known dependence of the free energy profile on the order parameter for first order ferroelectrics).

In the thermally induced nucleation limit, the domain nucleation process is analyzed as a thermally activated motion in the phase space of the system along the minimum energy path connecting the origin and one of the local minima. The relaxation time necessary for the stable domain formation at U_{cr} is maximal and the critical slowing down appears in accordance with the general theory of phase transitions. Within the framework of the activation rate theory, the domain nucleation takes place at a higher activation voltage U_a determined from the condition $\Phi(U_a) = E_a$, corresponding to the activation time $\tau = \tau_0 \exp(E_a/k_B T)$. For instance, the activation energy $E_a = 20k_B T$ corresponds to a relatively fast nucleation time $\tau \sim 10^{-3}$ s for phonon relaxation time $\tau_0 = 10^{-12}$ s, while the condition $E_a \leqslant 2k_B T$ corresponds to 'instant' or thermal nucleation.

The difference between the voltages corresponding to the formation of a saddle point and a stable domain, $U_S - U_{cr}$, determines the width of the thermodynamic hysteresis loop (see figures 31(*e*)–(*g*)). More realistic models of piezoresponse hysteresis loop formation consider domain wall pinning effects. In the weak pinning limit, the domain growth in the forward direction is assumed to follow the thermodynamic energy minimum, while with decreasing bias, the domain remains stationary due to domain wall pinning by lattice and atomic defects. For stronger pinning, the domain size is limited by the wall mobility in the tip field and ferroelectric (as, e.g., studied for domain wall dynamic by Molotskii in [311]), and the full analysis of this problem remains the matter of future research.

3.3.2. Analytical treatment for Landauer geometry. The integral expressions for the free energy components in equation (3.1*b*) are extremely complex, and can be evaluated analytically only for simple domain configurations. Here we summarize the Pade approximations for the individual terms in the free energy $\Phi(r, l, U) = \Phi_S(r, l) + \Phi_p(r, l, U) + \Phi_D(r, l)$ of the semi-ellipsoidal domain for ferroelectric semiconductors allowing for Debye screening and uncompensated surface charges.

The domain wall energy has the form

$$\Phi_S(r, l) = \pi \psi_S l r \left(\frac{r}{l} + \frac{\arcsin\sqrt{1 - r^2/l^2}}{\sqrt{1 - r^2/l^2}} \right) \approx \frac{\pi^2 \psi_S l r}{2} \left(1 + \frac{2(r/l)^2}{4 + \pi(r/l)} \right), \tag{3.2}$$

where r is the semi-ellipsoid domain radius, l is the domain length.

The Pade approximation for the depolarization energy of a semi-ellipsoidal domain including the effects of Debye screening in the material is

$$\Phi_{DL}(r, l) = \frac{4\pi P_S^2 r^2}{\varepsilon_0 \kappa} \frac{R_d n_D(r, l)}{4n_D(r, l) + 3R_d(\gamma/l)}, \tag{3.3a}$$

where

$$n_D(r, l) = \frac{(r\gamma/l)^2}{1 - (r\gamma/l)^2} \left(\frac{\operatorname{arcth}\left(\sqrt{1 - (r\gamma/l)^2}\right)}{\sqrt{1 - (r\gamma/l)^2}} - 1 \right) \tag{3.3b}$$

is the depolarization factor, $\kappa = \sqrt{\varepsilon_a \varepsilon_c}$ is the effective dielectric constant of the medium, and, $\gamma = \sqrt{\varepsilon_c/\varepsilon_a}$ is the anisotropy factor. For an infinite Debye length (i.e. a rigid dielectric), equation (3.3*a*) becomes the well-known Landauer depolarization energy.

The energy of the depolarization field created by the surface charges $(\sigma_S - P_S)$ located on the domain face has the form

$$\Phi_{DS}(r, l) \approx \frac{4\pi r^3 R_d}{\varepsilon_0 (16\kappa r + 3\pi R_d(\kappa + \varepsilon_e))} \times \left((\sigma_S - P_S)^2 + \frac{2P_S(\sigma_S - P_S)}{1 + (l/r\gamma)} \right). \tag{3.4}$$

The surface charge density σ_S is $-P_S \leqslant \sigma_S \leqslant P_S$, while $\sigma_S = -P_S$ without screening charges.

The driving force for the switching process is the interaction energy determined by the electrostatic field structure produced by the probe. The Pade approximation for the interaction energy between a spherical tip and the surface based on image charge series is

$$\Phi_p(r, l, U) \approx 4\pi\varepsilon_0\varepsilon_e U R_0 \sum_{m=0}^{\infty} q_m \times \frac{R_d((\sigma_S - P_S) F_W(r, 0, d - r_m) + 2P_S F_W(r, l, d - r_m))}{\varepsilon_0 \left((\kappa + \varepsilon_e) R_d + 2\kappa\sqrt{(d - r_m)^2 + r^2} \right)}. \tag{3.5}$$

The image charges q_m are located at distances r_m from the spherical tip center, where

$$q_0 = 1, \qquad q_m = \left(\frac{\kappa - \varepsilon_e}{\kappa + \varepsilon_e} \right)^m \frac{\sinh(\theta)}{\sinh((m + 1)\theta)}, \tag{3.6a}$$

$$r_0 = 0, \quad r_m = R_0 \frac{\sinh(m\theta)}{\sinh((m + 1)\theta)}, \quad \cosh(\theta) = \frac{d}{R_0}. \tag{3.6b}$$

Here R_0 is the tip radius of curvature, ΔR is the distance between the tip apex and the sample surface, so $d = R_0 + \Delta R$. The function

$$F_W(r, l, z) \approx \frac{r^2}{\sqrt{r^2 + z^2} + z + (l/\gamma)} \tag{3.7}$$

is the Pade approximation of a cumbersome exact expression obtained originally by Molotskii [309].

Under the typical condition $\Delta R \ll R_0$, i.e. when the tip is in contact with the surface, equation (3.5) can be approximated as

$$\Phi_p(r, l) \approx \frac{R_d U C_t/\varepsilon_0}{(\kappa + \varepsilon_e) R_d + 2\kappa\sqrt{d^2 + r^2}} \times \left(\frac{(\sigma_S - P_S) r^2}{\sqrt{r^2 + d^2} + d} + \frac{2P_S r^2}{\sqrt{r^2 + d^2} + d + (l/\gamma)} \right), \tag{3.8}$$

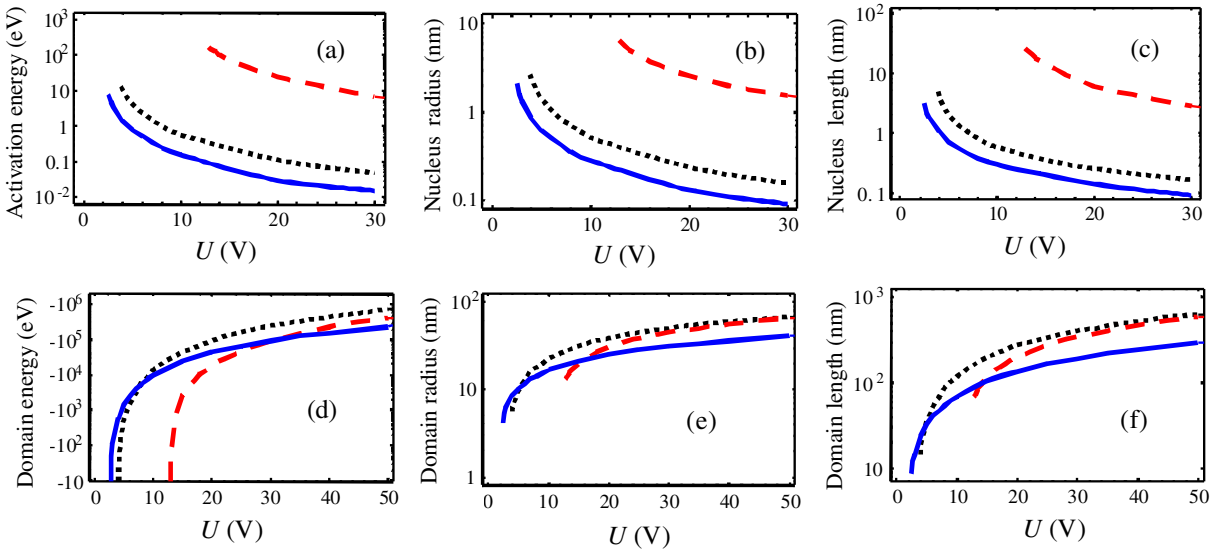

Figure 32. Calculated bias dependence of (*a*) activation energy for nucleation (eV) and nucleus (*b*) radius and (*c*) length and (*d*) equilibrium domain energy (eV) and (*e*) radius and (*f*) length. Solid curves represent a modified point charge approximation of the tip; dotted ones correspond to the exact series for the sphere–tip interaction energy, dashed curves represent the capacitance model. Material parameters are given in figure 31. Calculations are performed for complete screening, $\sigma_S = -P_S$. Reproduced from [317].

where d is the equivalent charge–surface distance and C_t is the effective tip capacitance.

Based on the evolution of the free energy surfaces, like those presented in figure 34, the following scenario for hysteresis loop formation in the thermodynamic limit emerges. Below the bias U_S, domain formation is thermodynamically impossible. On increasing the bias above U_S, the local minimum corresponding to a metastable domain appears. The domain becomes thermodynamically stable above a critical bias U_{cr}. For an infinitely slow process, domain nucleation below the tip becomes possible at this bias. Realistically, nucleation will proceed at a higher bias when the activation energy for nucleation becomes sufficiently low to enable nucleation in the finite experimental time. On subsequent increase in the tip bias, the domain size increases. However, due to the $1/r$ decay of electrostatic fields, the domain size always remains finite. On decreasing the bias, the domain becomes metastable at U_{cr} and disappears at U_S, resulting in intrinsic thermodynamic hysteresis in the hysteresis loop shape (see figure 31(*g*)).

Shown in figure 32 are the activation energies for nucleation (*a*), critical nucleus sizes (*b*), (*c*), domain energy (*d*) and equilibrium domain sizes (*e*), (*f*) calculated in the framework of the sphere–plane, modified point-charge and capacitance models (compare dotted, solid and dashed curves in figure 32). Note that the critical domain shape is close to the semi-spherical result independent of the model, whereas equilibrium domain is always prolate (compare figures 32(*b*) and (*c*) with figures 32(*e*) and (*f*)). From figure 32, domain formation is impossible below a certain nucleation bias, U_{cr}, while above this voltage, the nucleus sizes rapidly decrease with bias.

The description of the thermodynamics and kinetics of domain switching can be considerably facilitated by a closed-form analytical expression for the bias dependence of characteristic points on the free energy map. The approximate parametrical dependences for hysteresis curves $U(r)$ valid for $r < d$ have the form

$$\begin{cases} U(r) \approx \left(\left[3\sqrt{2f_S} \right.\right. \\ \quad \left. + \sqrt{18f_S + 8(1-\sigma_S/P_S)(3f_D(1-\sigma_S/P_S)^2(r/d)^2 - f_S)}\right] \\ \quad \left. \times \left[4\sqrt{f_U}\,(1-\sigma_S/P_S)\,\sqrt{r/d}\right]^{-1}\right)^2 \\ l(r) \approx 2\gamma d\left(\sqrt{\dfrac{2f_U U}{f_S}}\sqrt{r/d} - 1\right) \end{cases}, \tag{3.9}$$

where $f_S = \pi^2\psi_S d^2\gamma$, $f_D = 4P_S^2 d^3/3\varepsilon_0(\kappa+\varepsilon_e)$, $f_U = R_d(C_t/\varepsilon_0)P_S d/2(\kappa+\varepsilon_e)R_d + 4\kappa d$, $C_t \approx 4\pi\varepsilon_0\varepsilon_e R_0(\kappa+\varepsilon_e/2\kappa)$ and $d = \varepsilon_e R_0/\kappa$. Using equations (3.9) and condition $\Phi(r,l) = 0$, the following approximate expressions for critical voltage U_{cr} and sizes $r(U_{cr})$, $l(U_{cr})$ are derived:

$$U_{cr} = \sqrt{\frac{f_D f_S}{1-\sigma_S/P_S}}\frac{1}{2f_U} \times \frac{\left(3+\sqrt{9-4\,(1-\sigma_S/P_S)}\right)^2}{\sqrt{3-(1-\sigma_S/P_S)+\sqrt{9-4\,(1-\sigma_S/P_S)}}}, \tag{3.10}$$

$$r\,(U_{cr}) = d\sqrt{\frac{f_S}{f_D\,(1-\sigma_S/P_S)^3}} \times \sqrt{3-(1-\sigma_S/P_S)+\sqrt{9-4\,(1-\sigma_S/P_S)}}, \tag{3.11}$$

$$l\,(U_{cr}) = 2\gamma d\left(\frac{3+\sqrt{9-4\,(1-\sigma_S/P_S)}}{1-\sigma_S/P_S} - 1\right). \tag{3.12}$$

Note that approximate dependences (equations (3.10)–(3.12)) cannot reflect the exact behavior of the system at $\sigma_S \to P_S$ allowing for the fact that one cannot neglect the Landauer energy (3.3*a*) and (3.3*b*) at $(1-\sigma_S/P_S) \to 0$. However, one can see that domain nucleation disappears at $\sigma_S \to P_S$ as should be expected, because the interaction energy disappears.

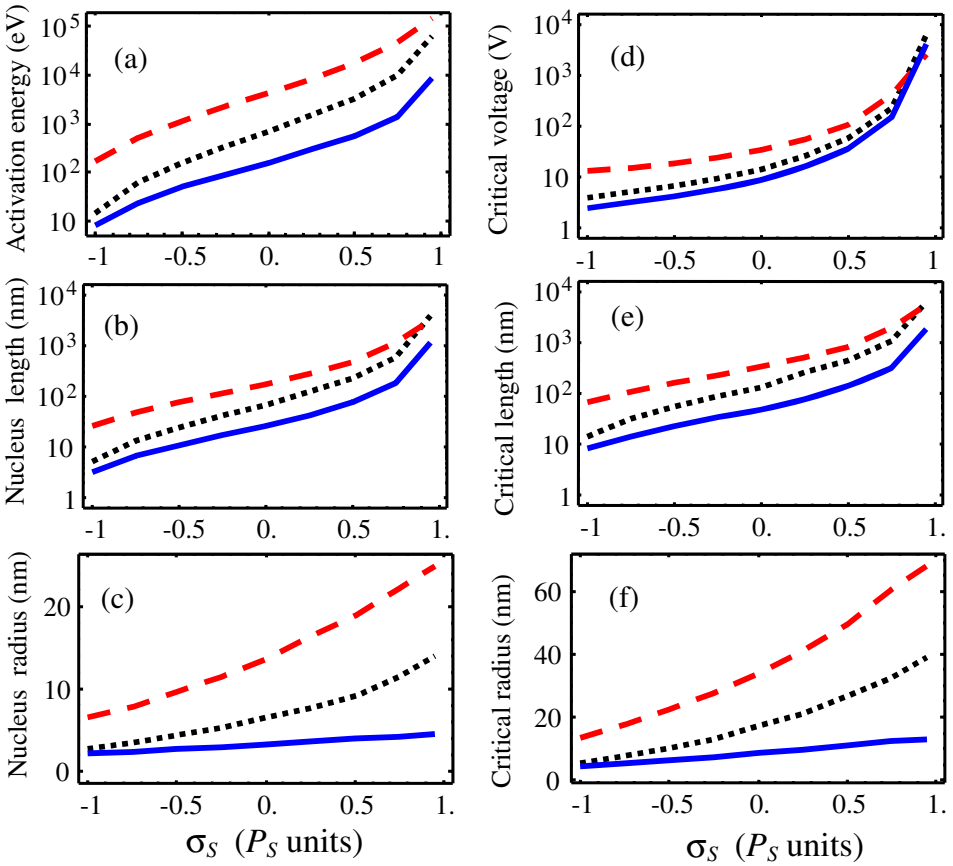

Figure 33. (*a*) Activation energy (eV) at U_{cr} and nucleus sizes (*b*), (*c*); (*d*) critical voltage U_{cr} (V), critical domain sizes (nm): length $l(U_{cr})$ (*e*) and radius $r(U_{cr})$ (*f*) versus surface charge density σ_S (in P_S units). Solid curves correspond to EPCM model of the tip; dotted ones correspond to the exact series for the sphere–tip interaction energy, dashed curves represent the capacitance approximation. Material parameters are given in caption to figure 31. Reproduced from [317].

3.3.3. Surface screening effects. Theoretical descriptions of nanodomain formation in the field of a local probe under ambient conditions should take into consideration the layer of adsorbed water located below the tip apex [277], and, more generally, the dynamic and static surface charging and screening phenomena.

The relevance of the specific screening mechanism on polarization switching dynamics depends on the relationship between the corresponding relaxation time, τ_S, and voltage pulse time, τ_U (i.e. the recording time of the domain). 'Fast' screening mechanisms with $\tau_S \leqslant \tau_U$ significantly affect the switching process, whereas the 'slow' ones with $\tau_S \gg \tau_U$ can be ignored. However, these slow mechanisms can significantly affect the domain stability after switching by providing additional channels for minimizing depolarization energy.

The role of environmental effects and screening mechanisms on switching can be illustrated as follows. Shown in figure 33 are the activation energies for nucleation (*a*) and nucleus sizes (*b*), (*c*), critical voltage (*d*) and sizes (*e*), (*f*) calculated in the framework of the sphere–plane model, the modified point charge model and the capacitance approximation under different screening conditions on the surface, i.e. σ_S values. It is clear from the figure that all critical parameters rapidly increase under the charge density σ_S increase from $-P_S$ to $+P_S$. In particular, the activation barrier for nucleation at the onset of domain stability (see figure 33(*a*)) is minimal for complete screening at $\sigma_S = -P_S$ (10 eV) and increases up to 10^5 eV for $\sigma_S \to +P_S$. However, the barrier height strongly decreases with further voltage increase $U > U_{cr}$ at all σ_S values. Note that the barrier calculated in the inhomogeneous electric field of the tip is 3–5 orders lower than the one calculated by Landauer for the homogeneous electric field. The values obtained at $\sigma_S > -P_S$ are still too high for thermal fluctuations to cause the domain nucleation at $U \approx U_{cr}$. Thus the observed domains could either originate at higher voltages in the perfect ferroelectric sample, or nucleation must be defect-related.

This analysis suggests that environmental effects and surface states will critically influence polarization switching processes in PFM. In particular, the dependence of critical voltage U_{cr} values over ambient conditions (if any) could clarify the surface screening influence. As a recent example, Terabe *et al* [318] have demonstrated that values of U_{cr} on $+Z$ and $-Z$ cuts of LNO or LTO crystals differ by a factor of 2, illustrating the effect of the surface state on the switching mechanism.

3.3.4. Switching in the presence of defects. In the mesoscopic models considered above, the defect can affect the

thermodynamics of domain switching through the electric field that directly couples to domain energy (random field defect), as suggested by Gerra *et al* [81]. Note that random bond defects, which affect the ferroelectric phase stability, cannot be analyzed within the rigid ferroelectric approximation (since P is not constant), and require numerical or analytical solutions to full time-dependent Ginzburg–Landau equations, as analyzed in section 5.

In order to take into account the influence of the defects we added the interaction energy Φ_d between the defect electric field and the polarization of a nascent domain to the free energy considered in section 3.3.1. The full energy is then

$$\Phi(\boldsymbol{r}, U) = \Phi_S(\boldsymbol{r}) + \Phi_D(\boldsymbol{r}) + \Phi_P(\boldsymbol{r}, U) + \Phi_d(\boldsymbol{r}), \quad (3.13)$$

where the surface, Φ_S, and depolarization, Φ_D, contributions to the free energy of the defect are listed in equations (3.2) and (3.5), respectively (here we suppose that surface charges are completely compensated, neglect bulk screening and consider the effective point charge model for the tip field). The defect contribution for a field-type defect is

$$\Phi_d(\boldsymbol{r}) = -2P_S \int_V d^3x \cdot E_3^d(\boldsymbol{x}), \quad (3.14)$$

where $\boldsymbol{E}^d(\boldsymbol{x})$ is the electric field created by the defects and vector $\boldsymbol{r}$ describes the domain geometry (e.g. sizes and position).

Similar to switching in the defect-free case, analytical theory requires simplifying assumptions on the domain geometry. Here, we assume that the semi-ellipsoidal domain is axi-symmetric, i.e. it has radius r and length l, but allows for a defect to influence the domain center (shifted by y_0 compared with the tip location).

In [319, 320], a model of a laterally localized surface field defect with characteristic radius, r_d, and penetration depth $h_d \ll r_d$, located at the point $\{x_{01}, 0, 0\}$, while the longitudinal component of electric field is

$$E_3^d(\boldsymbol{x}) = E_S \exp\left(-\frac{(x-x_{01})^2 + x_2^2}{r_d^2} - \frac{x_3}{h_d}\right). \quad (3.15)$$

The relevant values of the penetration depth are $h_d \sim 1$–2 nm, maximal field strength $E_S = 10^8$–10^{10} V m^{-1} and the defect radius is $r_d \sim 1$–50 nm. For larger radius, the defect becomes significantly larger than the PFM tip size, and hence can be approximated by the homogeneous surface field considered in [81]. Similarly, field strength below $\sim 10^8$ V m^{-1} is well below the fields at the tip–surface junction during the PFM experiment, and hence these weak defects are unlikely to affect the nucleation process.

For Gaussian field defect, the free energy components are

$$\Phi_P(r, l, y_0, U) = -\frac{4\pi U P_S d r^2 l/\gamma}{\left(\sqrt{r^2 + d^2 + y_0^2} + d\right)\left(\sqrt{r^2 + d^2 + y_0^2} + d + l/\gamma\right)}, \quad (3.16a)$$

$$\Phi_d(r, l, x_{01}, y_0) = -2\pi r_d^2 h_d P_S E_S \left(1 - \exp\left(-\frac{l}{h_d}\right)\right) \times \left(1 - \exp\left(-\frac{r^2}{r_d^2}\right)\right) \exp\left(-\frac{(x_{01} - y_0)^2}{r_d^2}\right). \quad (3.16b)$$

To describe the nucleus position analytically we performed minimization on y_0 of the free energy under the conditions $r < 2d$, $l \leqslant 2\gamma d$ typically valid in a saddle point(s) and derived the set of approximate expressions for the shift y_0 at $x_{01} \neq 0$:

$$y_0(U) = \begin{cases} \dfrac{x_{01} E_S \exp\left(-x_{01}^2/r_d^2\right)}{E_S \exp\left(-x_{01}^2/r_d^2\right) + U r_d^2 (d + h_d)/2d^3 h_d}, & U E_S > 0, \\ \dfrac{2\gamma d^3 h_d x_{01}}{r_d^2 (d + h_d)} \dfrac{E_S}{U} \exp\left(-\left(2\gamma \dfrac{d^3}{r_d^2} \dfrac{E_S}{U} - 1\right)^2 \dfrac{x_{01}^2}{r_d^2}\right), & U E_S < 0. \end{cases} \quad (3.17)$$

Equations (3.17) qualitatively describe the cases of nucleus repulsion ($y_0 < 0$) at $E_S < 0$ and attraction ($y_0 > 0$) at $E_S > 0$ as well as $y_0 \to 0$ at $x_{01} \gg r_d$. As anticipated, $y_0 \to 0$ at high voltages. For the stable domains with sizes $l \gg r$ and $l \gg h_d$ we obtained that $y_0 \approx 0$ for all voltages $U > \gamma |E_S| d^2 h_d / r_d^2$. At $x_{01} = 0$ and biases $0 < U < -2\sqrt{2}(\gamma E_S d^3 h_d / r_d^2 (d + h_d))$, the (non-universal) ring structure of radius $r_d \sqrt{\ln(-2\sqrt{2}\gamma E_S d^3 h_d / U r_d^2 (d + h_d))}$ is most probable.

For a favorable field defect ($E_S > 0$), domain nucleation can be either activationless at a high enough built-in field, or the activation barrier is lowered compared with an ideal material, rendering the process feasible at lower biases. For an unfavorable field defect ($E_S < 0$), or in its absence ($E_S = 0$), the domain formation process is always characterized by the activation energy, E_a, determined as the free energy value in the saddle point. Minimization of the free energy on the nucleus sizes r and l leads to the estimation of the activation barrier $E_a(U)$:

$$E_a(U) = \frac{2\pi \psi_S^3}{3} \left(\frac{3 P_S d \cdot U}{\gamma \left(\sqrt{d^2 + y_0^2} + d\right)^2} - \frac{P_S^2}{3\varepsilon_0 \varepsilon_{11}} + \frac{3}{2} P_S E_S \exp\left(-\frac{(x_{01} - y_0)^2}{r_d^2}\right) F(h_d) \right)^{-2}. \quad (3.18)$$

Here, the function $F(h_d) \cong \exp(-9\varepsilon_0 \psi_S / 8 h_d P_S^2)$. The corresponding nucleus sizes are $l_S(U) \sim r_S(U) \cong \sqrt{3E_a(U)/2\pi\psi_S}$, $r < 2d$, $l < 2d$.

Activation voltages $U_a^0(E_S = 0)$ and $U_a^{\pm}(E_S \neq 0)$ corresponding to different polarization signs $\pm P_S$ (or, equivalently, forward and reverse switching) can be determined numerically from the free energy using the conditions $\Phi(U_a^0, E_S = 0, \pm P_S, l_S, r_S) = E_a$ and $\Phi(U_a^{\pm}, E_S, \pm P_S, l_S, r_S) = E_a$ or estimated analytically from equations (3.18). The following expressions were derived for the defect-free case:

$$U_a^0 \cong \pm \frac{4}{3} \gamma d \left(\sqrt{\frac{2\pi \psi_S^3}{3 E_a P_S^2}} + \frac{|P_S|}{3\varepsilon_0 \varepsilon_{11}} \right) \quad (3.19a)$$

and for defect-mediated switching:

$$U_{\rm a}^{\pm} \cong \pm\frac{\gamma}{3d}\left(\sqrt{d^2+y_0^2}+d\right)^2\left(\sqrt{\frac{2\pi\psi_{\rm S}^3}{3E_{\rm a}P_{\rm S}^2}}+\frac{|P_{\rm S}|}{3\varepsilon_0\varepsilon_{11}}\right) - \Delta U\,(E_{\rm S})\,, \tag{3.19b}$$

$$\Delta U\,(E_{\rm S}) = \frac{\gamma}{2d}\left(\sqrt{d^2+y_0^2}+d\right)^2 E_{\rm S} \times \exp\left(-\frac{(x_{01}-y_0)^2}{r_{\rm d}^2}\right) F\,(h_{\rm d})\,. \tag{3.19c}$$

Here, $E_{\rm a}$ is the potential barrier height chosen as a condition for thermally induced nucleation, e.g. 2–20$k_{\rm B}T$. The lateral domain nucleus shift, y_0, can be estimated from equation (3.17) self-consistently.

From the analysis above, the effect of a defect on the hysteresis loop shape can be predicted as follows. In the presence of a defect, the hysteresis loop is broadened by the factor $(\sqrt{1+y_0^2/d^2}+1)^2-4$ compared with the defect-free case (equation (3.19*b*)). Furthermore, the loop is shifted along the voltage axis by the value ΔU due to domain-defect interactions. The value ΔU exponentially decreases with the distance $|x_{01}-y_0|$ from the defect center.

Voltage dependence of the domain activation energy $E_{\rm a}$ is shown in figure 34(*a*).

Dependences of activation voltages $U_{\rm a}^{0,\pm}$ (at levels 2 and 20$k_{\rm B}T$) on the distance x_{01} from the defect center are depicted in figure 34(*c*) for a material with PZT-6B parameters. The activation barrier may be extremely low in the vicinity of the positive surface field defect with field strength $E_{\rm S} > 10^8\,{\rm V\,m^{-1}}$. Curves 4 and 5 demonstrate that the surface state disappears at $U_{\rm S}^{+} \approx -5$ V. For a negative surface field defect no surface state exists and the activation barrier drastically increases, as follows from curves 1 and 2. For defects with equal absolute field strength, the role of a positive defect in facilitating nucleation is much more long range than a negative one. This reflects the fact that the domain has a much more preferential direction away from the defect than toward the defect. Similar analysis for the reversed domain nucleation with $P_{\rm S} < 0$ affected by a negative surface field $E_{\rm S} < 0$ requires the introduction of voltage $U_{\rm S}^{-}$ corresponding to the surface state disappearance ($U_{\rm a}^{-}=0$ is possible).

We compare the influence of the defect field and location on the voltage dependence of equilibrium domain and nucleus sizes in figure 35. From figure 35(*a*), the equilibrium domain sizes are insensitive to the defect position and the field strength at the chosen material parameters. Only the positions of the origins of the curves (corresponding to activation voltage $U_{\rm a}^{-,0}$ or $U_{\rm S}^{+}$) are sensitive to the defect characteristics. The reason for this behavior is the condition $U_{\rm a}^{-} \gg U_{\rm cr}^{-}$ ($U_{\rm a}^{-} \gtrsim 20$ V and $U_{\rm cr}^{-} \lesssim 3$ V). The critical voltage $U_{\rm cr}$ depends on the defect characteristics, but it governs the thermodynamic domain formation only at a close activation barrier $U_{\rm a} \sim U_{\rm cr}$. At voltages $U \gg U_{\rm cr}$ domain growth becomes almost independent of the initial critical point. In contrast, the bias dependence of nucleus sizes is sensitive to the surface field defect, as demonstrated in figures 35(*b*) and (*c*). This analysis suggests that the primary influence of the surface field effect on the domain switching is the shift of activation energy (saddle point on the free energy surface), while equilibrium domain size is almost unaffected.

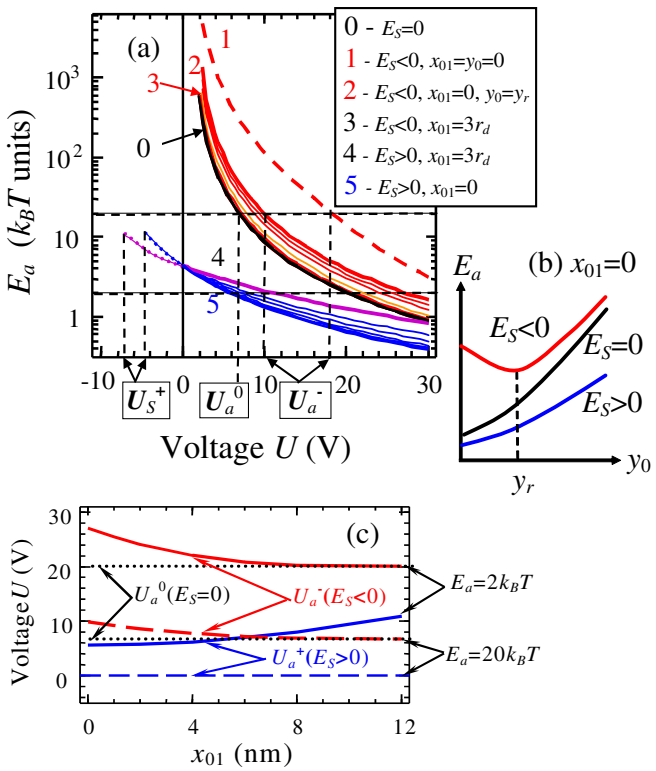

Figure 34. (*a*) Dependence of the energy barrier (in $k_{\rm B}T$ units) on the applied voltage U for surface field defect of $r_{\rm d} = 4$ nm, $h_{\rm d} = 0.8$ nm, field strength $E_{\rm S}$ located at position x_{01}. Curve 0 corresponds to $E_{\rm S} = 0$. Curve 1 corresponds to the saddle $y_0 = 0$ (corresponding to the highest barrier, see schematics (*b*) for $E_{\rm a}(y_0)$) at $E_{\rm S} = -10^9\,{\rm V\,m^{-1}}$, $x_{01} = 0$; curve 2 corresponds to the saddle $y_0 = y_r \neq 0$ (corresponding to the lowest barrier, see schematics (*c*) for $E_{\rm a}(y_0)$) at $E_{\rm S} = -10^9\,{\rm V\,m^{-1}}$, $x_{01} = 0$; curve 3 is calculated at $E_{\rm S} = -10^9\,{\rm V\,m^{-1}}$, $x_{01} = 3r_{\rm d}$; curve 4 is calculated at $E_{\rm S} = +10^9\,{\rm V\,m^{-1}}$, $x_{01} = 3r_{\rm d}$; curve 5 is calculated at $E_{\rm S} = +10^9\,{\rm V\,m^{-1}}$, $x_{01} = 0$. Intermediate thin curves are calculated at $x_{01} = 2r_{\rm d}$; $1.5r_{\rm d}$; $r_{\rm d}$ and $0.5r_{\rm d}$ nm correspondingly. (*c*) Dependence of the activation voltage $U_{\rm a}$ at level 2 and 20$k_{\rm B}T$ on the distance to defect center, x_{01}. Reproduced from [320]. Copyright 2008, American Physical Society.

3.3.5. Minimum writable domain size. It is instructive to extend the analysis in section 3.3.4 to determine the minimal domain size that can be formed in an SPM field tip [321]. From the condition $\Phi_{\rm min}(r_{\rm min}, U) = 0$, we derived the following expressions for $U_{\rm cr}$ and $r_{\rm min}(U_{\rm cr})$ valid for the domain nucleation in a thin film with thickness $h \leqslant \sqrt{\varepsilon_{\rm c}\varepsilon_{\rm a}}R_0$:

$$U_{\rm cr}(h) \approx \sqrt{\frac{8\psi_{\rm S}}{3\pi}}\frac{(\kappa R_0\,(R_{\rm d}+2h)+(\kappa+\varepsilon_{\rm e})\,hR_{\rm d})}{R_{\rm d}\sqrt{\varepsilon_0\,(\kappa+\varepsilon_{\rm e})\,h}} \times\left(\varepsilon_{\rm e}\frac{\kappa+\varepsilon_{\rm e}}{\kappa-\varepsilon_{\rm e}}\ln\left(\frac{\kappa+\varepsilon_{\rm e}}{2\varepsilon_{\rm e}}\right)\right)^{-1}, \tag{3.20}$$

$$r_{\rm min}\,(U_{\rm cr}) \approx \sqrt{\frac{3\pi\psi_{\rm S}\varepsilon_0\,(\kappa+\varepsilon_{\rm e})}{2\,(\sigma_{\rm S}\,(U_{\rm cr})-P_{\rm S})^2}}\cdot h. \tag{3.21}$$

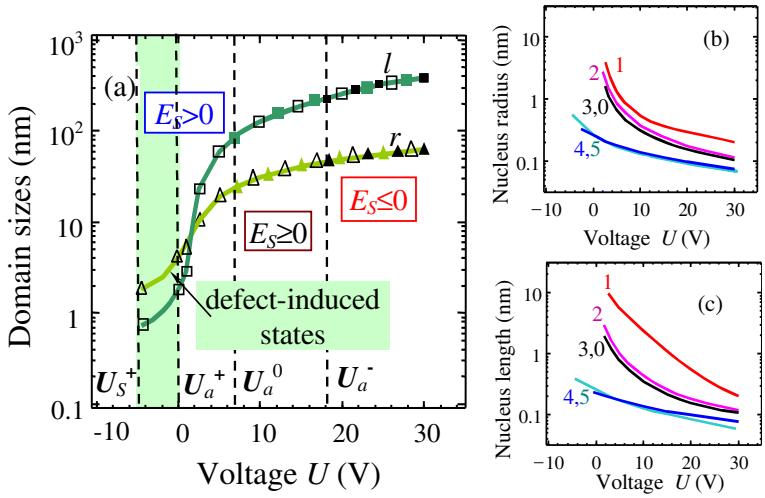

Figure 35. (*a*) Equilibrium domain radius r and length l dependence on the applied voltage for different surface fields, E_S: $E_S = +10^9$ V m^{-1} (empty symbols); $E_S = 0$ (filled symbols) and $E_S = -10^9$ V m^{-1} (black symbols). (*b*), (*c*) Voltage dependence of nucleus sizes in a saddle point. Curves 0–5 correspond to the same E_S and x_{01} values as described in figure 34. Reproduced from [320]. Copyright 2008, American Physical Society.

It is clear from equation (3.21), that in order to obtain domains of minimum radius, it is necessary to choose a ferroelectric medium with a high spontaneous polarization P_S, small domain wall energy, ψ_S, and permittivity, $\sqrt{\varepsilon_a \varepsilon_c}$, and large Debye screening radius (see denominator in equation (3.20)). For applications it seems important to decrease the film thickness h until ferroelectric phase exists [322]. However, the film thickness h should not be extremely small in order to prevent the sharp increase in $r_{min}(U_{cr})$ (denominator in equation (3.21)), so the optimum h value can be calculated numerically from the condition $r_{min}(U_{cr}(h)) = \min$. For the thickness-independent permittivity $\varepsilon_{a,c}$ we derived the approximation:

$$h_{opt} \approx \frac{(8\psi_S/3\pi)^{1/3}}{\varepsilon_0\left(\sqrt{\varepsilon_a\varepsilon_c}+\varepsilon_e\right)}\left(\frac{\varepsilon_0\sqrt{\varepsilon_a\varepsilon_c}\left(\sqrt{\varepsilon_a\varepsilon_c}-\varepsilon_e\right)}{\varepsilon_e \ln\left(\sqrt{\varepsilon_a\varepsilon_c}+\varepsilon_e/2\varepsilon_e\right)}\cdot\frac{2R_0}{E_m}\right)^{2/3}. \tag{3.22}$$

The optimization procedure based on equations (3.20)–(3.22) proves that it is possible to obtain stable domains of radius $d_{min} \approx 17$ nm under the voltage $U_{cr} \approx 6$–8 V in the films with thickness $h_{opt} \approx 70$–130 nm (see figure 36). Thus a nanodomain array can be written at ~86 Gbit cm^{-2} information density in the thin PZT films (compare with densities of 4–28 Gbit cm^{-2} reported in [64]). Note that in real materials, pinning can stabilize even smaller domains below the thermodynamics limit derived above.

4. Time and voltage spectroscopies in PFM

The understanding of the fundamental mechanisms for polarization switching, including domain nucleation and growth, wall pinning and the role of defects on these phenomena necessitates ferroelectric domain dynamics to be probed at multiple locations on sample surfaces. The imaging studies discussed in section 3 provide visual images of domain formations, wall geometry and their evolution at different stages of growth. However, the primary limitation of these studies of domain growth

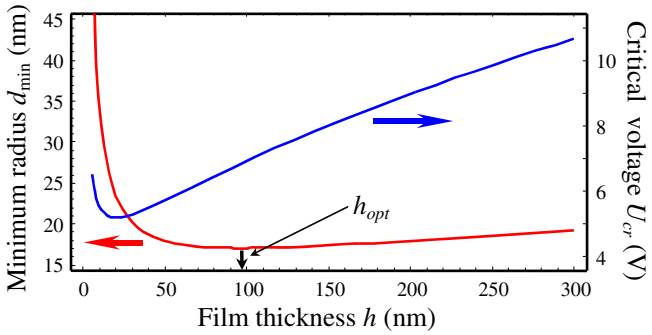

Figure 36. Minimal domain radius and critical voltage versus the thickness of a $PbZr_{0.2}Ti_{0.8}O_3$ (PZT20/80) film. Reproduced from [321]. Copyright 2006, American Physical Society.

is the large times required to perform multiple switching and imaging steps even at a single spatial point. At the same time, with the possible exception of single crystals, large variability of disorder and defect densities precludes direct comparison of data acquired at different locations.

An alternative approach to study domain dynamics in the PFM experiment is based on local spectroscopic measurements, in which a domain switching and electromechanical detection are performed simultaneously, yielding local electromechanical hysteresis loop. The in-field hysteresis loop measurements were first reported by Birk *et al* [116] using an STM tip and Hidaka *et al* [129] using an AFM tip. In this method, the response is measured simultaneously with the application of the dc electric field. Correspondingly, the measured PFM signal contains significant (non-hysteretic) electrostatic contribution to the signal. To avoid this problem, a technique to measure remanent loops was reported by Guo *et al* [323]. In this case, the response is determined after the dc bias is turned off, minimizing the electrostatic contribution and associated noise to the signal. However, domain relaxation after the bias is turned off is possible.

In a parallel development, Roelofs *et al* [159] demonstrated the acquisition of both vertical and lateral

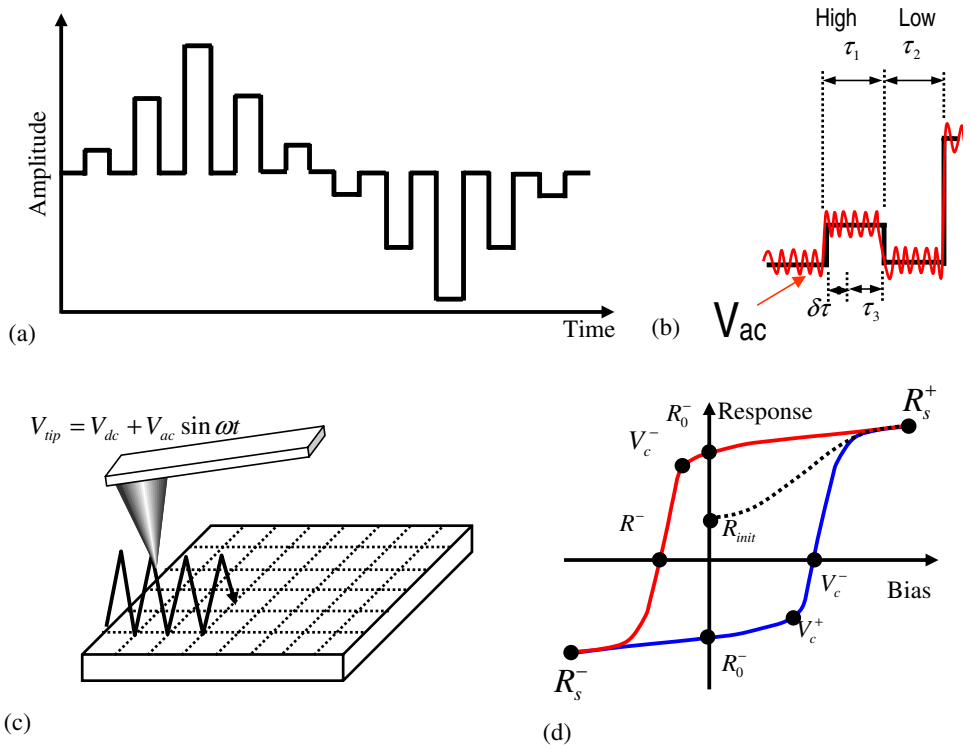

Figure 37. (*a*) Switching and (*b*) probing waveforms in SS-PFM. (*c*) Data acquisition sequence. (*d*) Schematics of well-saturated electromechanical hysteresis loop in the PFM experiment. Forward and reverse coercive voltages, V^+ and V^-, nucleation voltages, V_c^+ and V_c^-, forward and reverse saturation and remanent responses, R_0^+, R_0^-, R_s^+ and R_s^-, are shown. Also shown is the initial response, R_{init}. The work of switching A_s is defined as the area within the loop. The imprint bias and maximum switchable polarization are defined as $\mathrm{Im} = V_0^+ - V_0^-$ and $R_m = R_s^+ - R_s^-$ correspondingly. Adapted with permission from [328]. Copyright 2006, American Institute of Physics.

hysteresis loops. This approach was later used by several groups to probe crystallographic orientation and microstructure effects on switching behavior [157, 162, 324–327]. Recently, PFM spectroscopy has been extended to an imaging mode using an algorithm for fast (30–100 ms) hysteresis loop measurements developed by Jesse *et al* [328]. In the switching spectroscopy PFM (SS-PFM), hysteresis loops are acquired at each point of the image and analyzed to yield 2D maps of imprint, coercive bias and work of switching, providing a comprehensive description of the switching behavior of the material at each point.

Below, we summarize the technical aspects of voltage and time spectroscopy in PFM, discuss relevant theoretical aspects and summarize recent experimental advances.

4.1. Experimental apparatus for PFS and SS-PFM

During the acquisition of a hysteresis loop piezoresponse force spectroscopy (PFS), the tip is fixed at a given location on the surface and the waveform $V_{tip} = V_{probe}(t) + V_{ac} \cos \omega t$ is applied to the tip. V_{ac} is the amplitude of the PFM driving signal. The probing signal, $V_{probe}(t)$, is shown in figure 37 and is composed of a sequence of pulses with amplitude, V_i, and length, τ_1 (HIGH state) separated by intervals of zero bias lasting for τ_2 (LOW state). The measured responses yield on-field and off-field hysteresis loops.

To generate SS-PFM maps, the hysteresis loops are acquired over $M \times M$ point mesh with spacing, l, between points. The hysteresis curves are collected at each point and stored in a 3D data array for subsequent analysis. Parameters describing the switching process such as positive and negative coercive bias, imprint voltage and saturation response can be extracted from the data sets and plotted as 2D maps; alternatively, hysteresis loops from selected point(s) can be extracted and analyzed.

An ideal hysteresis loop for electromechanical measurements is shown in figure 37(*d*). Acquired at each point is a hysteresis loop containing the forward, $R^+(V)$, and reverse, $R^-(V)$, branches. The zero of $R^+(V)$ defines positive coercive bias, V^+, and the zero of $R^-(V)$ defines negative coercive bias, V^-. The imprint is defined as $\mathrm{Im} = (V^+ + V^-)/2$. The values of $R_0^+ = R^+(0)$ and $R_0^- = R^-(0)$ define positive and negative remanent responses, while $R_0 = R_0^+ - R_0^-$ is the remanent switchable response. Finally, $R^+(+\infty) = R^-(+\infty) = R_s^+$ and $R^+(-\infty) = R^-(-\infty) = R_s^-$ are the saturation responses and $R_s = R_s^+ - R_s^-$ is the maximal switchable response. In some cases, contributions of electrostatic signals (tip electrode) or bimorph-like substrate bending (macroscopic capacitors) necessitate the introduction of vertical offset to symmetrize the loop. Finally, the forward and reverse domain nucleation voltages, V_c^+ and V_c^-, corresponding to the cross-over between constant and rapidly changing regions of the loop, are attributable to domain nucleation below the tip. Additionally, the *effective work of switching* is defined as the area within a hysteresis loop,

$$A_s = \int_{-\infty}^{+\infty} \left(R^+(V) - R^-(V)\right) \mathrm{d}V. \qquad (4.1)$$

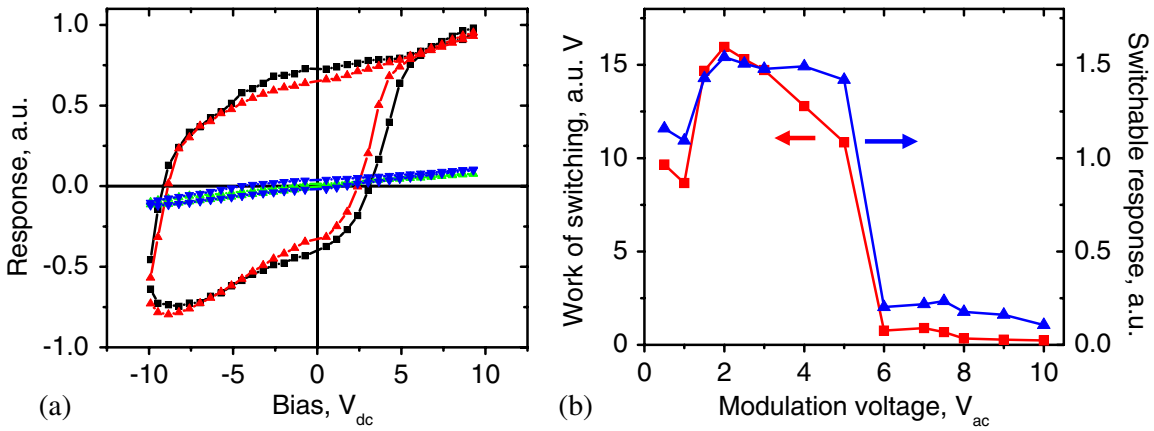

Figure 38. The driving bias effect on the hysteresis loop shape. (*a*) Hysteresis loops for PZT thin film for (■) 1.5 V_{pp}, (▲) 4 V_{pp}, (▼) 6 V_{pp} and (●) 8 V_{pp} driving amplitudes. (*b*) Driving bias dependence of effective work of switching and saturation response. Reprinted from [329]. Copyright 2006, American Institute of Physics.

These parameters provide a measure of the switching properties of the material.

4.1.1. Effect of imaging conditions on hysteresis loops. As in any spectroscopic method, PFS and SS-PFM are highly susceptible to a large number of external and internal factors that affect the veracity of spectroscopic data acquisition. The detailed analysis of instrumental factors is reported in [329]. Below, we discuss the effect of measurement parameters on PFS.

4.1.2.1. Probing bias and the bias window. One important consideration in PFM and SS-PFM is the choice of driving voltage, V_{ac}, and bias window of measurements, $V_{dc} \in (V_{min}, V_{max})$. Ideally the measurements are performed in the low signal limit, $V_{ac} \ll (V^+ + V^-)$. However, practical considerations such as maximizing the signal strength often necessitate the use of high driving voltages, in particular for materials with relatively low piezoelectric coupling. The effect of a finite probing bias on the loop shape strongly depends on the fundamental hysteresis loop formation mechanism and bias frequency, and cannot be explained by a simple model. Here, we summarize the experimental studies of the driving bias effect.

Shown in figure 37(*a*) are experimentally observed hysteresis loops obtained on a pulsed-laser deposition grown PZT thin film (70 nm) for different probing biases. The loops are normalized by bias amplitude to ensure similar units. Note that for V_{ac} below the coercive bias, the loop shape remains largely unchanged—the loops slightly narrow indicating the onset of switching, but the variation in relevant parameters is relatively small (figure 37(*b*)). Conversely, modulation amplitudes greater than the coercive bias effectively result in a collapse of the loop to a straight line. The changes in the effective work of switching and switchable response as a function of V_{ac} are shown in figure 38(*b*). The small variation in relevant characteristics for small biases is presumably due to a relatively larger noise level. Note that the behavior in figure 38 is reproducible and the shape is regained when small biases are used demonstrating that the collapse in the loop shape cannot be attributed to the damage to the conductive tip coating or the surface. Thus, for certain materials, voltages at ∼2/3 of the coercive bias level can be used to yield high-quality loops. At the same time, for materials with small coercive bias, e.g. ferroelectric nanodots, ultrathin films, etc, imaged at large modulation voltages, the absence of hysteresis loops can be erroneously interpreted as evidence for non-ferroelectric state.

The dependence of the loop parameters on the bias window is illustrated in figure 39. The hysteresis loops become saturated when the bias windows exceed 20 V (figure 49(*a*)). The origins of the slight downward trend are unclear but can possibly be attributed to reverse switching induced by charge injection at the surface [304]. The bias window dependence of switchable polarization is illustrated in figure 39(*b*). Note the good agreement between the values obtained from fitting and those measured directly from the loop. Figure 39(*c*) illustrates the dependence of the positive and negative nucleation biases on the bias window. Despite the relatively large error in the determination of nucleation bias, the values are nearly bias-window independent, suggesting that the loop formation is controlled by the nucleation process. Finally, figure 39(*d*) illustrates the bias window dependence of the effective work of switching as determined from functional fitting and the direct integration of the area below the curve. The values obtained are in good agreement and also illustrate that the leveling-off of hysteresis parameters at large voltages are indicative of loop saturation.

4.1.2.2. Ambient effects. One of the well-known factors affecting SPM measurements under ambient conditions is the presence of wetting water layers and associated capillary tip–surface forces as described in section 3.2.5. Here, we present experimental evidence illustrating the possible role of ambient conditions on hysteresis measurements by PFM.

Shown in figure 40(*a*) is the PFM hysteresis loop obtained on a freshly prepared (buffered HF etch followed by O_2 annealing) atomically flat STO (1 0 0) surface. Shown are the average values and error bars corresponding to standard deviations determined from 64 hysteresis loops acquired on an 8×8 mesh of points separated by 100 nm. Note that clear hysteretic behavior can be seen despite the fact that the surface is (nominally) non-ferroelectric. We attribute

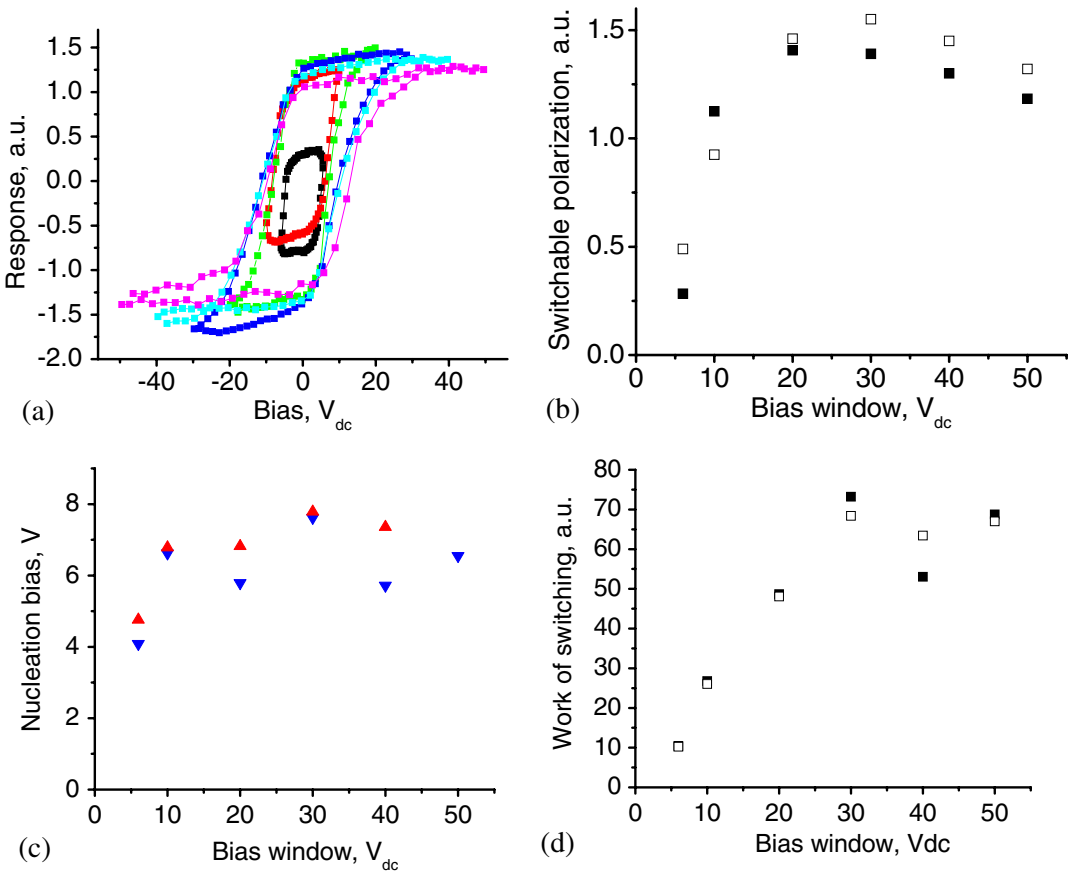

Figure 39. (*a*) Evolution of PFM hysteresis loops on an epitaxial PZT film as a function of bias. (*b*) Bias window dependence of switchable polarization. (*c*) Bias dependence of (▲) positive and (▼) negative nucleation bias. (*d*) Bias window dependence of effective work of switching. Shown in (*b*) and (*d*) are values determined from the functional fit (■) and by direct integration of the area below the loop (□). Reprinted from [329]. Copyright 2006, American Institute of Physics.

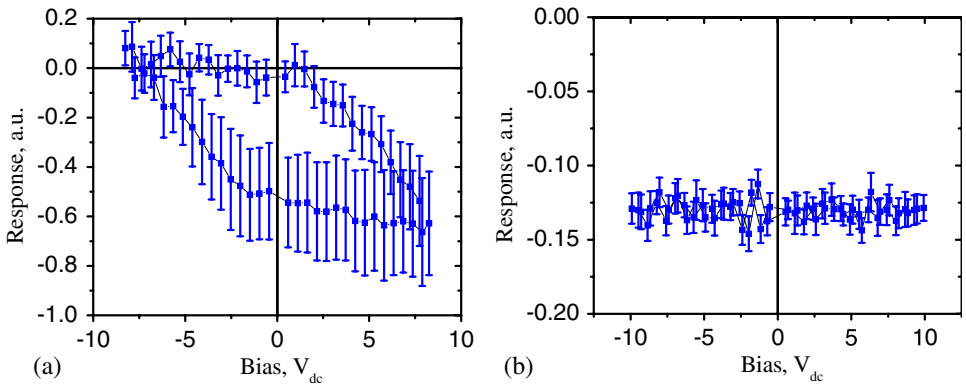

Figure 40. The effect of ambient conditions on the hysteresis loop shape. (*a*) Hysteresis loops for a clean insulting STO surface. (*b*) Hysteresis loop for conductive $SrRuO_3$/STO thin film. Reprinted from [329]. Copyright 2006, American Institute of Physics.

this behavior to the electrocapillary condensation of water layers at the tip–surface junction [330, 331], resulting in an 'unsaturated' electromechanical hysteresis loop. For comparison, figure 40(*b*) shows hysteresis loops obtained on a conductive $SrRuO_3$/STO surface. This surface is extremely stable in air and conductive (i.e. low energy electron diffraction pattern can be observed after air exposure) [332] and no hysteresis loops are measured, thus confirming that the behavior observed on the STO (1 0 0) surface is not an instrumental artifact. While this observation is not necessarily universal, it does illustrate that spurious hysteretic contributions to electromechanical measurements can exist when operating under ambient conditions.

4.2. Phenomenological theory of domain loop formation

The progress in experimental methods has stimulated parallel development of theoretical models to relate PFM hysteresis loop parameters and materials properties. A number of such models are based on the interpretation of phenomenological

characteristics of PFS hysteresis loops similar to macroscopic P–E loops, such as slope, imprint bias and vertical shift. In particular, the slope of the saturated part of the loop was originally interpreted as electrostriction; the later studies have demonstrated the dominant role of linear electrostatic contribution to the signal.

Several groups analyzed the effect of non-uniform materials properties, including the presence of regions with non-switchable polarization on parameters such as imprint and vertical shift. In thin films, vertical shift of the PFM hysteresis loops was interpreted in terms of non-switchable layer by Saya *et al* [333]. Alexe *et al* [334] analyzed the hysteresis loop shape in ferroelectric nanocapacitors with top electrodes, obtaining the estimate for the switchable volume of a nanocapacitor. Similar analysis was applied to ferroelectric nanoparticles developed by a self-patterning method [335] by Ma and Hesse [336]. In all cases, the results were interpreted in terms of ~ 10 nm non-switchable layers, presumably at the ferroelectric–electrode interface.

A number of authors attempted to relate local PFM loops and macroscopic P–E measurements, often demonstrating good agreement between the two [337]. This suggests that despite the fundamentally different mechanism in local and macroscopic switching, there may be deep similarities between tip-induced and macroscopic switching processes. A framework for analysis of PFM and macroscopic loops based on the Landau theory was developed by Ricinsi *et al* [338–340], demonstrating an approach to extract local switching characteristics from hysteresis loop shape using first order reversal curve diagrams.

In parallel with tip-induced switching studies, a number of groups combined local detection by PFM with uniform switching field imposed through the thin top electrode to study polarization switching in ferroelectric capacitor structures. In this case, switching field is nearly uniform. Spatial variability in switching behavior was discovered by Gruverman *et al* and attributed to strain [341] and flexoelectric [241] effects. In subsequent works, domain nucleation during repetitive switching cycles was shown to be initiated in the same defect regions, indicative of the frozen disorder in ferroelectric structures [342, 343].

Finally, in a few cases, 'abnormal' hysteresis loops having shapes much different from that in figure 37 have been reported. Abplanalp *et al* have attributed the inversion of electromechanical response to the onset of ferroelectroelastic switching [344]; this behavior was later interpreted as backswitching, as analyzed in detail in section 3.2.5. Harnagea has attributed the abnormal contrast to the in-plane switching in ferroelectric nanoparticles [194, 337]. Finally, a variety of unusual hysteresis loop shapes including possible Barkhausen jumps and fine structures associated with topographic and structural defects have been observed by the group of Kalinin [329, 345].

The rapidly growing number of experimental observations and recent developments in PFS instrumentation and data acquisition and analysis methods require understanding not only phenomenological, but also quantitative parameters of hysteresis loops, such as the numerical value of coercive bias and the nucleation threshold. Kalinin *et al* [325] have extended the 1D model by Ganpule *et al* [160] to describe PFM loop shape in the thermodynamic limit. Kholkin [346] has postulated the existence of nucleation bias from PFM loop observations, in agreement with theoretical studies by Abplanalp [344], Kalinin *et al* [347], Molotskii [348], Emelyanov [349], Morozovska and Eliseev [321]. Finally, Jesse *et al* [328] have analyzed hysteresis loop shape in kinetic and thermodynamic limits for domain formation. However, in all cases, the model was essentially 1D, ignoring the fundamental physics of domain switching. Below, we summarize the approaches for data acquisition and interpretation of PFM spectroscopy.

4.3. Hysteresis loop formation

Analytical theory of PFM hysteresis loop formation is required to understand the underlying mechanisms behind loop formation and extract material properties from spectroscopic data. Below, we summarize the results of 3D approaches in the rigid ferroelectric approximation. A detailed analysis of the hysteresis loop formation in the phase-field models is presented in section 5.

The tip-induced domain growth process during hysteresis loop measurements in semi-infinite material comprises the stages of domain nucleation, and subsequent forward and lateral domain growth. On reverse bias, both (a) shrinking of the formed domain and (b) nucleation of the domain of opposite polarity are possible. The analysis of the domain dynamics in PFS should qualitatively describe the individual stages in figure 41.

4.3.1. 3D Decoupling theory

4.3.1.1. Piezoelectric response in final and intermediate states. The analysis in section 3 derives the thermodynamics of domain evolution with bias. To calculate the shape of the PFM hysteresis loop, the geometric parameters of the domain, i.e. length l and radius r, must be related to the measured PFM signal. This relationship, once established, will be equally applicable to the thermodynamic theory developed in section 3, the kinetic theory developed by Molotskii and Shvebelman [311] and for data analysis in the PFM experiment.

To establish the relationship between domain parameters and the PFM signal, we utilize the decoupling Green function theory by Felten *et al* [182]. Measured in a PFS experiment is the electromechanical response related to the size of ferroelectric domain formed below the tip. Hence, to calculate the shape of the PFM hysteresis loop, the electromechanical response change induced by the semi-ellipsoidal domain is required. For the system containing the semi-ellipsoidal domain with semi-axes r and l, the following expression for the vertical PFM response $d_{33}^{\text{eff}} = u_3/U$ was found after integration of equation (2.11) for $x_3 = 0$, $\rho = 0$, as

$$d_{33}^{\text{eff}} = d_{31}g_1(\gamma, r, l, y_0) + d_{15}g_2(\gamma, r, l, y_0) + d_{33}g_3(\gamma, r, l, y_0), \tag{4.2}$$

$$g_i(\gamma, r, l, y_0) = f_i(\gamma) - 2w_i(\gamma, r, l, y_0). \tag{4.3}$$

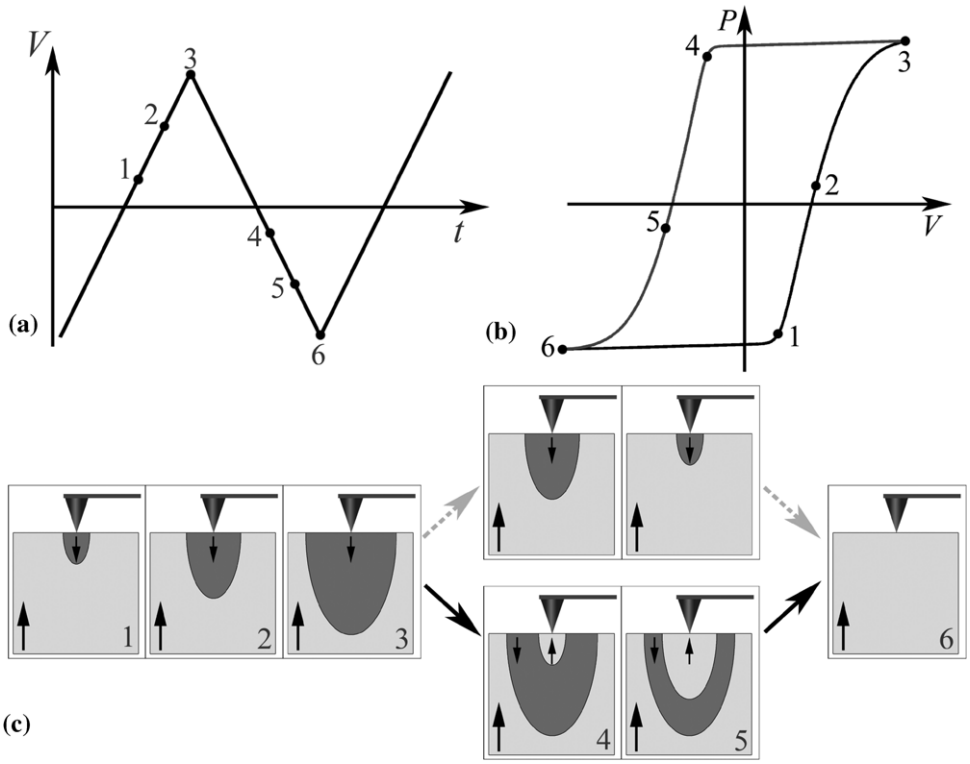

Figure 41. Domain evolution with bias depending on different pinning strengths of the material. (*a*) Time dependence of voltage and (*b*) schematics of hysteresis loop. (*c*) Schematics of the domain growth process. In the purely thermodynamics case (dashed arrows), the domain shrinks with decreasing voltage (path 3–4). To account for realistic loop, the domain size does not change on (3–4) and the domain of opposite polarity nucleates on path (4–6). At point 6, antiparallel domain walls annihilate. Reproduced from [314]. Copyright 2006, American Institute of Physics.

Here, the functions $w_i = 0$ in the initial and $w_i = f_i$ in the final state. The functions f_i are $f_1 = (2(1+\gamma)\nu+1)/(1+\gamma)^2$, $f_2 = -\gamma^2/(1+\gamma)^2$, $f_3 = -(1+2\gamma)/(1+\gamma)^2$ and define the electromechanical response in the initial and final states of switching process [184]. Functions w_i are dependent on the domain sizes r, l and the domain shift with respect to the tip apex, and can be reduced to the integral representations:

$$w_3(\gamma,r,l,y_0) = -\frac{3}{2\pi}\int_0^{2\pi} d\varphi \int_0^{\pi/2} d\theta \cos^3\theta \sin\theta \frac{R_{dw}(\theta,\varphi)}{R_G(\theta,R_{dw}(\theta,\varphi))}, \quad (4.4a)$$

$$w_2(\gamma,r,l,y_0) = \frac{3}{2\pi}\int_0^{2\pi} d\varphi \int_0^{\pi/2} d\theta \left(\frac{\gamma d+\cos\theta R_{dw}(\theta,\varphi)}{R_G(\theta,R_{dw}(\theta,\varphi))}-1\right)\cos^2\theta\cdot\sin\theta, \quad (4.4b)$$

$$w_1(\gamma,r,l,y_0) = \frac{1}{2\pi}\int_0^{2\pi} d\varphi \int_0^{\pi/2} d\theta \left(3\cos^2\theta - 2(1+\nu)\right) \times \cos\theta\sin\theta \frac{R_{dw}(\theta,\varphi)}{R_G(\theta,R_{dw}(\theta,\varphi))}, \quad (4.4c)$$

where the function $R_{dw}(\theta,\varphi)$ is determined by the shape of the domain, and $R_G(\theta, R_{dw}) = \sqrt{(\gamma d+\cos\theta R_{dw})^2+\gamma^2\sin^2\theta R_{dw}^2}$ is related to the probe electrostatic potential in the domain wall point determined by $R_{dw}(\theta,\varphi)$. Note that equations (4.4*a*)–(4.4*c*) can be extended to arbitrary rotationally invariant domain geometries, e.g. cylindrical or conic, as determined by the functional form of $R_{dw}(\theta,\varphi)$. For instance, the ellipsoidal domain wall shape corresponds to

$$R_{dw}(\theta) = \frac{rl}{\sqrt{r^2\cos^2\theta + l^2\sin^2\theta}}, \quad (4.5a)$$

while for the case of prolate semiellipsoid ($r \ll l$) or cylinder, shifted on distance y_0 we derived at $|y_0| < r$,

$$R_{dw}(\theta,\varphi) = \frac{|y_0|\cos\varphi + \sqrt{r^2 - y_0^2\sin^2\varphi}}{\sin\theta}. \quad (4.5b)$$

Using approximate expressions derived for $y_0 = 0$, approximate analytical relationship between the radius of a prolate semiellipsoidal domain, r, lateral shift, $|y_0|$, and the PFM signal can be determined:

$$d_{33}^{\text{eff}}(r,y_0) \approx \left(\frac{3}{4}d_{33}^*\left(1-\frac{16r}{\pi d+8r}+\frac{8\pi d(\pi d+24r)}{r(\pi d+8r)^3}y_0^2\right) + \frac{d_{15}}{4}\left(1-\frac{16r}{3\pi d+8r}+\frac{24\pi d(3\pi d+24r)}{r(3\pi d+8r)^3}y_0^2\right)\right) \quad (4.6a)$$

Here, the material is regarded as dielectrically isotropic, $\gamma = 1$, $r = r(U)$ is the voltage dependent domain radius and $d_{33}^* = d_{33} + (1+4\nu)d_{31}/3$. In the defect-free case, the relationship between the PFM signal and domain size is

$$d_{33}^{\text{eff}}(r,y_0) \approx \frac{3}{4}d_{33}^*\left(1-\frac{16r}{\pi d+8r}\right)+\frac{d_{15}}{4}\left(1-\frac{16r}{3\pi d+8r}\right). \quad (4.6b)$$

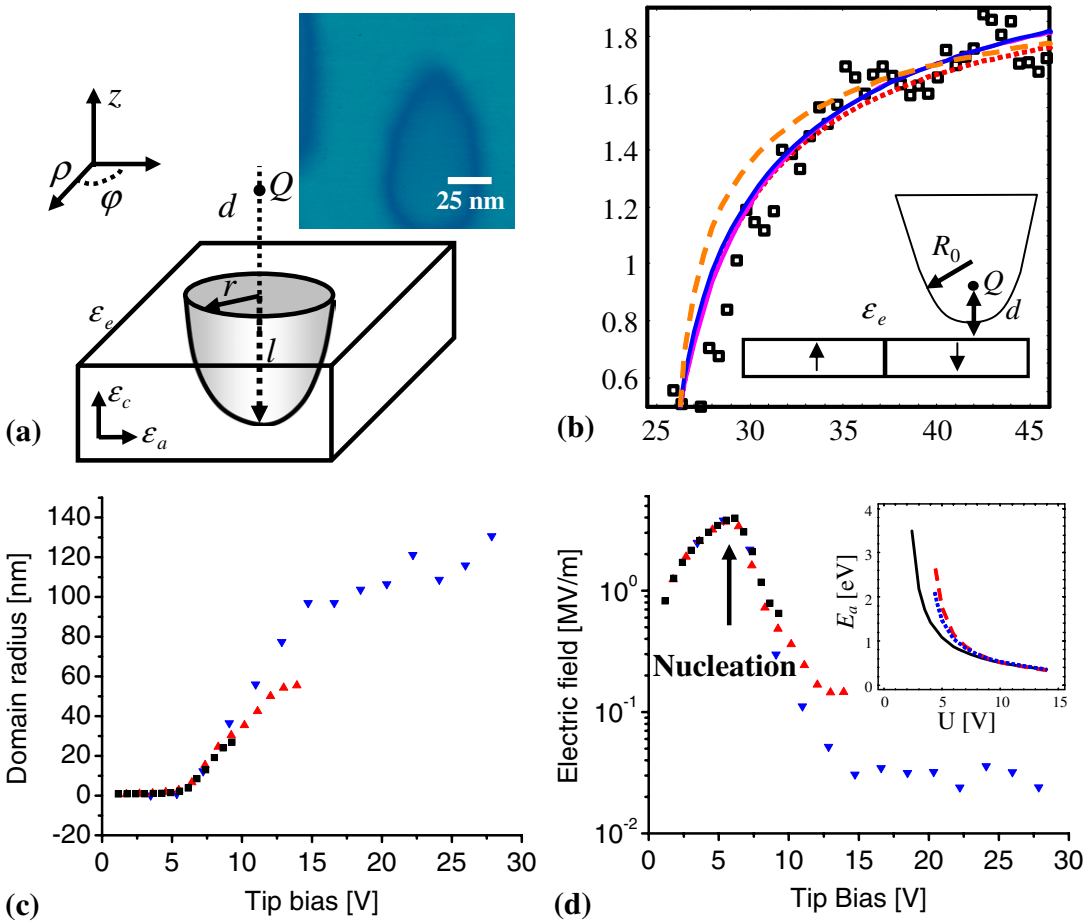

Figure 42. (*a*) Schematic of the tip interaction with a semiellipsoidal domain and high-resolution PFM amplitude image of a domain wall in BFO. (*b*) Domain wall profile and fit for several tip models. (*c*) Domain radius deconvoluted from the hysteresis data in the point charge model. (*d*) Electric field on the domain boundary. (Inset) Activation energy for different models. Reproduced from [350]. Copyright 2007, National Academy of Sciences.

Equations (4.2)–((4.6*a*) and (4.6*b*)) allow one to deconvolute nascent domain sizes from the hysteresis loops of piezoelectric response, as shown in [350]. The domain parameters are calculated self-consistently from the decoupling Green function theory by using tip geometry determined from the domain wall profile (figure 42). The critical parameters of the nucleating domain and the activation energy for nucleation are determined. In particular, the electric field at the domain wall at nucleation was estimated to be close to intrinsic thermodynamic field, a conclusion later confirmed by direct temperature-dependent measurements of nucleation biases by UHV PFM [295].

4.3.1.2. Modeling loop shape in weakly pinned limit. In this section we analyze the shape of the piezoresponse loop for PZT in the weak pinning limit. To calculate the thermodynamic hysteresis loop shape from the bias dependence of the domain size, we assume that the domain evolution follows the equilibrium domain size on the forward branch of the hysteresis loop. The corresponding piezoelectric loops calculated using the thermodynamic parameters derived in section 3 using formulae in subsection 4.3.1.1 are shown in figures 43.

Numerically, the results obtained within the EPCM of the tip at $R_d \to \infty$ can be well approximated by $d_{33}^{\text{eff}} = d_\infty(1 - \sqrt{U_0/U})$. The deviation from $d_{33}^{\text{eff}} = d_\infty(1 - U_0/U)$ obtained within the framework of 1D model [180, 325] could be related to the dimensionality of the problem.

It is clear from figures 43(*b*) and (*d*) that the modified point charge model gives the narrower loop that saturates more quickly than the exact series for sphere–tip interaction energy and moreover quicker than the capacitance approximation. This can be explained taking into account the fact that the distance d between the effective point charge Q and the sample surface is smaller in $\kappa/\varepsilon_e \approx 6$ times than the first ones from the image charges caused by the tip with curvature R_0.

In [314] the effect of surface screening and bulk Debye screening on piezoresponse loop shape, coercive voltage and saturation rate was studied. It appeared that the effect of surface and Debye screening on piezoresponse loop shape is complementary with respect to domain nucleation and loop saturation behavior, namely:

(i) The surface screening strongly influences the domain nucleation and the initial stage of growth. The coercive voltage (loop width) and nucleation voltages are controlled by σ_S value. At the same time, piezoresponse weakly depends on σ_S at high voltages, i.e. surface screening does not affect the saturation law.

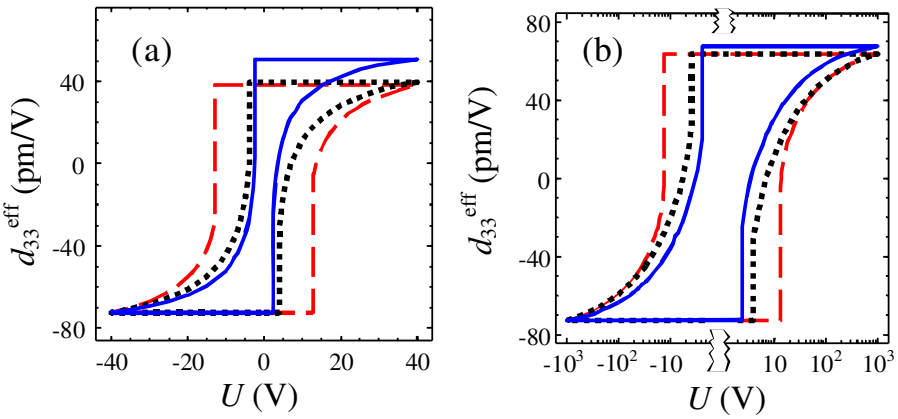

Figure 43. Piezoelectric response as the function of applied voltage for PZT6B and $\sigma_S = -P_S$ in linear (*a*) and logarithmic (*b*) scales. Solid curves represent EPCM approximation of the tip; dotted ones correspond to the exact series for sphere–tip interaction energy; dashed curves are the capacitance approximation. $d_{33} = 74.94$, $d_{31} = -28.66$ and $d_{15} = 135.59\,\mathrm{pm\,V^{-1}}$; whereas saturated value $d_{33}^{\rm eff} = 72.5\,\mathrm{pm\,V^{-1}}$ is depicted by arrows in parts (*b*) and (*d*). Reproduced from [317].

(ii) The Debye screening radius R_d strongly influences the piezoresponse at high voltages and thus determines the saturation law (i.e. high voltage tails of hysteresis loop), whereas nucleation voltage depends on R_d relatively weakly. The piezoresponse saturates much quicker at small R_d values than at big ones. The reason for this effect is explained by the quick vanishing of the tip potential at small R_d radii.

4.3.1.3. Implications for switching mechanism. Experimentally obtained hysteresis loops nearly always demonstrate much faster saturation than the loops predicted from thermodynamic theory. This behavior can be ascribed to several possible mechanisms, including (a) delayed domain nucleation (compared with thermodynamic model), (b) finite conductivity and faster decay of electrostatic fields in the material, (c) kinetic effects on domain wall motion and (d) surface screening and charge injection effects. These mechanisms are discussed in detail below:

(a) *Delayed nucleation*: the activation barrier for nucleation is extremely sensitive to the maximal electric field in the tip–surface junction region, which can be significantly reduced by surface adsorbates, quantum effects due to a finite Thomas–Fermi length in the tip material, polarization suppression at surfaces, etc. These factors are significantly less important for determining the fields at larger separation from contact, and hence affect primarily domain nucleation, rather than subsequent domain wall motion. Poor tip–surface contact can lead to a rapid jump from the initial to the final state. This effect will result in a sudden onset of switching, increasing the nucleation bias and rendering the loop more square-shaped. However, the theory in section 4 suggests that to account for experimental observations, the nucleated domain size should be significantly larger than the tip size, and that nucleation should occur only for very high voltages. Given the generally good agreement between experimental and theoretical nucleation biases, we believe this effect does not explain the experimental findings.
(b) *Conductivity and finite Debye length*: the second possible explanation for the observed behavior is the finite conductivity of the sample and/or the surrounding medium. In this case, screening by free carriers will result in a cross-over from a power law to an exponential decay of electrostatic fields at a depth comparable to the Debye length. This was shown to result in self-limiting effect in domain growth. Given that in most materials studied to date the Debye lengths are on the order of micrometers, this explanation cannot universally account for the experimental observations.
(c) *Domain wall motion kinetics*: in a realistic material, domain growth will be affected by the kinetics of domain wall motion. In the weak pinning regime, the domain size is close to the thermodynamically predicted size, while in the kinetic (strong pinning) regime the domain is significantly smaller. Both domain length and radius will grow slower than predicted by the thermodynamic model. The detailed effect of pinning on domain shape is difficult to predict, since the field decays faster in the z-direction, but at the same time surface pinning can dominate the wall dynamics. In either case, pinning is likely to broaden the hysteresis loop compared with its thermodynamic shape, and is unlikely to affect nucleation, contrary to experimental observations.
(d) *Surface conductivity effect*: one of the most common factors in AFM experiments under ambient conditions is the formation and diffusion of charged species, as analyzed in section 3.2.5. Here we note that surface charging can result in rapid broadening of the domain in the radial direction, i.e. the electrical radius of tip–surface contact grows with time. Given that only the part of the surface in contact with the tip results in cantilever deflection (i.e. the electrical radius is much larger than the mechanical radius), this will result in rapid saturation of the hysteresis loop. Note that similar effects were observed in, e.g., dip-pen nanolithography [300] and the kinetics of this process is very similar to the experimentally observed logarithmic kinetics of tip-induced domain growth. Estimating carrier mobility at $D \sim 10^{-11}\,\mathrm{m^2\,s^{-1}}$, diffusion length in 10 s is 1 μm. At the same time, the surface charge diffusion is unlikely to affect the nucleation stage, since the latter is controlled by the region of maximal electric field directly at the tip–surface junction. Also, charge dynamics is unlikely to affect PFM imaging, since the characteristic frequencies are significantly larger and at 100 kHz the diffusion length is 10 nm.

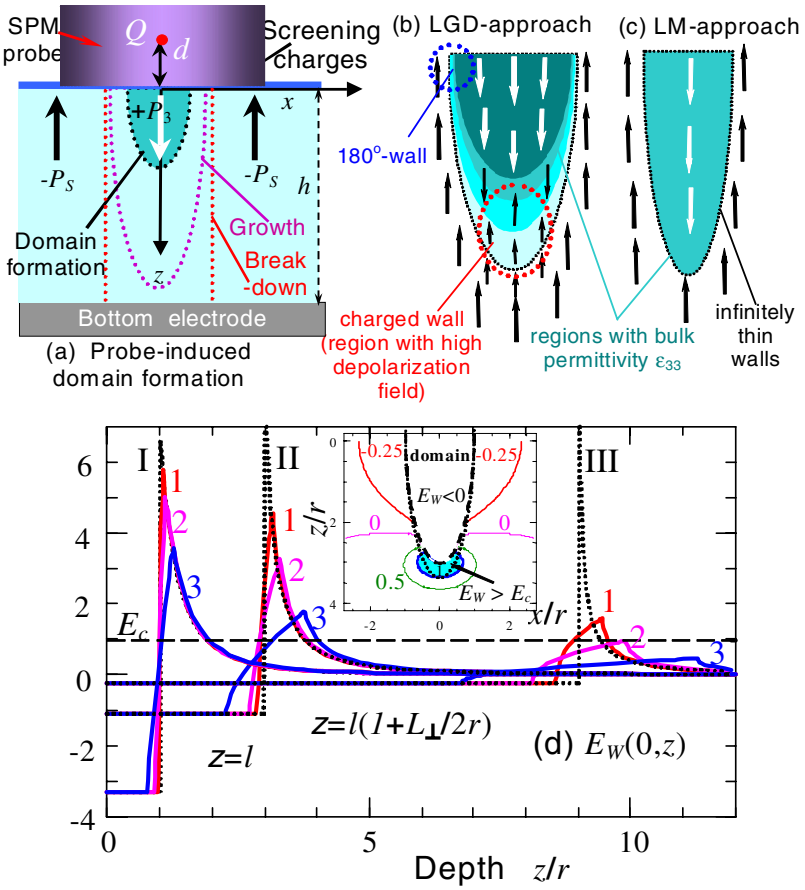

Figure 44. (*a*) Schematics of the domain nucleation caused by the strongly inhomogeneous electric field of the biased SPM probe in contact with the sample surface. (*b*), (*c*) Characteristic aspects of the LGD approach (*b*) and rigid LM approach (*c*). (*d*) Depth distribution of depolarization field, $E_W(\rho = 0, z)/E_c$, for different domain aspect ratios: length to radius $l/r = 1,\ 3,\ 9$ (group of curves I, II and III), $L_\perp = 0$ (dotted curves) and $L_\perp/r = 0.1,\ 0.2,\ 0.5$ (solid curves 1, 2, 3). Dashed line corresponds to thermodynamic coercive field E_c. Inset: mechanism of domain breakdown in the case of infinitely thin counter domain wall. Constant lines of the Landauer depolarization field ratio $E_W(\rho, z)$ for semi-ellipsoidal domain with radius r and length l in LNO. Dashed contour is the initial domain boundary. Filled areas indicate the region where depolarization field, E_W, is more than the thermodynamic coercive field E_c. Dotted contour shows the new domain boundary originated from the polarizing effect of the counter domain wall. Reproduced from [351].

4.3.2. Ginsburg–Landau model of local polarization switching and piezoresponse loop formation

4.3.2.1. Landau–Ginzburg–Devonshire theory. The majority of theoretical work analyzing the domain formation process in PFM utilized the rigid ferroelectric approximation and assumed infinitely thin domain walls. However, the self-consistent description of the SPM probe-induced domain formation in ferroelectrics and other ferroics requires an analytical approach based on the Landau–Ginzburg–Devonshire (LGD) thermodynamic theory. For ferroelectrics, LGD describes the dynamics of a continuous spatial distribution of the polarization vector $\boldsymbol{P}$ in an arbitrary electric field and the nonlinear long-range polarization interactions (correlation effects) [3]. In this manner, the LGD approach avoids the typical limitations (sharp walls and field-independent polarization values) of the rigid ferroelectric Landauer–Molotskii (LM) approach (compare figures 44(*b*) and 1(*c*)). Charge-neutral 180° domain walls do not cause the depolarization electric field and usually are ultra-thin. However, the charged (or counter) domain wall at the domain apex creates a strong depolarization field due to uncompensated bound charges ($\mathrm{div}\boldsymbol{P} \neq 0$). The charged wall inevitably appears at the tip of the nucleating domain (figure 44(*b*)).

The strong *positive* depolarization field in front of the infinitely thin charged domain wall causes the spontaneous increase in the domain length leading to the domain wall breakdown into the depth of the sample. Complementary to the LM approach evolved for infinitely thin domain walls, the LGD approach provides the solution of the paradox: the domain vertical growth should be accompanied by the increase in the width of the charged domain wall (see figure 45(*d*)). The width increase smears the jump of the depolarization field at the domain tip, and the domain wall broadening and propagation are completed once the field in front of the wall becomes smaller than the coercive field.

Below, we illustrate the application of the GLD approach for analytical calculation of hysteresis loop on the ideal surface [351] and in the presence of pre-existing 180° domain wall [352]. The approximate analytical expressions for the equilibrium distribution of *surface* polarization were derived from the *free energy functional* by a direct variational method.

We consider the spontaneous polarization $P_3(\boldsymbol{r})$ of ferroelectrics directed along the polar axis, z. The

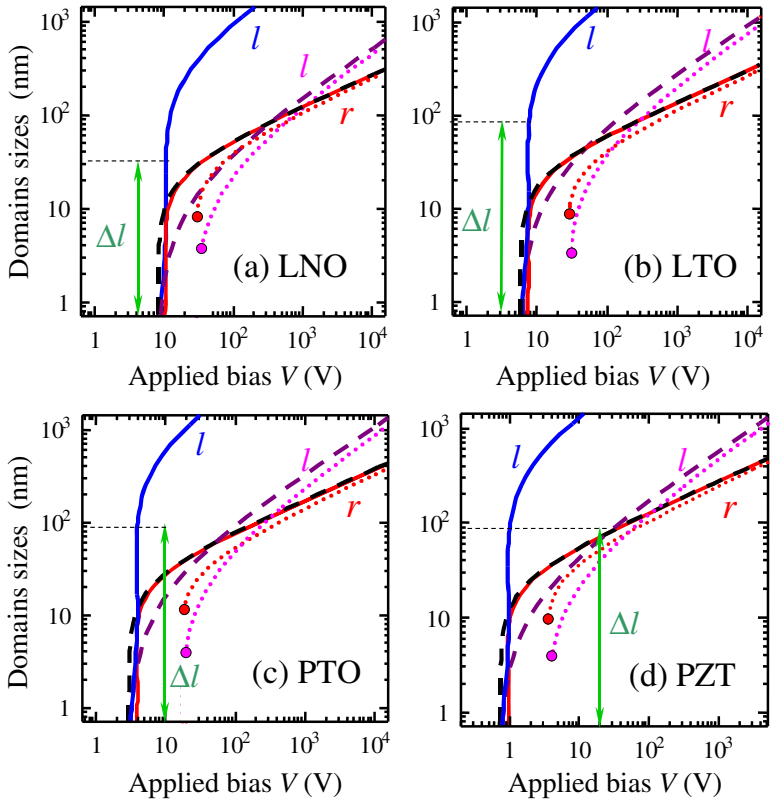

Figure 45. Domain length $l(V)$ and radius $r(V)$ bias dependence calculated within the LGD approach for typical ferroelectric materials: LNO ($LiNbO_3$ with $\varepsilon_{11} = 84$, $\varepsilon_{33} = 30$, $\alpha = -1.95 \times 10^9\,\mathrm{m\,F^{-1}}$, $\beta = 3.61 \times 10^9\,\mathrm{m^5\,C^{-2}\,F^{-1}}$, $P_S = 0.73\,\mathrm{C\,m^{-2}}$); LTO ($LiTaO_3$ with $\varepsilon_{11} = 54$, $\varepsilon_{33} = 44$, $\alpha = -1.31 \times 10^9\,\mathrm{m\,F^{-1}}$, $\beta = 5.04 \times 10^9\,\mathrm{m^5\,C^{-2}\,F^{-1}}$, $P_S = 0.51\,\mathrm{C\,m^{-2}}$); PTO ($PbTiO_3$ with $\varepsilon_{11} = 124$, $\varepsilon_{33} = 67$, $\alpha = -3.42 \times 10^8\,\mathrm{m\,F^{-1}}$, $\beta = -2.90 \times 10^8\,\mathrm{m^5\,C^{-2}\,F^{-1}}$, $\delta = 1.56 \times 10^9\,\mathrm{m^5\,C^{-2}\,F^{-1}}$, $P_S = 0.75\,\mathrm{C\,m^{-2}}$); PZT ($PbZr_{40}Ti_{60}O_3$ with $\varepsilon_{11} = 497$, $\varepsilon_{33} = 197$, $\alpha = -1.66 \times 10^8\,\mathrm{m\,F^{-1}}$, $\beta = 1.44 \times 10^8\,\mathrm{m^5\,C^{-2}\,F^{-1}}$, $\delta = 1.14 \times 10^9\,\mathrm{m^5\,C^{-2}\,F^{-1}}$, $P_S = 0.57\,\mathrm{C\,m^{-2}}$). Effective distance $d = 25\,\mathrm{nm}$, $\varepsilon_{33}^{\mathrm{b}} \leqslant 5$, $L_\perp = 1\,\mathrm{nm}$, sample thickness $h \to \infty$. Solid curves are calculated case iii, dotted curves correspond to case ii, dashed curves correspond to case i. Reproduced from [351].

sample is dielectrically isotropic in transverse directions, i.e. permittivities $\varepsilon_{11} = \varepsilon_{22}$, while ε_{33} may be different. The dependence of in-plane polarization components on electric field is linearized as $P_{1,2} \approx -\varepsilon_0(\varepsilon_{11} - 1)\partial\varphi(\boldsymbol{r})/\partial x_{1,2}$. The conventional relation between piezoelectric coefficients $d_{ijk} = 2\varepsilon_0\varepsilon_{il}Q_{jklm}P_m$ in Voigt notation acquires the explicit forms $d_{33} = 2\varepsilon_0\varepsilon_{33}Q_{11}P_3$, $d_{31} = 2\varepsilon_0\varepsilon_{33}Q_{12}P_3$, $d_{15} = 2\varepsilon_0\varepsilon_{11}Q_{44}P_3$, where Q_{ij} are the electrostriction tensor components in Voigt notation and ε_0 is the universal dielectric constant.

The problem for quasi-static electrostatic potential $\varphi(\boldsymbol{r})$ follows from the Maxwell equations, namely

$$\begin{cases} \varepsilon_{33}^{\mathrm{b}}\dfrac{\partial^2\varphi}{\partial z^2} + \varepsilon_{11}\left(\dfrac{\partial^2\varphi}{\partial x^2} + \dfrac{\partial^2\varphi}{\partial y^2}\right) = \dfrac{1}{\varepsilon_0}\dfrac{\partial P_3}{\partial z}, \\ \varphi(x, y, z = 0) = V_{\mathrm{e}}(x, y), \quad \varphi(x, y, z \to \infty) = 0. \end{cases} \tag{4.7}$$

Here we introduced dielectric permittivity of the background or reference state [353] as $\varepsilon_{33}^{\mathrm{b}}$. Typically $\varepsilon_{33}^{\mathrm{b}} \leqslant 10$; its origin can be related to electronic polarizability and/or reorientation of impurity dipoles.

Potential distribution produced by the SPM probe on the surface can be approximated as $V_{\mathrm{e}}(x, y) \approx Vd/\sqrt{x^2 + y^2 + d^2}$, where V is the applied bias, d is the effective distance determined by the probe geometry [314, 320]. The potential is normalized assuming the condition of perfect electrical contact with the surface, $V_{\mathrm{e}}(0, 0) \approx V$. In the case of the local point charge model, the probe is represented by a single charge $Q = 2\pi\varepsilon_0\varepsilon_{\mathrm{e}}R_0V(\kappa + \varepsilon_{\mathrm{e}})/\kappa$ located at distance $d = \varepsilon_{\mathrm{e}}R_0/\kappa$ for a spherical tip apex with curvature R_0 ($\kappa \approx \sqrt{\varepsilon_{33}\varepsilon_{11}}$ is the effective dielectric constant determined by the 'full' dielectric permittivity ε_{33} in the z-direction, ε_{e} is the ambient dielectric constant), or $d = 2R_0/\pi$ for a flattened tip represented by a disk of radius R_0 in contact with the sample surface.

In the framework of LGD phenomenology, the spatial–temporal evolution of the polarization component P_3 of the second order ferroelectric is described by the Landau–Khalatnikov equation:

$$-\tau\frac{\mathrm{d}}{\mathrm{d}t}P_3 = \alpha P_3 + \beta P_3^3 - \xi\frac{\partial^2 P_3}{\partial z^2} - \eta\left(\frac{\partial^2 P_3}{\partial x^2} + \frac{\partial^2 P_3}{\partial y^2}\right) - E_3, \tag{4.8}$$

where $\xi > 0$ and $\eta > 0$ are the gradient terms, the expansion coefficient, $\beta > 0$, for the second order phase transitions considered hereafter and τ is the Khalatnikov coefficient (relaxation time). In the absence of (microscopic) pinning centers or for weak pinning of viscous friction type the domain wall equilibrium profile can be found as the stationary solution of equation (4.8). Rigorously, the coefficient α should be taken as renormalized by the elastic stress as $(\alpha - 2Q_{ij33}\sigma_{ij})$ [354, 355]. Hereafter we neglect the striction effects, which are relatively small for ferroelectrics such as LTO and LNO [356].

Initial and boundary conditions for polarization in equation (4.8) are

$$P_3(\boldsymbol{r}, t \leqslant 0) = P_0(x), \qquad \left(P_3 - \lambda \frac{\partial P_3}{\partial z}\right)\Big|_{z=0} = 0. \tag{4.9}$$

Polarization distribution $P_0(x)$ satisfies equation (4.8) at zero external bias, $V_e = 0$.

Reported extrapolation length λ values are 0.5–50 nm [357]. Hereafter, second order ferroelectrics with large extrapolation length, $\lambda \gg \sqrt{\xi}$, are considered. Infinite extrapolation length $\lambda \to \infty$ corresponds to the situation of perfect atomic surface structure without defects or damaged layer.

4.3.2.2. Probe-induced domain formation and ferroelectric breakdown through the film. The analysis of the domain switching produced by the probe field requires the analytical description of the depolarization field produced by the counter domain wall. Since for most ferroelectrics the tip size is larger than the correlation length, $L_\perp \ll d$, this approximation is used hereinafter. Applying direct variational method to the linearized solution of equation (4.8), we obtained that in the actual region $z \gg L_z$, the gradient effects lead to the unessential renormalization of expansion coefficient α as $\alpha \to \alpha_R = \alpha(1 + (1 + \gamma^{-2})L_\perp^2/d^2)$. The approximation is rather rigorous outside the domain wall region. Hence, coupled equations (4.7) and (4.8) can be rewritten as

$$\begin{cases} \gamma_P^2(P_3)\dfrac{\partial^2\varphi}{\partial z^2} + \dfrac{\partial^2\varphi}{\partial x^2} + \dfrac{\partial^2\varphi}{\partial y^2} = 0, \\ \alpha_R P_3 + \beta P_3^3 + \delta P_3^5 = -\dfrac{\partial\varphi}{\partial z}, \\ \varphi(x, y, z = 0) = V_e(x, y), \quad P_3(r \gg d, z < 0) \to -P_S. \end{cases} \tag{4.10}$$

Polarization-dependent anisotropy factor $\gamma_P[P_3]$ is introduced as

$$\gamma_P(P_3) = \sqrt{\frac{\varepsilon_{33}^b}{\varepsilon_{11}} + \frac{1}{\varepsilon_{11}\varepsilon_0\left(\alpha_R + 3\beta P_3^2 + 5\delta P_3^4\right)}}. \tag{4.11}$$

Note that the dielectric susceptibility $\chi \sim (\alpha_R + 3\beta P_3^2 + 5\delta P_3^4)^{-1}$ is positive for thermodynamically stable states.

Then the spatial distribution of the polarization can be found as the solution of the nonlinear algebraic equation

$$\alpha_R P_3(\rho, z) + \beta P_3^3(\rho, z) + \delta P_3^5(\rho, z) = E_3(\rho, z). \tag{4.12}$$

We emphasize that the effective field E_3 is the sum of the probe field $E_e(\rho, z)$ and depolarization field $E_W(\rho, z)$. The left-hand side of equation (4.12) describes the conventional ferroelectric hysteresis. Thus, under the absence of the pinning field, a thermodynamically stable domain wall boundary $\rho(z)$ can be determined from equation (4.12) as the coercive point, i.e. under the condition $\alpha_R + 3\beta P_3^2(\rho, z) + 5\delta P_3^4(\rho, z) = 0$ valid at coercive field: $E_3(\rho, z) = E_c$.

The intrinsic coercive field E_c is well known [358] as

$$E_c = \begin{cases} \dfrac{2}{3\sqrt{3}}\sqrt{-\dfrac{\alpha_R^3}{\beta}}, & \text{for the second order ferroelectrics,} \\ \dfrac{2}{5}\left(2\beta + \sqrt{9\beta^2 - 20\alpha_R\delta}\right) \\ \quad \times \left(\dfrac{2\alpha_R}{-3\beta - \sqrt{9\beta^2 - 20\alpha_R\delta}}\right)^{3/2}, & \text{for the first order.} \end{cases} \tag{4.13}$$

Note that this analysis essentially reproduces early arguments of Kolosov [123], stating that the domain size in a PFM experiment corresponds to the region in which tip-induced field exceeds coercive field. Here, we obtain a similar result; however, the field is now intrinsic (rather than macroscopic) coercive field renormalized by the depolarization field of the nascent domain.

The bias dependences of the domain length $l(V)$ and radius $r(V)$ calculated from the equation $E_3(\rho, z) = E_c$ are shown in figure 45 for typical ferroelectric materials including $LiTaO_3$, $PbTiO_3$ and $PbZr_{40}Ti_{60}O_3$ in three limiting cases:

(i) Perfect screening of domain wall depolarization field by free charges. For this case there are no resulting charge at the wall and no depolarization field (see dashed curves in figure 45).
(ii) No motion of the charged domain wall by depolarization field and no screening charges. This case has unclear physical interpretation and shown by dotted curves in figure 45 for comparison.
(iii) The motion of the charged domain wall by the maximal depolarization field is considered. The situation is typical in the absence of screening or very slow screening (see solid curves in figure 45).

The remarkable aspect of the above analysis is that the domain radius r calculated from equations (4.12) is always finite at finite intrinsic domain wall width $L_\perp \neq 0$. This reflects the fact that spontaneous polarization re-orientation takes place inside the localized spatial region, where the resulting electric field absolute value is more that thermodynamic coercive field, i.e. $|E_3| > E_c$, while the hysteresis phenomenon appeared in the range $|E_3| < E_c$ as anticipated within the LGD approach considering nonlinear correlation effects. The domain breakdown through the sample depth appears for infinitely thin domain walls ($L_\perp \to 0$), i.e. under the absence of domain wall correlation energy ($\xi, \eta \to 0$). The microscopic origin of the domain tip elongation in the region where the probe electric field is much smaller than the intrinsic coercive field is the positive depolarization field appearing in front of the moving charged domain wall (see figure 44(*c*)). Note, that the *activationless* hysteresis phenomenon calculated within the LGD approach corresponds to the *metastable state*, in contrast to activation mechanism of the stable domain formation calculated within the energetic LM approach.

Within the rigid LM approach the domain walls are regarded infinitely thin and polarization absolute value is constant: $-P_S$ outside and $+P_S$ inside the domain (if any). Semi-ellipsoidal domain radius r and length l are calculated

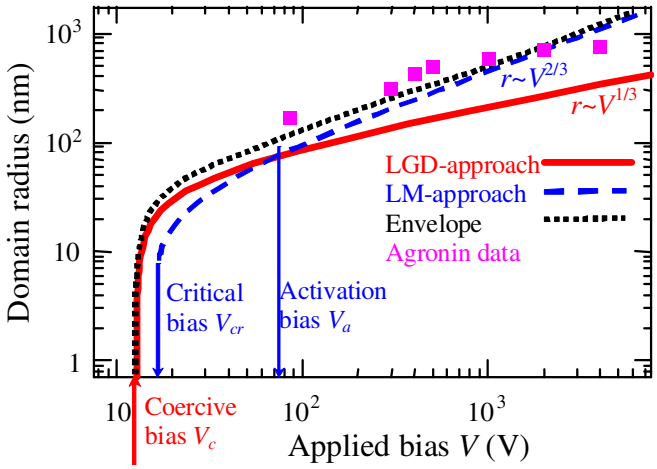

Figure 46. Diagram demonstrating the main features of probe-induced domain formation calculated within the LGD approach (solid curves), LM approach (dashed curves) and their envelope (dotted curve). LNO material parameters are the same as in figure 45, $\psi_S = 0.35\,\mathrm{J\,m^{-2}}$, probe surface separation $d = 50$ nm. Squares are experimental data reported by Agronin *et al* [359]. Reproduced from [351].

from the free energy excess consisting of the interaction energy, the domain wall surface energy ψ_S and the depolarization field energy. Nonlinear correlation energy contribution is absent within the rigid approximation. Within the LM approach, the depolarization field energy vanishes as $1/l$, while the interaction energy is maximal at $l \to \infty$, the condition of negligible surface energy leads to the domain breakdown $l \to \infty$ and the subsequent macroscopic region re-polarization even at infinitely small bias (if only $VP_S > 0$), while the hysteresis phenomena or threshold bias (saddle point) are absent. Under finite domain wall energy, the critical bias V_{cr} and energetic barrier E_a of stable domain formation exist. Activation (or nucleation) bias V_a is determined from the condition $E_a(V_a) = n\,k_B T$, where the numerical factor $n = 1 \ldots 25$. Usually $V_a \gg V_{cr}$ for thick films.

In figure 46 we compare the main features of the probe-induced domain formation calculated within the intrinsic LGD approach and the energetic LM approach. For consistency between the approaches we used the Zhirnov expression [354] for the domain wall surface energy

$$\psi_S = \sqrt{\left(1 + \frac{2\left(\left(Q_{11}^2 + Q_{12}^2\right)s_{11} - 2Q_{11}Q_{12}s_{12}\right)}{\beta\left(s_{11}^2 - s_{12}^2\right)}\right)\eta} \times \frac{(-2\alpha)^{3/2}}{3\beta}, \tag{4.14}$$

where Q_{ij} are the electrostriction tensor, s_{ij} are the elastic compliances.

4.3.2.3. Probe interaction with domain walls. The analytical model for the interaction of the biased SPM probe and existing domain walls opens the way for experimental studies of microscopic mechanisms of domain wall polarization interaction with electric field that can be studied in strongly inhomogeneous fields of biased force microscope probe. This problem is similar to that of domain wall pinning on a charged impurity, where the SPM probe acts as a 'charged impurity' with controlled strength (controlled by tip bias) positioned at a given separation from the domain wall. In this context, the problem of the infinitely thin ferroelectric domain wall interaction with a charged point defect was considered by Sidorkin [360]; however, neither correlation effects (e.g. finite intrinsic width of domain walls) nor rigorous depolarization field influence were taken into account. For the description of domain wall equilibrium position the Laplace tension conception (whose applicability to ferroelectrics has not been studied in detail) was used instead of the conventional LGD theory, thermodynamic Miller–Weinreich approach [86] or their combination with molecular dynamics and Monte-Carlo simulations as proposed by Rappe *et al* [88]. However, they studied domain wall profile changes in homogeneous external field.

Below we consider the interaction of ferroelectric 180° domain wall polarization with a strongly inhomogeneous electric field of biased force microscope probe within LGD thermodynamic approach using direct variational method (see figure 47).

The solution of equation (4.8) for the initial flat domain wall profile positioned at $x = x_0$ is $P_0(x) = P_S \tan h((x - x_0)/2L_\perp)$, where the correlation length is $L_\perp = \sqrt{-\eta/2\alpha}$, and the spontaneous polarization is $P_S^2 = -\alpha/\beta$.

Polarization distribution at the sample surface was derived as

$$P_3(x, y, 0) \approx P_0(x) - \sqrt{\frac{\varepsilon_{11}\varepsilon_0}{-2\alpha}} \times \frac{P_V d^2}{\sqrt{d^2 + x^2 + y^2}\left(d^2 + x^2 + y^2 + L_\perp d\right)}.$$

The variational amplitude P_V should be found from Landau–Khalatnikov equation

$$\tau\frac{\mathrm{d}}{\mathrm{d}t}P_V + w_1 P_V + w_2(x_0)\,P_V^2 + w_3 P_V^3 = V(t), \tag{4.15}$$

with parameters

$$w_1 = 1, \quad w_2(x_0) = -\frac{3\beta P_S x_0}{\sqrt{(L_\perp + d)^2 + x_0^2}}\frac{\sqrt{-2\alpha\varepsilon_{11}\varepsilon_0}}{4\alpha^2(L_\perp + d)},$$

$$w_3 = \frac{\beta\varepsilon_{11}\varepsilon_0}{4\alpha^2(L_\perp + d)^2}.$$

In the decoupling approximation and object transfer functions approach (see [182, 183, 186, 352]), Pade approximations for the bias V dependence of effective piezoelectric response $PR(V) = u_3(x = 0, y = 0)/V$ were found as

$$PR(V, x_0) = d_0^{\mathrm{eff}}(x_0) - \frac{\varepsilon_0\varepsilon_{11}}{\gamma} \times \sum_{i=1}^{4}\frac{B_i(\gamma)\cdot\ln\left(e + b_i(\gamma)/C\right)P_V(V, x_0)}{\left(b_i(\gamma) + \ln\left(e + b_i(\gamma)/C\right)\right)\left(L_\perp + d\ln\left(e + b_i(\gamma)/C\right)\right)}, \tag{4.16}$$

where $d_0^{\mathrm{eff}}(x_0)$ is the bias-independent PFM profile of the flat 180° domain wall located at distance x_0 from the tip apex. Response $d_0^{\mathrm{eff}}(x_0)$ was calculated in [361]. Dielectric anisotropy factor $\gamma = \sqrt{(\varepsilon_{33} + \varepsilon_{33}^{\mathrm{b}})/\varepsilon_{11}}$. Constants $e \approx 2.718\,28\ldots$ is the natural logarithm base

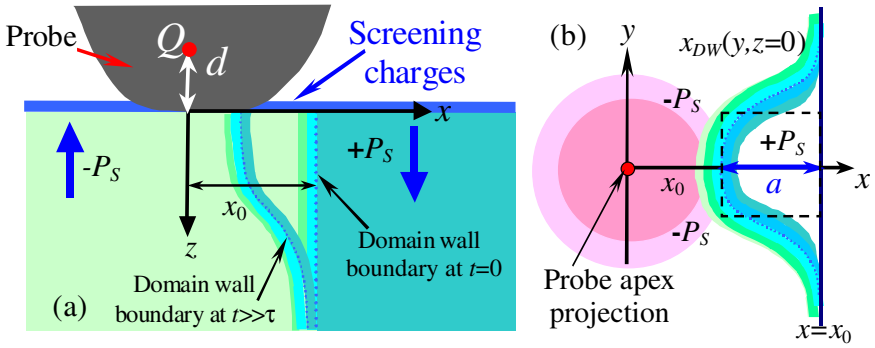

Figure 47. (*a*) Schematics of ferroelectric 180° domain wall boundary curved by the strong localized electric field of the biased probe in contact with the sample surface. (*b*) Wall curvature at the sample surface in quasi-continuous media approximation (solid curves and a grayscale level). Dashed rectangle corresponds to the schematics of activation field calculations used by Miller and Weinreich for rigid polarization model, where the distance a is equal to the lattice constant. Reproduced from [352]. Copyright 2008, American Physical Society.

and $C \approx 0.577\,216\ldots$ is Euler's constant. Constants $b_1(\gamma) = \gamma^2/(1+\gamma)^2$, $b_2(\gamma) = \gamma/(1+\gamma)$, $b_3(\gamma) = (\gamma/2)((1+2\gamma)/(1+\gamma)^2)$, $b_4(\gamma) = (16-15\gamma^2)\gamma/4(1+\gamma)^2$ and $B_1(\gamma) = -2\varepsilon_0\varepsilon_{33}Q_{12}(\gamma/(1+\gamma)^2)$, $B_2(\gamma) = (1+2\nu)2\varepsilon_0\varepsilon_{33}Q_{12}(1/(1+\gamma))$, $B_3(\gamma) = 2\varepsilon_0\varepsilon_{33}Q_{11}((1+2\gamma)/(1+\gamma)^2)$, $B_4(\gamma) = 2\varepsilon_0\varepsilon_{11}Q_{44}(\gamma^2/(1+\gamma)^2)$ (ν is the Poisson ratio).

Static thermodynamic coercive biases $V_c^{\pm}(x_0)$ for both polarization and piezoresponse hysteresis loops should be found from the condition $dV/dP_V = 0$, namely $V_c^{\pm}(x_0) = (w_2(2w_2^2 - 9w_3) \pm 2(w_2^2 - 3w_3)^{3/2})/27w_3^2$. It is easy to show that ΔV_c is defined only for the case of $x_0^2 \geqslant 2(L_\perp + d)^2$. Only in this region is the bistability possible. Far from the wall ($x_0 \gg d$) corresponding coercive biases are symmetric, namely $V_c^{\pm} = \pm((L_\perp + d)/\sqrt{-2\alpha\varepsilon_{11}\varepsilon_0})(2\alpha P_S/3\sqrt{3})$.

The phase diagram in coordinates $\{x_0, d\}$ that contains domain wall bending regime (no hysteresis, $V_c^{\pm} = 0$) to the domain nucleation far from the wall (almost symmetric hysteresis loop with $V_c^{+} \approx -V_c^{-}$) and intermediate regime (asymmetric hysteresis with $V_c^{+} \neq -V_c^{-}$) is shown in figure 48.

The analysis in figure 48 illustrates that for small tip–surface separations the domain wall displacement is activationless, corresponding to the wall bending toward or away from the probe. For intermediate separations, the process is affected by depolarization field induced by wall bending, corresponding to thermodynamics nucleation biases reduced relative to bulk values and appearance of significant loop imprint. Finally, for large tip–surface separations, the wall does not affect nucleation below the tip. From figure 49(*a*) it is seen that the loop halfwidth *monotonically increases* with an increase in the distance x_0. Viscous friction leads to the loop broadening and smearing far from the wall, while near the wall the loop originates much earlier than without pinning (compare solid and dotted curves in figures 49(*a*)–(*c*)).

This analysis is performed for the case of ferroelectric material with second order phase transition in the absence of lattice and defect pinning. It can further be extended to incorporate lattice effects through the introduction of lattice discreteness or periodic pinning potentials.

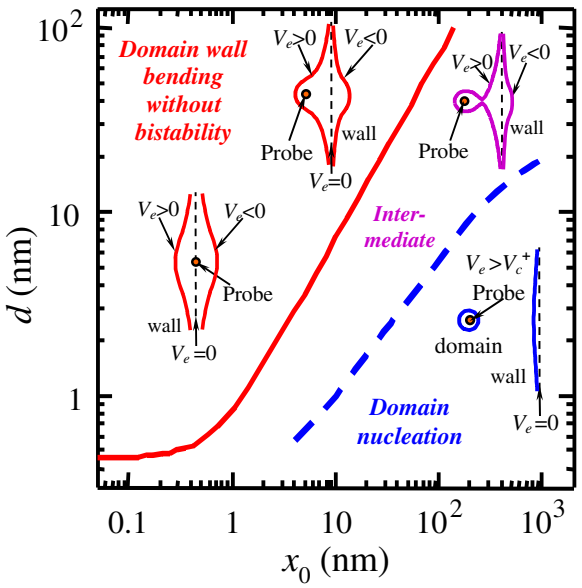

Figure 48. Phase diagram in coordinates $\{x_0, d\}$. Boundaries between the regions of different bias dependence of P_3: activationless domain wall bending, domain nucleation far from the wall (hysteresis) and intermediate regimes are shown schematically. Material parameters correspond to $LiNbO_3$. Reproduced from [352]. Copyright 2008, American Institute of Physics.

4.4. SS-PFM of polarization dynamics in low-dimensional ferroelectrics

Despite relatively short history, SS-PFM has been established as a powerful technique for the characterization of switching behavior in nanoscale ferroelectric materials. Below, we summarize some of the recent applications of SS-PFM and advances made in the understanding of polarization reversal mechanisms.

4.4.1. Work of switching in ferroelectric nanoparticles. One of the first demonstrations of SS-PFM was the studies of polarization reversal of and within ferroelectric nanoparticles [362]. The topography, mixed PFM and SS-PFM images of initial piezoresponse, switchable piezoresponse and the work of switching of a single 70 nm diameter nanoparticle are shown

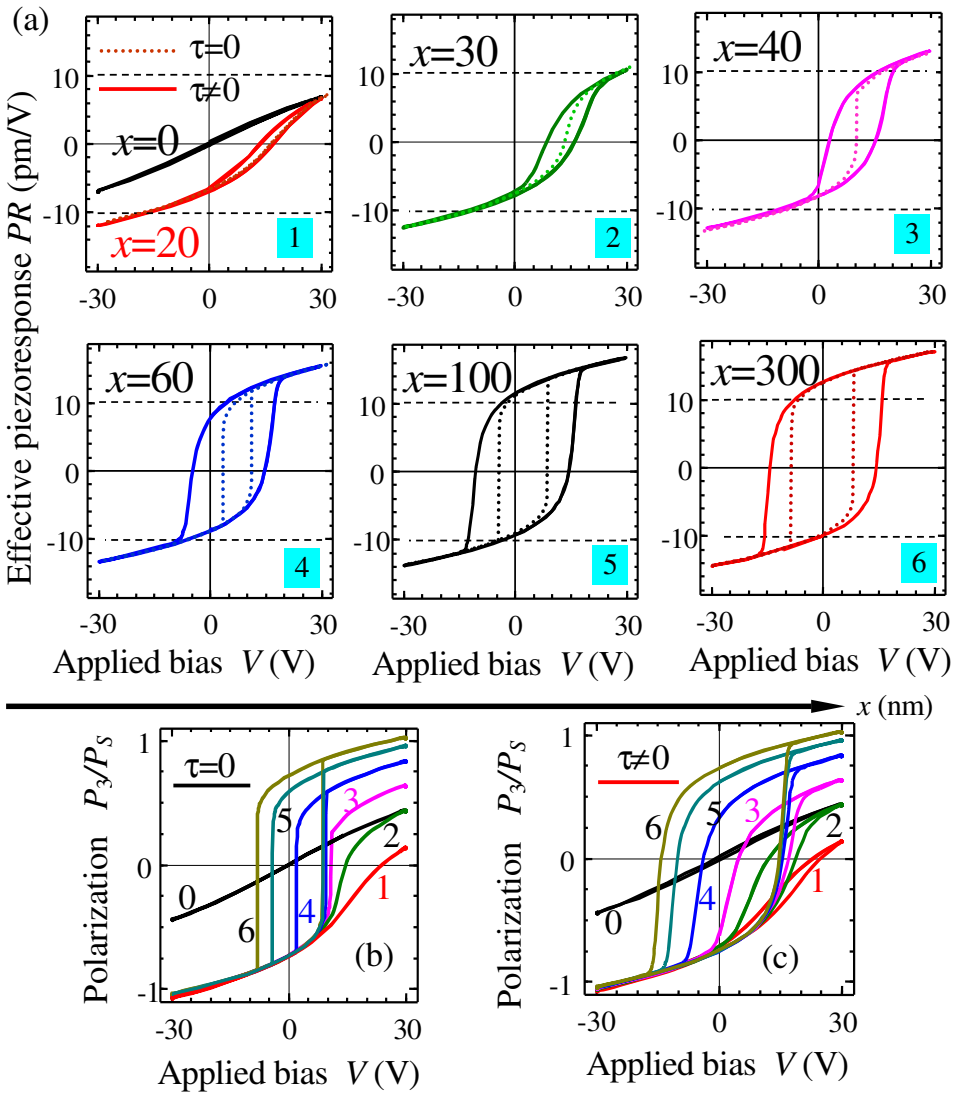

Figure 49. (*a*) Effective piezoelectric response (pm V^{-1}) versus applied bias (V) calculated from equation (2) for different distances x_0 from the domain wall for $x = 0$, 20, 30, 40, 60, 100, 300 nm (plots 1–6). Dotted curves are static dependences calculated at $\tau = 0$, while solid curves are kinetic loops calculated for $\tau = 10^{-8}$ s and applied bias frequency $f = 500$ kHz. (*b*), (*c*) Normalized polarization P_3 versus applied bias for $\tau = 0$ (*b*) and $\tau = 10^{-8}$ s (*c*) for $x = 0$, 20, 30, 40, 60, 100, 300 nm (curves 0–6). Effective distance $d = 25$ nm. Material parameters for LNO are $\varepsilon_{11} = 84$, $\alpha = -2 \times 10^9$ SI units, $P_S = 0.75\,\mathrm{C\,m^{-2}}$. Poisson ratio is $\nu = 0.3$; electrostriction coefficients are $Q_{44} = 0.038$, $Q_{12} = -0.003$, $Q_{11} = 0.016\,\mathrm{m^4\,C^{-2}}$; $L_\perp = 1$ nm.

in figure 50. A two-layer model for the nanoparticle consisting of a switchable (ferroelectric) layer characterized by the presence of a built-in electric field and a non-switchable (frozen polarization) layer as shown in figure 50 was introduced and relevant parameters were analyzed using the 1D model, as described previously [180, 334]. Specifically, the vertical shift of a hysteresis loop is related to the relative thickness of the non-switchable polarization component and defines the distribution of the frozen polarization within the system, while the lateral shift of the hysteresis loop defines the built-in field in the ferroelectric component.

4.4.2. Imaging of multiferroic structures. The role of interfaces on ferroelectric switching behavior and on multiferroic coupling ferroelectric–ferromagentic heterostructures [363] was studied in [104]. Topography, PFM and SS-PFM (work of switching, PNB and NNB) images for a BFO–$CoFe_2O_4$ (CFO) nanostructure sample are shown in figure 51, along with characteristic loops from the BFO, CFO and BFO–CFO interface regions. The corresponding bias parameters are defined in figure 51(*h*). The SS-PFM maps illustrate that coercive and nucleation biases are uniformly distributed within the ferroelectric regions and do not exhibit any systematic trends in the vicinity of the interface. While the work of switching and the electromechanical response are reduced in the vicinity of the interfaces, analysis of the SS-PFM data shows that this is a purely geometric effect due to the reduction of the domain volume at the interface [104].

4.4.3. Disorder potential mapping. The role of defects as nucleation centers in polarization reversal is the central theme of ferroelectric switching models and at the heart of

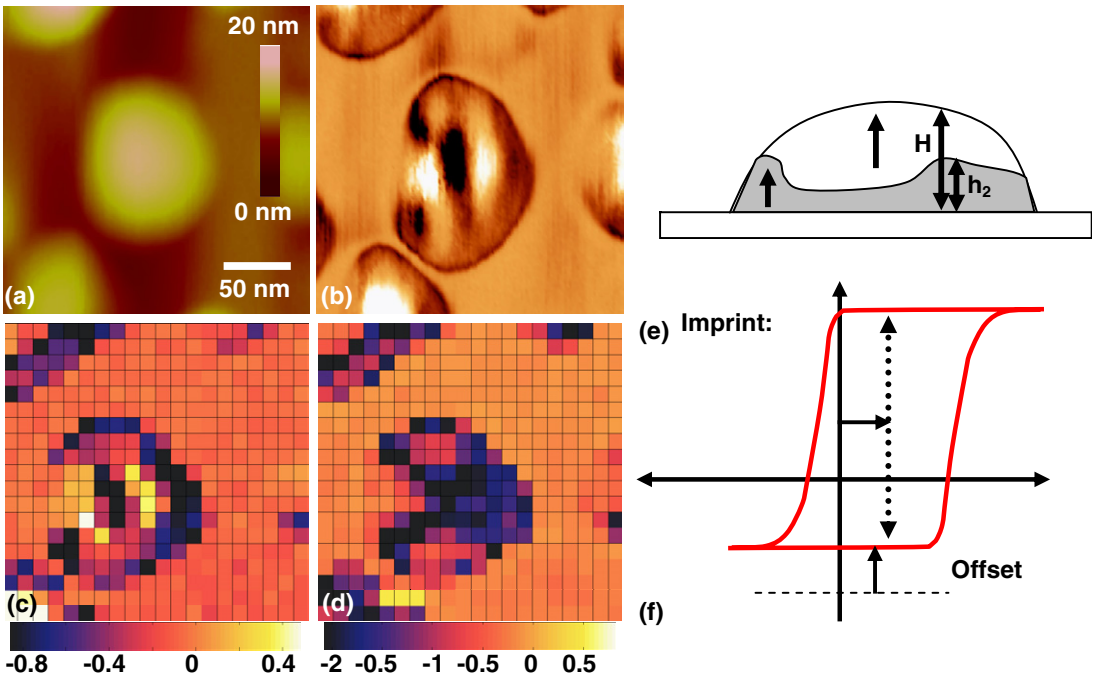

Figure 50. (*a*) Topography, (*b*) mixed PFM, (*c*) initial piezoresponse and (*d*) the work of switching for the nanoparticle shown in (*a*). (*e*) Schematic showing the polarization within a nanoparticle and (*f*) the corresponding loop which is shifted along the voltage axis due to imprint and the response axis due to the frozen polarization. Reproduced from [362]. Copyright 2008, John Wiley and Sons, Inc.

device behavior; however, experimental studies of specific nucleation centers are quite challenging given the predicted size of nucleation centers (below 10 nm), low densities in high quality films, and the difficulties distinguishing nucleation from domain wall propagation.

SS-PFM has allowed real-space imaging of nucleation centers in ferroelectrics via mapping positive and negative nucleation biases. To relate the PNB and NNB maps to local materials properties, RB disorder was introduced as a variation in wall energy, $\psi_S(x, y) = \psi_S^0\alpha(x, y)$ (or, equivalently, thickness), and RF disorder is introduced as built-in polarization disorder, $P_S(x, y) = P_S^0(1 + \beta(x, y))$, or frozen polarization. Here, ψ_S^0 and P_S^0 correspond to the parameters of the ideal material and $\alpha(x, y)$ and $\beta(x, y)$ describe variations in materials properties on length scales larger than the characteristic nucleating domain size (~2 nm, as estimated from activation energy). The local nucleation bias is then $U_{cr}^2 = A\psi_S(x, y)P_S(x, y)$, where A is a constant determined by the tip properties and the dielectric properties of the material. Assuming that the latter are position independent, the positive and negative nucleation biases are

$$U_+^2 = A\psi_S^0 P_S^0\alpha\,(x, y)\,(1 + \beta\,(x, y))\,, \qquad (4.17a)$$

$$U_-^2 = A\psi_S^0 P_S^0\alpha\,(x, y)\,(1 - \beta\,(x, y))\,. \qquad (4.17b)$$

Thus, analysis of the nucleation biases allows the random bond and random field components of the disorder potential to be separated and subsequently correlated with the local microstructure (figure 52).

4.4.4. Barkhausen jumps at the nanoscale. The analysis of hysteresis loops from a variety of materials systems has shown that often the loops possess fine features, as shown in figure 53. The features are highly localized, reproducible and in some cases are associated with the visible structural defects. The studies by the Alexe group have associated the presence of the fine structure features with the proximity to a ferroelastic domain wall [364, 365]. Bdikin *et al* [366] have performed simultaneous imaging and spectroscopic studies and illustrated that the fine structure is associated with the non-monotonic jumps in wall motion, i.e. individual pinning events (figure 54). Notably, the defect–defect spacing in the high-quality epitaxial films can be of the order of 100–300 nm [367], well above the resolution of the PFM. Hence, single defect imaging can be feasible provided that (a) the defect signature in hysteresis loop measurements is known and (b) the sensitivity of the method is sufficient to detect a single defect. Recently, single-defect imaging from SS-PFM was demonstrated (figure 54) [319].

4.5. Time resolved spectroscopies of ferroelectrics

One of the most interesting aspects of ferroelectric behavior is the polarization dynamics. In most materials, domain nucleation occurs at the ~nanosecond time scale, and wall velocities are extremely high. Consequently, PFM limited to ~100 Hz bandwidth for spectroscopy and ~1 mHz for imaging cannot be expected to provide direct time resolved information on ferroelectric domain resolution, necessitating the development of stroboscopic modes [342, 343, 368] or alternative time-resolved probes such as focused x-ray [369]. However, an important exception is the relaxor ferroelectric and ferroelectric polymers that often have extremely large (hours to days) relaxation times, enabling PFM-based dynamic studies. Furthermore, domain wall dynamics at small fields

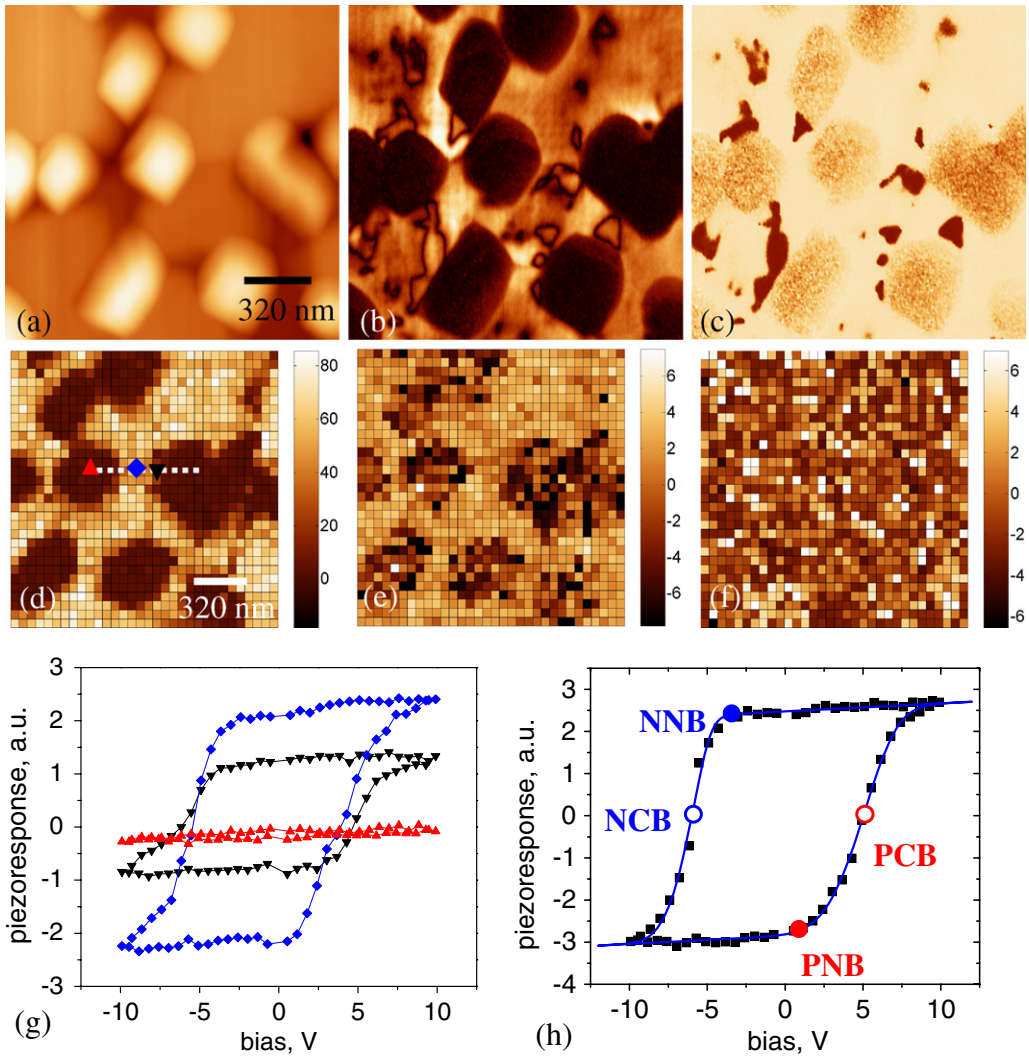

Figure 51. SS-PFM of multiferroic BFO–CFO nanostructures. (*a*) Topography, PFM (*b*) amplitude, and (*c*) phase images. (*d*) SS-PFM map of the work of switching and (*e*), (*f*) maps of the positive and negative nucleation biases, respectively. (*g*) Representative loops from BFO (♦), CFO (▲) and the BFO–CFO hetereostructure interface (▼). (*h*) Loop with coercive and nucleation biases indicated. Reproduced from [104]. Copyright 2007, IOP Publishing.

can be extremely slow, as thus directly accessible by the PFM time spectroscopy measurements.

4.5.1. Single point spectroscopy. Single point time-resolved PFS (TR-PFS) was developed to study local retention and relaxation behavior in ferroelectrics. In TR-PFS, a dc voltage setting pulse is applied to the probe for a duration t_1, and then the bias is turned off for the following duration, t_2 (figure 55(*a*)). The evolution of the electromechanical response during this second stage is measured using an ac voltage. The sequence can be repeated and the results averaged as necessary.

This approach was pioneered by Kholkin for relaxor ferroelectrics [250]. He demonstrated strong variability of relaxation behavior between the $0.9Pb(Mg_{1/3}Nb_{2/3})O_3$–$0.1PbTiO_3$ (PMN–10PT) grains with different orientations. The relaxation process was shown to consist of two stages, the rapid initial decrease in the response and slow (typically stretched exponent) decay of the contrast. Subsequently, this approach was applied for ferroelectric poly(vinylidene fluoride) (PVDF) [137, 370]. Recently TR-PFS has been used to investigate relaxation behavior in PVDF nanomesas [131] and in ferroelectric relaxors [371, 372]. In figure 55(*b*), relaxation curves for PMN–10PT, LNO and mica are shown. The observed dynamics suggest that the contribution of possible instrumental and atmospheric artifacts (e.g. electrocapillary effect) to relaxation is minimal. Relaxation curves for PMN–10PT in bias-on (during the application of 10 V pulse) and bias-off (after bias pulse) states are shown in figure 55(*c*).

An example of single-point relaxation data collected in the time interval from 10 ms to 100 s is shown in figure 55(*d*). The relaxation can be well described by the Kohlrausch–William–Watts (KWW) law, $R = R_0 + R_1 f(t)$, where R_0 and R_1 are the non-relaxing and relaxing polarization components and $f(t) = \exp(-(t/\tau_{KWW})^{\beta})$. The local KWW exponent, $\beta \approx 0.4$, which is much larger than the macroscopic value determined from dielectric spectra ($\beta \approx 0.09$). The fits using power-law and exponential relaxation all failed.

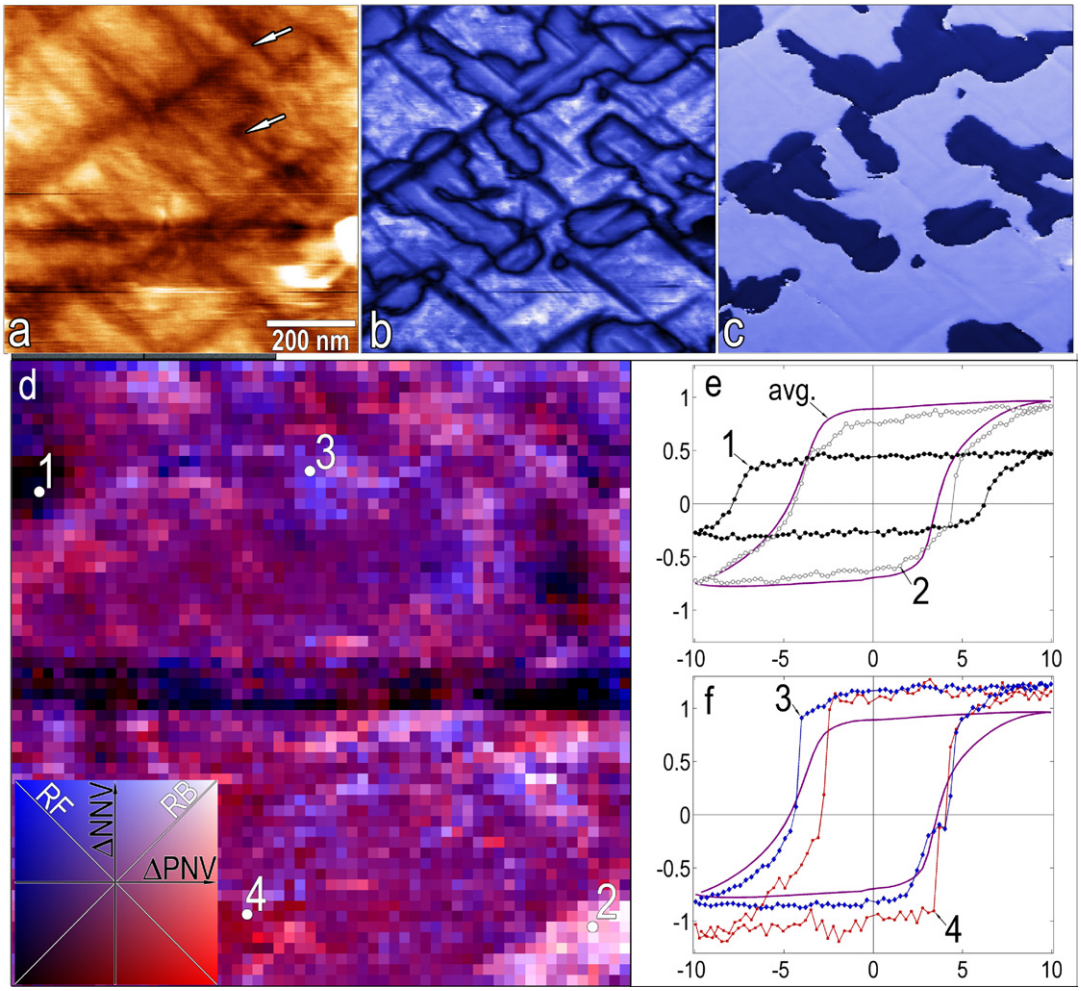

Figure 52. (*a*) Surface topography, (*b*) PFM amplitude and (*c*) PFM phase of an epitaxial PZT film. (*d*) Qualitative random field (RF) and random bond (RB) disorder map. The RF disorder is defined as $(|PNB| - |NNB|)/2$, the RB disorder is defined as $(|PNB| + |NNB|)/2$. Hysteresis loops illustrating the effect of (*e*) RF and (*f*) RB disorder on the loop shape (comp. figure 1). Reproduced from [65]. Copyright 2008, Nature Publishing Group.

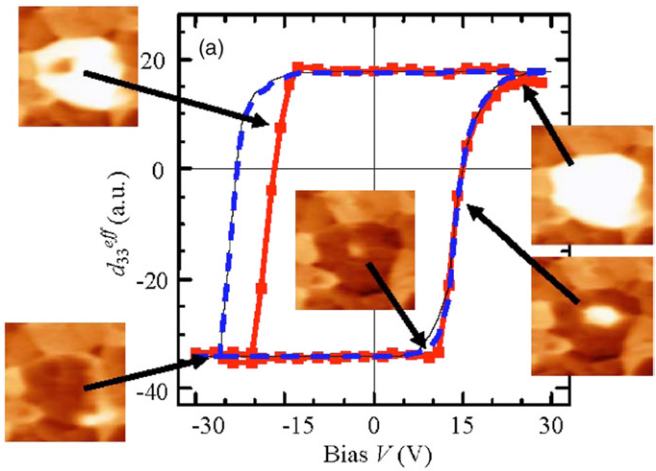

Figure 53. Hysteresis loop with the corresponding domain images. Reproduced from [366]. Copyright 2008, American Institute of Physics.

4.5.2. Spatially resolved time spectroscopy imaging. The single point TR-PFS can be extended to a mapping method to explore spatial variability of relaxation behavior. The measurements are performed on a densely spaced grid of points, yielding the 3D $PR(x, y, t)$ data arrays, where PR is the piezoresponse signal, (x, y) is the coordinate and t is the time. An analysis of the resulting $PR(x, y, t)$ using functional fit $PR(t) = f(\alpha, t)$, where $\alpha = \alpha_1, \ldots, \alpha_n$ is an n-dimensional parameter vector, allows maps of $\alpha_i(x, y)$ describing the spatial variability of relaxation behavior to be constructed. As an example, the fit using the stretched exponential law, $PR(t) = A_0 + A_1 \exp(-(t/\tau)^{\beta})$ with $n = 4$ yields spatially resolved maps of relaxing, A_1, and non-relaxing, A_0, polarization components, relaxation time, τ, and exponent, β (not shown). Alternatively, the fitting can be performed using power law or logarithmic function.

The TR-PFM data were fitted using a logarithmic function and the resulting spatial maps of offset, $B_0(x, y)$, and slope, $B_1(x, y)$, are shown in figures 56(*a*) and (*b*). A number of relaxation curves extracted from regions of dissimilar contrast in figure 56(*a*), (*b*) are shown in figures 56(*c*) and (*d*). Note that relaxation behavior varies between adjacent locations, illustrating the presence of mesoscopic dynamic inhomogeneity on the ergodic relaxor surface. The slope distribution is relatively narrow, $B_1 = -0.10 \pm 0.02$ within the image, and close to Gaussian. In comparison, the distribution of offsets is broader, $B_1 = -1.5 \pm 0.5$, and is strongly

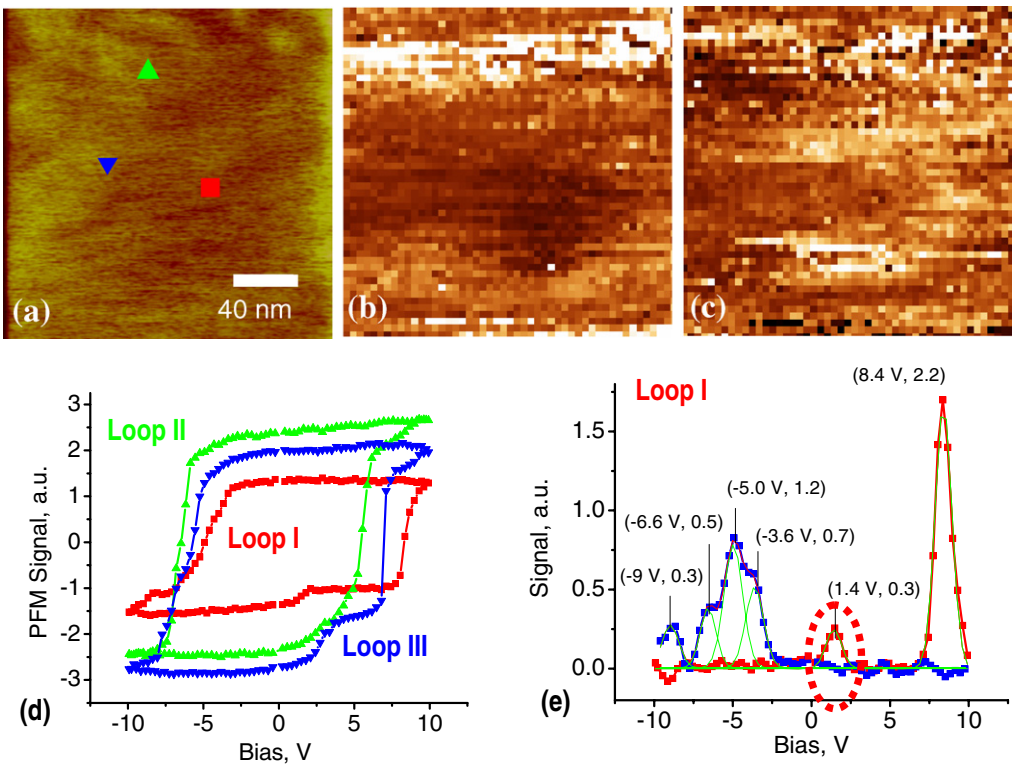

Figure 54. (*a*) Topography, (*b*) 2D map of negative nucleation bias. (*c*) Integral fine structure map for the forward branch of the hysteresis loop. (*d*) Loops from locations marked in (*a*) and (*e*) hysteresis loop fine structure in loop I. Reproduced from [319]. Copyright 2008, American Institute of Physics.

asymmetric. This observation suggests that the amplitude of the pulse-induced polarization varies significantly from point to point, while the kinetics of the observed logarithmic relaxation is more uniform.

4.6. Switching in ferroelectric capacitors

Switching in ferroelectric capacitors was extensively studied by the Gruverman [241, 341], Stolichnov [373–376] and Noh [377] groups in the context of applications to FeRAM. It is well recognized that polarization switching in capacitors is initiated at a relatively small number of defect sizes, and the switching process proceeds though domain wall motion. PFM can be employed to study capacitor switching in the stroboscopic mode, in which domain pattern changes as a function of voltage pulse length and amplitude are measured [93–95, 241, 378] This step-by-step switching [342, 343, 368] approach can be used to measure the domain kinetics (nucleation and growth) during polarization reversal and the results can be compared with experimental macroscopic results and with theory [81, 377, 379–383]. As discussed in section 2.3.3.5, this approach is limited by the resolution of PFM on capacitor structures, which is determined by the structure thickness rather than tip–surface contact area.

Despite this limitation, this approach was extensively used to study imprint and flexoelectric effects in capacitors [241], variability of switching behavior in capacitor structures [341, 378], interplay between nucleation and domain wall motion [368] and nucleation probability distribution in capacitors [377]. Noteworthy is that similar studies can be performed dynamically (using real-time resolution) using focused x-rays [369]. However, since the top electrode covers the surface of the ferroelectric, it is not possible to correlate the surface structure with the nucleation sites, nor is it possible to rule out the influence of the metal–ferroelectric interface roughness.

The second approach for probing polarization dynamics in capacitors is based on SS-PFM, as reported recently [384]. It has been shown that in polycrystalline materials, switching often proceeds through the formation of correlated clusters containing 10^2–10^3 grains, presumably stabilized by elastic interactions active on the length scale of film thickness.

Finally, studies of in-plane capacitor switching using a combination of in-plane electric field and PFM imaging (i.e. capacitor cross-section studies) merit separate discussion. This approach was introduced by Lu *et al* [385] and Gysel *et al* [386] using beveled and cross-sectioned planar capacitors, and further developed by Balke *et al* using specially fabricated structures [387]. These measurements allow the nucleation and lateral wall growth stages to be visualized directly and to establish the relationship between these processes and the field history of the sample. Ultimately, these studies can be performed in the electron microscopy geometry, potentially providing insight into domain nucleation and wall motion mechanisms on the sub-10 nanometer and atomic levels.

5. Phase-field simulations of local ferroelectric switching mechanism

Polarization switching under PFM is a temporal and spatial evolution process driven by a highly inhomogeneous external

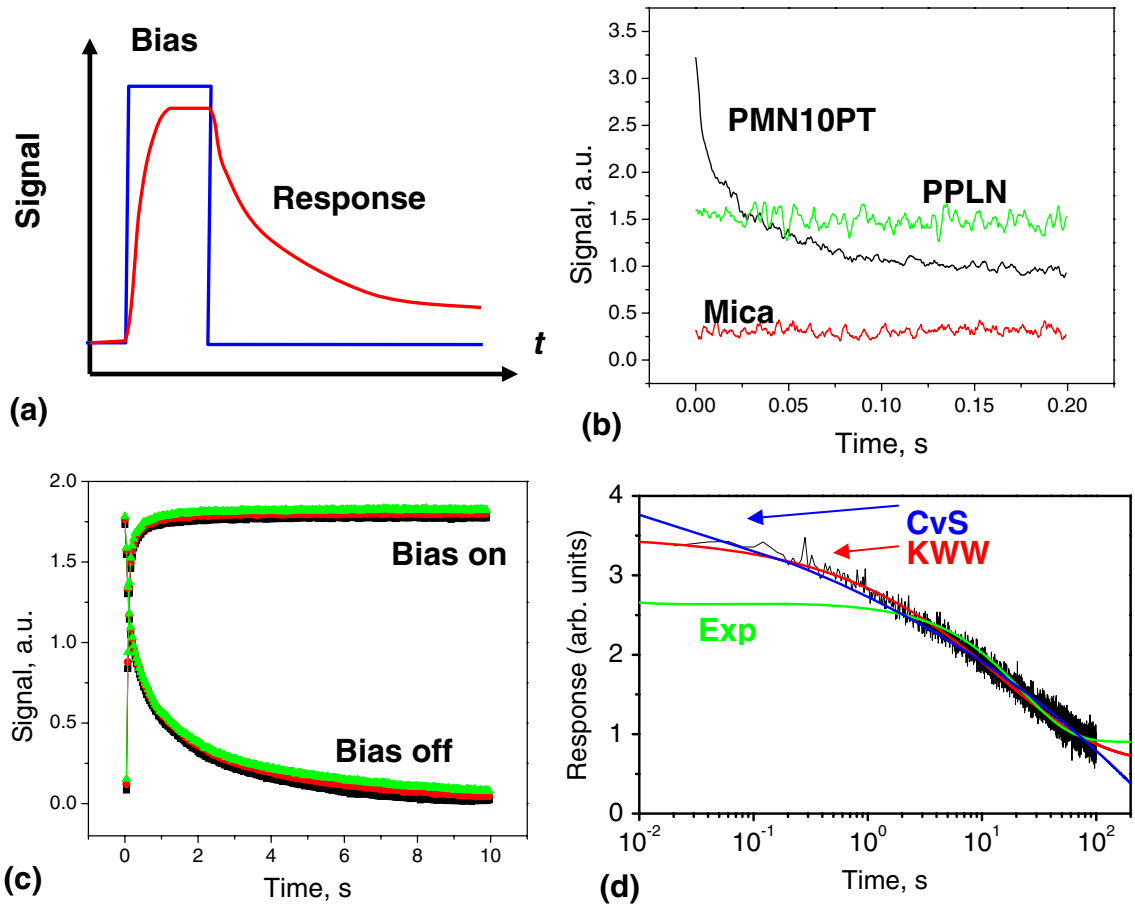

Figure 55. (*a*) Schematic of relaxation measurement. (*b*) Relaxation curves for PMN–10PT, LNO and mica. (*c*) Relaxation curves for PMN–10PT in bias-on (during the application of 10 V pulse) and bias-off (after bias pulse) states. (*d*) Several fits of the experimental relaxation curves. Panels (*a*) and (*d*) reproduced from [372]. Copyright 2009, American Physical Society.

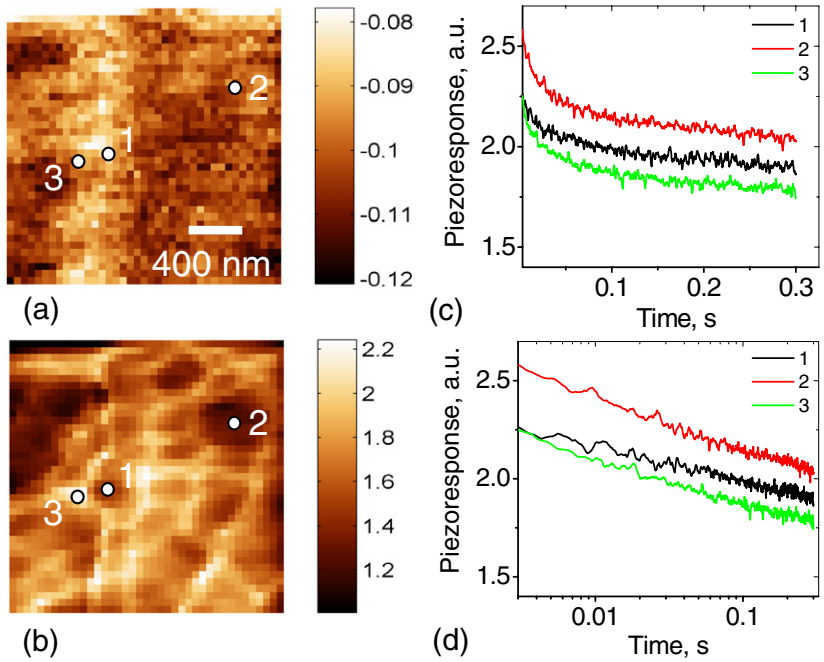

Figure 56. Spatially resolved maps of (*a*) slope and (*b*) offset in the logarithmic relaxation law. Relaxation curves from selected locations in (*c*) linear and (*d*) logarithmic scale. Histograms of (*e*) slope and (*f*) offset. Reproduced from [371]. Copyright 2009, American Institute of Physics.

field. It involves a complex coupling of long-range electromechanical interactions in a highly inhomogeneous and nonequilibrium system. Analytical solutions for the spatial and temporal distributions of polarization, electric field and stress during switching under PFM are generally not possible although semi-analytical solutions for the polarization distributions corresponding to the critical states or stable states have been attempted, as summarized in sections 3 and 4. To better understand the polarization switching mechanisms in PFM, a number of efforts to model the polarization evolution process using the phase-field method [65, 263, 295, 350, 388, 389] have been attempted. One of the main advantages for the phase-field method is the fact that one is able to model the temporal/spatial evolution of arbitrary domain morphologies under an applied electric field without explicitly tracking the positions of domain walls. Secondly, the inhomogeneous electric field and stress field distributions accompanying the polarization switching are readily available. Furthermore, the effect of structural defects such as grain boundaries, surfaces, dislocations and random defects can be incorporated without significantly increasing the computational time. Phase-field models have previously been applied to domain evolution during ferroelectric phase transitions and domain switching, effect of random defects and dislocations, as well as strain effect on transition temperatures and domain structures in thin films [390].

5.1. Phase-field method

During polarization switching the polarization distribution is always inhomogeneous, i.e. it depends on the spatial positions. In the phase-field approach, one employs the spatial distribution of local spontaneous polarization $\boldsymbol{P}(\boldsymbol{x}) = (P_1(\boldsymbol{x}), P_2(\boldsymbol{x}), P_3(\boldsymbol{x}))$ to describe a domain structure. Using the free energy for the unpolarized and unstrained crystal as the reference, the local free energy density as a function of strain and polarization using the Landau–Devonshire theory of ferroelectrics is

$$\begin{aligned} f_{\text{bulk}}(\varepsilon(\boldsymbol{x}), P(\boldsymbol{x})) &= \tfrac{1}{2}\alpha_{ij} P_i(\boldsymbol{x}) P_j(\boldsymbol{x}) \\ &+\tfrac{1}{4}\gamma_{ijkl} P_i(\boldsymbol{x}) P_j(\boldsymbol{x}) P_k(\boldsymbol{x}) P_l(\boldsymbol{x}) \\ &+\tfrac{1}{6}\omega_{ijklmn} P_i(\boldsymbol{x}) P_j(\boldsymbol{x}) P_k(\boldsymbol{x}) P_l(\boldsymbol{x}) P_m(\boldsymbol{x}) P_n(\boldsymbol{x}) + \cdots \\ &\tfrac{1}{2} c_{ijkl}\varepsilon_{ij}(\boldsymbol{x})\varepsilon_{kl}(\boldsymbol{x}) - \tfrac{1}{2} q_{ijkl}\varepsilon_{ij}(\boldsymbol{x}) P_k(\boldsymbol{x}) P_l(\boldsymbol{x}), \end{aligned} \tag{5.1}$$

where α_{ij}, γ_{ijkl} and ω_{ijklmn} are the phenomenological Landau expansion coefficients and c_{ijkl} and q_{ijkl} are the elastic and electrostrictive constant tensors, respectively. All the coefficients are generally assumed to be constant except α_{ij} which is linearly proportional to temperature, i.e. $\alpha_{ij} = \alpha^{\text{o}}_{ij}(T - T_{\text{o}})$, where T_{o} is the Curie temperature.

It should be noted that the coefficients in equation (5.1) correspond to zero strain while experiments are usually conducted at zero stress. In order to use the materials constants and Landau coefficients from stress-free conditions, we rewrite the free energy for zero stress. One first obtains the spontaneous strain, i.e. the strain or crystal deformation at zero stress,

$$\varepsilon^{\text{o}}_{ij}(P_k) = \tfrac{1}{2} s_{ijmn} q_{mnkl} P_k P_l = Q_{ijkl} P_k P_l, \tag{5.2}$$

where Q_{ijkl} are the electrostrictive coefficients measured experimentally. Substituting the spontaneous strain from equation (5.2) for the strain in equation (5.1), we have the free energy at zero stress as

$$\begin{aligned} g_{\text{bulk}}(P(\boldsymbol{x})) &= \tfrac{1}{2}\alpha_{ij} P_i(\boldsymbol{x}) P_j(\boldsymbol{x}) \\ &+\tfrac{1}{4}\gamma'_{ijkl} P_i(\boldsymbol{x}) P_j(\boldsymbol{x}) P_k(\boldsymbol{x}) P_l(\boldsymbol{x}) \\ &+\tfrac{1}{6}\omega_{ijklmn} P_i(\boldsymbol{x}) P_j(\boldsymbol{x}) P_k(\boldsymbol{x}) P_l(\boldsymbol{x}) P_m(\boldsymbol{x}) P_n(\boldsymbol{x}) + \cdots, \end{aligned} \tag{5.3}$$

where the α_{ij} and ω_{ijklmn} remain the same for zero stress as for zero strain, but γ_{ijkl} at constant strain is changed to γ'_{ijkl} at zero stress with

$$\gamma'_{ijkl} = \gamma_{ijkl} - 2c_{mnop} Q_{mnij} Q_{opkl}. \tag{5.4}$$

The free energy at zero strain and that at zero stress are related by

$$f_{\text{bulk}}\left(\varepsilon_{ij}(\boldsymbol{x}), P(\boldsymbol{x})\right) = g_{\text{bulk}}(P(\boldsymbol{x})) + f_{\text{elast}}\left(P_i(\boldsymbol{x}), \varepsilon_{ij}(\boldsymbol{x})\right),$$

where

$$\begin{aligned} f_{\text{elast}}\left(P(\boldsymbol{x}), \varepsilon_{ij}(\boldsymbol{x})\right) &= \tfrac{1}{2} c_{ijkl}\left(\varepsilon_{ij}(\boldsymbol{x}) - \varepsilon^{o}_{ij}(\boldsymbol{x})\right) \\ &\times \left(\varepsilon_{kl}(\boldsymbol{x}) - \varepsilon^{o}_{kl}(\boldsymbol{x})\right). \end{aligned} \tag{5.5}$$

For a domain structure, the electrostatic energy contains contributions from an external applied field E^{ex}, the energy due to inhomogeneous polarization distribution $\delta P_i(\boldsymbol{x}) = P_i(\boldsymbol{x}) - \bar{P}_i$ and the depolarization energy F_{dep} if the crystal is finite and the surface polarization charge is not fully compensated:

$$\begin{aligned} F_{\text{elec}} &= \int_V f_{\text{elec}}(P_i(\boldsymbol{x}), E_i(\boldsymbol{x}))\,\mathrm{d}V = -\int_V P_i(\boldsymbol{x}) E^{\text{ex}}_i(\boldsymbol{x})\mathrm{d}V \\ &-\tfrac{1}{2}\int_V E_i(\boldsymbol{x})\delta P_j(\boldsymbol{x})\mathrm{d}V + F_{\text{dep}}\left(\bar{P}_i\right), \end{aligned} \tag{5.6}$$

where $\bar{P}_i$ is the average polarization and E_i is the ith component of the electric field generated by the heterogeneous polarization distribution $\delta P_{\text{i}}(\boldsymbol{x})$.

The total free energy of an inhomogeneous domain structure is given by Ginzburg–Landau free energy functional:

$$\begin{aligned} F = \int_V [&f_{\text{bulk}}(P_i) + f_{\text{grad}}(\partial P_i/\partial x_j) + f_{\text{elast}}(P_i, \varepsilon_{ij}) \\ &+ f_{\text{elec}}(P_i, E_i)]\mathrm{d}^3x \end{aligned} \tag{5.7}$$

in which f_{bulk} is the bulk free energy density, f_{grad} is the gradient energy that is only nonzero around domain walls and other interfaces where the polarization is inhomogeneous,

$$f_{\text{grad}} = \tfrac{1}{2} G_{ijkl} P_{i,j} P_{k,l}, \tag{5.8}$$

where $P_{i,j} = \partial P_i/\partial x_j$ and G_{ijkl} is the gradient energy coefficient.

To obtain the elastic strain energy density f_{elast} in equation (5.5), one needs to solve the mechanical equilibrium equation for a given domain structure. For a bulk single crystal with periodic boundary conditions, one can use Khachaturyan's elasticity theory [391, 392]. For thin films, the mechanical boundary conditions become more complicated. The top surface is stress-free and the bottom surface is constrained by the substrate. As it has been shown in [393, 394], the solution to the mechanical equilibrium equations for

a film–substrate system can be obtained by combining Khachaturyan's mesoscopic elasticity theory [391, 392] and the Stroh formalism of anisotropic elasticity [395]. In obtaining the elastic energy, the local distributions of mechanical displacements, strain and stress are also readily available for a given domain structure and external boundary conditions.

Similarly, the electrical energy density, f_{elec}, in equation (5.6) can be obtained by solving the electrostatic equation. For the simple case that the depolarization field is compensated and the external field is uniform, we have the electrostatic energy for a single crystal,

$$\int_V f_{\text{elec}} \mathrm{d}^3 V = \frac{1}{2} \int \frac{\left| n_i P_i^{\text{o}}(\boldsymbol{g}) \right|^2}{n_j \kappa_{jk} n_k} \frac{\mathrm{d}^3 g}{(2\pi)^3} - \left(E_i^{\text{ex}} \bar{P}_i \right) V, \quad (5.9)$$

where $P_k^{\text{o}}(\boldsymbol{g}) = \int_V P_k^{\text{o}}(\boldsymbol{x}) \mathrm{e}^{-\mathrm{i}\boldsymbol{g}\cdot\boldsymbol{x}} \mathrm{d}^3 x$, κ_{jk} is the dielectric constant tensor and n_i is the ith component of unit vector, $g_i/|g|$. In equation (5.9), the reciprocal space origin, $\boldsymbol{g} = 0$, is excluded in the integration. Equation (5.9) shows the dependence of electrostatic energy on dielectric constants, the domain structure and the external applied field. For electric boundary conditions that are inhomogeneous at the boundary, e.g. under PFM, the electrostatic equilibrium equation is solved using a specified inhomogeneous boundary condition for the electric potential, ϕ,

$$\phi_{\text{substrate-film interface}} = 0, \phi_{\text{film surface}} = \phi_1(x_1, x_2) \quad (5.10)$$

using the same strategy as the elastic solution for thin films [396].

With all the important energetic contributions to the total free energy, the temporal evolution of the polarization vector field, and thus the domain structure, is then described by the time-dependent Ginzburg–Landau (TDGL) equations,

$$\frac{\partial P_i(\boldsymbol{x}, t)}{\partial t} = -L \frac{\delta F}{\delta P_i(\boldsymbol{x}, t)}, \quad (5.11)$$

where L is the kinetic coefficient related to the domain-wall mobility. For a given initial distribution of polarization, numerical solution to equation (5.11) yields the temporal and spatial evolution of polarization, and thus domain switching under an external field.

5.2. Modeling the electric potential distribution from PFM

To model the domain writing process by PFM, one needs quantitative information on the electric potential or electric field distribution produced by the probe. The actual distribution will depend on the size and shape of the probe, and its accurate determination is difficult and requires finite-element-type of calculations with the knowledge of precise probe geometry. Most existing theories and numerical simulations of ferroelectric domain switching under PFM assumed point-charge-type of electric potential distributions. For example, in phase-field simulations of domain switching under PFM, the tip-induced electric potential distribution on a sample surface is approximated by a two-dimensional Lorentz-like function [350, 388],

$$\phi_1(x_1, x_2) = \phi_0 \left[\frac{\gamma^2}{\left(x_1 - x_1^0\right)^2 + \left(x_2 - x_2^0\right)^2 + \gamma^2} \right], \quad (5.12)$$

where x_1 and x_2 are the coordinates on the surface, (x_1^0, x_2^0) is the location of the tip (the peak of distribution) and γ is the distance from the tip over which the applied electric potential reduces to half of its peak value, ϕ_0.

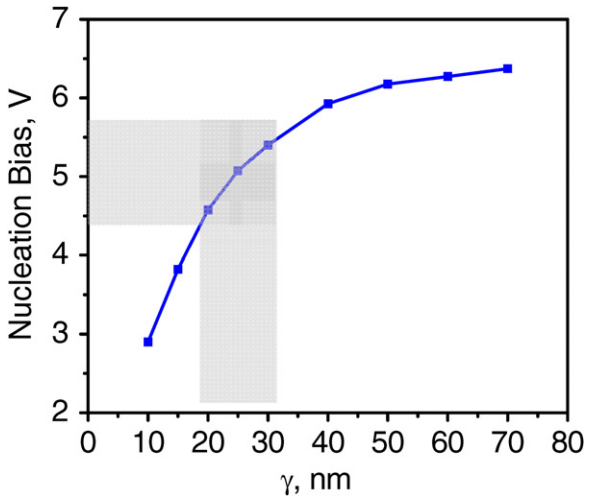

Figure 57. Variation of nucleation voltage as a function of effective tip size.

5.3. Nucleation bias

The nucleation bias is defined as the minimum applied electric potential required to nucleate a new domain under PFM. To determine the nucleation bias of a new domain in a phase-field simulation, one starts with a single crystal single ferroelectric domain state and impose an electric potential distribution according to equation (5.12) as the electric boundary conditions. One then gradually increases the potential value ϕ_0 with small intervals. The minimum potential value at which a new domain appears under PFM is determined as the nucleation bias. However, it should be noted that the nucleation bias is strongly sensitive to the probe geometry, or in our simple potential model, to the parameter γ. As an example, the dependence of nucleation bias on γ was demonstrated using a $BiFeO_3$ epitaxial thin film consisting of a single rhombohedral domain with polarization direction along $[\bar{1}\,\bar{1}\,1]$ [1]. To find the critical nucleation potential, the potential ϕ_0 was slowly increased in increment of 0.05 V. At a sufficiently high value of ϕ_0, a new rhombohedral domain with polarization along $[\bar{1}\,\bar{1}\,\bar{1}]$ was found to nucleate below the tip, and the corresponding value for ϕ_0 was identified as the nucleation potential. The nucleation bias as a function of γ is shown in figure 57. For the ranges of tip parameters consistent with the measured domain wall width, the nucleation bias is $\sim 4.8 \pm 0.5$ V.

Since there are no defects or thermal fluctuations considered in the model, the nucleation bias in a phase-field

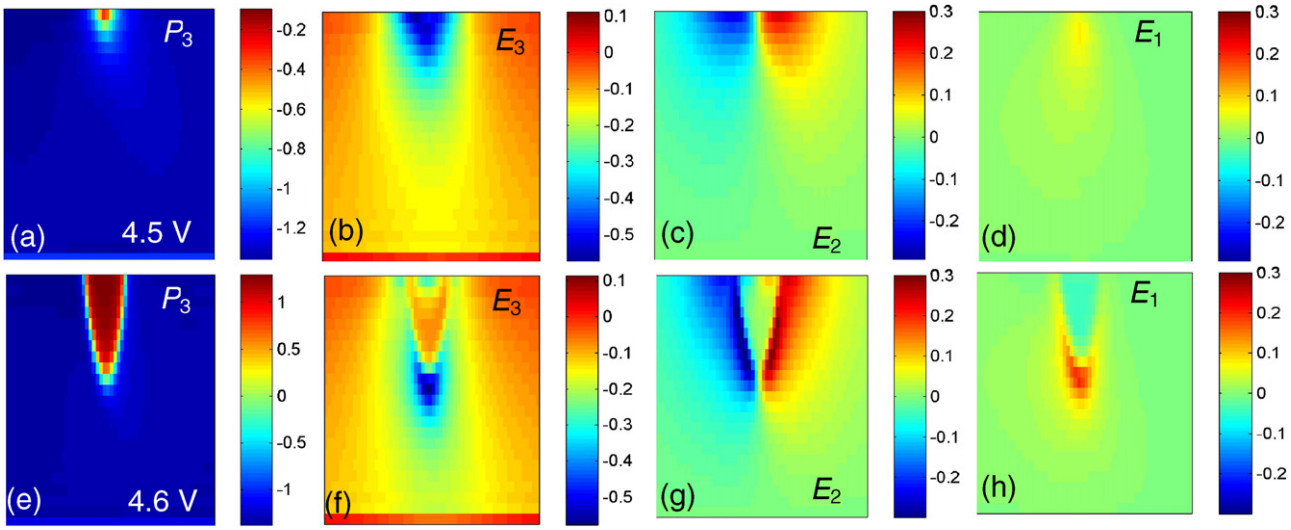

Figure 58. Evolution of polarization and electric field before (*a*)–(*d*) and after (*e*)–(*h*) nucleation. Shown are (*a*),(*e*) vertical polarization component, (*b*), (*f*) vertical electric field, (*c*), (*g*) field in the image plane and (*d*), (*h*) electric field perpendicular to the image plane [345]. Copyright 2009, John Wiley and Sons, Inc.

simulation corresponds to intrinsic thermodynamic switching in the local field produced PFM tip. The fact that the voltage required to nucleate a domain intrinsically within a matrix is on the order of a few volts for tip radius of ∼30 nm indicates that the non-uniform electric field under a PFM tip is sufficient to induce intrinsic polarization switching on an ideal surface even for moderately low tip biases. This is also supported by PFM measurements and phase-field predictions of temperature dependence of nucleation bias which shows a nearly linear dependence of nucleation bias on temperature. The linear temperature dependence of the nucleation bias can also easily be obtained for intrinsic switching using the direct variational method which considers intrinsic (rather than infinitely thin) width of domain wall and variable magnitude of polarization. The small temperature dependence of the nucleation bias arises primarily from the temperature dependence of the dielectric constants and the spontaneous polarization.

5.4. Mesoscopic switching mechanism in a single domain

The domain switching mechanism under PFM can be monitored by the evolution of the polarization distribution and electric fields. An example is shown in figure 58 [345]. Below the nucleation threshold, the applied electric field from a PFM leads to polarization inhomogeneity under the tip without nucleation (figure 58(*a*)). The degree of inhomogeneity increases with the applied PFM electric potential. As expected, based on the equation for the PFM potential, the out-of-plane (normal) component (E3) of the electric field (figure 58(*b*)) is symmetric while the in-plane component (E2) anti-symmetric with both positive and negative values (figure 58(*c*)). Above the nucleation threshold, switching takes place, leading to the reversal of the out-of-plane polarization component, i.e. corresponds to 71° ferroelastic switching for the case of a rhombohedral domain in a (0 0 1) oriented film (figure 58(*e*)). The nucleation of a needle-like domain is consistent with the minimization of the depolarization energy. In the mean time, the out-of-plane component of the electric field displays both positive and negative regions after nucleation (figure 58(*f*)) while the in-plane component E2 (figure 58(*g*)) now has also significant values inside the film. With continuous application of the PFM tip, the domain will eventually penetrate through the film.

5.5. Local ferroelectric switching across a ferroelastic twin wall

Ferroelectric thin films are seldom perfect and often contain various structural defects such as twin walls, dislocations and grain boundaries. Since the electric and stress fields around structural defects in a ferroelectric thin film are inhomogeneous, it is expected that the nucleation bias at or near a structural defect will be different from a single domain state. The role of a single ferroelastic twin boundary in the magnitude of nucleation bias has been studied using a specific example of tetragonal $PbZr_{0.2}Ti_{0.8}O_3$ ferroelectric thin film [388]. For a thin film attached to a substrate, the stable domain state depends on the strain imposed by a substrate. In this example, we introduced a symmetric, compressive biaxial strain of 0.3%, i.e. $\varepsilon^s_{11} = \varepsilon^s_{22} = -0.003$. Under such a condition, the stable domain structure is a *c*/*a* domain mixture where *c* and *a* represent domains with out-of-plane and in-plane polarization directions, respectively. Figure 59 shows an *a*-domain (in red color) with polarization direction along the [0 1 0] direction embedded in a *c*-domain matrix (light green) with polarization direction along the [0 0 $\bar{1}$] direction. The PFM tip parameter, γ, is chosen to be 30 nm. As in the case of determining the intrinsic nucleation bias, the potential ϕ_0 was increased gradually in steps of 0.025 V. The applied electric potential at which a tetragonal domain with polarization along [0 0 1] nucleated below or near the tip was identified as the nucleation potential. The nucleation bias was determined along the line marked by A–M–N–B across two ferroelastic twin boundaries, where each dot shows the location of the PFM tip. Figure 59(*c*) plots the variation of the nucleation voltage with position along the line A–M–N–B. The value indicated by each square symbol

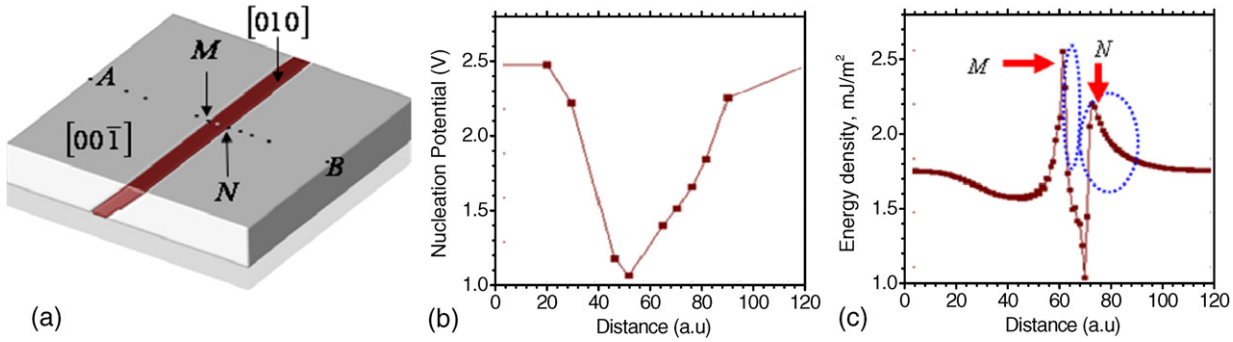

Figure 59. (*a*) Domain structure of epitaxial $PbZr_{0.2}Ti_{0.8}O_3$ thin film with a pre-existing a_2-positive domain (polarization along [0 1 0]) within a matrix of *c*-negative domain (polarization along [0 0 −1] under short-circuit boundary condition. The dots show the locations of the PFM tip along the profile A–M–N–B; (*b*) spatial distribution of nucleation potential at selected locations; (*c*) distribution of electrostatic energy density (MJ m^{-3}) without applied potential [388]. Copyright 2008, American Institute of Physics.

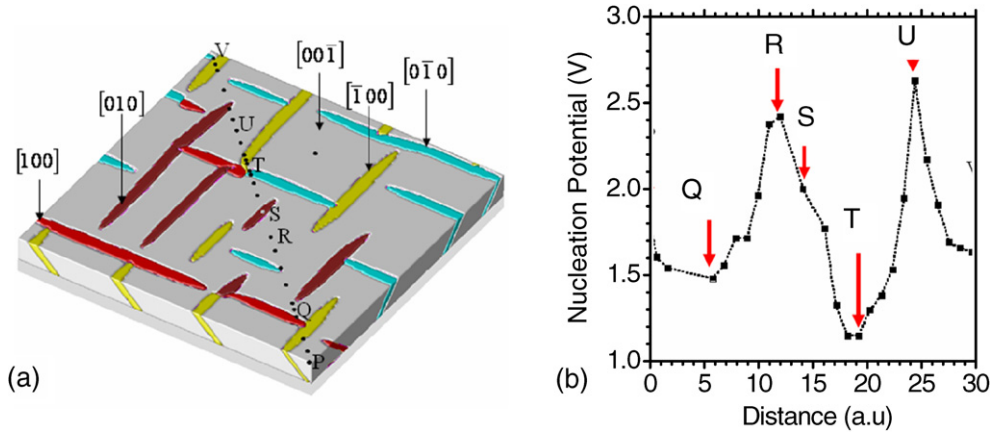

Figure 60. (*a*) Domain structure of an (0 0 1)-oriented epitaxial $PbZr_{0.2}Ti_{0.8}O_3$ thin film; (*b*) spatial distribution of the nucleation potential along the profile P–Q–R–S–T–U–V [388]. Copyright 2008, American Institute of Physics.

represents the nucleation potential corresponding to a dot in figure 59(*a*). It is shown that the potential required to nucleate a 180° domain is lower near the ferroelastic twin defects (∼1.6 V) as compared with ∼2.6 V away from the twin defect within the matrix. It is also found that the two parallel twin walls are not equivalent. The potential required to nucleate a 180° domain is lower near the left twin boundary compared with the right one.

The origins of the asymmetric variation of the nucleation voltage near the two twin walls can be easily understood by analyzing the electrostatic energy density on the surface of the thin film without any applied electric potential (figure 59(*c*)). The observation that the locations of the lowest nucleation voltage (figure 59(*b*)) do not coincide with the locations of the twin walls (point M or N in figure 59(*c*)) in the initial domain structure in figure 59(*a*) can be attributed to the in-plane electric field of PFM which slightly displaces the wall positions. Finally, the small *a*-domain size (∼10 nm) was not resolved since the tip parameter γ was 30 nm, and hence only a single large asymmetric dip in the nucleation voltage near the *a*-domain is observed.

5.6. Nucleation potential distribution in a domain structure

As shown above that the nucleation potential is different near ferroelastic twin walls and within a homogeneous domain matrix, it is expected that the nucleation potential is inhomogeneous within a domain structure. As an example, the spatial distribution of nucleation voltage was probed in a more realistic domain structure of PZT epitaxial thin film (figure 60(*a*)) using phase-field simulations [388]. The domain structure is generated under a short-circuit boundary condition starting from an initial paraelectric state with small random perturbations. Each of the colors represents a tetragonal variant. The domain structure consists of a_1 and a_2 domains embedded in a *c*-domain matrix. To understand the correlation between the spatial variation of nucleation voltage and with the locations of ferroelectric twin walls and wall junctions, the PFM tip position was moved along the line P–Q–R–S–T–U–V in figure 60(*a*). The nucleation voltage as a function of position is recorded in figure 60(*b*). It is observed that the nucleation potential is correlated with the number of local twin domain variants. For example, the nucleation voltage is highest within the *c*-domain matrix (points R and U) followed by a single twin wall (point S), and then by the area where a_1 and a_2 intersect (point Q). The lowest nucleation potential is observed near the triple junctions (point T) where three domains meet.

Remarkably, these examples illustrate that the combination of the phase-field modeling and piezoresponse force microscopy and spectroscopy studies effectively allow us to study polarization dynamics at the level of a single mesoscopic

defect and decipher associated mechanisms. This provides a crucial missing step between the macroscopic statistical theories, and atomistic-scale electron microscopy and density functional studies of phase transitions in solids. Given the ubiquity of electromechanical phenomena in solids, including energy storage materials (e.g. Li-ion batteries), Jahn–Teller solids, etc this combined approach can be expected to be applicable well beyond the ferroelectric and multiferroic materials studied to date.

6. Advanced topics in PFM of ferroelectrics

6.1. Polarization mediated surface chemistry

The surface of ferroelectric (and other polar) materials is characterized by the presence of bound polarization charge, screening charge and band bending, which may be used to enable a broad range of applications including 2DEG-based devices, molecular assembly, adsorption, chemical reactions, etc. Domain decoration of ferroelectric surfaces was first demonstrated in the 1950s and 1960s [397–399]. Domain-specific surface chemistry has been demonstrated by friction force microscopy, and continues to be a topic of interest today. The combination of PFM-based domain patterning and domain specific chemical reactivity opens a natural pathway for the fabrication of ferroelectric based device structures.

Notably, photochemical deposition has been demonstrated by Giocondi *et al* [45, 400], Jones *et al* [401–403], Dunn *et al* [48, 404] and Liu *et al* [405] and has been used to fabricate nanowires [50, 51] and complex nanostructures [46, 49]. Recently, adsorption of charged polystyrene [406] and the assembly of virus particles [407] and DNA [408] have all been demonstrated.

6.2. PFM in a liquid environment

6.2.1. Imaging in a liquid environment. Two of the most detrimental effects on resolution in PFM arise from capillary forces due to the presence of a water layer on the surface and non-local electrostatic interactions between the sample and the conductive tip and cantilever beam. The surface water layer leads to the presence of liquid necks when the AFM tip contacts the sample surface, increasing the effective tip–sample contact area and thus reducing the resolution (see section 3.2.5). Non-local electrostatic forces can lead to long-range tip–sample interactions that can preclude high resolution studies of the local piezoelectric response [409]. By imaging electromechanical response in a liquid environment, i.e. by controlling the dielectric constant of the imaging media, it would be possible to eliminate both the capillary and the long-range electrostatic forces. Liquid PFM was demonstrated in 2006 and showed an order of magnitude improvement in resolution for a bulk ceramic PZT sample [410]. The ability to image electromechanical coupling in a liquid environment may open the door to studies of soft and biological piezoelectrically active materials, the potential for which has been suggested and the challenges outlined [111, 411]. Recently, PFM has been demonstrated in a tapping or intermittent contact mode in liquid, which may assist in the imaging of electromechanical coupling in biological systems [412].

6.2.2. Polarization switching in solution. As previously mentioned, one limitation of imaging through a top electrode is that the domain structure and nucleation sites cannot be related to surface topography without removing the top electrode. Using a tip as a top electrode allows the domain dynamics to be studied locally. In ambient, an applied dc voltage of sufficient magnitude will result in the nucleation of a domain directly under the tip. In de-ionized water, however, the application of a dc voltage will result in electrochemical reactions. Switching in solvents of low to intermediate conductivity combined with liquid PFM allows the spatial extent of the applied field to be controlled independently of the local piezoresponse measurement [413]. Through the choice of solvent, it has been shown that it is possible to nucleate a single domain, switch an entire sample surface and even partially switch a large region (figure 61), much like the step-by-step switching studies described earlier (section 4.5). This allows an additional tool for nucleation site visualization. Future progress in this area requires specially fabricated shielded probes (figure 62) [414, 415] similar to those produced for scanning electrochemical microscopy [416, 417].

6.3. PFM and transport measurements

The interest in combined PFM–conductivity measurements stems both from the non-volatile memory applications and potential for electroresitive memory devices. The early work of Gruverman *et al* explored the relationship between domain dynamics and conductivity at interfaces in thin films [418]. The combination of local electromechanical and conductivity measurements has shown a relation between current and pinning [261] at the bicrystal grain boundary in BFO. These studies have addressed the intrinsic conductivity mediated by the structural defects only weakly affected by polarization.

Following early work on ferroelectric diodes, much attention has been devoted to electroresistances in ferroelectric heterostructures. An extensive review of this area has recently been provided by Watanabe [419]. The work by Rodriguez Contreras [420] has sparked an extensive search for theoretical mechanisms [42, 421] and experimental demonstrations of electroresistance in conductor–ferroelectric–conductor junctions. However, in many cases, the presence of extended defects and oxygen vacancy accumulation has precluded identification of polarization mediated transport mechanisms. The use of the PFM approach allowed localization of field within small defect free regions, allowing the direct unambiguous probing of polarization-controlled tunneling into ferroelectric surface [308, 422]. In parallel, increased conductivity at domain walls in bismuth ferrite is due to structurally driven changes in the local potential and bandgap at a domain wall [267]. This increased conductivity likely plays a role in the observed relaxation of ferroelastically

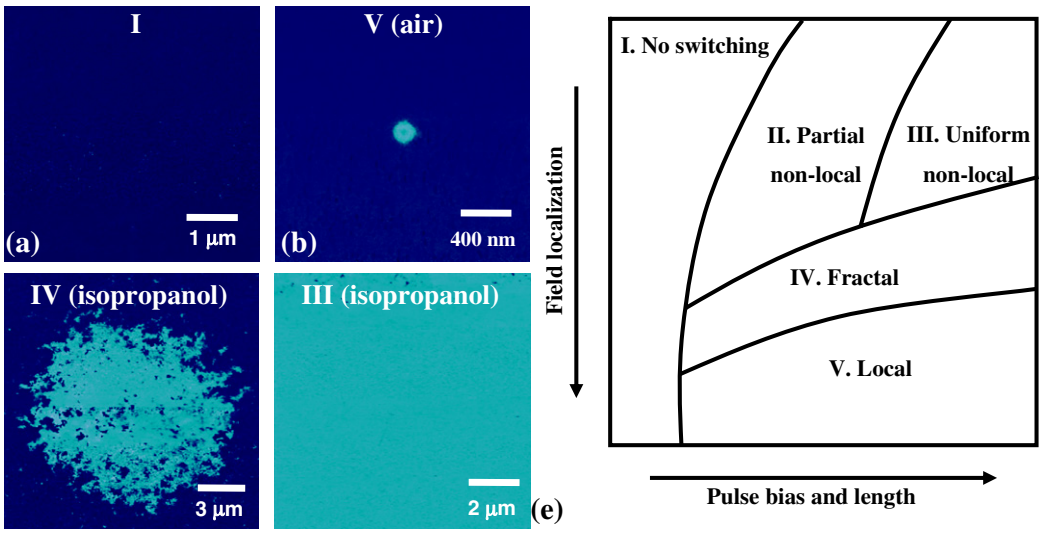

Figure 61. (*a*)–(*d*) PFM phase images illustrating domain morphology in regions I–V and the choice of solvent for the phase map in (*e*). (*e*) Schematic parameter diagram of possible switching modes versus field localization and pulse parameters. Reproduced from [413]. Copyright 2007, American Physical Society.

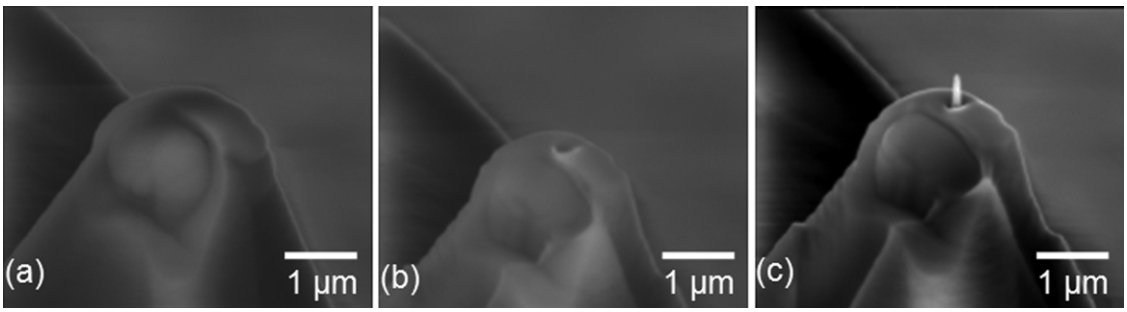

Figure 62. Fabrication steps for insulated PFM probe for imaging in liquid environment. Reproduced from [414]. Copyright 2007, American Institute of Physics.

switched regions [269] and may be of concern to bismuth ferrite capacitor based applications.

7. Summary

Strong coupling between order parameters and electromechanical response in ferroelectric materials enables a local probe approach for studying the static domain structures and polarization dynamics. The unique image formation mechanism of PFM and its spectroscopic and dynamic modes have rendered them a quantitative and powerful method for probing ferroelectrics on the nanometer level, and have opened new venues in understanding the role of defects on switching, polarization ordering in relaxors and many other applications. The future will undoubtedly see atomic level studies on an engineered defect structure (including imaging in vacuum and in liquid), perhaps on a single unit cell level. A new generation of dynamic PFM modes is emerging to allow high energy resolution spectroscopy and of weakly piezoelectric materials. The combination of PFM and EM methods offers the opportunity for imaging atomic rearrangements during polarization switching *in situ*. These developments will lead to new advancements in areas such as information technologies, data storage, energy technologies, electrophysiology, as well as new serendipitous areas we can only imagine.

Acknowledgments

This work was sponsored by the Center for Nanophase Materials Sciences, Oak Ridge National Laboratory, managed and operated by UT-Battelle, LLC for the Office of Basic Energy Sciences, US Department of Energy (SVK, BJR) and by the DOE under the grant number DOE DE-FG02-07ER46417 (LQC). BJR also acknowledges the support of UCD Research. The authors are grateful to E A Eliseev and S Choudhury for their contributions to this work and to the numerous authors who provided permission to reproduce their work here. SVK gratefully acknowledges the collaboration with Stephen Jesse, Nina Balke, Maxim Nikiforov, Katyayani Seal, Peter Maksymovych and Alexander Tselev, as well as Roger Proksch (Asylum Research). He is also grateful to numerous CNMS users and attendees of the PFM workshop series, discussions with whom have contributed immensely to the writing of this paper.

References

[1] von Hippel A, Breckenridge R G, Chesley F G and Tisza L 1946 *J. Ind. Eng. Chem.* **38** 1097
[2] Wul B M 1946 *J. Phys. USSR* **10** 95
Wul B M 1946 *Nature* **157** 808

Wul B and Goldman J M 1946 *C. R. Acad. Sci. URSS* **51** 21
[3] Lines M E and Glass A M 1977 *Principles and Applications of Ferroelectric and Related Materials* (Oxford: Clarendon Press)
[4] Jona F and Shirane G 1962 *Ferroelectric Crystals* (New York: Macmillan)
[5] Fatuzzo E and Merz W J 1967 *Ferroelectricity* (Amsterdam: North-Holland)
[6] Burfoot J C 1967 *Ferroelectrics* (London: Van Nostrand-Reinhold)
[7] Haertling G H 1999 *J. Am. Ceram. Soc.* **82** 797
[8] Cady W G 1946 *Piezoelectricity: An Introduction to the Theory and Applications of Electromechanical Phenomena in Crystals* (New York: McGraw-Hill)
[9] Trolier-Mckinstry S and Muralt P 2004 *J. Electroceram.* **12** 7
[10] Polla D L and Francis L F 1998 *Annu. Rev. Mater. Sci.* **28** 563
[11] Muralt P 1997 *Integr. Ferroelectr.* **17** 297
[12] Muralt P 2000 *J. Micromech. Microeng.* **10** 136
[13] Waser R (ed) 2005 *Nanoelectronics and Information Technology: Advanced Electronic Materials and Novel Devices* (Berlin: Wiley-VCH)
[14] Muralt P 2001 *Rep. Prog. Phys.* **64** 1339
[15] Haertling G H 1987 *Ferroelectrics* **75** 25
[16] Furukawa Y, Kitamura K, Takekawa S, Niwa K and Hatano H 1998 *Opt. Lett.* **23** 1892
[17] Kim S and Gopalan V 2001 *Appl. Phys. Lett.* **78** 3015
[18] Dayal K and Bhattacharya K 2007 *J. Appl. Phys.* **102** 064102
[19] Esaki L, Laibowitz R B and Stiles P J 1971 *IBM Tech. Discl. Bull.* **13** 2161
Chang L L and Esaki L 1971 *IBM Tech. Discl. Bull.* **14** 1250
[20] Ross I M 1957 *US Patent* No 2,791,760
[21] Wolf R, Blom P W M and Krijn M P C 1996 *US Patent* No 5,541,422
[22] Xu Y 1991 *Ferroelectric Materials and Their Applications* (Amsterdam: North-Holland)
[23] Setter N *et al* 2006 *J. Appl. Phys.* **100** 051606
[24] Ahn C H, Triscone J-M and Mannhart J 2003 *Nature* **424** 1015
[25] Ahn C H, Rabe K M and Triscone J-M 2004 *Science* **303** 488
[26] Ahn C H *et al* 2006 *Rev. Mod. Phys.* **78** 1185
[27] Ramesh R and Schlom D G 2008 *MRS Bull.* **33** 1006
[28] Ramesh R, Aggarwal S and Auciello O 2001 *Mater. Sci. Eng.* R **32** 191
[29] Scott J F 2007 *Science* **315** 954
[30] Schlom D G, Chen L Q, Eom C B, Rabe K M, Streiffer S K and Triscone J-M 2007 *Annu. Rev. Mater. Res.* **37** 589
[31] Schlom D G, Chen L-Q, Pan X, Schmehl A and Zurbuchen M A 2008 *J. Am. Ceram. Soc.* **91** 2429
[32] Wang J *et al* 2003 *Science* **299** 1719
[33] Ederer C and Spaldin N A 2004 *Nature Mater.* **3** 849
[34] Lottermoser L, Lonkai T, Amann U, Hohlwein D, Ihringer J and Fiebig M 2004 *Nature* **430** 541
[35] Fiebig M 2005 *J. Phys. D: Appl. Phys.* **38** R123
[36] Kimura T, Goto T, Shintani H, Ishizaka K, Arima T and Tokura Y 2003 *Nature* **426** 55
[37] Hur N, Park S, Sharma P A, Ahn J S, Guha S and Cheong S-W 2004 *Nature* **429** 392
[38] Ramesh R and Spaldin N A 2007 *Nature Mater.* **6** 21
[39] Cheong S-W and Mostovoy M 2007 *Nature Mater.* **6** 13
[40] Eerenstein W, Mathur N D and Scott J F 2006 *Nature* **442** 759
[41] Fiebig M 2005 *J. Phys. D: Appl. Phys.* **38** R123
[42] Tsymbal E Y and Kohlstedt H 2006 *Science* **313** 181
[43] Watanabe Y, Bednorz J G, Bietsch A, Gerber Ch, Widmer D, Beck A and Wind S J 2001 *Appl. Phys. Lett.* **78** 3738
[44] Szot K, Speier W, Bihlmayer G and Waser R 2006 *Nature Mater.* **5** 312
[45] Giocondi J L and Rohrer G S 2001 *Chem. Mater.* **13** 241
[46] Kalinin S V, Bonnell D A, Alvarez T, Lei X, Hu Z and Ferris J H 2002 *Nano Lett.* **2** 589
[47] Li D, Zhao M H, Garra J, Kolpak A M, Rappe A M, Bonnell D A and Vohs J M 2008 *Nature Mater.* **7** 473
[48] Dunn S, Sharp S and Burgess S 2009 *Nanotechnology* **20** 115604
[49] Kalinin S V, Bonnell D A, Alvarez T, Lei X, Hu Z, Shao R and Ferris J H 2004 *Adv. Mater.* **16** 795
[50] Hanson J N, Rodriguez B J, Nemanich R J and Gruverman A 2006 *Nanotechnology* **17** 4946
[51] Haussmann A, Milde P, Erler C and Eng L M 2009 *Nano Lett.* **9** 763
[52] Cho Y, Hashimoto S, Odagawa N, Tanaka K and Hiranaga Y 2006 *Nanotechnology* **17** S137
[53] Scott J F 2000 *Ferroelectric Memories* (Berlin: Springer)
[54] Hong S and Park N 2007 *Resistive Probe Storage: Read/Write Mechanism. In Scanning Probe Microscopy: Electrical and Electromechanical Phenomena on the Nanoscale* ed S V Kalinin and A Gruverman (New York: Springer)
[55] Yadlovker D and Berger S 2005 *Phys. Rev.* B **71** 184112
[56] Geneste G, Bousquet E, Junquera J and Ghosez P 2006 *Appl. Phys. Lett.* **88** 112906
[57] Luo Y, Szafraniak I, Zakharov N D, Nagarajan V, Steinhart M, Wehrspohn R B, Wendroff J H, Ramesh R and Alexe M 2003 *Appl. Phys. Lett.* **83** 440
[58] Morrison F D, Ramsay L and Scott J F 2003 *J. Phys.: Condens. Matter* **15** L527
[59] Wang C L and Smith S R P 1995 *J. Phys.: Condens. Matter* **7** 7163
[60] Morozovska A N, Eliseev E A and Glinchuk M D 2006 *Phys. Rev.* B **73** 214106
[61] Morozovska A N, Glinchuk M D and Eliseev E A 2007 *Phys. Rev.* B **76** 014102
[62] Eliseev E A and Morozovska A N 2009 *J. Mater. Sci.* **44** 5149
[63] Glinchuk M D, Eliseev E A and Morozovska A N 2008 *Phys. Rev.* B **78** 134107
[64] Tybell T, Paruch P, Giamarchi T and Triscone J-M 2002 *Phys. Rev. Lett.* **89** 097601
[65] Jesse S *et al* 2008 *Nature Mater.* **7** 209
[66] Scott J F 2006 *J. Phys.: Condens. Matter* **18** R361
[67] Dawber M, Rabe K M and Scott J F 2005 *Rev. Mod. Phys.* **77** 1083
[68] Rabe K, Ahn C H and Triscone J-M (ed) 2007 *Physics of Ferroelectrics: A Modern Perspective, Topics in Applied Physics* vol 105 (Berlin: Springer)
[69] Ginzburg V L, Gorbatsevich A A, Kopayev Y V and Volkov B A 1984 *Solid State Commun.* **50** 339
[70] Gorbatsevich A A and Kopayev Y V 1994 *Ferroelectrics* **161** 321
[71] Naumov I I, Bellaiche L and Fu H X 2004 *Nature* **432** 737
[72] Naumov I and Bratkovsky A M 2008 *Phys. Rev. Lett.* **101** 107601
[73] Ponomareva I, Naumov I I, Kornev I, Fu H and Bellaiche L 2005 *Phys. Rev.* B **72** 140102
[74] Wang J, Kamlah M, Zhang T-Y, Li Y and Chen L Q 2008 *Appl. Phys. Lett.* **92** 162905
[75] Prosandeev S, Ponomareva I, Kornev I and Bellaiche L 2008 *Phys. Rev. Lett.* **100** 047201
[76] Prosandeev S, Ponomareva I, Kornev I, Naumov I and Bellaiche L 2006 *Phys. Rev. Lett.* **96** 237601
[77] Gruverman A, Wu D, Fan H-J, Vrejoiu I, Alexe M, Harrison R J and Scott J F 2008 *J. Phys.: Condens. Matter* **20** 342201
[78] Rodriguez B J, Gao X S, Liu L F, Lee W, Naumov I I, Bratkovsky A M, Hesse D and Alexe M 2009 *Nano Lett.* **9** 1127
[79] Landauer R 1957 *J. Appl. Phys.* **28** 227
[80] Molotskii M, Kris R and Rosenman G 2000 *J. Appl. Phys.* **88** 5318

[81] Gerra G, Tagantsev A K and Setter N 2005 *Phys. Rev. Lett.* **94** 107602
[82] Bratkovsky A M and Levanyuk A P 2000 *Phys. Rev. Lett.* **85** 4614
[83] Kay H F and Dunn J W 1962 *Phil. Mag.* **7** 2027
[84] Dawber M, Chandra P, Littlewood P B and Scott J F 2003 *J. Phys. C: Solid State Phys.* **15** L393
[85] Merz W J 1954 *Phys. Rev.* **95** 690
[86] Miller R C and Weinreich G 1960 *Phys. Rev.* **117** 1460
[87] Burtsev E V and Chervonobrodov S P 1982 *Ferroelectrics* **45** 97
[88] Shin Y-H, Grinberg I, Chen I-W and Rappe A M 2007 *Nature* **449** 881
[89] Natterman T, Shapir Y and Vilfan I 1990 *Phys. Rev.* B **42** 8577
[90] Kolton A B, Rosso A, Albano E V and Giamarchi T 2006 *Phys. Rev.* B **74** 140201
[91] Kleemann W 2007 *Annu. Rev. Mater. Res.* **37** 415
[92] Sidorkin A S 2006 *Domain Structure in Ferroelectrics and Related Materials* (Cambridge: Cambridge International Science)
[93] Avrami M 1939 *J. Chem. Phys.* **7** 1003
[94] Kolmogorov A N 1937 *Izv. Akad. Nauk USSR; Ser. Math.* **3** 355
[95] Ishibashi Y and Takagi Y 1971 *J. Phys. Soc. Japan* **31** 506
[96] Ishibashi Y 1986 *Japan. J. Appl. Phys.* **24** 126
[97] Scott J F, Kammerdiner L, Parris M, Traynor S, Ottenbacher V, Shawabkeh A and Oliver W F 1988 *J. Appl. Phys.* **64** 787
[98] Shur V Ya, Rumyantsev E L, Nikolaeva E V and Shishkin E I 2003 *Integr. Ferroelectr.* **59** 1493
[99] Dawber M, Gruverman A and Scott J F 2006 *J. Phys.: Condens. Matter* **18** L71
[100] Fridkin V M 1980 *Ferroelectric Semiconductors* (New York: Consultants Bureau)
[101] Smolenskii G A 1984 *Ferroelectrics and Related Materials* (Amsterdam: Gordon and Breach)
[102] http://www.asylumresearch.com/Gallery/Cypher/Cypher9.shtml
[103] Shvartsman V V and Kholkin A L 2007 *J. Appl. Phys.* **101** 064108
[104] Rodriguez B J, Jesse S, Baddorf A P, Zhao T, Chu Y H, Ramesh R, Eliseev E A, Morozovska A N and Kalinin S V 2007 *Nanotechnology* **18** 405701
[105] Gruverman A 2004 *Ferroelectric Nanodomains* in *Encyclopedia of Nanoscience and Nanotechnology* vol 3 ed H S Nalwa (Los Angeles: American Scientific Publishers) p 359
[106] Kalinin S V and Gruverman A (ed) 2007 *Scanning Probe Microscopy of Electrical and Electromechanical Phenomena at the Nanoscale* (Berlin: Springer)
[107] Alexe M and Gruverman A (ed) 2004 *Nanoscale Characterization of Ferroelectric Materials* (Heidelberg: Springer)
[108] Hong S (ed) 2004 *Nanoscale Phenomena in Ferroelectric Thin Films* (Dordrecht: Kluwer)
[109] Gruverman A and Kholkin A 2006 *Rep. Prog. Phys.* **69** 2443
[110] Kalinin S V, Rodriguez B J, Jesse S, Karapetian E, Eliseev E A and Morozovska A N 2007 *Annu. Rev. Mater. Res.* **37** 189
[111] Rodriguez B J, Kalinin S V, Jesse S, Thompson G, Vertegel A, Hohlbauch S and Proksch R 2008 *Microsc. Today* **16** 28
[112] Binnig G, Quate C F and Gerber C 1986 *Phys. Rev. Lett.* **56** 930
[113] Binnig G, Rohrer H, Gerber C and Weibel E 1982 *Appl. Phys. Lett.* **40** 178
[114] Gerber C and Lang H P 2006 *Nature Nanotechnol.* **1** 3
[115] Günther P, Glatz-Reichenbach J and Dransfeld K 1991 *J. Appl. Phys.* **69** 7895
[116] Birk H, Glatz-Reichenbach J, Jie L, Schreck E and Dransfeld K 1991 *J. Vac. Sci. Technol.* B **9** 1162
[117] Güthner P and Dransfeld K 1992 *Appl. Phys. Lett.* **61** 1137
[118] Luthi R, Haefke H, Grütter P, Güntherodt H-J, Szcześniak L and Meyer K P 1993 *Surf. Sci.* **285** L498
[119] Bae M K, Horiuchi T, Hara K, Ishibashi Y and Matsushige K 1994 *Japan. J. Appl. Phys., Part 1* **33** 1390
[120] Takata K, Kushida K, Torii K and Miki H 1994 *Japan. J. Appl. Phys., Part 1* **33** 3193
[121] Takata K 1996 *J. Vac. Sci. Technol.* B **14** 882
[122] Franke K, Besold J, Haessler W and Seegebarth C 1994 *Surf. Sci. Lett.* **302** L283
[123] Kolosov O, Gruverman A, Hatano J, Takahashi K and Tokumoto H 1995 *Phys. Rev. Lett.* **74** 4309
[124] Gruverman A, Kolosov O, Hatano J, Takahashi K and Tokumoto H 1995 *J. Vac. Sci. Technol.* B **13** 1095
[125] Gruverman A, Auciello O and Tokumoto H 1996 *Appl. Phys. Lett.* **69** 3191
[126] Gruverman A, Hatano J and Tokumoto H 1997 *Japan. J. Appl. Phys., Part 1* **36** 2207
[127] Gruverman A, Auciello O, Ramesh R and Tokumoto H 1997 *Nanotechnology* **8** 38
[128] Gruverman A, Auciello O and Tokumoto H 1998 *Annu. Rev. Mater. Sci.* **28** 101
[129] Hidaka T, Maruyama T, Sakai I, Saitoh M, Wills L A, Hiskes R, Dicarolis S A and Amano J 1997 *Integr. Ferroelectr.* **17** 319
[130] Rodriguez B J, Jesse S, Kalinin S V, Kim J, Ducharme S and Fridkin V 2007 *Appl. Phys. Lett.* **90** 122904
[131] Rodriguez B J, Jesse S, Kim J, Ducharme S and Kalinin S V 2008 *Appl. Phys. Lett.* **92** 232903
[132] Matsushige K, Yamada H, Tanaka H, Horiuchi T and Chen X Q 1998 *Nanotechnology* **9** 208
[133] Kimura K, Kobayashi K, Yamada H, Horichi T, Ishida K and Matsushige K 2003 *Appl. Phys. Lett.* **82** 4050
[134] Noda K, Ishida K, Kubono A, Horiuchi T, Yamada H and Matsushige K 2001 *Japan. J. Appl. Phys., Part 1* **40** 4361
[135] Matsushige K and Yamada H 2002 *Ann. New York Acad. Sci.* **960** 1
[136] Gysel R, Stolichnov I, Tagantsev A K, Setter N and Mokrý P 2008 *J. Appl. Phys.* **103** 084120
[137] Gaynutdinov R V, Lysova O A, Tolstikhina A L, Yudin S G, Fridkin V M and Ducharme S 2008 *Appl. Phys. Lett.* **92** 172902
[138] Rodriguez B J, Gruverman A, Kingon A I, Nemanich R J and Ambacher O 2002 *Appl. Phys. Lett.* **80** 4166
[139] Stoica T, Calarco R, Meijers R and Lüth H 2007 *Appl. Surf. Sci.* **253** 4300
[140] Rodriguez B J, Gruverman A, Kingon A I and Nemanich R J 2002 *J. Cryst. Growth* **246** 252
[141] Dalmau R, Schlesser R, Rodriguez B J, Nemanich R J and Sitar Z 2005 *J. Cryst. Growth* **281** 68
[142] Scrymgeour D A, Sounart T L, Simmons N C and Hsu J W P 2007 *J. Appl. Phys.* **101** 014316
[143] Zhao M H, Wang Z L and Mao S X 2004 *Nano Lett.* **4** 587
[144] Fan H J, Werner P and Zacharias M 2006 *Small* **2** 700
[145] Halperin C, Mutchnik S, Agronin A, Molotskii M, Urenski P, Salai M and Rosenman G 2004 *Nano Lett.* **4** 1253
[146] Kalinin S V, Rodriguez B J, Jesse S, Thundat T and Gruverman A 2005 *Appl. Phys. Lett.* **87** 053901
[147] Rodriguez B J, Kalinin S V, Shin J, Jesse S, Grichko V, Thundat T, Baddorf A P and Gruverman A 2006 *J. Struct. Bio.* **153** 151
[148] Kalinin S V, Rodriguez B J, Shin J, Jesse S, Grichko V, Thundat T, Baddorf A P and Gruverman A 2006 *Ultramicroscopy* **106** 334

[149] Habelitz S, Rodriguez B J, Marshall S J, Marshall G W, Kalinin S V and Gruverman A 2007 *J. Dent. Res.* **86** 908
[150] Gruverman A, Wu D, Rodriguez B J, Kalinin S V and Habelitz S 2007 *Biochem. Biophys. Res. Commun.* **352** 142
[151] Minary-Jolandan M and Yu M-F 2009 *Nanotechnology* **20** 085706
[152] Minary-Jolandan M and Yu M-F 2009 *ACS Nano* **3** 1859
[153] Gruverman A, Rodriguez B J and Kalinin S V 2006 *J. Scanning Probe Microsc.* **1** 1
[154] Binetti V R, Schiffman J D, Leaffer O D, Spanier J E and Schauer C L 2009 *Integr. Biol.* **1** 324
[155] Kalinin S V, Rodriguez B J, Kim S-H, Hong S-K, Gruverman A and Eliseev E A 2008 *Appl. Phys. Lett.* **92** 152906
[156] Eng L M, Abplanalp M and Günter P 1998 *Appl. Phys.* A **66** S679
[157] Eng L M, Güntherodt H J, Schneider G A, Köpke U and Muñoz Saldaña J 1999 *Appl. Phys. Lett.* **74** 233
[158] Abplanalp M, Eng L M and Günter P 1998 *Appl. Phys.* A **66** S231
[159] Roelofs A, Böttger U, Waser R, Schlaphof F, Trogisch S and Eng L M 2000 *Appl. Phys. Lett.* **77** 3444
[160] Ganpule C S, Nagarajan V, Hill B K, Roytburd A L, Williams E D, Alpay S P, Roelofs A, Waser R and Eng L M 2002 *J. Appl. Phys.* **91** 1477
[161] Roelofs A, Pertsev N A, Waser R, Schlaphof F, Eng L M, Ganpule C, Nagarajan V and Ramesh R 2002 *Appl. Phys. Lett.* **80** 1424
[162] Rodriguez B J, Gruverman A, Kingon A I, Nemanich R J and Cross J S 2004 *J. Appl. Phys.* **95** 1958
[163] Rodriguez B J, Gruverman A, Kingon A I, Nemanich R J and Cross J S 2005 *Appl. Phys. A: Mater. Sci. Process.* **80** 99
[164] Kalinin S V, Rodriguez B J, Jesse S, Shin J, Baddorf A P, Gupta P, Jain H, Williams D B and Gruverman A 2006 *Microsc. Microanal.* **12** 206
[165] Rodriguez B J, Callahan C, Kalinin S V and Proksch R 2007 *Nanotechnology* **18** 475504
[166] Kos A B and Hurley D C 2008 *Meas. Sci. Technol.* **19** 015504
[167] Nath R, Chu Y-H, Polomoff N A, Ramesh R and Huey B D 2008 *Appl. Phys. Lett.* **93** 072905
[168] Jesse S, Kalinin S V, Proksch R, Baddorf A P and Rodriguez B J 2007 *Nanotechnology* **18** 435503
[169] Harnagea C, Alexe M, Hesse D and Pignolet A 2003 *Appl. Phys. Lett.* **83** 338
[170] Huey B D, Ramanujan C, Bobji M, Blendell J, White G, Szoszkiewicz R and Kulik A 2004 *J. Electroceram.* **13** 287
[171] Meyer E, Hug H J and Bennewitz R 2004 *Scanning Probe Microscopy: The Lab on a Tip* (Berlin: Springer)
[172] Giannakopoulos A E and Suresh S 1999 *Acta Mater.* **47** 2153
[173] Chen W Q and Ding H J 1999 *Acta Mech. Solida Sin.* **12** 114
[174] Karapetian E, Sevostianov I and Kachanov M 2000 *Phil. Mag.* B **80** 331
[175] Kalinin S V, Karapetian E and Kachanov M 2004 *Phys. Rev.* B **70** 184101
[176] Karapetian E, Kachanov M and Kalinin S V 2005 *Phil. Mag.* **85** 1017
[177] Johnson K L 1985 *Contact Mechanics* (Cambridge: Cambridge University Press)
[178] Smythe W R 1950 *Static and Dynamic Electricity* (New York: McGraw-Hill)
[179] Jackson J D 1975 *Classical Electrodynamics* 2nd edn (New York: Wiley)
[180] Ganpule C S, Nagarjan V, Li H, Ogale A S, Steinhauer D E, Aggarwal S, Williams E, Ramesh R and De Wolf P 2000 *Appl. Phys. Lett.* **77** 292
[181] Agronin A, Molotskii M, Rosenwaks Y, Strassburg E, Boag A, Mutchnik S and Rosenman G 2005 *J. Appl. Phys.* **97** 084312
[182] Felten F, Schneider G A, Muñoz Saldaña J and Kalinin S V 2004 *J. Appl. Phys.* **96** 563
[183] Scrymgeour D A and Gopalan V 2005 *Phys. Rev.* B **72** 024103
[184] Kalinin S V, Eliseev E A and Morozovska A N 2006 *Appl. Phys. Lett.* **88** 232904
[185] Eliseev E A, Kalinin S V, Jesse S, Bravina S L and Morozovska A N 2007 *J. Appl. Phys.* **102** 014109
[186] Morozovska A N, Eliseev E A, Bravina S L and Kalinin S V 2007 *Phys. Rev.* B **75** 174109
[187] Lur'e A I 1964 *Three-Dimensional Problems of the Theory of Elasticity* (New York: Interscience Publishers)
[188] Landau L D and Lifshitz E M 1998 *Theory of Elasticity* Theoretical Physics vol 7 (Oxford: Butterworth-Heinemann)
[189] Du X, Belegundu U and Uchino K 1997 *Japan. J. Appl. Phys., Part 1* **36** 5580
[190] Du X, Zheng J, Belegundu U and Uchino K 1998 *Appl. Phys. Lett.* **72** 2421
[191] Du X, Wang Q-M, Belegundu U, Bhalla A and Uchino K 1999 *Mater. Lett.* **40** 109
[192] Kalpat S, Du X, Abothu I R, Akiba A, Goto H and Uchino K 2001 *Japan. J. Appl. Phys., Part 1* **40** 713
[193] Harnagea C, Pignolet A, Alexe M and Hesse D 2001 *Integr. Ferroelectr.* **38** 23
[194] Harnagea C 2001 *PhD Thesis* Martin-Luther-Universität Halle-Wittenburg, Halle, Germany
[195] Newnham R E 2005 *Properties of Materials: Anisotropy, Symmetry, Structure* (New York: Oxford University Press)
[196] Rayleigh L 1896 *Phil. Mag.* S **5** 167
[197] Kalinin S V, Jesse S, Rodriguez B J, Shin J, Baddorf A P, Lee H N, Borisevich A and Pennycook S J 2006 *Nanotechnology* **17** 3400
[198] den Dekker A J 1997 *J. Opt. Soc. Am.* A **14** 547
[199] Bertero M and Boccacci P 1998 *Introduction to Inverse Problems in Imaging* (Bristol: Institute of Physics Publishing)
[200] Strassburg E, Boag A and Rosenwaks Y 2005 *Rev. Sci. Instrum.* **76** 083705
[201] Meyer B and Vanderbilt D 2002 *Phys. Rev.* B **65** 104111
[202] Gull S F and Daniell G J 1978 *Nature* **272** 686
[203] McGibbon A J, Pennycook S J and Jesson D E 1999 *J. Microsc. Oxford* **195** 44
[204] Puetter R C and Yahil A 1999 *Astronomical Data Analysis Software and Systems VIII* (*ASP Conference Series* vol 172) ed D M Mehringer *et al* (San Francisco: ASP) p 307
[205] Nellist P D and Pennycook S J 1998 *J. Microsc. Oxford* **190** 159
[206] Shibata N, Pennycook S J, Gosnell T R, Painter G S, Shelton W A and Becher P F 2004 *Nature* **428** 730
[207] Mesa G, Dobado-Fuentes E and Sáenz J J 1996 *J. Appl. Phys.* **79** 39
[208] Gomez-Monivas S, Froufe-Perez L S, Caamano A J and Sáenz J J 2001 *Appl. Phys. Lett.* **79** 4048
[209] Sacha G M, Sahagún E and Sáenz J J 2007 *J. Appl. Phys.* **101** 024310
[210] Belaidi S, Girard P and Leveque G 1997 *J. Appl. Phys.* **81** 1023
[211] Morozovska A N, Eliseev E A and Kalinin S V 2006 *Appl. Phys. Lett.* **89** 192901
[212] Tian L, Vasudevarao A, Morozovska A N, Eliseev E A, Kalinin S V and Gopalan V 2008 *J. Appl. Phys.* **104** 074110
[213] Jungk T, Hoffmann A and Soergel E 2006 *Appl. Phys. Lett.* **86** 042901

[214] Jungk T, Hoffmann A and Soergel E 2009 *New J. Phys.* **11** 033029
[215] Christman J A, Woolcott R R, Kingon A I and Nemanich R J 1998 *Appl. Phys. Lett.* **73** 3851
[216] Morozovska A N, Svechnikov S V, Eliseev E A and Kalinin S V 2007 *Phys. Rev.* B **76** 054123
[217] Morozovska A N, Eliseev E A and Kalinin S V 2007 *J. Appl. Phys.* **102** 074105
[218] Kalinin S V, Jesse S, Rodriguez B J, Eliseev E A, Gopalan V and Morozovska A N 2007 *Appl. Phys. Lett.* **90** 212905
[219] Ovchinnikov O, Jesse S and Kalinin S V 2009 *Nanotechnology* **20** 255701
[220] Hong S, Colla E L and Kim E 1999 *J. Appl. Phys.* **86** 607
[221] Woo J, Hong S, Setter N, Shin H, Jeon J-U, Pak Y E and No K 2001 *J. Vac. Sci. Technol.* B **19** 818
[222] Paruch P, Giamarchi T, Tybell T and Triscone J-M 2006 *J. Appl. Phys.* **100** 051608
[223] Chen Y C, Lin Q R and Chu Y H 2009 *Appl. Phys. Lett.* **94** 122908
[224] Rosenman G, Urenski P, Agronin A, Rosenwaks Y and Molotskii M 2003 *Appl. Phys. Lett.* **82** 103
[225] Terabe K, Nakamura M, Takekawa S, Kitamura K, Higuchi S, Gotoh Y and Cho Y 2003 *Appl. Phys. Lett.* **82** 433
[226] Rodriguez B J, Nemanich R J, Kingon A, Gruverman A, Kalinin S V, Terabe K, Liu X Y and Kitamura K 2005 *Appl. Phys. Lett.* **86** 012906
[227] Agronin A, Molotskii M, Rosenwaks Y, Rosenman G, Rodriguez B J, Kingon A I and Gruverman A 2006 *J. Appl. Phys.* **99** 104102
[228] Liu X Y, Kitamura K and Terabe K 2006 *Appl. Phys. Lett.* **89** 142906
[229] Kan Y, Lu X, Wu X and Zhu J 2006 *Appl. Phys. Lett.* **89** 262907
[230] Liu X Y, Terabe K and Kitamura K 2007 *Phys. Scr.* **T129** 103
[231] Kan Y, Lu X, Bo H, Huang F, Wu X and Zhu J 2007 *Appl. Phys. Lett.* **91** 132902
[232] Zeng H, Shimamura K, Villora E G, Takekawa S and Kitamura K 2007 *Phys. Scr.* **T129** 108
[233] Pertsev N A, Petraru A, Kohlstedt H, Waser R, Bdikin I K, Kiselev D and Kholkin A L 2008 *Nanotechnology* **19** 375703
[234] Paruch P, Giamarchi T and Triscone J-M 2005 *Phys. Rev. Lett.* **94** 197601
[235] Catalan G, Béa H, Fusil S, Bibes M, Paruch P, Barthélémy A and Scott J F 2008 *Phys. Rev. Lett.* **100** 027602
[236] Tanaka K, Kurihashi Y, Uda T, Daimon Y, Odagawa N, Hirose R, Hiranaga Y and Cho Y 2008 *Japan. J. Appl. Phys.* **47** 3311
[237] Fujimoto K and Cho Y 2003 *Appl. Phys. Lett.* **83** 5265
[238] Cho Y, Fujimoto K, Hiranaga Y, Wagatsuma Y, Onoe A, Terabe K and Kitamura K 2002 *Appl. Phys. Lett.* **81** 4401
[239] ITRS, http://www.itrs.net
[240] Lee J H, Choi M R, Oh Y J and Jo W 2007 *Appl. Phys. Lett.* **91** 072906
[241] Gruverman A, Rodriguez B J, Kingon A I, Nemanich R J, Tagantsev A K, Cross J S, Tsukada M and Horii Y 2003 *Appl. Phys. Lett.* **83** 728
[242] Liu X Y, Kitamura K, Terabe K and Takekawa S 2007 *J. Appl. Phys.* **102** 014101
[243] Li X, Terabe K, Hatano H and Kitamura K 2005 *Japan. J. Appl. Phys.* **44** L1550
[244] Liu X Y, Kitamura K, Terabe K, Zeng H and Yin Q 2007 *Appl. Phys. Lett.* **91** 232913
[245] Kan Y, Bo H, Lu X, Cai W, Liu Y and Zhu J 2008 *Appl. Phys. Lett.* **92** 172910
[246] Oliver W C and Pharr G M 1992 *J. Mater. Res.* **7** 1564
[247] Lovinger A J 1983 *Science* **220** 1115
[248] Bokov A A and Ye Z-G 2006 *J. Mater. Sci.* **41** 31
[249] Kleemann W 2006 *J. Mater. Sci.* **41** 129
[250] Shvartsman V V, Kholkin A L, Tyunina M and Levoska J 2005 *Appl. Phys. Lett.* **86** 222907
[251] Pertsev N A and Zembilgotov A G 1994 *Macromolecules* **27** 6936
[252] Paruch P and Triscone J-M 2006 *Appl. Phys. Lett.* **88** 162907
[253] Agronin A, Rosenwaks Y and Rosenman G 2006 *Appl. Phys. Lett.* **88** 072911
[254] Ganpule C S, Nagarajan V, Ogale S B, Roytburd A L, Williams E D and Ramesh R 2000 *Appl. Phys. Lett.* **77** 3275
[255] Ganpule C S, Roytburd A L, Nagarajan V, Hill B K, Ogale S B, Williams E D, Ramesh R and Scott J F 2002 *Phys. Rev.* B **65** 014101
[256] Vasudevarao A, Morozovska A N, Jesse S, Kalinin S V and Gopalan V, unpublished
[257] McGibbon M M, Browning N D and Chisholm M F 1994 *Science* **266** 102
[258] Chisholm M F and Pennycook S J 2006 *Phil. Mag.* **86** 4699
[259] Browning N D, Buban J P, Moltaji H O, Pennycook S J, Duscher G, Johnson K D, Rodrigues R P and Dravid V P 1999 *Appl. Phys. Lett.* **74** 2638
[260] Kalinin S V *et al* 2009 *Adv. Mater.* **22** 314
[261] Rodriguez B J, Chu Y H, Ramesh R and Kalinin S V 2008 *Appl. Phys. Lett.* **93** 142901
[262] Wu A, Vilarinho P M, Wu D and Gruverman A 2008 *Appl. Phys. Lett.* **93** 262906
[263] Gruverman A, Cross J S and Oates W S 2008 *Appl. Phys. Lett.* **93** 242902
[264] Chen L, Ouyang Q, Ganpule C S, Nagarajan V, Ramesh R and Roytburd A L 2004 *Appl. Phys. Lett.* **84** 254
[265] Xu F, Trolier-McKinstry S, Ren W, Xu B M, Xie Z L and Hemker K J 2001 *J. Appl. Phys.* **89** 1336
[266] Chu Y H *et al* 2008 *Nature Mater.* **7** 478
[267] Yang C-H *et al* 2009 *Nature Mater.* **8** 485
[268] Seidel J *et al* 2009 *Nature Mater.* **8** 229
[269] Cruz M P, Chu Y-H, Zhang J X, Yang P L, Zavaliche F, He Q, Shafer P, Chen L Q and Ramesh R 2007 *Phys. Rev. Lett.* **99** 217601
[270] Zavaliche F, Shafer P, Ramesh R, Cruz M P, Das R R, Kim D M and Eom C B 2005 *Appl. Phys. Lett.* **87** 252902
[271] Shafer P, Zavaliche F, Chu Y H, Yang P-L, Cruz M P and Ramesh R 2007 *Appl. Phys. Lett.* **90** 202909
[272] Balke N, Choudhury S, Jesse S, Huijben M, Chu Y H, Baddorf A P, Chen L Q, Ramesh R and Kalinin S V 2009 *Nature Nanotech.* **4** 868
[273] Bratkovsky A M and Levanyuk A P 2001 *Phys. Rev.* B **63** 132103
[274] Zhou C and Newns D M 1997 *J. Appl. Phys.* **82** 3081
[275] Dagata J 2007 *Electrical and Electromechanical Phenomena on the Nanoscale by Scanning Probe Microscopy* vol 2 ed S V Kalinin and A Gruverman (Berlin: Springer)
[276] Cunningham S, Larkin I A and Davis J H 1998 *Appl. Phys. Lett.* **73** 123
[277] Bonnell D (ed) 2000 *Scanning Probe Microscopy and Spectroscopy* (New York: Wiley-VCH)
[278] Hu J, Xiao X D and Salmeron M 1995 *Appl. Phys. Lett.* **67** 476
[279] Sugimura H, IshidaY, Hayashi K, Takai O and Nakagiri N 2002 *Appl. Phys. Lett.* **80** 459
[280] Dagata J A, Inoue T, Itoh J, Matsumoto K and Yokoyama H 1998 *J. Appl. Phys.* **84** 6891
[281] Kalinin S V and Bonnell D A 2000 *J. Appl. Phys.* **87** 3950
[282] Kalinin S V, Johnson C Y and Bonnell D A 2002 *J. Appl. Phys.* **91** 3816
[283] Peter F, Szot K, Waser R, Reichenberg B, Tiedke S and Szade J 2004 *Appl. Phys. Lett.* **85** 2896
[284] Woicik J C, Li H, Zschack P, Karapetrova E, Ryan P, Ashman C R and Hellberg C S 2006 *Phys. Rev.* B **73** 024112

[285] Henrich V E and Cox P A 1994 *The Surface Science of Metal Oxides* (Cambridge: Cambridge University Press)
[286] Spanier J E, Kolpak A, Grinberg I, Urban J J, Ouyang L, Yun W S, Rappe A M and Park H 2006 *Nano Lett.* **6** 735
[287] Kalinin S V and Bonnell D A 2004 *Nano Lett.* **4** 560
[288] Kalinin S V and Bonnell D A 2001 *Phys. Rev.* B **63** 125411
[289] Kim Y, Bae C, Ryu K, Ko H, Kim Y K, Hong S and Shin H 2009 *Appl. Phys. Lett.* **94** 032907
[290] Yun Y, Wang J and Altman E I 2008 *J. Catal.* **253** 295
[291] Zhao M H, Bonnell D A and Vohs J M 2008 *Surf. Sci.* **602** 2849
[292] Wang R V *et al* 2009 *Phys. Rev. Lett.* **102** 047601
[293] Fong D D *et al* 2006 *Phys. Rev. Lett.* **96** 127601
[294] Peter F, Kubacki J, Szot K, Reichenberg B and Waser R 2006 *Phys. Status Solidi* a **203** 616
[295] Maksymovych P, Jesse S, Huijben M, Ramesh R, Morozovska A, Choudhury S, Chen L Q, Baddorf A P and Kalinin S V 2009 *Phys. Rev. Lett.* **102** 017601
[296] Kalinin S V and Bonnell D A 2004 *Nano Lett.* **4** 555
[297] Verdaguer A, Sacha G M, Bluhm H and Salmeron M 2006 *Chem. Rev.* **106** 1478
[298] Sacha G M, Verdaguer A and Salmeron M 2006 *J. Phys. Chem.* B **110** 14870
[299] Weeks B L, Vaughn M W and DeYoreo J J 2005 *Langmuir* **21** 8096
[300] Sheehan P E and Whitman L J 2002 *Phys. Rev. Lett.* **88** 156104
[301] Dahan D, Molotskii M, Rosenman G and Rosenwaks Y 2006 *Appl. Phys. Lett.* **89** 152902
[302] Kholkin A L, Bdikin I K, Shvartsman V V and Pertsev N A 2007 *Nanotechnology* **18** 095502
[303] Kim Y, Bühlmann S, Hong S, Kim S-H and No K 2007 *Appl. Phys. Lett.* **90** 072910
[304] Bühlmann S, Colla E and Muralt P 2005 *Phys. Rev.* B **72** 214120
[305] Garcia R, Martinez R V and Martinez J 2006 *Chem. Soc. Rev.* **35** 29
[306] Dagata J A, Schneir J, Harary H H, Evans C J, Postek M T and Bennett J 1990 *Appl. Phys. Lett.* **56** 2001
[307] Krämer S, Fuierer R R and Gorman C B 2003 *Chem. Rev.* **103** 4367
[308] Garcia V, Fusil S, Bouzehouane K, Enouz-Vedrenne S, Mathur N D, Barthélémy A and Bibes M 2009 *Nature* **460** 81
[309] Molotskii M 2003 *J. Appl. Phys.* **93** 6234
[310] Molotskii M, Agronin A, Urenski P, Shvebelman M, Rosenman G and Rosenwaks Y 2003 *Phys. Rev. Lett.* **90** 107601
[311] Molotskii M and Shvebelman M 2005 *Phil. Mag.* **85** 1637
[312] Molotskii M 2005 *J. Appl. Phys.* **97** 014109
[313] Molotskii M and Shvebelman M 2004 *Ferroelectrics* **301** 67
[314] Morozovska A N, Svechnikov S V, Eliseev E A, Jesse S, Rodriguez B J and Kalinin S V 2007 *J. Appl. Phys.* **102** 114108
[315] Hanggi P, Talkner P and Borkovec M 1990 *Rev. Mod. Phys.* **62** 251
[316] Tinoco I 2004 *Annu. Rev. Biophys. Biomol. Struct.* **33** 363
[317] Morozovska A N, Svechnikov S V, Eliseev E A, Jesse S, Rodriguez B J and Kalinin S V 2006 Piezoresponse force spectroscopy of ferroelectric materials arXiv:cond-mat/0610764
[318] Xue D, Wu S, Zhu Y, Terabe K, Kitamura K and Wang J 2003 *Chem. Phys. Lett.* **377** 475
[319] Kalinin S V, Jesse S, Rodriguez B J, Chu Y H, Ramesh R, Eliseev E A and Morozovska A N 2008 *Phys. Rev. Lett.* **100** 155703
[320] Morozovska A N, Svechnikov S V, Eliseev E A, Rodriguez B J, Jesse S and Kalinin S V 2008 *Phys. Rev.* B **78** 054101
[321] Morozovska A N and Eliseev E A 2006 *Phys. Rev.* B **73** 104440
[322] Glinchuk M D, Eliseev E A and Stephanovich V A 2002 *Physica* B **332** 356
[323] Guo H Y, Xu J B, Wilson L H, Xie Z, Luo E Z, Hong S B and Yan H 2002 *App. Phys. Lett.* **81** 715
[324] Kim I D, Avrahami Y, Tuller H L, Park Y B, Dicken M J and Atwater H A 2005 *Appl. Phys. Lett.* **86** 192907
[325] Kalinin S V, Gruverman A and Bonnell D A 2004 *Appl. Phys. Lett.* **85** 795
[326] Eng L M, Güntherodt H-J, Rosenman G, Skliar A, Oron M, Katz M and Eger D 1998 *J. Appl. Phys.* **83** 5973
[327] Desfeux R, Legrand C, Da Costa A, Chateigner D, Bouregba R and Poullain G 2006 *Surf. Sci.* **600** 219
[328] Jesse S, Baddorf A P and Kalinin S V 2006 *Appl. Phys. Lett.* **88** 062908
[329] Jesse S, Lee H N and Kalinin S V 2006 *Rev. Sci. Instrum.* **77** 073702
[330] Lyuksyutov S F, Paramonov P B and Vaia R A cond-mat/0505457
[331] Gómez-Moñivas S, Sáenz J J, Calleja M and García R 2003 *Phys. Rev. Lett.* **91** 056101
[332] Shin J, Kalinin S V, Lee H N, Christen H M, Moore R G, Plummer E W and Baddorf A P 2004 *J. Mater. Res.* **19** 3447
[333] Saya Y, Watanabe S, Kawai M, Yamada H and Matsushige K 2000 *Japan. J. Appl. Phys.* **39** 3799
[334] Alexe M, Harnagea C, Hesse D and Gösele U 2001 *Appl. Phys. Lett.* **79** 242
[335] Szafraniak I, Harnagea C, Scholz R, Bhattacharyya S, Hesse D and Alexe M 2003 *Appl. Phys. Lett.* **83** 2211
[336] Ma W and Hesse D 2004 *Appl. Phys. Lett.* **84** 2871
[337] Harnagea C, Pignolet A, Alexe M, Hesse D and Gösele U 2000 *Appl. Phys.* A **70** 261
[338] Ricinschi D, Mitoseriu L, Stancu A, Postolache P and Okuyama M 2004 *Integr. Ferroelectr.* **67** 103
[339] Ricinschi D, Noda M, Okuyama M, Ishibashi Y, Iwata M and Mitoseriu L 2003 *J. Korean Phys. Soc.* **42** S1232
[340] Ricinschi D and Okuyama M 2002 *Integr. Ferroelectr.* **50** 159
[341] Gruverman A, Rodriguez B J, Kingon A I, Nemanich R J, Cross J S and Tsukada M 2003 *Appl. Phys. Lett.* **82** 3071
[342] Gruverman A, Rodriguez B J, Dehoff C, Waldrep J D, Kingon A I, Nemanich R J and Cross J S 2005 *Appl. Phys. Lett.* **87** 082902
[343] Dehoff C, Rodriguez B J, Kingon A I, Nemanich R J, Gruverman A and Cross J S 2005 *Rev. Sci. Instrum.* **76** 023708
[344] Abplanalp M, Fousek J and Gunter P 2001 *Phys. Rev. Lett.* **86** 5799
[345] Rodriguez B J, Choudhury S, Chu Y H, Bhattacharyya A, Jesse S, Seal K, Baddorf A P, Ramesh R, Chen L-Q and Kalinin S V 2009 *Adv. Funct. Mater.* **19** 2053
[346] Shvartsman V V, Pertsev N A, Herrero J M, Zaldo C and Kholkin A L 2005 *J. Appl. Phys.* **97** 104105
[347] Kalinin S V, Gruverman A, Rodriguez B J, Shin J, Baddorf A P, Karapetian E and Kachanov M 2005 *J. Appl. Phys.* **97** 074305
[348] Molotskii M and Winebrand E 2005 *Phys. Rev.* B **71** 132103
[349] Emelyanov A Yu 2005 *Phys. Rev.* B **71** 132102
[350] Kalinin S V, Rodriguez B J, Jesse S, Chu Y H, Zhao T, Ramesh R, Choudhury S, Chen L Q, Eliseev E A and Morozovska A N 2007 *Proc. Natl Acad. Sci. USA* **104** 20204
[351] Morozovska A N, Eliseev E A, Svechnikov S V, Maksymovych P and Kalinin S V 2008 arXiv:0811.1768
[352] Morozovska A N, Kalinin S V, Eliseev E A, Gopalan V and Svechnikov S V 2008 *Phys. Rev.* B **78** 125407
[353] Woo C H and Zheng Y 2007 *Appl. Phys.* A **91** 59
[354] Zhirnov V A 1959 *Zh. Eksp. Theor. Fiz.* **35** 1175

Zhirnov V A 1959 *Sov. Phys.—JETP* **8** 822
[355] Cao W and Cross L E 1991 *Phys. Rev.* B **44** 5
[356] Eliseev E A, Morozovska A N, Kalinin S V, Li Y L, Jie Shen, Glinchuk M D, Chen L Q and Gopalan V 2008 Surface effect on domain wall width in ferroelectrics arXiv:0802.2559
[357] Jia C L, Nagarajan V, He J-Q, Houben L, Zhao T, Ramesh R, Urban K and Waser R 2007 *Nature Mater.* **6** 64
[358] Ducharme S, Fridkin V M, Bune A V, Palto S P, Blinov L M, Petukhova N N and Yudin S G 2000 *Phys. Rev. Lett.* **84** 175
[359] Agronin A, Rosenwaks Y and Rosenman G 2004 *Appl. Phys. Lett.* **85** 452
[360] Sidorkin A S 2006 *Domain Structure in Ferroelectrics and Related Materials* (Cambridge: Cambridge International Science Publishing)
[361] Morozovska A N, Eliseev E A, Svechnikov G S, Gopalan V and Kalinin S V 2008 *J. Appl. Phys.* **103** 124110
[362] Rodriguez B J, Jesse S, Alexe M and Kalinin S V 2008 *Adv. Mater.* **20** 109
[363] Zheng H *et al* 2004 *Science* **303** 661
[364] Le Rhun G, Vrejoiu I and Alexe M 2007 *Appl. Phys. Lett.* **90** 012908
[365] Le Rhun G, Vrejoiu I, Pintilie L, Hesse D, Alexe M and Gosele U 2006 *Nanotechnology* **17** 3154
[366] Bdikin I K, Kholkin A L, Morozovska A N, Svechnikov S V, Kim S-H and Kalinin S V 2008 *Appl. Phys. Lett.* **92** 182909
[367] Vrejoiu I, Le Rhun G, Zakharov N D, Hesse D, Pintilie L and Alexe M 2006 *Phil. Mag.* **86** 4477–86
[368] Gruverman A, Wu D and Scott J F 2008 *Phys. Rev. Lett.* **100** 097601
[369] Gregoriev A, Do D-H, Kim D M, Eom C-B, Adams B, Dufresne E M and Evans P G 2006 *Phys. Rev. Lett.* **96** 187601
[370] Bystrov V S, Bdikin I K, Kiselev D A, Yudin S, Fridkin V M and Kholkin A L 2007 *J. Phys. D: Appl. Phys.* **40** 4571
[371] Kalinin S V, Rodriguez B J, Jesse J, Morozovska A N, Bokov A A and Ye Z-G 2009 *Appl. Phys. Lett.* **95** 142902
[372] Kalinin S V, Rodriguez B J, Budai J D, Jesse S, Morozovska A N, Bokov A A and Ye Z-G 2010 *Phys. Rev.* B **81** 064107
[373] Stolichnov I A, Tagantsev A K, Setter N, Cross J S and Tsukada M 1999 *Appl. Phys. Lett.* **74** 3552
[374] Stolichnov I, Tagantsev A, Setter N, Cross J S and Tsukada M 1999 *Appl. Phys. Lett.* **75** 1790
[375] Stolichnov I, Tagantsev A, Colla E, Gentil S, Hiboux S, Baborowski J, Muralt P and Setter N 2000 *J. Appl. Phys.* **88** 2154
[376] Stolichnov I, Colla E, Tagantsev A, Bharadwaja S S N, Hong S, Setter N, Cross J S and Tsukada M 2002 *Appl. Phys. Lett.* **80** 4804
[377] Kim D J, Jo J Y, Kim T H, Yang S M, Chen B, Kim Y S and Noh T W 2007 *Appl. Phys. Lett.* **91** 132903
[378] Christman J, Kim S-H, Maiwa H, Maria J-P, Rodriguez B, Kingon A and Nemanich R 2000 *J. Appl. Phys.* **87** 8031
[379] So Y W, Kim D J, Noh T W, Yoon J-G and Song T K 2005 *Appl. Phys. Lett.* **86** 092905
[380] So Y W, Kim D J, Noh T W, Yoon J-G and Song T K 2005 *J. Korean Phys. Soc.* **46** 40
[381] Jo J Y, Han H S, Yoon J-G, Song T K, Kim S-H and Noh T W 2007 *Phys. Rev. Lett.* **99** 267602
[382] Tagantsev A K, Stolichnov I, Setter N, Cross J S and Tsukada M 2002 *Phys. Rev.* B **66** 214109
[383] Lia W and Alexe M 2007 *Appl. Phys. Lett.* **91** 262903
[384] Bintachitt P, Trolier-McKinstry S, Seal K, Jesse J and Kalinin S V 2009 *Appl. Phys. Lett.* **94** 042906
[385] Lu X, Schlaphof F, Grafstrom S, Loppacher C, Eng L, Suchaneck G and Gerlach G 2002 *Appl. Phys. Lett.* **81** 3215
[386] Gysel R, Tagantsev A K, Stolichnov I, Setter N and Pavius M 2006 *Appl. Phys. Lett.* **89** 082906
[387] Balke N, Ramesh R and Kalinin S V 2010 submitted
[388] Choudhury S, Zhang J X, Li X L, Chen L Q, Jia Q X and Kalinin S V 2008 *Appl. Phys. Lett.* **93** 162901
[389] Ng N, Ahluwalia R, Su H B and Boey F 2009 *Acta Mater.* **57** 2047
[390] Chen L Q 2008 *J. Am. Ceram. Soc.* **91** 1835
[391] Khachaturyan A G 1983 *Theory of Structural Transformations in Solids* (New York: Wiley)
[392] Khachaturyan A G and Shatalov G A 1969 *Sov. Phys.—JETP* **29** 557 (Engl. Transl.)
[393] Li Y L, Hu S Y, Liu Z K and Chen L Q 2001 *Appl. Phys. Lett.* **78** 3878
[394] Li Y L, Hu S Y, Liu S K and Chen L Q 2002 *Acta Mater.* **50** 395
[395] Stroh A N 1962 *J. Math. Phys.* **41** 77
[396] Li Y L, Hu S Y, Liu Z K and Chen L Q 2002 *Appl. Phys. Lett.* **81** 427
[397] Person G L and Feldmann W L 1958 *J. Phys. Chem. Solids* **9** 28
[398] Distler G I, Konstantinova V P, Gerasimov V M and Tolmacheva G A 1968 *Nature* **218** 762
[399] Distler G I 1968 *J. Cryst. Growth* **3** 175
[400] Giocondi J L and Rohrer G S 2001 *J. Phys. Chem.* B **105** 8275
[401] Jones P, Gallardo D E and Dunn S 2008 *Chem. Mater.* **20** 5901
[402] Jones P and Dunn S 2007 *Nanotechnology* **18** 185702
[403] Jones P M and Dunn S 2009 *J. Phys. D: Appl. Phys.* **42** 065408
[404] Dunn S, Jones P M and Gallardo D E 2007 *J. Am. Chem. Soc.* **129** 8724
[405] Liu X, Kitamura K, Terabe K, Hatano H and Ohashi N 2007 *Appl. Phys. Lett.* **91** 044101
[406] Habicht S, Nemanich R J and Gruverman A 2008 *Nanotechnology* **19** 495303
[407] Dunn S and Cullen D 2004 *Appl. Phys. Lett.* **85** 3537
[408] Haussmann A, Wenzel M T, Grafström S, Härtling T, Loppacher C and Eng L M. ISFD9 2006 poster; http://ppprs1.phy.tu-dresden.de/~loppacher/publikationen/pdf/Haussmann_isfd9-2006.pdf
[409] Kalinin S V and Bonnell D A 2002 *Phys. Rev.* B **65** 125408
[410] Rodriguez B J, Jesse S, Baddorf A P and Kalinin S V 2006 *Phys. Rev. Lett.* **96** 237602
[411] Kalinin S V, Rodriguez B J, Jesse S, Seal K, Proksch R, Hohlbauch S, Revenko I, Thompson G L and Vertegel A A 2007 *Nanotechnology* **18** 424020
[412] Rodriguez B J, Jesse S, Habelitz S, Proksch R and Kalinin S V 2009 *Nanotechnology* **20** 195701
[413] Rodriguez B J, Jesse S, Baddorf A P, Kim S-H and Kalinin S V 2007 *Phys. Rev. Lett.* **98** 247603
[414] Rodriguez B J, Jesse S, Seal K, Baddorf A P, Kalinin S V and Rack P 2007 *Appl. Phys. Lett.* **91** 093130
[415] Frederix P L T M, Gullo M R, Akiyama T, Tonin A, de Rooij N F, Staufer U and Engel A 2005 *Nanotechnology* **16** 997
[416] Kranz C, Friedbacher G, Mizaikoff B, Lugstein A, Smoliner J and Bertagnolli E 2001 *Anal. Chem.* **73** 2491
[417] Macpherson J V and Unwin P R 2000 *Anal. Chem.* **72** 276
[418] Gruverman A, Isobe C and Tanaka M 2001 *Mater. Res. Soc. Symp. Proc.* **655** CC8.5
[419] Watanabe Y 2007 *Ferroelectrics* **349** 190
[420] Rodríguez Contreras J, Kohlstedt H, Poppe U, Waser R, Buchal C and Pertsev N A 2003 *Appl. Phys. Lett.* **83** 4595
[421] Kohlstedt H, Pertsev N A, Rodríguez Contreras J and Waser R 2005 *Phys. Rev.* B **72** 125341
[422] Maksymovych P, Jesse S, Yu P, Ramesh R, Baddorf A P and Kalinin S V 2009 *Science* **324** 1421